Carbon-based Electrodes in Neuroscience:

Fundamental Electrochemistry and Nanoelectrode Development

Zijun Shao

Jilin city, Jilin, China

Bachelor of Science,

Sichuan University,

Chengdu, Sichuan, China, 2017

A Dissertation Presented to the Graduate Faculty of the University of Virginia in Candidacy for the Degree of Doctor of Philosophy

Department of Chemistry

University of Virginia

April, 2023

Abstract

For decades, carbon-fiber microelectrodes (CFMEs) have been a fundamental tool coupled with fast-scan cyclic voltammetry (FSCV) for real-time neurotransmitter detection. Although CFMEs have been widely used and have good electrochemical performance, the limitations cannot be ignored, including the lack of selectivity, poor fouling resistance, and size incompatible with synapse measurements. This dissertation aims to overcome the limitations of CFMEs by using various carbon-based electrodes and studying their electrochemical behaviors and aspects of sensing performance and mass transport near the electrode surface.

Chapter 1 describes the fundamental theories of FSCV, different types of electroactive neurotransmitters, surface properties of carbon nanomaterials, and techniques of nanofabrication. Chapter 2 and 3 introduces CNT yarn microelectrodes and the role of thin layer electrochemistry in selective detecting multiple neurotransmitters with FSCV, including cationic catecholamines and anionic neurochemicals. Chapter 4 explores the electrochemical performance of carbon nanospike (CNS) nanoelectrodes, which are fabricated by depositing CNSs on an etched metal wire. Chapter 5 introduces a uniformly-coated, MPCVD synthesized nanodiamond electrodes with excellent electrode fouling resistance. It then explores the electrochemical behavior after surface treatment with oxygen plasma in neurotransmitter detection. Chapter 6 addresses the development of a long, straight, and nano-sized needle with the novel 3D nano-printing technique and the optimization of the carbon electrode shape. Chapter 7 covers the challenges and future directions of electrochemical sensing performance using carbon nanomaterials and nanofabrication techniques.

Overall, this dissertation focuses on the surface chemistry of carbon nanomaterials and how it affects neurotransmitter sensing, and addresses new methods to develop carbon-based electrodes for electrochemical sensing. This dissertation addresses how we overcome the limitations of CFMEs with FSCV, which may benefit the field in monitoring neurochemicals.

Table of Contents

Acknowledgement

I would like to express my sincere gratitude to my advisor, Dr. Jill Venton, for her guidance and support throughout my PhD career. As a teacher, her Youtube videos about electrochemistry and FSCV has benefit my study; as a scientist, her advices were valuable and helped me stay on track. I thank Dr. Venton for managing such a friendy and diverse lab with different backgounds but the same warm heart. I would like to acknowledge all labmates in Venton lab for their assistance in helping me study and prepare my presentation. Special thanks to my mentors, Dr. Pumidech Puthongkham and Dr. Qun Cao, who trained me on the FSCV system and taught me electrochemistry and provided suggestions. Special thanks to my labmate, Kelly Dunham, who joined the lab the same year with me, for her kindly help in daily life and detailed notes in the group meeting.

I am also deelply grateful to those talented scientist in the Oak Ridge National Labrotory, including Nickolay Lavrik, Leslie Wilson, and Dale Hensley, who trained my on the instruments and provided professional suggestions. Nick guided my in the 3D printing project, Leslie synthesized nanodiamond and Dale synthesized carbon nanospikes for me. During the mass shut-down in COVID-19 pandemic, they kept preparing and sending samples to me, which avoided my project stoppage. Without their cooperation, my research would not have been finished.

Finally, I thank my family for their support and being a solid back of me for 5 years. I wish them health and long life. I thank my cousin for bring a new life of my niece. I wish them a great success and happiness. I would also like to acknowledge my friends, Xueni Huang and Xiao Ma, who are also a lovely couple and entertained my

life. Special thanks to Yuanyu Chang for his multi-identity: a good friend in college, a nice colleage in lab, and a patient and careful husband in life. We’ve been knowing each other for 10 years and I am grateful for the amazing time we spent together.

Chapter 1

Introduction

1.1 Fast-Scan Cyclic Voltammetry for Neurotransmitter Detection

Electrochemistry enables the study of chemical processes involving electron transfer and has been applied in solving a wide range of analytical chemical problems. Electrochemical sensing is now the gold standard for the characterization and quantification of neurotransmitters, which carry chemical messages between neurons. To monitor neurotransmission in vivo, various electrochemical techniques have been applied, such as amperometry, differential pulse voltammetry, and cyclic voltammetry.[1–4] Fast-scan cyclic voltammetry (FSCV), which is modified from classical cyclic voltammetry, was popularized by R. M. Wightman after the 1980s and it is the most popular electrochemical method to measure neurotransmitters by now.[5,6]

1.1.1 Fundamentals of Fast-Scan Cyclic Voltammetry

Fast-scan cyclic voltammetry is a type of voltammetry that uses an extremely fast scan rate (typically 400 V/s), which is about a hundred to a thousand times higher than conventional cyclic voltammetry (normal scan rate of 100 mV/s).[3,7] FSCV is always performed at microelectrodes to reduce the massive electric double layer charging current.[5,8–10] The fast scan rate of FSCV enables rapid measurement of neurotransmitters with a subsecond temporal resolution.[11,12] Figure 1.1A shows a typical FSCV waveform for dopamine detection using carbon-fiber microelectrodes (CFMEs). The potential ramps from -0.4 V to 1.3 V and back to -0.4V with a scan rate of 400 V/s, thus, one measurement only takes 8.5 ms. The typical repetition frequency of one FSCV measurement is 10 Hz, so the holding time between two cycles is 91.5 ms. The relatively long time at holding potential between each cycle enables more adsorption for cationic dopamine molecules. One can also regulate the repetition frequency to achieve different goals. Figure 1.1A also illustrates the dopamine waveform at 100 Hz, where the holding time for each cycle largely decreases to 1.5 ms.[13,14]

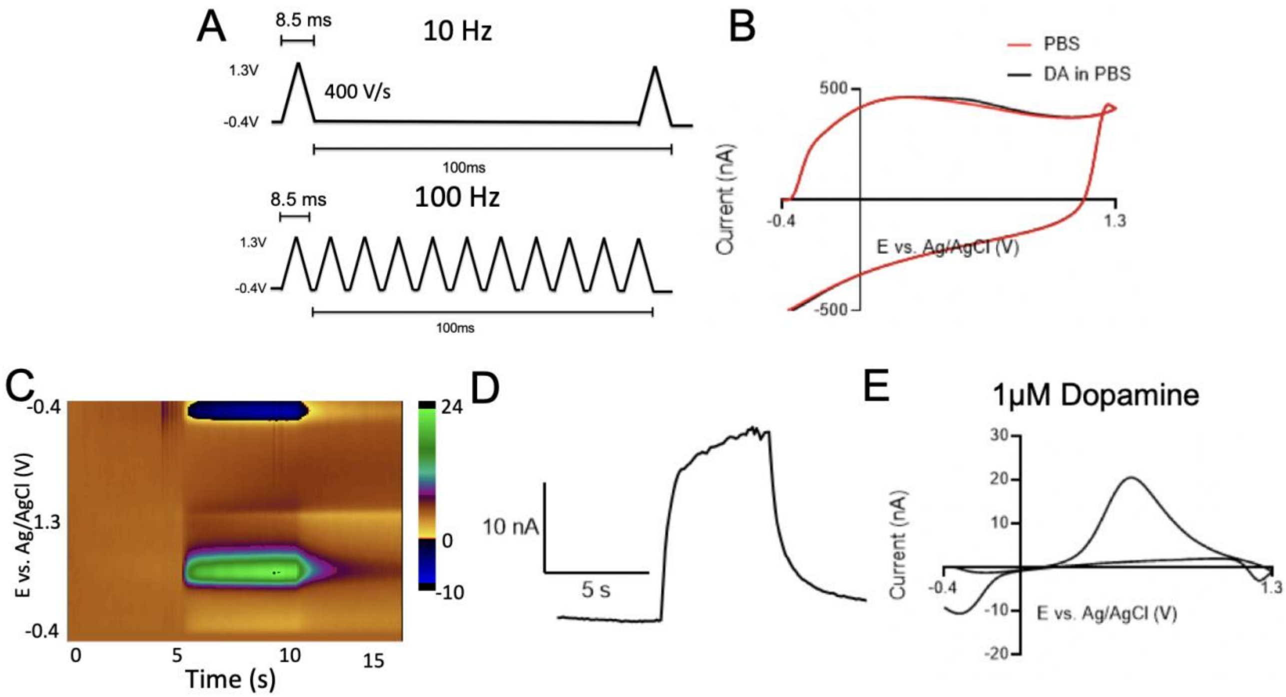

Figure 1.1. FSCV detection of dopamine. (A) a typical triangle waveform for dopamine at 10 Hz and 100 Hz. Potential ramps from -0.4 V to 1.3 V and back with scan rate of 400 V/s. (B) Background charging current of PBS buffer and 1 μM dopamine solution. (C) False color plot of one measurement. (D) Current vs. time curve, collected by taking a horizontal trace on the color plot. (E) Background subtracted cyclic voltammogram for 1 μM dopamine.

When applying potential to the electrode, the ions around the electrode surface are rearranged and the electric double layer charging forms to generate a non-Faradaic background charging current, which can be calculated by

$$i_{BG} = vCd$$

The charging current (i) is proportional to scan rate (v), and electrical double layer capacitance (Cd).[15] In conventional cyclic voltammetry, the background current is usually small and negligible, however, the charging current becomes large in FSCV because it is proportional to the scan rate. When measuring FSCV signals of electroactive species, the Faradaic current from redox reactions is small compared with the charging current (Figure 1B).[1,3,16] Therefore, it is necessary to subtract the background to produce unique cyclic voltammograms for electroactive species. Figure 1D shows the background-subtracted CV of 1 mM dopamine. With a scan rate of 400 V/s, a typical dopamine CV has an oxidation peak that occurs at 0.6 V and a reduction peak at -0.2 V, which is different from conventional CV. There are several reasons for the unique CV shapes: First, the peak-to-peak separation is large because of the extremely fast scan rate. Second, the symmetrical CV shape, instead of the duck-shape, is due to the adsorption-controlled process of dopamine detection.[1,17,18] Finally, the oxidation peak current is larger than the reduction peak, because the redox product DOQ has less adsorption affinity than dopamine.

More information is shown in the false color plot (Figure 1D) to visualize large amounts of data in a three-dimensional way. The x-axis shows the time of a single run, the y-axis is the potential, and the false color represents the current. The green color means oxidation current, whereas the blue means reduction. The color plot illustrates the 15-second injection of a single run that dopamine solution was injected at 5 s, followed with PBS buffer rinsing at 10 s. The color plot provides rich information in one data file, including current vs. time, current vs. potential, peak-o-peak separation, and time response.

1.1.2 Carbon Fiber Microelectrodes for Neurotransmitter Detection

Carbon-fiber microelectrodes (CFMEs) have been the standard electrodes for neurotransmitter detection in real-time because their good biocompatibility and small size (7 μm diameter) allow less damage to the tissue.[18–21] Carbon fibers have the same chemical structure as graphite, which are both sp2 hybridized. Carbon fibers have a good electrochemical performance because the extended conjugation enables fast electron transfer kinetics and a low RC resistance.[22,23] In addition, the surface of carbon fibers contains oxygen functional groups that favor the adsorption of cationic neurotransmitters, such as dopamine, by electrostatic interactions.[24,25]

CFMEs demonstrate a good sensitivity and reliable performance in neurotransmitter detection with FSCV, however, there are drawbacks that limit CFMEs in biological applications. First, the 7 μm diameter is relatively large for measurements in the neuron synapse, which has a submicron width.[26,26,27] Second, the temporal resolution of CFMEs is relatively low. FSCV has always been performed at 10 Hz because a higher repetition frequency dramatically reduces the electrochemical signals.[28,29] Third, CFMEs are not capable to differentiate electroactive neurotransmitters with similar oxidation peak positions, such as catecholamines.[4,30–32] Fourth, CFMEs suffer from severe electrode fouling that insulated film covers the surface and negatively affects the electrochemical performance.[33–37] Thus, it is vital to develop new carbon-based microelectrodes to overcome limitations in neurotransmitter detection. The theme of this dissertation is new strategies to overcome limitations of electrochemical detection of neurotransmitters.

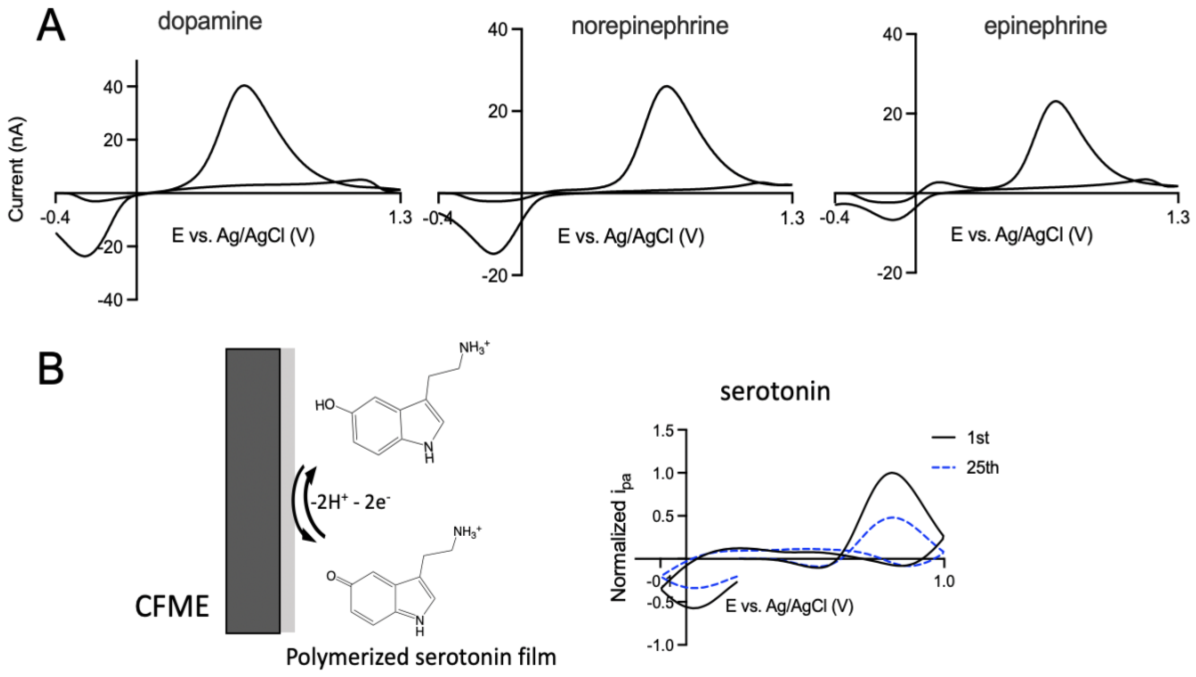

Figure 1.2. (A) CVs of dopamine, norepinephrine and epinephrine that obtained at CFMEs. (B) Illustration of electrode fouling in serotonin measurement.

1.2 Electrochemistry of Common Neurochemicals

Neurotransmitters are chemical messengers that transfer information between neurons and other cells. Typically, neurotransmitters are synthesized in neurons and packed in specialized synaptic vesicles, and then released by exocytosis.[19,32,38] The sensing of electroactive neurotransmitters is challenging because the concentration of released neurotransmitters is low and changed on a subsecond timescale. The dysregulation of neurotransmission causes cognitive dysfunctions, such as Parkinson’s disease, Alzheimer’s disease, depression, and drug addiction.[8,38–41]

1.2.1 Catecholamines

Catecholamine neurotransmitters, including dopamine, norepinephrine, and epinephrine, are monoamines with a catechol moiety derived from a tyrosine precursor. Dopamine (DA) modulates motor and cognitive functions and the reward system, and is also a standard analyte to evaluate new electrochemical sensors.[13,14,42] Norepinephrine influences sleep and wakefulness, attention, and feeding behavior.[43,44] Epinephrine causes fight or flight responses and has been used as a common emergency medicine.[44–46] The formal potentials of catecholamines are all +0.2 V vs Ag/AgCl, because they share the similar chemical structure and same catechol moiety that can undergo redox reactions.[47,48] Figure 1.3 shows the redox mechanism of dopamine as an example. Dopamine is oxidized to dopamine-ortho-quinone (DOQ) via a two-electron process at a potential higher than 0.2 V vs. Ag/AgCl. Then, DOQ undergoes a cyclization reaction via Michael addition to leucodopamine, which can further be oxidized to dopaminechrome.[49,50] Norepinephrine and epinephrine undergo similar two-electron oxidation pathways and generate the final products norepinephrinechrome and epinephrinechrome. In conventional cyclic voltammetry, the secondary oxidation signals are barely detected due to the slow detection and low concentration, whereas in FSCV with a sub-second time scale, the secondary peaks are observable. Chapter 2 will discuss more on the electrochemical signals of catecholamines at carbon microelectrodes and the unique observation of secondary reactions.

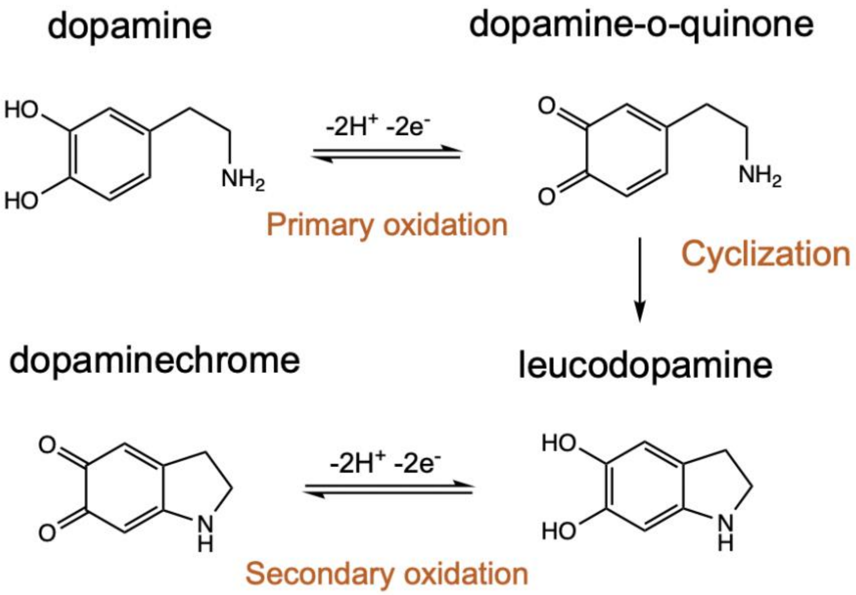

Figure 1.3. Mechanism of dopamine oxidation.

1.2.2 Anionic Neurochemicals

In addition to neurotransmitters, many other electroactive neurochemicals play an important role and interfere with neurotransmission in the brain, for example, ascorbic acid (AA) and 3,4-dihydroxyphenylacetic acid (DOPAC).[51–53] Both neurochemicals are anionic at physiological pH 7.4 and present in the brain. AA is one of the most abundant antioxidants (1 to 2 mM in whole brain) in the central nervous system and DOPAC is a major metabolite of dopamine.[51,54] Figure 1.4 shows the redox mechanisms of DOPAC and AA at carbon electrodes. AA and DOPAC interfere with the detection of dopamine because they both have higher concentrations than dopamine in the brain with oxidation peaks at similar positions.[55,56] Thus, many studies have concentrated on the development of an electrochemical sensor for higher sensitive and selective simultaneous detection. Differential pulse voltammetry (DPV) has been widely investigated to differentiate dopamine from the interference of DOPAC and AA by showing slight peak shifts in the voltammograms, whereas it is not suitable for rapid neurotransmitter detection.[4,31] However, the detection of anionic species with FSCV needs a higher concentration than normal, because anions are electrostatically repelled by the negative holding and lead to a smaller concentration near the electrode. Chapter 3 will cover methods for selective detection of dopamine with interference of AA and DOPAC based on the combination effect of thin-layer electrochemistry and electrostatic effect.

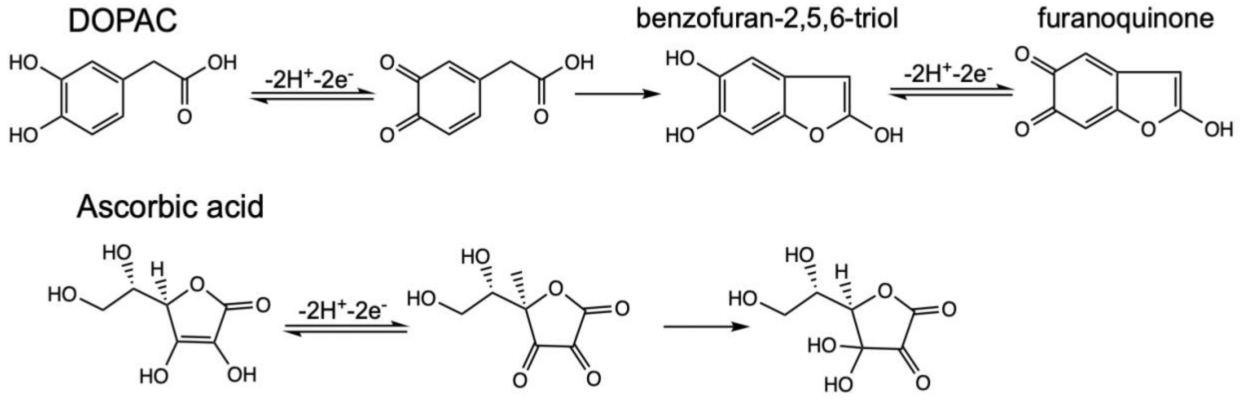

Figure 1.4. Redox pathways of DOPAC and AA.

1.2.3 Neurotransmitter Fouling

In neurochemical detection, electrode fouling is a major concern because it negatively affects the electrode performance by reducing surface area, electron transfer kinetics, and sometimes stability.[33,57,58] The fouling agent could be macro-size biomolecules, such as proteins, or polymeric species whose polymer byproducts prevent species of interest from physically attaching to the electrode surface by electrostatic force or hydrophobic interactions.[37,59,60] Typical polymeric electroactive neurotransmitters include histamine, serotonin, tyramine, and octopamine.[37,61,62] Fouled electrodes have less sensitivity and slower kinetics during measurement, thus, the fouling resistance is vital for electrochemical sensor development.

Serotonin (5-hydroxytryptamine) is an indolamine neurotransmitter that regulates diverse physiological processes, including depression, anxiety disorders, and sleep regulation.[63,64] Serotonin oxidation involves a two-electron redox reaction on the indole ring. The positive oxidation product is easily dimerized with another serotonin molecule to generate byproducts, which rapidly polymerize to form a macromolecule film and foul the electrode (Figure 1.2). In addition, the metabolite of serotonin, 5-hydroxyindole acetic acid (5HIAA), also undergoes a similar polymerization pathway that causes more electrode fouling.[41,65] Other fouling neurotransmitters, including tyramine and histamine, also form insulating polymer films and block the electrode surface, which dramatically affects the electrochemical performance of carbon electrodes. Thus, many strategies have been investigated to improve the anti-fouling property of the electrode, such as changing the surface hydrophobicity and coating with foul resisted materials.[36,37,60] Chapter 5 will cover the development of nanodiamond microelectrodes with a high fouling resistance.

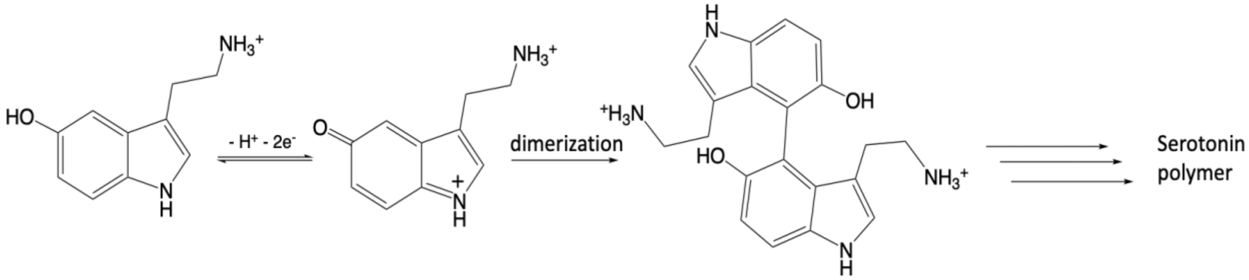

Figure 1.5. Mechanism of serotonin polymerization.

1.3 Fabrication of Carbon Electrodes

1.3.1 Drop-casting, Dip-coating and Electrophoretic deposition

Drop casting and dip coating are simple ways to manually coat a thin film of nanomaterials on electrodes for small-scale purposes, where nanomaterial-contained dispersion is added to the surface. Both methods are followed by evaporation of the volatile solvent with nanomaterials spread on the solid substrate.[24] The thickness of the coating is controllable by the volume and concentration of the solution. Drop-casting and dip-coating enable nanomaterial coating without introducing extra external factors, such as mechanical stress. Electrophoretic deposition of electroplating uses electrostatic force or electrochemical reactions to assist nanomaterial deposition on a conducting surface. These methods are easy to operate and widely used to deposit commercial-available carbon nanomaterials on solid substrates, but the coating is usually not uniform, which requires additional optimization.[66] Different approaches are used to modify carbon electrodes with nanoparticles depending on the structure and material.

1.3.2 Chemical vapor deposition of carbon nanomaterials

Chemical vapor deposition (CVD) is the most common thin-film deposition technique to produce solid nanomaterials with high quality, high yield, and high performance. In typical CVD, volatile precursors react and decompose on the solid substrate to deposit the desired material film, followed by a cleaning process that uses gas flow to remove volatile byproducts from the reaction chamber.[67,68] As a diffusive, gas-driven process, it allows better surface coverage on uneven surfaces. CVD technique has various formats to achieve a wide range of deposition, which are classified by the mechanism to initiate the chemical reactions, for example, low-pressure CVD, ultra-high vacuum CVD, microwave plasma-assisted CVD, and plasma-enhanced CVD, etc.[68]

Carbon nanotubes are widely synthesized via CVD and usually requires catalyst, including Fe, Ni, Mo, and Co, which have good carbon diffusibility and carbon solubility.[68,69] CVD-synthesis of CNTs is advantageous because of mass fabrication, high yield, relatively low temperature (500 to 1100 C), and structure control. Depending on the different temperatures, vapor pressures, and catalyst concentrations, CNTs are grown with controllable structures and morphology including their alignment, length, wall number, and diameter. In the CVD chamber, the gas-phased-carbon precursor adheres to the substrate and decomposes on metal catalyst particles, which will be removed in the post-procedure depending on requirements.[22,67] Atomic carbon saturates the metal nanoparticles and undergoes a series of nucleation reactions. Based on the adherence between the catalyst and substrate, CNTs precipitate from the catalyst nanoparticle following either tip-growth or root-growth mechanism. For example, Choi et al. reported the synthesis of CNTs with microwave plasma-enhanced CVD (MWCVD) at a temperature ranging from 520 to 700 C that CNTs curl at the low temperature, whereas become straight at temperatures above 600 C.[70,71] Liquid injection chemical vapor deposition (LICVD) allows mass fabrication of vertically aligned CNT with high purity. With pumping metallocene-hydrocarbon solution during synthesis, additional catalysts are not required.[67,72]

Carbon nanospikes (CNSs), a spike-like sp2-hybridized carbon material, are also synthesized via plasma-enhanced CVD (PECVD), which uses radio frequency, alternating current frequency, or direct current discharge to generate the plasma of the reacting gases.[73,74] PECVD allows deposition at a lower temperature while maintaining good conformity, high quality, and high deposition rates because the existence of plasma provides extra energy to drive the nucleation reactions. Due to the relatively low reaction temperature, the PECVD process creates less stress between the deposited thin film and solid substrates with different thermal expansion. The growth of CNSs via PECVD does not require a metal catalyst, thus, it enables a high-yield, high-purity, and mass-scale coating.[75,76]

Another carbon-based material that is not based on graphene is diamond, and synthesis of diamonds with CVD has also garnered attention because of its cheap cost and high controllability. By regulating the gas precursors, vacuum pressure, and reacting temperature in the CVD chamber, various types of diamonds can be synthesized, including single-crystal diamonds, doped diamonds, and polycrystalline diamonds.[77,78] These different processing parameters also affect the hardness, conductivity, and optical properties of a synthetic diamond. Microwave plasma CVD (MPCVD) is one of the effective CVD processes that enable the growth of polycrystalline/nanodiamond, where a microwave power source is used to generate plasma by increasing the internal energy of the gas molecules. Saturday et al. (Figure 1.6) reported the growth of polycrystalline diamond film via MPCVD. By regulating the content of methane, hydrogen, and argon in the gas mixture, different grain sizes and thermal conductivity of polycrystalline diamond are produced.[79] In addition, CVD can be used to synthesize other carbon allotropes including fullerenes, carbon nanofibers (CNF), graphene, carbide-derived carbon (CDC), and carbon nano-onion (CNO).[80–83] Generally, CVD is considered to be low-cost compared with other synthetic techniques such as laser ablation and arc discharge, but it requires a long-time growth of carbon materials.

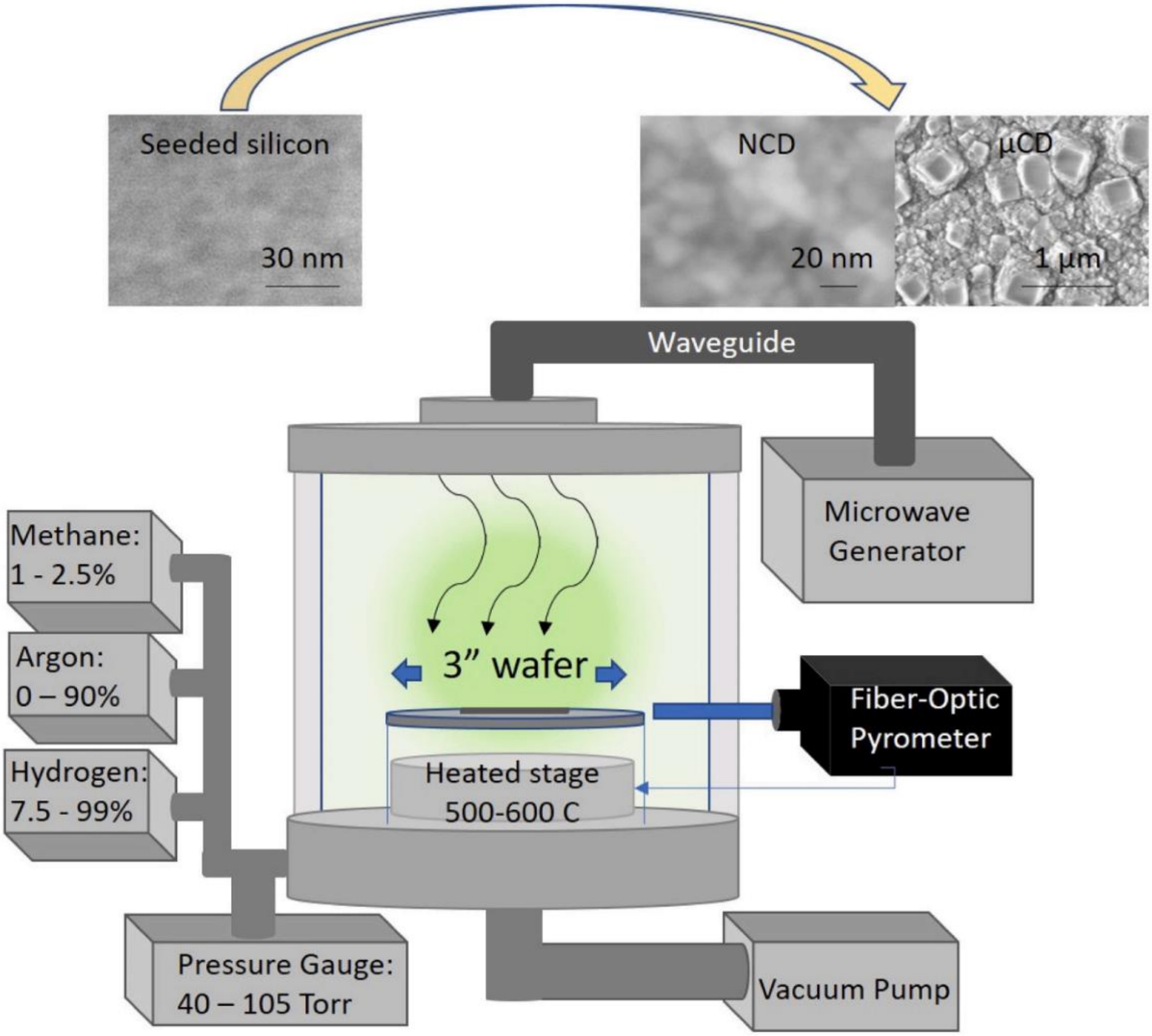

Figure 1.6. A schematic of nanocrystalline diamond synthesis using MPCVD. Reprinted from Elsevier (Saturday, Leo, et al, Diamond and Related Materials 113 (2021): 108279.).

1.3.3 Photolithography and Direct Laser Writing

Photolithography, or optical lithography, is a microfabrication technique that uses light to transfer a pattern from an optical mask onto a substrate coated with a photoresist film. Photoresist is a light-sensitive chemical that either breaks down or hardens when exposed to a light source. SU-8 is a common epoxy-based negative-tone photoresist, which means it gets cross-linked under the ultraviolet light.[84–86] Figure 1.6 illustrates a typical photolithography process to create a pattern on a silicon chip. The viscous SU-8 photoresist is spin-coated on a Si wafer and covered by an optical mask with a designed pattern. Under the UV light, the exposed SU-8 photoresist hardens by chemical cross-linking, whereas the rest under the mask remains soluble and is washed away during development. The hardened part remains on the wafer after rinsing; the pattern is transferred from the mask to the Si substrate. Photolithography is the most common microfabrication technique and is widely used in fabricating integrated chips and microfluidic chips, however, it has limitations. First, the resolution of photoresist is largely dependent of the diffraction limit of light. Second, it is not suitable for curved surfaces that generate shadows under the light.[85,86]

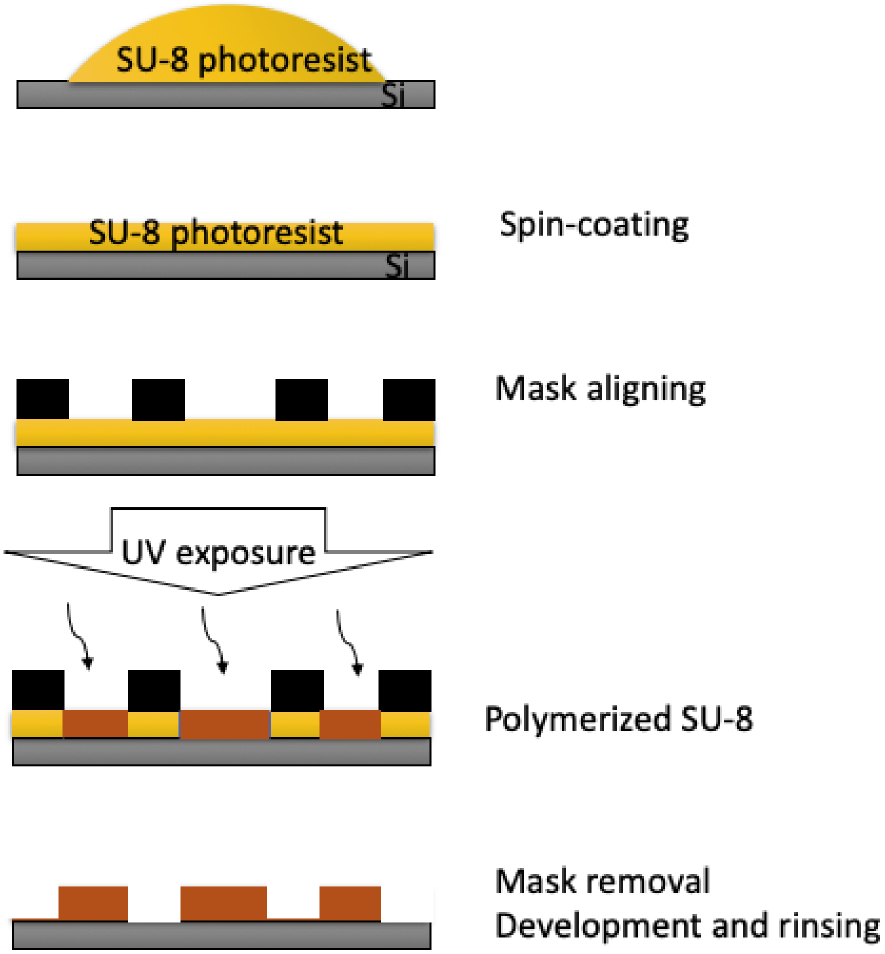

Figure 1.7. Schematic illustration of photolithography process using SU-8 photoresist.

Direct laser writing (DLW) is a laser-assisted photolithography process that allows three-dimensional printing, which utilizes two photons adsorption to polymerize the photosensitive material. It was first designed to write patterns of metals for electronic devices, but now has extensive applications in rapid prototyping of structures with fine features, such as micromechanic and microfluidic devices. Unlike optical photolithography, DLW does not require layer-by-layer fabrication or recoating but it offers high resolution in nano-size.[87–89] Materials are also not limited to wafers. DLW uses a high-intensity laser beam to focus on an interior spot of a transparent material, which absorbs photons to polymerize and construct complex structures. DLW enables the fabrication of tailored complex structures directly from a digital file; thus it guarantees consistency in constructing a large number of samples. 3D nanoprinting is developed from DLW with 100 nm resolution and has been applied in carbon electrode development.[90] Figure 1.7 illustrates the fabrication process of 3D-printed carbon microelectrodes. Niobium wires are mounted on the stage to serve as a metal substrate and then covered with a drop of SU-8 photoresist. The laser beam is able to focus on the tip of wires and print designed structures by triggering the chemical cross-linking reaction. After development and rinsing, the hardened structures are built on the Nb tip. To fabricate carbon electrodes, a pyrolysis process is needed to carbonize the polymerized photoresist. After the thermal annealing at around 900 C, the structures are transformed to a glassy carbon-like material with well-retained shapes but shrinkage in size.[90]

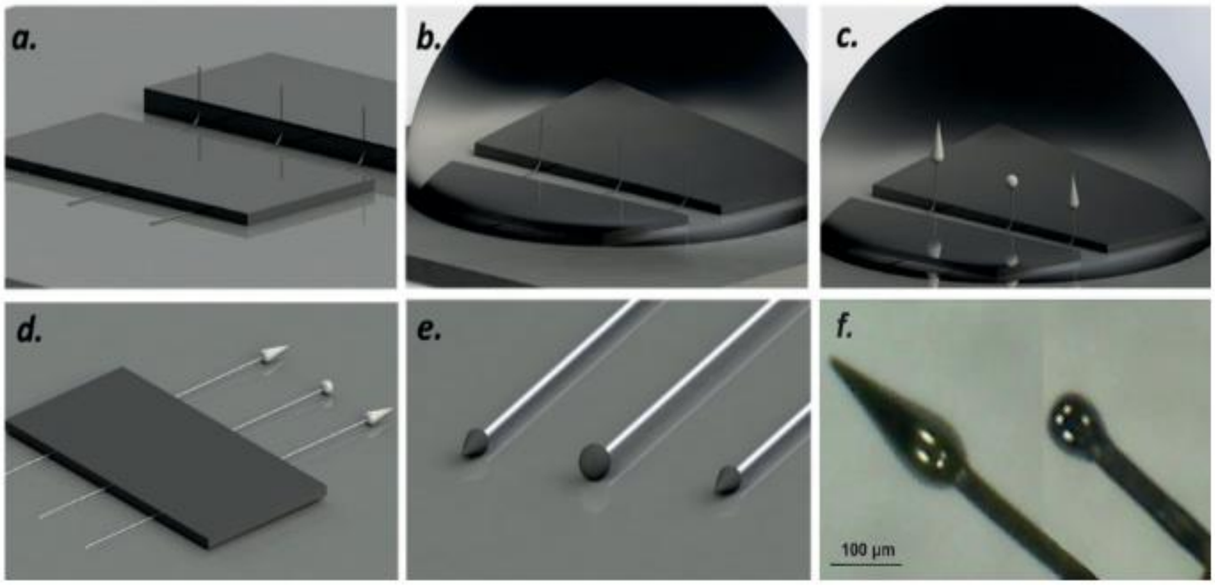

Figure 1.8. The fabrication of 3D-printed carbon microelectrode. Reprinted from Wiley (C Yang, Q Cao, et al, *Angewandte Chemie International Edition*, 2018).

1.4 Surface Structure of Carbon Microelectrodes

1.4.1 Overview

For decades, carbon has been extensively investigated as electrodes in electrochemistry owing to its conductivity, wide potential window, and relatively inert chemistry. Of general interest are numerous works based on traditional carbon materials not limited to glassy carbon and graphite, which serve as a basic tool in sensing, energy storage, and super capacitors. More recently, micro- or nano-sized carbon electrodes have been incorporated into electrochemical sensors for neurotransmitter detections based on their benefits of biocompatibility, low cost, and electrocatalytic activity of biomolecules.[22,68] In bioanalytical studies, reducing the electrode size is extensively studied, because a smaller size means less damage to the tissue and more possibility for accurate measurements in biological systems. In addition to their large surface-to-volume ratio and effective surface area, carbon nanomaterials favor interfacial adsorption and electron transfer kinetics, which benefits electrochemical sensing.[22]

1.4.2 Surface chemical structure of carbon nanomaterials

The surface structure of carbon can be classified by the hybridization of carbon atoms. Figure 1.9 shows various well-known carbon allotropes including graphene, graphite, carbon nanotubes, diamond, and fullerene, each of which possesses different structures and electrochemical properties.[62] The largest group of carbon nanomaterial is sp2-hybridized, such as graphene and carbon nanotubes (CNTs), which have a high electric conductivity due to their extended conjugated structures. Graphene is a single sheet of hexagonal sp2 carbon lattice and it becomes graphite with multiple layers. Graphite can be considered as graphene sheets with basal planes stacking in parallel, and edge planes vertical to basal planes. Highly oriented pyrolytic graphite and crystalline graphite are relatively uncommon; instead, most graphite materials contain a variety of sites and functional oxide groups that favor the adsorption of biomolecules at edge planes. Glassy carbon (GC) with a graphitic structure is a common electrode material in electrochemistry. Carbon fibers also have a graphite structure with a diameter of 6 mm and have been used as a standard material in electrochemical sensing with FSCV for decades.

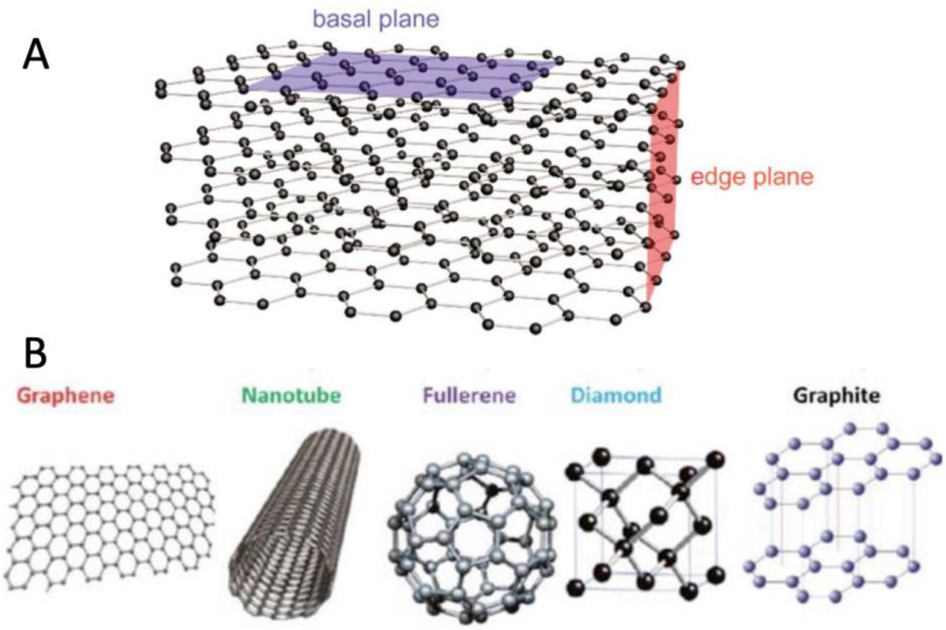

Figure 1.9. (A) Schematic illustration of edge plane and basal plane of graphite. (B) Various carbon allotropes. Reprinted from Royal Society of Chemistry (Q Cao, P Puthongkham, BJ Venton, *Analytical Methods*, 2019).

Other sp2-hybridized carbon materials are considered as different shapes of graphene. Carbon nanotubes are the most popular sp2 carbon allotropes with hollow cylinder structures that are rolled up from graphene layers and terminated with a fullerene hemisphere. They have customizable sizes based on the number of graphene sheets. Single-walled CNTs (SWCNTs) have a diameter around 1 nm, whereas multi-walled CNTs (MWCNTs) are larger, which is up to 50 nm with multiple graphene layers.[91] Considering the difficulty of isolating and mounting the single tubes, CNTs are sometimes twisted into a fiber or a yarn in a large-scale with robust mechanical and electrochemical properties. Carbon nanospikes (CNSs) are another form of graphene with a spike-like shape with size around 50 nm. CNTs and CNSs have better electrochemical properties than graphene and graphene due to the more edge planes and defect sites, which lead to a higher density of electronic states and faster electron transfer rate.

Moreover, the oxide groups added to the edge planes, including hydroxyl group and carbonyl group, benefit the adsorption of biomolecules in electrochemical sensing.[73,76]

Another type of carbon nanomaterial is sp3-hybridized, which has less conductivity than sp2 carbon. Diamond is the most common sp3 carbon and it has the highest hardness and thermal conductivity in nature. Pure diamonds have a wide potential window and inert chemistry, but conductivity is low due to the complete sp3-hybridized carbon terminated with hydrogen, which limits the application in electrochemistry.[77,78] However, the electron transfer can be sufficiently improved by introducing impurities or defects, which are usually doped with electron-deficient boron. Boron-doped diamond (BDD) is a common material for electrochemical studies and can be fabricated on a micro-scale. Interestingly, nano-size diamonds, which are so-called nanodiamonds (NDs), have different structures than macro-scale diamonds. NDs are created under a high pressure and have similar properties as tetrahedral amorphous carbon. Recently, plasma-assisted CVD becomes a more regular way to synthesize NDs. Unlike diamonds, nano-size diamonds with CH_4/Ar plasma assisting during synthesis have randomly oriented crystalline structure and increasing content of sp2 carbon atoms, which makes ND electrodes with distinct electrochemical properties. NDs have a much higher surface-to-volume ratio that enhances the active surface area of the electrode.[58,79]

1.4.3 Carbon nanoelectrodes

The majority of carbon electrodes in electrochemical analysis are several microns wide and are unable to measure in neuronal synapses, which are typically 0.02 micron wide; thus, a reduction of size is useful for neural studies. Nanoelectrodes cause minimal tissue damage, probe a local cellular environment, and have enhanced electrochemistry. The ultra-small scale leads to less charging current, enhanced radial diffusion, and a high current density at the electrode surface. Because noise is proportional to background current, signal to noise ratios are good for nanoelectrodes even though absolute currents are small.

Carbon nanoelectrodes have various designs as Figure 1.10 shows. Carbon nanopipettes were fabricated by depositing carbon on the inside of the nanopipettes, which have nano-sized opening, specifically approximately 30-60 nm for quartz and 150-200 nm for borosilicate glass.[92,93] The thickness of deposited carbon is controllable to make the nanoelectrode either a solid tip or open tip. Coating a thin layer of carbon nanomaterial on a nano-sized substrate also enables detection with a robust and reliable electrochemical performance.[75] Flame etching and electrochemical wet etching are another effective strategy to reduce the size of carbon-fiber microelectrodes to nanoscale. Because of their extremely small size, nanoelectrodes exhibit a highly efficient diffusional mass transport with spherical diffusion at the edge; therefore, the current density is high. The nanosize causes minimal tissue damage, and enables exploring small organisms and synapses.[94]

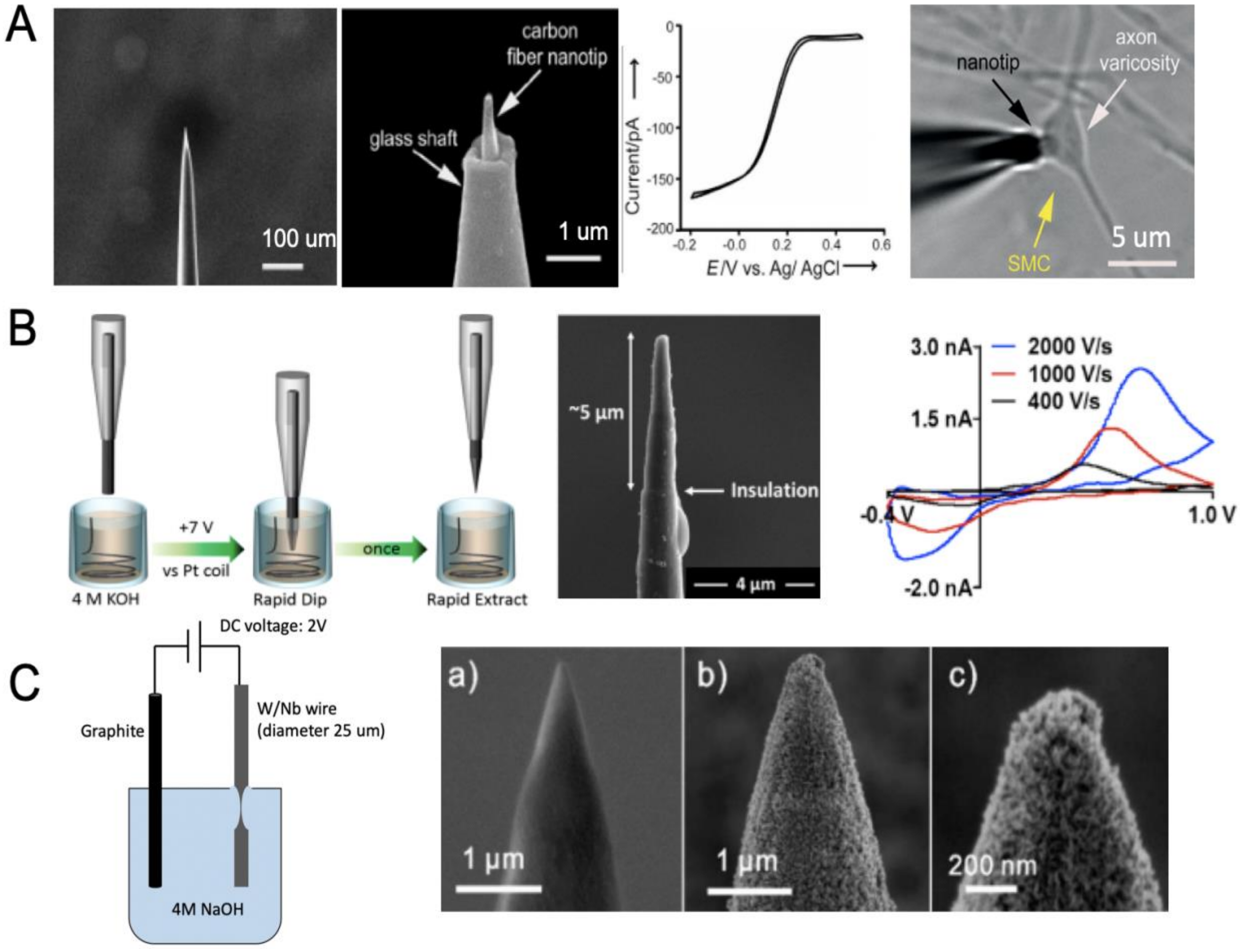

Figure 1.10. Different designs of carbon nanoelectrode. (A) Flame-etched carbon fiber nanoelectrode. (B) Wet-etched carbon fiber nanoelectrode. (C) CNS nanoelectrode. Panel A is reprinted by permission from Wiley (Li, Yu-Tao, et al. *Angewandte Chemie International Edition* (2014)), panel B from the American Chemical Society (Roberts, James G., et al. *ACS nano* (2020)), and panel C from Royal Society of Chemistry (Cao, Qun, et al. *Nano letters* (2020).).

1.4.4 Carbon microelectrodes with Surface Roughness/Surface Geometry

For decades, it was widely accepted that carbon materials perform different in surface chemistry because of their complex molecular structures, including the type of hybridization, conjugation structures, defects and surface functional groups. As an electron transfer-involved chemical change, the electrochemical process is largely affected by the surface chemistry during the redox reactions. Figure 1.13A shows a typical schematic illustration of mass transfer pathways in dopamine redox reaction. Dopamine (DA) molecules diffuse from the bulk solution to the area near the electrode surface by mass transfer and then adsorb on the surface. The adsorbed dopamine molecules are oxidized to dopamine-o-quinone (DOQ) with a sufficient potential applied. The product DOQ molecules can desorb from the electrode surface and diffuse into the bulk solution. Reversibly, the reduction of DOQ follows the same pathways. Abundant research has been focusing on modification of carbon electrodes, including surface functionalization with chemical groups and coating with various carbon nanomaterials, to help molecule adsorption on the surface.[2,13]

Recently, more studies have explored the effects of three-dimensional geometric structure of carbon electrodes in electrochemistry, especially on porous surface or surface with large roughness. Surface geometry and roughness play important roles in electrochemical analysis by increasing the surface-to-volume ratio and changing the mass transfer near the surface. Kant proposed a model to describe the electric double layer dynamics of a porous electrodes with amperometry and electrochemical impedance spectroscopy, and his work explains how diffusion dynamics are influenced by electrode geometry, shape, and size.[95] Compton's group also reported that a thin layer diffusion phenomenon was observed at MWCNT electrodes with nanoscopic structures on the surface.[23] Moreover, more studies have demonstrated that surface geometry affects mass transfer process that a unique trapping effect was observed at porous carbon microelectrodes that diffusion is restricted near the surface with a large roughness. As Figure 1.13B shows, the trapping effect occurs when the diffusion of molecules is restricted by the surface geometry that they can be easily captured by the electrode before escaping. The trapping effect is a unique phenomenon related to thin-layer electrochemistry and is only observed in FSCV with a subsecond time scale, because trapping occurs when the roughness of the electrode surface is larger than the diffusion layer thickness of that species. The diffusion layer thickness δ in one-dimension can be calculated by

$$\delta = (2Dt)^{1/2}$$

where D is the diffusion coefficient of a species and t is time, which is usually several milliseconds in one FSCV cycle.[15] In conventional cyclic voltammetry, it is not possible to restrict molecules near the surface for several seconds. The restricted diffusion has been observed in various carbon electrode materials, including MWCNT/ta-C film, laser-induced graphite, and MWCNT arrays.[96,97] The studies of trapping effect at CNT yarn microelectrodes will be explored in Chapter 2 and 3.

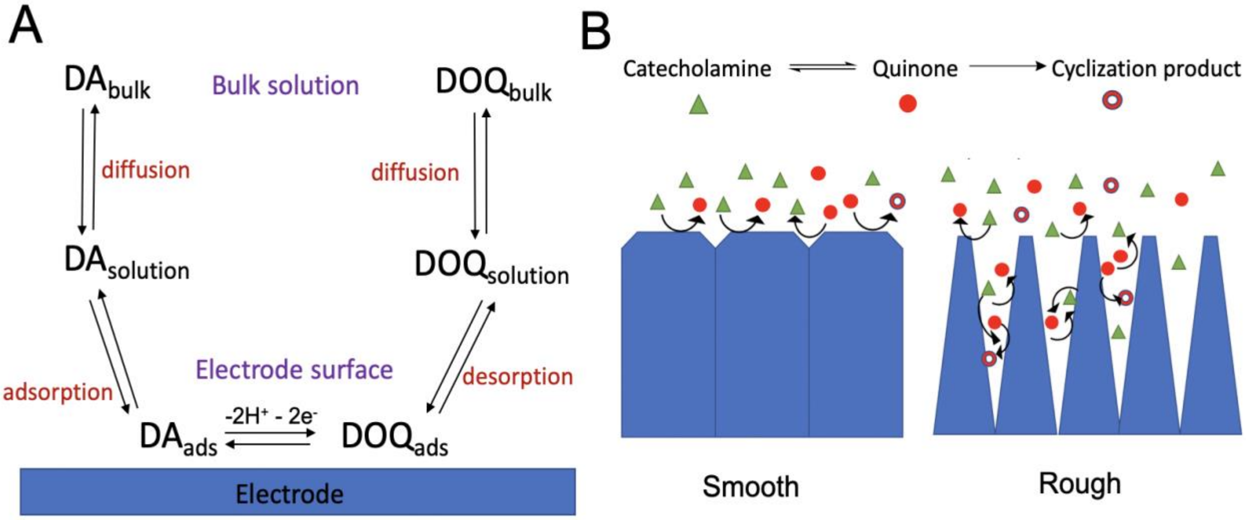

Figure 1.11. (A) Schematic illustration of pathway for electrochemical detection of dopamine (B) Mass transfer comparison of catecholamine redox reactions at electrodes with smooth and rough surface.

1.5 Overview of the Dissertation

For decades, CFMEs have been a gold standard for rapid neurotransmitter detection with FSCV, however, many improvements are needed to improve the sensing performance of analytical investigations. This dissertation aims to develop novel carbon-based microelectrodes to overcome the limitation of traditional CFMEs in neurotransmitter detection with higher selectivity, temporal resolution, spatial resolution, and fouling resistance. Various carbon nanomaterials, including CNTs, CNS, and nanodiamonds, are used to meet different requirements in microelectrode fabrication.

Chapter 2 explores the thin layer electrochemistry at CNT yarn microelectrode (CNTYMEs) and cavity nanopipette electrodes (CNPEs) for catecholamine neurotransmitter detection. The differentiation of dopamine, norepinephrine, and epinephrine by electrochemical sensing has long been a great challenge, because they have similar chemical structures and the same chemical moiety for redox reactions, thus, the CV shapes are highly similar. CNT yarn microelectrodes with micron-size surface roughness trap molecules at the near-surface area to promote continuous redox cycling, as a result, it is possible for neurotransmitter measurement at a higher repetition frequency with less signal decay. In addition, the trapping effect favors the cyclization of catecholamine to generate a secondary oxidation peak on the cyclic voltammogram, which enables the differentiation by CV shapes. Similar results are observed at CNPEs, which trap molecules in the restricted cavity area. This chapter demonstrates a method for highly selective catecholamine detection and introduces a novel application of the thin layer electrochemistry in neurotransmitter measurement with FSCV.

Chapter 3 extends the FSCV study using CNT yarn microelectrodes to discriminate dopamine from other anionic neurochemicals, including DOPAC and ascorbic acid (AA), which both have a much higher concentration than dopamine in the brain. For decades, substantial efforts have been devoted for differentiate dopamine from DOPAC and AA with differential pulse voltammetry (DPV); however, DPV is not capable of rapid detection. Here, we performed FSCV with CNT yarn microelectrodes and successfully discriminated dopamine with interference by CV shapes. At physiological pH 7.4, anionic DOPAC and AA molecules have opposite electrostatic interactions with cationic dopamine. The trapping effect also amplifies the side reactions of three molecules at different pH to generate different CVs for selective detection of dopamine.

Chapter 4 illustrates the fabrication of carbon nanospike-based nanoelectrodes that enable neurotransmitter detection at the level of synapses and small brain areas. PECVD-synthesized CNS is uniformly deposited on a piece of pre-etched Niobium wire with a nano-size tip. The thickness of the CNS layer is precisely controlled by the deposition time and it effectively covers the entire meta surface while maintaining a submicron-sized tip. The nanoelectrode has fast electron transfer kinetics and good electrochemical performance in detecting various neurotransmitters with FSCV. Compared with other nanoelectrode designs, this method is easy to conduct and allows mass fabrication.

Chapter 5 demonstrates the development of an antifouling nanodiamond microelectrode and compares the electrochemical performance after oxygen plasma etching. Nanodiamonds (NDs) are better material for electrochemical sensing than bulk diamonds due to the large surface area, abundant defect sites, and functional groups on the surface. From previous studies, an uneven coating of NDs also makes CFMEs more resistant to electrode fouling because it changes the hydrophobicity of the electrode. Here, we fabricate ND microelectrodes by uniformly coating a thin ND film on Niobium wires via microwave plasma chemical vapor deposition (MP-CVD), which are further treated with oxygen plasma. With more oxide groups added to the ND microelectrodes, the hydrophilic surface has slightly decreased fouling resistance, however, the sensitivity dramatically increased so that the negative effect from electrode fouling can be neglected.

Chapter 6 demonstrates a novel 3D printing method using photolithography to develop a carbon-based nanoelectrode on metal wires. In the 3D nano-printing process, the negative-tone photoresist became polymerized and hardened by two-photon absorption and finally generated a glassy carbon surface after pyrolysis. Previously, we successfully developed a disk-shape nanoelectrode by exposing the carbon surface on the tip. However, the bottom size is large and the tip may curl during annealing, which needs to be improved for implantation in small organisms. In this chapter, we propose a new method using pulling stress during pyrolysis to construct a long and straight needle structure with a submicron size. This method overcomes the limitations of the previous design that it will cause much less damage to the tissue and largely reduce the block of vision during implantation.

Overall, this dissertation utilizes the surface chemistry of various carbon nanomaterials to enhance the electrochemical performance in neurotransmitter detection. More challenges and future directions of new designs and applications are addressed in Chapter 6.

1.6 References

(1) Bath, B. D.; Michael, D. J.; Trafton, B. J.; Joseph, J. D.; Runnels, P. L.; Wightman, R. M. Subsecond Adsorption and Desorption of Dopamine at Carbon-Fiber Microelectrodes. *Anal. Chem.* **2000**, *72* (24), 5994–6002. https://doi.org/10.1021/ac000849y.

(2) Venton, B. J.; Wightman, R. M. Psychoanalytical Electrochemistry: Dopamine and Behavior. *Anal. Chem.* **2003**, *75* (19), 414–421. https://doi.org/10.1021/ac031421c.

(3) Robinson, D. L.; Venton, B. J.; Heien, M. L. A. V.; Wightman, R. M. Detecting Subsecond Dopamine Release with Fast-Scan Cyclic Voltammetry in Vivo. *Clin. Chem.* **2003**, *1773*, 1763–1773.

(4) Lane, R. F.; Hubbard, A. T. Differential Double Pulse Voltammetry at Chemically Modified Platinum Electrodes for in Vivo Determination of Catecholamines. *Anal. Chem.* **1976**, *48* (9), 1287–1292. https://doi.org/10.1021/ac50003a009.

(5) Wightman, R. M. Microvoltammetric Electrodes. *Anal. Chem.* **1981**, *53* (9), 1125A-1134A. https://doi.org/10.1021/ac00232a004.

(6) Wightman, R. M.; Wipf, D. O. High-Speed Cyclic Voltammetry. *Acc. Chem. Res.* **1990**, *23* (3), 64–70. https://doi.org/10.1021/ar00171a002.

(7) Baur, J. E.; Kristensen, E. W.; May, L. J.; Wiedemann, D. J.; Wightman, R. M. Fast-Scan Voltammetry of Biogenic Amines. *Anal. Chem.* **1988**, *60* (13), 1268–1272.

(8) Chandra, S.; Siraj, S.; Wong, D. K. Y. Recent Advances in Biosensing for Neurotransmitters and Disease Biomarkers Using Microelectrodes. *ChemElectroChem* **2017**, *4* (4). https://doi.org/10.1002/celc.201600810.

(9) Du, X.; Wu, L.; Cheng, J.; Huang, S.; Cai, Q.; Jin, Q.; Zhao, J. Graphene Microelectrode Arrays for Neural Activity Detection. *J. Biol. Phys.* **2015**, *41* (4), 339–347. https://doi.org/10.1007/s10867-015-9382-3.

(10) Castagnola, E.; Garg, R.; Rastogi, S. K.; Cohen-Karni, T.; Cui, X. T. 3D Fuzzy Graphene Microelectrode Array for Dopamine Sensing at Sub-Cellular Spatial Resolution. *Biosens. Bioelectron.* **2021**, *191* (June), 113440. https://doi.org/10.1016/j.bios.2021.113440.

(11) Jacobs, C. B.; Ivanov, I. N.; Nguyen, M. D.; Zestos, A. G.; Venton, B. J. High Temporal Resolution Measurements of Dopamine with Carbon Nanotube Yarn Microelectrodes. *Anal. Chem.* **2014**, *86* (12), 5721–5727. https://doi.org/10.1021/ac404050t.

(12) Mendoza, A.; Asrat, T.; Liu, F.; Wonnenberg, P.; Zestos, A. G. Carbon Nanotube Yarn Microelectrodes Promote High Temporal Measurements of Serotonin Using Fast Scan Cyclic Voltammetry. *Sensors* **2020**, *20* (4), 1173. https://doi.org/10.3390/s20041173.

(13) B. Jill Venton * and Qun Cao. Fundamentals of Fast-Scan Cyclic Voltammetry for Dopamine Detection. **2020**. https://doi.org/10.1039/c9an01586h.

(14) John, C. E.; Jones, S. R. Fast Scan Cyclic Voltammetry of Dopamine and Serotonin in Mouse Brain Slices. In *Electrochemical Methods for Neuroscience*; Frontiers in Neuroengineering; CRC Press/Taylor & Francis: Boca Raton, FL, 2007; pp 49–62.

(15) Bard, A. J.; Faulkner, L. R. *Fundamentals and Fundamentals and Applications*; 2015; Vol. 8. https://doi.org/10.1016/B978-0-08-098353-0.00003-8.

(16) Wightman, R. M.; Amatore, C.; Engstrom, R. C.; Hale, P. D.; Kristensen, E. W.; Kuhr, W. G.; May, L. J. Real-Time Characterization of Dopamine Overflow and Uptake in the Rat Striatum. *Neuroscience* **1988**, *25* (2), 513–523.

(17) Atcherley, C. W.; Laude, N. D.; Parent, K. L.; Heien, M. L. Fast-Scan Controlled-Adsorption Voltammetry for the Quantification of Absolute Concentrations and Adsorption Dynamics. *Langmuir* **2013**, *29* (48), 14885–14892. https://doi.org/10.1021/la402686s.

(18) Bath, B. D.; Martin, H. B.; Wightman, R. M.; Anderson, M. R. Dopamine Adsorption at Surface Modified Carbon-Fiber Electrodes. *Langmuir* **2001**, *17* (22), 7032–7039. https://doi.org/10.1021/la0106844.

(19) Brazell, M. P.; Kasser, R. J.; Renner, K. J.; Feng, J.; Moghaddam, B.; Adams, R. N. Electrocoating Carbon Fiber Microelectrodes with Nafion Improves Selectivity for Electroactive Neurotransmitters. *J. Neurosci. Methods* **1987**, *22* (2), 167–172. https://doi.org/10.1016/0165-0270(87)90011-2.
(20) Cao, Q.; Lucktong, J.; Shao, Z.; Chang, Y.; Venton, B. J. Electrochemical Treatment in KOH Renews and Activates Carbon Fiber Microelectrode Surfaces. *Anal. Bioanal. Chem.* **2021**. https://doi.org/10.1007/s00216-021-03539-6.
(21) Huffman, M. L.; Venton, B. J. Carbon-Fiber Microelectrodes for in Vivo Applications. *Analyst* **2009**, *134* (1), 18–24. https://doi.org/10.1039/b807563h.
(22) McCreery, R. L. Advanced Carbon Electrode Materials for Molecular Electrochemistry. *Chem. Rev.* **2008**, *108* (7), 2646–2687. https://doi.org/10.1021/cr068076m.
(23) Akinoglu, E. M.; Kätelhön, E.; Pampel, J.; Ban, Z.; Antonietti, M.; Compton, R. G.; Giersig, M. Nanoscopic Carbon Electrodes: Structure, Electrical Properties and Application for Electrochemistry. *Carbon* **2018**, *130*, 768–774. https://doi.org/10.1016/j.carbon.2018.01.064.
(24) Chang, Y.; Venton, B. J. Optimization of Graphene Oxide-Modified Carbon-Fiber Microelectrode for Dopamine Detection. *Anal. Methods* **2020**, *12* (22), 2893–2902. https://doi.org/10.1039/d0ay00310g.
(25) Roberts, J. G.; Moody, B. P.; McCarty, G. S.; Sombers, L. A. Specific Oxygen-Containing Functional Groups on the Carbon Surface Underlie an Enhanced Sensitivity to Dopamine at Electrochemically Pretreated Carbon Fiber Microelectrodes. *Langmuir* **2010**, *26* (11), 9116–9122. https://doi.org/10.1021/la9048924.
(26) Cans, A. S.; Wittenberg, N.; Eves, D.; Karlsson, R.; Karlsson, A.; Orwar, O.; Ewing, A. Amperometric Detection of Exocytosis in an Artificial Synapse. *Anal. Chem.* **2003**, *75* (16), 4168–4175. https://doi.org/10.1021/ac0343578.
(27) Bolton, A. D.; Constantine-Paton, M. Synaptic Effects of Dopamine Breakdown and Their Relation to Schizophrenia-Linked Working Memory Deficits. *Front. Synaptic Neurosci.* **2018**, *10* (June), 1–10. https://doi.org/10.3389/fnsyn.2018.00016.
(28) Kile, B. M.; Walsh, P. L.; McElligott, Z. A.; Bucher, E. S.; Guillot, T. S.; Salahpour, A.; Caron, M. G.; Wightman, R. M. Optimizing the Temporal Resolution of Fast-Scan Cyclic Voltammetry. *ACS Chem. Neurosci.* **2012**, *3* (4), 285–292. https://doi.org/10.1021/cn200119u.
(29) Kristensen, E. W.; Kuhr, W. G.; Wightman, R. Mark. Temporal Characterization of Perfluorinated Ion Exchange Coated Microvoltammetric Electrodes for in Vivo Use. *Anal. Chem.* **1987**, *59* (14), 1752–1757. https://doi.org/10.1021/ac00141a003.
(30) Hawley, M. D.; Tatawawadi, S. V.; Piekarski, S.; Adams, R. N. Electrochemical Studies of the Oxidation Pathways of Catecholamines. *J. Am. Chem. Soc.* **1967**, *89* (2), 447–450. https://doi.org/10.1021/ja00978a051.
(31) Lane, R. F.; Hubbard, A. T.; Fukunaga, K.; Blanchard, R. J. Brain Catecholamines: Detection in Vivo by Means of Differential Pulse Voltammetry at Surface-Modified Platinum Electrodes. *Brain Res.* **1976**, *114* (2), 346–352. https://doi.org/10.1016/0006-8993(76)90678-8.
(32) Ribeiro, J. A.; Fernandes, P. M. V.; Pereira, C. M.; Silva, F. Electrochemical Sensors and Biosensors for Determination of Catecholamine Neurotransmitters: A Review. *Talanta* **2016**, *160*, 653–679. https://doi.org/10.1016/j.talanta.2016.06.066.
(33) Banerjee, I.; Pangule, R. C.; Kane, R. S. Antifouling Coatings: Recent Developments in the Design of Surfaces That Prevent Fouling by Proteins, Bacteria, and Marine Organisms. *Adv. Mater.* **2011**, *23* (6), 690–718. https://doi.org/10.1002/adma.201001215.
(34) Dunham, K. E.; Venton, B. J. Improving Serotonin Fast-Scan Cyclic Voltammetry Detection: New Waveforms to Reduce Electrode Fouling. *The Analyst* **2020**. https://doi.org/10.1039/d0an01406k.

(35) Feng, T.; Ji, W.; Tang, Q.; Wei, H.; Zhang, S.; Mao, J.; Zhang, Y.; Mao, L.; Zhang, M. Low-Fouling Nanoporous Conductive Polymer-Coated Microelectrode for in Vivo Monitoring of Dopamine in the Rat Brain. *Anal. Chem.* **2019**, *91* (16), 10786–10791. https://doi.org/10.1021/acs.analchem.9b02386.

(36) Geise, R. J.; Adams, J. M.; Barone, N. J.; Yacynych, A. M. Electropolymerized Films to Prevent Interferences and Electrode Fouling in Biosensors. *Biosens. Bioelectron.* **1991**, *6* (2), 151–160. https://doi.org/10.1016/0956-5663(91)87039-E.

(37) Hanssen, B. L.; Siraj, S.; Wong, D. K. Y. Recent Strategies to Minimise Fouling in Electrochemical Detection Systems. *Rev. Anal. Chem.* **2016**, *35* (1). https://doi.org/10.1515/revac-2015-0008.

(38) Barker, E. L.; Blakely, R. D. Structural Determinants of Neurotransmitter Transport Using Cross- Species Chimeras: Studies on Serotonin Transporter. *Methods Enzymol.* **1998**, *296* (1990), 475–498. https://doi.org/10.1016/S0076-6879(98)96035-9.

(39) Bucher, E. S.; Wightman, R. M. Electrochemical Analysis of Neurotransmitters. *Annu. Rev. Anal. Chem.* **2015**, *8* (1), 239–261. https://doi.org/10.1146/annurev-anchem-071114-040426.

(40) Aryal, B.; Lee, Y. Disease Model Organism for Parkinson Disease: Drosophila Melanogaster. *BMB Rep.* **2019**, *52* (4), 250–258. https://doi.org/10.5483/BMBRep.2019.52.4.204.

(41) Carta, M.; Carlsson, T.; Muñoz, A.; Kirik, D.; Björklund, A. Role of Serotonin Neurons in the Induction of Levodopa- and Graft-Induced Dyskinesias in Parkinson's Disease. *Mov. Disord.* **2010**, *25*, S174–S179. https://doi.org/10.1002/mds.22792.

(42) Borland, L. M.; Michael, A. C. Voltammetric Study of the Control of Striatal Dopamine Release by Glutamate. *J. Neurochem.* **2004**, *91* (1), 220–229. https://doi.org/10.1111/j.1471-4159.2004.02708.x.

(43) Bauknecht, P.; Jékely, G. Ancient Coexistence of Norepinephrine, Tyramine, and Octopamine Signaling in Bilaterians. *BMC Biol.* **2017**, *15* (1), 6. https://doi.org/10.1186/s12915-016-0341-7.

(44) Park, J.; Bhimani, R. V.; Bass, C. E. Review — In Vivo Electrochemical Measurements of Norepinephrine in the Brain: Current Status and Remaining Challenges. *J. Electrochem. Soc.* **2018**, *165* (12). https://doi.org/10.1149/2.0091812jes.

(45) Chen, S. M.; Peng, K. T. The Electrochemical Properties of Dopamine, Epinephrine, Norepinephrine, and Their Electrocatalytic Reactions on Cobalt(II) Hexacyanoferrate Films. *J. Electroanal. Chem.* **2003**, *547* (2), 179–189. https://doi.org/10.1016/S0022-0728(03)00220-1.

(46) Chen, S. M.; Chen, J. Y.; Vasantha, V. S. Electrochemical Preparation of Epinephrine/Nafion Chemically Modified Electrodes and Their Electrocatalytic Oxidation of Ascorbic Acid and Dopamine. *Electrochimica Acta* **2006**, *52* (2), 455–465. https://doi.org/10.1016/j.electacta.2006.05.027.

(47) Adams, R. N. Anodic Oxidation Pathways of Aromatic Hydrocarbons and Amines. *Acc. Chem. Res.* **1969**, *2* (6), 175–180. https://doi.org/10.1021/ar50018a003.

(48) Tse, D. C. S.; McCreery, R. L.; Adams, R. N. Potential Oxidative Pathways of Brain Catecholamines. *J. Med. Chem.* **1976**, *19* (1), 37–40. https://doi.org/10.1021/jm00223a008.

(49) Borovansky, J.; Edge, R.; Land, E. J.; Navaratnam, S.; Pavel, S.; Ramsden, C. A.; Riley, P. A.; Smit, N. P. M. Mechanistic Studies of Melanogenesis: The Influence of N-Substitution on Dopamine Quinone Cyclization. *Pigment Cell Res.* **2006**, *19* (2), 170–178. https://doi.org/10.1111/j.1600-0749.2006.00295.x.

(50) Xiang, L.; Lin, Y.; Yu, P.; Su, L.; Mao, L. Laccase-Catalyzed Oxidation and Intramolecular Cyclization of Dopamine: A New Method for Selective Determination of Dopamine with Laccase/Carbon Nanotube-Based Electrochemical Biosensors.

Electrochimica Acta **2007**, *52* (12), 4144–4152. https://doi.org/10.1016/j.electacta.2006.11.040.

(51) Roy, P. R.; Saha, M. S.; Okajima, T.; Park, S. G.; Fujishima, A.; Ohsaka, T. Selective Detection of Dopamine and Its Metabolite, DOPAC, in the Presence of Ascorbic Acid Using Diamond Electrode Modified by the Polymer Film. *Electroanalysis* **2004**, *16* (21), 1777–1784. https://doi.org/10.1002/elan.200303026.

(52) Shao, Z.; Venton, B. J. Different Electrochemical Behavior of Cationic Dopamine from Anionic Ascorbic Acid and DOPAC at CNT Yarn Microelectrodes. *J. Electrochem. Soc.* **2022**. https://doi.org/10.1149/1945-7111/ac4d67.

(53) Belaidi, F. S.; Civélas, A.; Castagnola, V.; Tsopela, A.; Mazenq, L.; Gros, P.; Launay, J.; Temple-Boyer, P. PEDOT-Modified Integrated Microelectrodes for the Detection of Ascorbic Acid, Dopamine and Uric Acid. *Sens. Actuators B Chem.* **2015**, *214*, 1–9. https://doi.org/10.1016/j.snb.2015.03.005.

(54) Cheng, H.; Li, L.; Zhang, M.; Jiang, Y.; Yu, P.; Ma, F.; Mao, L. Recent Advances on in Vivo Analysis of Ascorbic Acid in Brain Functions. *TrAC - Trends Anal. Chem.* **2018**, *109*, 247–259. https://doi.org/10.1016/j.trac.2018.10.017.

(55) Zetterström, T.; Sharp, T.; Collin, A. K.; Ungerstedt, U. In Vivo Measurement of Extracellular Dopamine and DOPAC in Rat Striatum after Various Dopamine-Releasing Drugs Implications for the Origin of Extracellular DOPAC. *Eur. J. Pharmacol.* **1988**, *148* (3), 327–334. https://doi.org/10.1016/0014-2999(88)90110-0.

(56) Basse-Tomusk, A.; Rebec, G. V. Regional Distribution of Ascorbate and 3,4-Dihydroxyphenylacetic Acid (DOPAC) in Rat Striatum. *Brain Res.* **1991**, *538* (1), 29–35. https://doi.org/10.1016/0006-8993(91)90372-3.

(57) Kawde, A. N.; Morsy, M. A.; Odewunmi, N.; Mahfouz, W. From Electrode Surface Fouling to Sensitive Electroanalytical Determination of Phenols. *Electroanalysis* **2013**, *25* (6), 1547–1555. https://doi.org/10.1002/elan.201300101.

(58) Puthongkham, P.; Venton, B. J. Nanodiamond Coating Improves the Sensitivity and Antifouling Properties of Carbon Fiber Microelectrodes. *ACS Sens.* **2019**, *4* (9). https://doi.org/10.1021/acssensors.9b00994.

(59) Peltola, E.; Sainio, S.; Holt, K. B.; Palomäki, T.; Koskinen, J.; Laurila, T. Electrochemical Fouling of Dopamine and Recovery of Carbon Electrodes. *Anal. Chem.* **2017**, *90* (2), 1408–1416. https://doi.org/10.1021/acs.analchem.7b04793.

(60) Shin, D.; Tryk, D. A.; Fujishima, A.; Merkoçi, A.; Wang, J. Resistance to Surfactant and Protein Fouling Effects at Conducting Diamond Electrodes. *Electroanalysis* **2005**, *17* (4), 305–311. https://doi.org/10.1002/elan.200403104.

(61) Liu, X.; You, S.; Ma, F.; Zhou, H. Characterization of Electrode Fouling during Electrochemical Oxidation of Phenolic Pollutant. *Front. Environ. Sci. Eng.* **2021**, *15* (4). https://doi.org/10.1007/s11783-020-1345-7.

(62) Kousar, A.; Peltola, E.; Laurila, T. Nanostructured Geometries Strongly Affect Fouling of Carbon Electrodes. *ACS Omega* **2021**. https://doi.org/10.1021/acsomega.1c03666.

(63) Abdalla, A.; Atcherley, C. W.; Pathirathna, P.; Samaranayake, S.; Qiang, B.; Peña, E. A.; Morgan, S. L.; Heien, M. L.; Hashemi, P. In Vivo Ambient Serotonin Measurements at Carbon-Fiber Microelectrodes. *Anal. Chem.* **2017**, *89* (18), 9703–9711. https://doi.org/10.1021/acs.analchem.7b01257.

(64) Bowman, M. A.; Vitela, M.; Clarke, K. M.; Koek, W.; Daws, L. C. Serotonin Transporter and Plasma Membrane Monoamine Transporter Are Necessary for the Antidepressant-like Effects of Ketamine in Mice. *Int. J. Mol. Sci.* **2020**, *21* (20), 1–22. https://doi.org/10.3390/ijms21207581.

(65) Colombo, M. L.; Sweedler, J. V.; Shen, M. Nanopipet-Based Liquid–Liquid Interface Probes for the Electrochemical Detection of Acetylcholine, Tryptamine, and Serotonin via Ionic Transfer. *Anal. Chem.* **2015**, *87* (10), 5095–5100. https://doi.org/10.1021/ac504151e.

(66) Shao, Z.; Chang, Y.; Venton, B. J. Carbon Microelectrodes with Customized Shapes for Neurotransmitter Detection: A Review. *Anal. Chim. Acta* **2022**, *1223*, 340165. https://doi.org/10.1016/j.aca.2022.340165.

(67) Manawi, Y. M.; Ihsanullah; Samara, A.; Al-Ansari, T.; Atieh, M. A. A Review of Carbon Nanomaterials' Synthesis via the Chemical Vapor Deposition (CVD) Method. *Materials* **2018**, *11* (5), 822. https://doi.org/10.3390/ma11050822.

(68) Meyyappan, M.; Delzeit, L.; Cassell, A.; Hash, D. Carbon Nanotube Growth by PECVD: A Review. *Plasma Sources Sci. Technol.* **2003**, *12* (2), 205–216. https://doi.org/10.1088/0963-0252/12/2/312.

(69) Aljumaily, M. M.; Alsaadi, M. A.; Das, R.; Abd Hamid, S. B.; Hashim, N. A.; AlOmar, M. K.; Alayan, H. M.; Novikov, M.; Alsalhy, Q. F.; Hashim, M. A. Optimization of the Synthesis of Superhydrophobic Carbon Nanomaterials by Chemical Vapor Deposition. *Sci. Rep.* **2018**, *8* (1), 1–12. https://doi.org/10.1038/s41598-018-21051-3.

(70) Choi, Y. C.; Shin, Y. M.; Lee, Y. H.; Lee, B. S.; Park, G. S.; Choi, W. B.; Lee, N. S.; Kim, J. M. Controlling the Diameter, Growth Rate, and Density of Vertically Aligned Carbon Nanotubes Synthesized by Microwave Plasma-Enhanced Chemical Vapor Deposition. *Appl. Phys. Lett.* **2000**, *76* (17), 2367–2369. https://doi.org/10.1063/1.126348.

(71) Li, Y. L.; Kinloch, I. A.; Windle, A. H. Direct Spinning of Carbon Nanotube Fibers from Chemical Vapor Deposition Synthesis. *Science.* **2004**, *304* (5668), 276–278. https://doi.org/10.1126/science.1094982.

(72) Guo, L.; Shanov, V.; Singh, R. N. Growth of Carbon Nanotubes by Microwave Plasma Chemical Vapor Deposition (MPCVD). *Ceram. Trans.* **2005**, *159* (July 2000), 177–183. https://doi.org/10.1002/9781118407158.ch19.

(73) Cao, Q.; Hensley, D. K.; Lavrik, N. V.; Venton, B. J. Carbon Nanospikes Have Better Electrochemical Properties than Carbon Nanotubes Due to Greater Surface Roughness and Defect Sites. *Carbon* **2019**, *155*, 250–257. https://doi.org/10.1016/j.carbon.2019.08.064.

(74) Shanta, A. S.; Al Mamun, K. A.; Hensley, D.; Lavrik, N. V.; Islam, S. K.; McFarlane, N. Carbon Nanospikes for Biosensing Applications. In *Engineering in Medicine and Biology Society (EMBC), 2017 39th Annual International Conference of the IEEE*; IEEE, 2017; pp 193–196.

(75) Cao, Q.; Shao, Z.; Hensley, D.; Venton, B. J. Carbon Nanospike Coated Nanoelectrodes for Measurements of Neurotransmitters. *Faraday Discuss.* **2021**. https://doi.org/10.1039/d1fd00053e.

(76) Zestos, A. G.; Yang, C.; Jacobs, C. B.; Hensley, D.; Venton, B. J. Carbon Nanospikes Grown on Metal Wires as Microelectrode Sensors for Dopamine. *Analyst* **2015**, *140* (21). https://doi.org/10.1039/c5an01467k.

(77) Butler, J. E.; Sumant, A. V. The CVD of Nanodiamond Materials. *Chem. Vap. Depos.* **2008**, *14* (7-8 SPEC. ISS.), 145–160. https://doi.org/10.1002/cvde.200700037.

(78) Danilenko, V. V. On the History of the Discovery of Nanodiamond Synthesis. *Phys. Solid State* **2004**, *46* (4), 595–599. https://doi.org/10.1134/1.1711431.

(79) Saturday, L.; Wilson, L.; Retterer, S.; Evans, N. J.; Briggs, D.; Rack, P. D.; Lavrik, N. Thermal Conductivity of Nano- and Micro-Crystalline Diamond Films Studied by Photothermal Excitation of Cantilever Structures. *Diam. Relat. Mater.* **2021**, *113* (January), 108279. https://doi.org/10.1016/j.diamond.2021.108279.

(80) Chen, L. F.; Zhang, X. D.; Liang, H. W.; Kong, M.; Guan, Q. F.; Chen, P.; Wu, Z. Y.; Yu, S. H. Synthesis of Nitrogen-Doped Porous Carbon Nanofibers as an Efficient Electrode Material for Supercapacitors. *ACS Nano* **2012**, *6* (8), 7092–7102. https://doi.org/10.1021/nn302147s.

(81) Bartolome, J. P.; Fragoso, A. Preparation and Characterization of Carbon Nano-Onions by Nanodiamond Annealing and Functionalization by Radio-Frequency Ar/O2 Plasma.

Fuller. Nanotub. Carbon Nanostructures **2017**, *25* (5), 327–334. https://doi.org/10.1080/1536383X.2017.1303604.
(82) Kovalenko, I.; Bucknall, D. G.; Yushin, G. Detonation Nanodiamond and Onion-like-Carbon-Embedded Polyaniline for Supercapacitors. *Adv. Funct. Mater.* **2010**, *20* (22), 3979–3986. https://doi.org/10.1002/adfm.201000906.
(83) Koehne, J. E.; Marsh, M.; Boakye, A.; Douglas, B.; Kim, I. Y.; Chang, S.-Y.; Jang, D.-P.; Bennet, K. E.; Kimble, C.; Andrews, R.; Meyyappan, M.; Lee, K. H. Carbon Nanofiber Electrode Array for Electrochemical Detection of Dopamine Using Fast Scan Cyclic Voltammetry. *The Analyst* **2011**, *136* (9), 1802–1805. https://doi.org/10.1039/c1an15025a.
(84) Glass, R.; Arnold, M.; Cavalcanti-adam, A.; Gorzolnik, B.; Mela, P.; Moeller, M. Nano-Structured Micropatterns by Combination of Block Copolymer Self-Assembly and UV Photolithography. *Nanotechnology* **2006**, *17(19)*, 5027. https://doi.org/10.1088/0957-4484/17/19/042.
(85) Pan, Y.; Miller, C.; Trepka, K.; Tao, Y. Wafer-Scale Photolithography of Ultra-Sensitive Nanocantilever Force Sensors. *Appl. Phys. Lett.* **2018**, *113* (8), 83103. https://doi.org/10.1063/1.5043479.
(86) Weineck, G.; Zastera, D.; Dallas, A. J. AMC Control in Photolithography: The Past Decade in Review. *Metrol. Insp. Process Control Microlithogr. XXIV* **2010**, *7638* (April 2010), 76383H. https://doi.org/10.1117/12.847258.
(87) Andriianov, V. S.; Mironov, V. S.; Smikhovskaia, A. V.; Khairullina, E. M.; Tumkin, I. I. Laser-Induced Synthesis of Carbon-Based Electrode Materials for Non-Enzymatic Glucose Detection. *Opt. Quantum Electron.* **2020**, *52* (1), 1–8. https://doi.org/10.1007/s11082-019-2155-7.
(88) Hong, Q.; Yang, L.; Ge, L.; Liu, Z.; Li, F. Direct-Laser-Writing of Three-Dimensional Porous Graphene Frameworks on Indium-Tin Oxide for Sensitive Electrochemical Biosensing. *The Analyst* **2018**, *143* (14), 3327–3334. https://doi.org/10.1039/C8AN00888D.
(89) Li, G. Direct Laser Writing of Graphene Electrodes. *J. Appl. Phys.* **2020**, *127* (1). https://doi.org/10.1063/1.5120056.
(90) Yang, C.; Cao, Q.; Puthongkham, P.; Lee, S. T.; Ganesana, M.; Lavrik, N. V.; Venton, B. J. 3D-Printed Carbon Electrodes for Neurotransmitter Detection. *Angew. Chem. - Int. Ed.* **2018**, *57* (43). https://doi.org/10.1002/anie.201809992.
(91) Shkodra, B.; Abera, B. D.; Cantarella, G.; Douaki, A.; Avancini, E.; Petti, L.; Lugli, P. Flexible and Printed Electrochemical Immunosensor Coated with Oxygen Plasma Treated SWCNTs for Histamine Detection. *Biosensors* **2020**, *10* (4), 1–12. https://doi.org/10.3390/bios10040035.
(92) Rees, H. R.; Anderson, S. E.; Privman, E.; Bau, H. H.; Venton, B. J. Carbon Nanopipette Electrodes for Dopamine Detection in Drosophila. *Anal. Chem.* **2015**, *87* (7), 3849–3855. https://doi.org/10.1021/ac504596y.
(93) Yang, C.; Hu, K.; Wang, D.; Zubi, Y.; Lee, S. T.; Puthongkham, P.; Mirkin, M. V.; Venton, B. J. Cavity Carbon-Nanopipette Electrodes for Dopamine Detection. *Anal. Chem.* **2019**, *91* (7), 4618–4624. https://doi.org/10.1021/acs.analchem.8b05885.
(94) Roberts, J. G.; Mitchell, E. C.; Dunaway, L. E.; McCarty, G. S.; Sombers, L. A. Carbon-Fiber Nanoelectrodes for Real-Time Discrimination of Vesicle Cargo in the Native Cellular Environment. *ACS Nano* **2020**. https://doi.org/10.1021/acsnano.9b07318.
(95) Kant, R.; Singh, M. B. Theory of the Electrochemical Impedance of Mesostructured Electrodes Embedded with Heterogeneous Micropores. *J. Phys. Chem. C* **2017**, *121* (13), 7164–7174. https://doi.org/10.1021/acs.jpcc.7b01287.
(96) Sims, M. J.; Rees, N. V.; Dickinson, E. J. F.; Compton, R. G. Chemical Effects of Thin-Layer Diffusion in the Electrochemical Detection of Nicotine on Basal Plane Pyrolytic Graphite (BPPG) Electrodes Modified with Layers of Multi-Walled Carbon Nanotubes

(MWCNT-BPPG). *Sens. Actuators B Chem.* **2010**, *144*, 153–158. https://doi.org/10.1016/j.snb.2009.10.055.

(97) Nasraoui, S.; Ameur, S.; Al-Hamry, A.; Ali, M. B.; Kanoun, O. Development of an Efficient Voltammetric Sensor for the Monitoring of 4-Aminophenol Based on Flexible Laser Induced Graphene Electrodes Modified with MWCNT-PANI. *Sensors* **2022**, *22* (3). https://doi.org/10.3390/s22030833.

Chapter 2

Thin layer cell behavior of CNT yarn and cavity carbon nanopipette electrodes: Effect on catecholamine detection

Chapter 2 was reprinted from *Electrochimica acta* 361 (**2020**): 137032. Copyright 2020 Elsevier.

Abstract

Carbon nanotube yarn microelectrodes (CNTYMEs) are an alternative to carbon-fiber microelectrodes (CFMEs) with interesting electrochemical properties because analyte is momentarily trapped in cavities between the CNTs. Here, we compare fast-scan cyclic voltammetry (FSCV) detection of catecholamines, including dopamine, norepinephrine, and epinephrine, at CNTYMEs, CFMEs, as well as cavity carbon nanopipette electrodes (CNPEs). At CFMEs, current decreases dramatically at high FSCV repetition frequencies. At CNTYMEs, current is almost independent of FSCV repetition frequency because the analytes are trapped in the crevices between CNTs, and thus the electrode acts like a thin-layer cell. At CFMEs, small cyclization product peaks are observed due to an intramolecular cyclization reaction to form leucocatecholamine, which is electroactive, and these peaks are largest for the secondary amine epinephrine. At CNTYMEs, more of the leucocatecholamine cyclization product is detected for all catecholamines because of the enhanced trapping effects, particularly at higher repetition rates where the reaction occurs more frequently and more product is accumulated. For epinephrine, the secondary peaks have larger currents than the primary oxidation peaks at 100 Hz, and similar trends are observed with faster scan rates and 500 Hz repetition frequencies. Finally, we examined CNPEs, which also momentarily trap neurotransmitters. Similar to CNTYMEs, at CNPEs, catecholamines have robust cyclization peaks, particularly at high repetition rates. Thus, CNTYMEs and CNPEs have thin layer cell behavior that facilitates high temporal resolution measurements, but catecholamines CVs are complicated by cyclization reactions. However, those additional peaks could be useful in discriminating the analytes, particularly epinephrine and norepinephrine.

2.1 Introduction

Fast-scan cyclic voltammetry (FSCV) is used to detect neurotransmitters *in vivo* because it has a rapid time resolution and provides a unique cyclic voltammogram (CV) that enables analyte identification.[1–4] Carbon-fiber microelectrodes (CFMEs) have strong adsorption for dopamine, enhancing the sensitivity and electron transfer.[5–7] However, FSCV for dopamine at CFMEs is usually limited to 10 Hz repetition frequency because at higher frequencies, the signal decreases dramatically when there is less time at the holding potential for dopamine to be adsorbed on the electrode surface.[8] Recently, carbon nanomaterial electrodes have been developed to enhance dopamine detection.[9,10] For example, a carbon nanotube yarn microelectrode (CNTYME), made from aligned carbon nanotube bundles twisted into a thread,[7,11,12] has highly sensitive dopamine detection with FSCV and a more reversible CV with smaller peak-to-peak separation (ΔE_p).[13,14] Our group demonstrated that at CNTYMEs, dopamine peak current is independent of the FSCV repetition frequency, which enables CNTYMEs to maintain a high sensitivity with improved temporal resolution.[9,15] This frequency independent response is due to surface roughness, as crevices on the scale of the diffusion layer trap dopamine, leading to thin layer cell electrochemical behavior.[16,17] Practically, this occurs at CNT yarns and fibers with micron scale surface roughness,[9,17,18] and the CNTYME performance is improved by increasing the surface roughness using laser activation or an anti-static gun.[19,20] Trapping effects are also observed at other electrodes, including cavity carbon nanopipette microelectrodes (CNPEs),[9,21] where cavity CNPEs have a nano-sized cavity at the tip that also gives rise to thin layer cell electrochemical behavior.[21] However, all the FSCV research on CNTYMEs and cavity CNPEs is focused on dopamine, and other neurotransmitters have not been studied.[13,19]

Dopamine, norepinephrine, and epinephrine are classified as catecholamine neurotransmitters due to their similar chemical structure.[22] Dopamine is the major neurotransmitter associated with reward, and is dysregulated during drug abuse, and also regulates locomotion and is depleted during Parkinson's disease.[23] Norepinephrine release in the brain influences sleep, attention, and feeding behavior.[24] Epinephrine causes fight or flight responses, such as increasing heart rate and contractility.[25] Catecholamines can be detected electrochemically, but their CVs are largely indistinguishable with normal oxidation limits at carbon electrodes.[26,27] However, Wightman's group also observed a second anodic peak for epinephrine at around 1.3 V due to the oxidation of the secondary amine group, which can be used to distinguish CVs of epinephrine and norepinephrine.[22,26,28] In 1967, Ralph Adams published oxidation pathways of catecholamines and showed that the o-quinone species produced by oxidation can be cyclized and produce leucocatecholamine products that undergo further redox reactions.[29] These leucocatecholamine oxidation peaks are larger for epinephrine, a secondary amine, but are typically observed only at high concentrations. More recently, Mao's group reported cyclization of dopamine at a carbon nanotube-based biosensor, which enhances selective dopamine detection in the presence of ascorbic acid and DOPAC (3,4-Dihydroxyphenylacetic acid).[30] In addition, we observed the cyclization products of dopamine in CNPEs with FSCV;[21] however, it is not clear how the cyclization of epinephrine and norepinephrine will be affected at electrodes with a structure that facilitates thin layer cell behavior.

The goal of this study is to compare the FSCV response of dopamine, norepinephrine, and epinephrine at CNTYMEs and CNPEs. Neurotransmitters were measured with FSCV with varied scan rates and repetition frequencies. At CNTYMEs and CNPEs, current is maintained for catecholamines at higher repetition frequencies, in contrast to CFMEs, where current decreases significantly with higher repetition frequencies. In addition, the secondary oxidation peaks that result from the cyclization reactions are larger at CNTYMEs and cavity CNPEs than at CFMEs. Secondary peaks are more prominent at high repetition rates because more product accumulates in a short amount of time. Epinephrine has the largest secondary anodic peak because it has a secondary amine group, which promotes cyclization, while norepinephrine has the smallest cyclization peak. Therefore, the differences in CV shapes at these electrodes might allow discrimination of the analytes. All of the catecholamines are detected with higher temporal resolution at CNTYMEs and CNPEs, but that secondary reactions due to cyclization are more prominent because of the trapping effects.

2.2 Experimental section

2.2.1 Electrode Fabrication

CFMEs were fabricated by inserting T-650 carbon fibers into a glass capillary (0.68mm ID X 1.2mm OD) and pulled by a glass puller (model PE-21, Narishige, Tokyo, Japan) to form a cylinder tip. The fiber was cut to 100 µm from the glass tip junction and insulated by Epon Resin 828 (Miller-Stephenson, Danbury, CT) mixed with 14% 1,3-phenylenediamine hardener at 85 °C. After overnight curing at room temperature, the electrodes were placed in the oven at 100°C for two hours and then transferred to the 150°C oven overnight.

Commercial carbon nanotube yarn with 50 µm diameter was purchased from the Nanoworld Lab, Department of Chemical and Environmental Engineering, University of Cincinnati. A glass capillary was pulled by a glass pipette puller and cut to have an opening about 100 µm. A piece of 1.5 cm long CNT yarn was gently inserted into the opening tip in the isopropanol solution to remove impurities on the surface and prevent the change of geometry by external force. When the capillary dried, the electrode open tip was then fully immerged and epoxied with Epon Resin 828. Curing procedure was the same as CFMEs, and electrodes were polished to a 45° angle on a fine diamond abrasive plate (Sutter Instruments model BV-10, Novato, CA). Finally, the electrodes were soaked in isopropanol solution for 10 minutes to remove impurities deposited during the polishing process.

2.2.2 Solutions and Electrochemistry

Dopamine hydrochloride, norepinephrine hydrochloride and epinephrine hydrochloride were purchased from Sigma-Aldrich (St. Louis, MO). Analytes were dissolved in 0.1 M $HClO_4$ to make 10 mM stock solutions and were diluted daily to 1 µM in PBS pH 7.4 buffer (131.25 mM NaCl, 3.00 mM KCl, 10 mM NaH_2PO_4, 1.2 mM $MgCl_2$, 2.0 mM Na_2SO_4, and 1.2 mM $CaCl_2$).

The buffer and analytes were supplied to the flow cell using a dual syringe pump and were injected through a six-port switching valve (Valco Instruments Co. Inc. Houston, TX).[31] Electrodes were filled with 1 M KCl and inserted into an electrode holder with a silver wire to connect to the headstage of the Dagan ChemClamp (Dagan, Minnesota). The applied triangular waveform was from -0.4 V to 1.3 V versus a Ag/AgCl reference electrode. Scan rate was 400 V/s with frequencies ranging from 10 Hz to 100 Hz, or 2000 V/s for frequencies from 5 Hz to 500 Hz. When multiple frequencies were tested, they were tested from low to high frequency and all three analytes were tested before changing to a higher frequency to prevent electro-activation of carbon electrode surface. FSCV data were acquired with HDCV software, developed at University of North Carolina, Chapel Hill. All CVs are averaged from 5 CVs across 0.5 s in time, and background subtracted by averaging 10 background CVs (1 s). For flow injection analysis data, CVs were taken at the end of a 5 s injection of analyte, to best highlight the secondary peaks which grow in over time.

2.2.3 Surface Characterization

For scanning electrochemical microscopy (SEM), CFMEs and CNTYMEs were taped on a flat aluminum stage. The polished surface of the CNT yarn disk electrode was placed upward to guarantee the image capture. SEM was performed on a ZEISS Merlin High-Resolution Scanning electron microscope (Oberkochen, Germany), provided by Center for Nanophase Materials Science (CNMS), Oak Ridge National Laboratory.

2.3 Results and Discussion

2.3.1 Surface characteristics

First, we compared the structural and electrochemical properties of CFMEs and CNTYMEs to detect catecholamines. Figure 1 shows the surfaces of CFMEs and CNTYMEs characterized by SEM. The T650 carbon fiber, 7 µm in diameter, has a relatively smooth surface, but also has striations (Fig. 1A). Polished disk electrodes are used for the CNTYME, and Figure 1B shows the center region, which has a forest structure formed by vertically aligned CNTs. The CNTYME has a rough surface, with many tufts of CNTs with crevices in between. R_Z is a roughness factor which represents the distance from the top of the highest peak to the lowest valley, and is about 0.95 μm for the CNTYME, similar to previous work.[20]

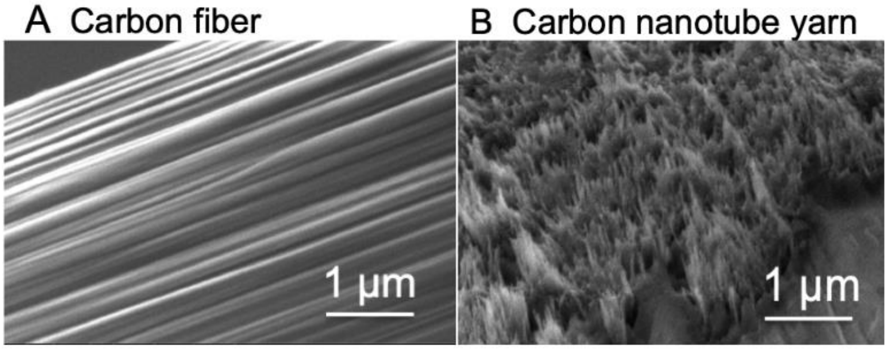

Figure 1. SEM images. **(A)** T650 carbon fiber surface, **(B)** CNTYME surface.

2.3.2 Oxidation current decays with higher repetition frequencies at CFMEs

To study the effect of repetition frequency on FSCV measurements, cyclic voltammograms of 1 µM catecholamines were measured at CFMEs at frequencies from 10 Hz to 100 Hz. Figure 2A shows a cyclic voltammogram of 1 μM dopamine, which has an oxidation peak for dopamine at 0.6 V and a reduction peak on the backwards scan around -0.2 V.[32] At 10 Hz, the reduction peak current (14 ± 2 nA) is less than the oxidation peak current (31 ± 3 nA), because dopamine-ortho-quinone (DOQ) has a larger desorption rate constant and desorbs more readily from the CFME.[8] At 100 Hz, oxidation currents are much smaller, less than 10 nA, but the CVs are more symmetrical and the oxidation currents (4.4 ± 0.5 nA) are more similar to the reduction currents (3.2 ± 0.3 nA). Similar CV features were also observed for norepinephrine and epinephrine (Fig. 2B and 2C). The peak currents at 10 Hz are larger than those at 100 Hz, and at 10 Hz, the oxidation peak currents at 0.6 V are larger than reduction peak currents at -0.2 V. Dopamine has the highest peak current among the three catecholamine analytes, likely due to stronger adsorption.

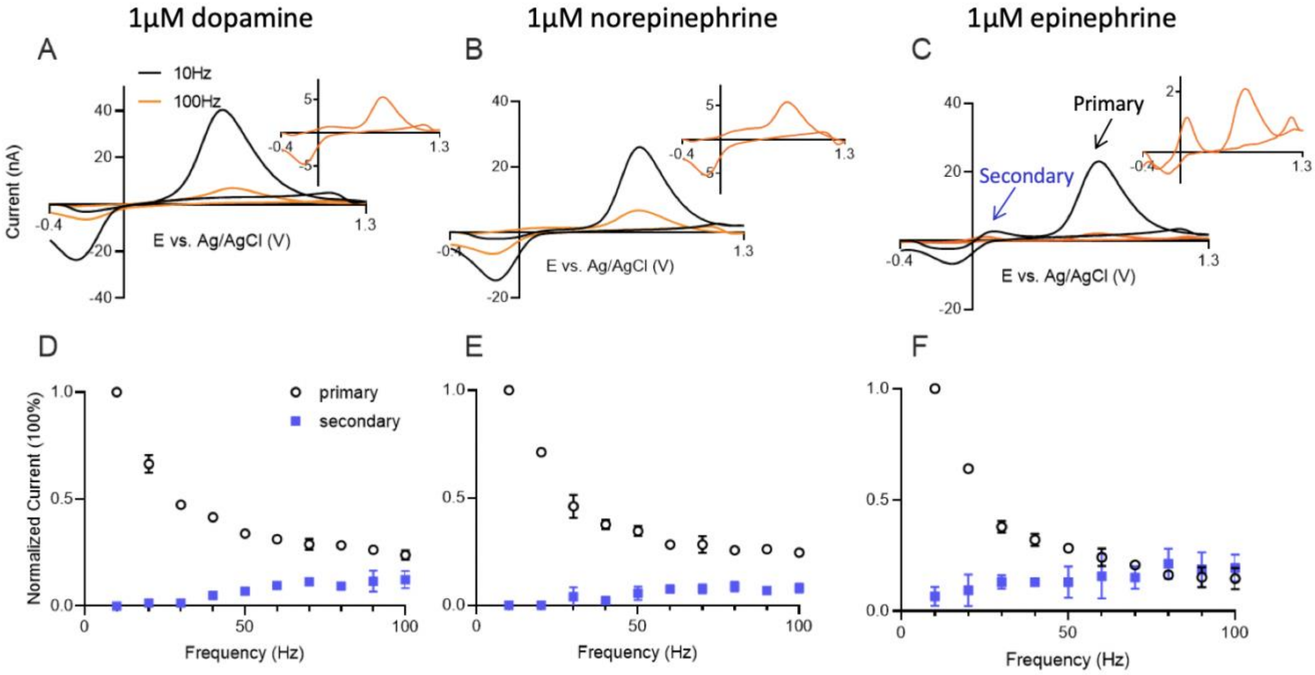

Figure 2. CFME-based detection of catecholamines at different FSCV frequencies. Cyclic voltammograms of **(A)** dopamine, **(B)** norepinephrine and **(C)** epinephrine at 10 Hz (black) and 100 Hz (orange) on CFME with FSCV. The dopamine waveform (-0.4V to 1.3V and back at 400V/s) was applied. Insets are CVs collected at 100 Hz signals. Normalized current (normalized to 10 Hz signal) of the primary and secondary oxidation peaks of **(D)** dopamine, **(E)** norepinephrine, and **(F)** epinephrine at various frequencies. *n* = 4 electrodes, error bars SEM.

Although the CVs of the three catecholamines have similar oxidation and reduction potentials, there are slight differences. For epinephrine, a secondary redox couple peak due to the intramolecular cyclization reaction is also present, with an oxidation peak at 0.15 V (Fig. 2C). Scheme 1 shows redox pathways and cyclization of catecholamines. The overall anodic pathway of catecholamines is an ECE (Electrochemical-Chemical-Electrochemical) mechanism.[26,33] The catecholamine is oxidized via an electrochemical reaction to generate a corresponding ortho-quinone molecule, which undergoes intramolecular cyclization to produce leucocatecholamine via a Michael addition reaction. This chemical process is irreversible, as leucocatecholamines cannot revert back to the original species once Michael addition occurs.[30] In the following electrochemical process, leucocatecholamine is further oxidized to an aminochrome; thus, a reversible oxidation couple with an oxidation peak at 0.15 V is observed in the cyclic voltammogram.[21,30,34] Epinephrine is the most favorable to undergo the cyclization side reaction, because the methyl group on the secondary amine of epinephrine acts as an electron donor making the nitrogen more nucleophilic, and making it easier to attack the ring structure of the quinone. Secondary peaks are therefore larger for epinephrine.[28] Epinephrine also has another oxidation peak that occurs at 1.3 V on back scan, which is due to the oxidation of the amine group.[28] As a secondary amine, the methylated amine group on epinephrine is more easily oxidized than the primary amines on dopamine and norepinephrine. Researchers have separated epinephrine from norepinephrine based on the peak at 1.3 V, which is much larger on the voltammogram of epinephrine.[22]

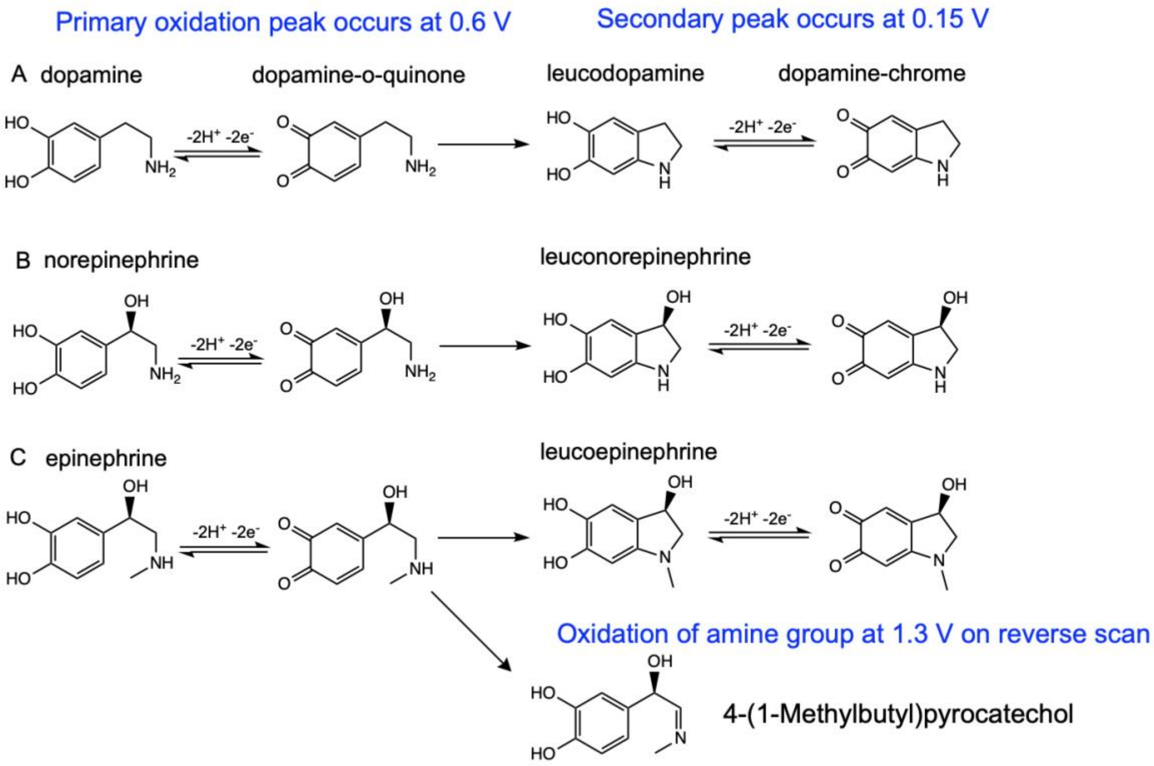

Scheme 1. Oxidation reaction schemes of **(A)** dopamine, **(B)** norepinephrine and **(C)** epinephrine.

Figure 2D-F plots the oxidation current vs repetition frequency at CFMEs. For dopamine (Fig. 2D), there is a dramatic decay of the primary oxidation current as FSCV repetition frequency increases. The current at 100 Hz is only 20% of that at 10 Hz. Norepinephrine and epinephrine (Fig. 2E, 2F) have similar trends as dopamine, with primary oxidation currents that decay with increasing frequency. With higher repetition frequency, all three analytes also have an increasing secondary peak current from the cyclization product. The decrease in primary oxidation current for epinephrine is larger than for norepinephrine and dopamine, but its secondary peak current increases the most. More epinephrine-o-quinone molecules are consumed in the chemical process and secondary peaks grow, but the primary peak decreases because less epinephrine-o-quinone is reduced back to epinephrine and detected on the next scan. Cyclization is observed more at 100 Hz than 10 Hz because the number of electrochemical cycles is increased; thus, if a given percentage of o-quinone species will cyclize on each scan, there is more of that cyclization product being accumulated with ten times more scans per second. Overall, the primary oxidation current for all the catecholamines at CFMEs decreases with increasing frequency, limiting the temporal response. Note that the overall amount of cyclization observed at CFMEs is low due to the diffusion of o-quinones.

2.3.3 CNTYMEs maintain high oxidation currents at higher repetition frequencies

Next, CNTYMEs were tested with 1 µM catecholamines at different FSCV repetition frequencies. Figure 3 shows the CVs of dopamine (Figure 3A), norepinephrine (Figure 3B), and epinephrine (Figure 3C) at 10 Hz and 100 Hz. The primary oxidation peak current of dopamine collected at CNTYMEs is 5.2 ± 0.2 nA at 10 Hz, which is smaller than that of CFMEs, because CNTYMEs are disk electrode that have a smaller surface area than the cylindrical CFMEs. The anodic current is 3.9 ± 0.2 nA, which is more reversible than CFMEs. At 100 Hz, the peak current for dopamine is only slightly decreased at CNYMEs and the secondary oxidation peak at 0.15 V is clearly observed. Norepinephrine has a similar CV shape as dopamine at different frequencies, but the secondary oxidation peak is harder to observe. Epinephrine, however, has multiple oxidation peaks and at 100 Hz, the primary peak is smaller than the secondary peaks at 0.15 V and 1.3 V. Compared to CFMEs, the reduction peaks for all three analytes are larger, particularly at high frequencies, indicating more reversibility. Thus, observation of secondary peaks is enhanced at CNTYMEs.

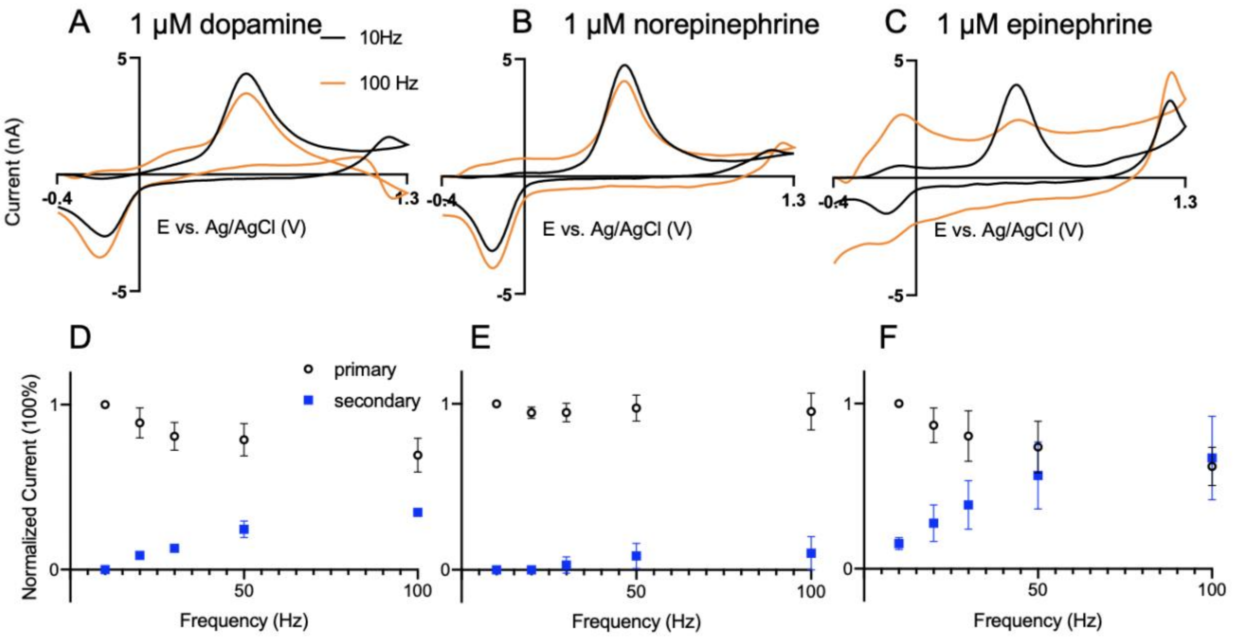

Figure 3. CNTYMEs for catecholamine detection. CVs at 10 Hz (black) and 100 Hz (orange) for **(A)** 1 µM dopamine, **(B)** 1 µM norepinephrine, and **(C)** 1 µM epinephrine. Normalized current vs repetition frequency for **(D)** dopamine, **(E)** norepinephrine, and **(F)** epinephrine. Both the primary oxidation peak (black) and the secondary oxidation peak (blue) from the cyclization reaction are plotted. *n* = 4

To understand the effects of repetition frequency on current, normalized oxidative currents for the primary and secondary reactions were plotted vs frequency (Fig. 3D, E, F). For dopamine and norepinephrine, the primary peak (0.6 V) decreases only slightly, while the secondary (0.15 V) oxidation peak increases at higher frequencies. Norepinephrine has little secondary peak and thus the current for the primary oxidation is nearly independent of repetition frequency. However, for epinephrine, the primary current drops more at high frequencies because there are more secondary reactions occurring. The primary peak drops as the epinephrine is consumed by the chemical reaction and the secondary peak rises due to reversible detection of the leucoepinephrine redox couple. At higher frequencies, there are more electrochemical scans and so more leucoepinephrine is accumulated, since the cyclization reaction is an irreversible process.

2.3.4 Enhanced secondary peaks at CNTYMEs

To compare CNTYMEs and CFMEs, Figure 4 shows the normalized CVs for dopamine, norepinephrine, and epinephrine at 100 Hz. The primary oxidation current was normalized to account for difference in surface area between CNTYME and CFME. CNTYMEs have larger secondary peaks for all three analytes than CFMEs. For epinephrine, secondary peaks for CNTYMEs are larger than primary peaks for CNTYMEs, but not for CFMEs. Secondary peaks are larger at CNTYMEs because the o-quinone and cyclization products become trapped in the crevices between CNTs and therefore are more likely to be detected. In a 5 second injection of analyte in a flow cell, CV shapes change at different time points. Figure 5 shows the CVs early after exposure to the analyte (Fig. 5A) and late in the 5 s exposure to the analyte at CNTYMEs. At the later time point (4 s into the injection) the CVs have higher secondary peak currents because more cyclized molecules accumulated near the electrode surface over time. Epinephrine has the highest secondary peak current increase because it forms more cyclization products, while the norepinephrine CV does not change much over time because it is not as likely to cyclize. The peak-to-peak separation (∆Ep) is smaller at CNTYMEs for the primary oxidation, due to faster electron transfer kinetics at CNTs,[7] and the secondary peak potentials also shift to more negative potentials due to catalytic effects. The increasing oxidation peak at 1.3 V at CNTYMEs may also result from the electrocatalytic effect because the reaction can occur at lower potentials, so there is more time for the reaction to occur with the given potential limits.[7]

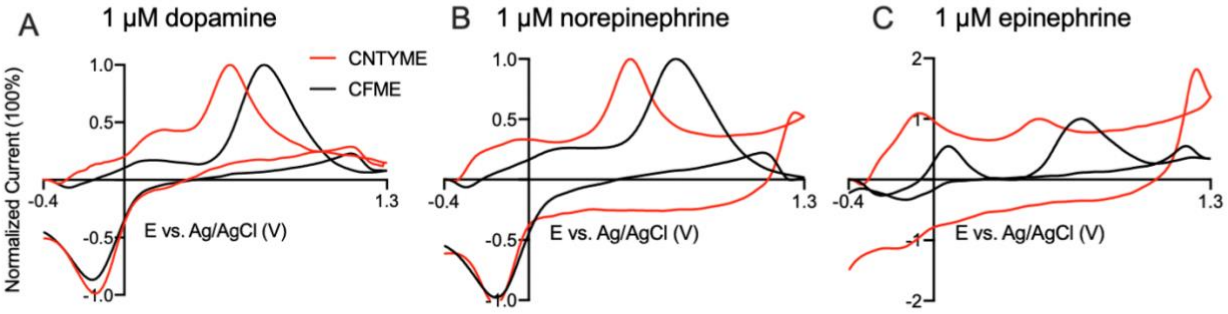

Figure 4. Comparison of CVs for catecholamines at CNTYMEs and CFMEs at 100 Hz. **(A)** dopamine, **(B)** norepinephrine, and **(C)** epinephrine.

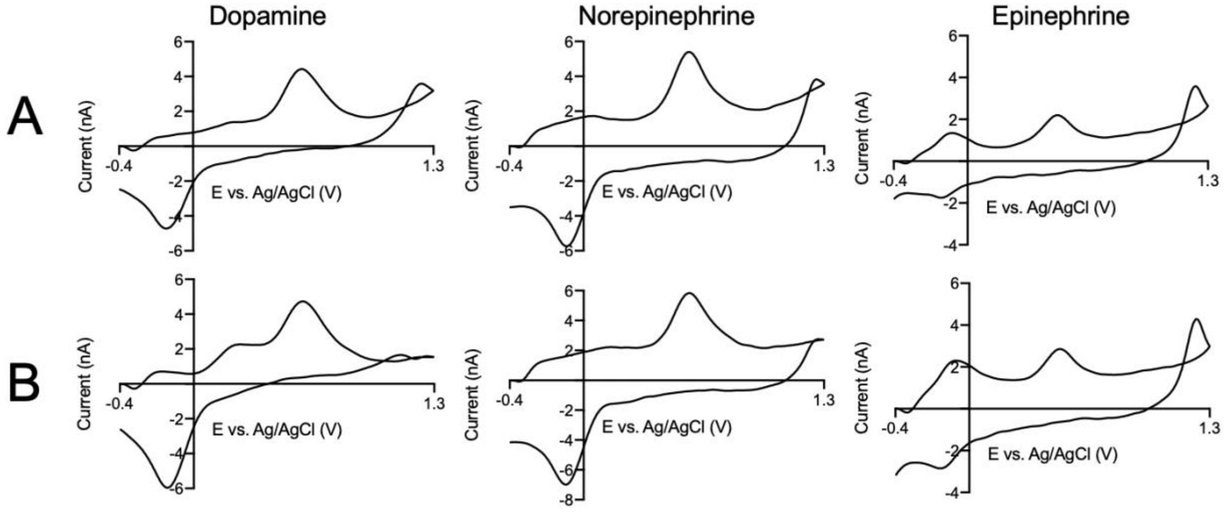

Figure 5. CV of dopamine, norepinephrine and epinephrine collected at different time points: (A) 4 s and (B) 9 s in one scan.

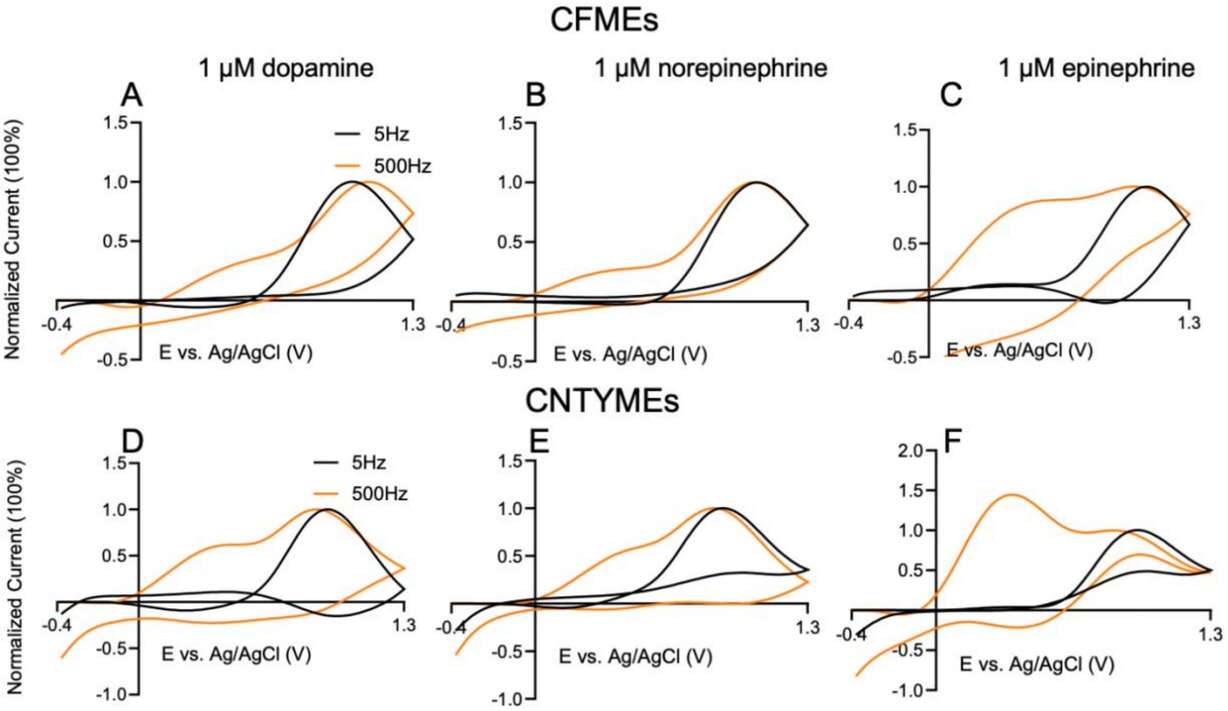

Figure 6. Cyclic voltammogram with 2000V/s scan rate and 5 Hz (black) and 500 Hz (orange) repetition frequencies. At CFMEs: **(A)** dopamine, **(B)** norepinephrine, and **(C)** epinephrine. At CNTYMEs: (**D)** dopamine, **(E)** norepinephrine, **(F)** epinephrine. CVs normalized to make primary oxidation current 100 %.

Using a scan rate of 400 V/s allows a maximum frequency of ~115 Hz. To understand the behavior at higher repetition frequencies, higher scan rates were employed. With a scan rate of 2000 V/s, the scan time is reduced to 1.7 ms, which allows a maximum repetition frequency of about 500 Hz. Figure 6 compares a 2000 V/s scan rate with 5 Hz or 500 Hz repetition frequencies for CFMEs and CNTYMEs. The anodic currents were normalized to the primary oxidative current to compare the relative heights of the secondary peaks. Cyclic voltammograms at 2000 V/s have a larger ΔE_p, because peaks shift with scan rate in FSCV due to sluggish electron transfer.[35] The primary anodic peak occurs around 1.0 V at CFMEs and 0.8 V at CNTYMEs, and secondary peak occurs at 0.5 V, whereas reduction peaks are not observed. Overall, there are dramatically larger secondary peaks for dopamine, norepinephrine, and epinephrine at 500 Hz at CNTYMEs and those secondary peaks are larger than at CFMEs. Epinephrine, the catecholamine with the most cyclization reaction, has the largest secondary peak, which predominates over the primary peak.

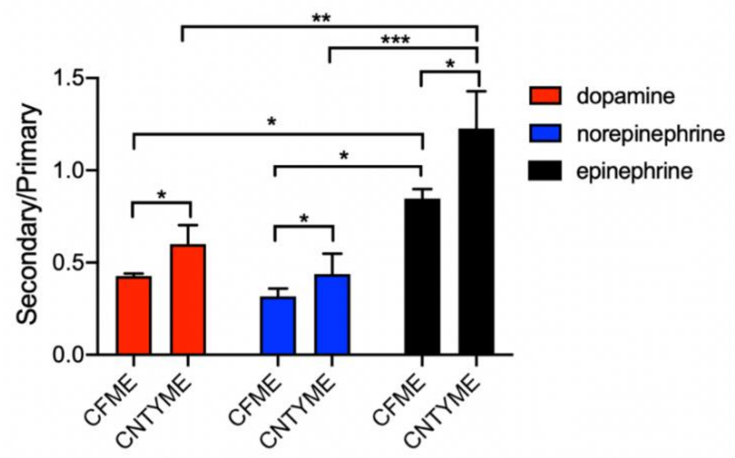

Figure 7. Ratios of secondary to primary anodic peak currents for catecholamines at CNTYMEs and CFMEs. Peak currents were obtained at 500 Hz, with a scan rate of 2000 V/s (Two-way ANOVA with Tukey's multiple comparison test, error bars are SEM with n = 4). * $p<0.05$, **$p < 0.01$, ***$p<0.001$

Ratios of primary to secondary anodic current were further analyzed for the three catecholamines. At 500 Hz (2000 V/s, Fig. 7), the secondary to primary peak ratio for dopamine is approximately 0.6 at CNTYMEs, while it is 0.4 for norepinephrine, and 1.2 for epinephrine. A ratio larger than 1 means the secondary peak current is larger the primary current. There is a significant main effect of analyte (Two-way ANOVA with Tukey's multiple comparison test, $p < 0.001$, n = 4 electrodes) and electrode type ($p = 0.0244$) on the current ratios (Figure 7). The secondary peak current ratios at CNTYMEs are significantly larger than those at CFMEs for all three analytes ($p < 0.1$). At both CFMEs and CNTYMEs, epinephrine has larger ratio of secondary peak currents than dopamine or norepinephrine, because it easily cyclizes. CNTYMEs have a rougher surface that traps the analyte and enhances the secondary oxidation peaks.

2.3.5 Cavity carbon nanopipette microelectrodes are also frequency independent with more secondary peaks

To prove that the enhancement of secondary peaks is due to trapping effects, we tested another type of electrode with a geometry that is known to momentarily trap analytes. Cavity carbon-nanopipette microelectrodes (CNPEs) have tip diameters of 200-400 nm and a cavity that is 500 nm long. Their electrochemical properties have been tested for dopamine,[21,36–38] and FSCV detection of dopamine is frequency independent due to the trapping effect within the cavity. Here, we explored the current response of dopamine, norepinephrine, and epinephrine at different frequencies at cavity CNPEs. The surface area of cavity CNPEs is much smaller than CFMEs and CNTYMEs[36] so 10 µM dopamine, norepinephrine, and epinephrine were tested.

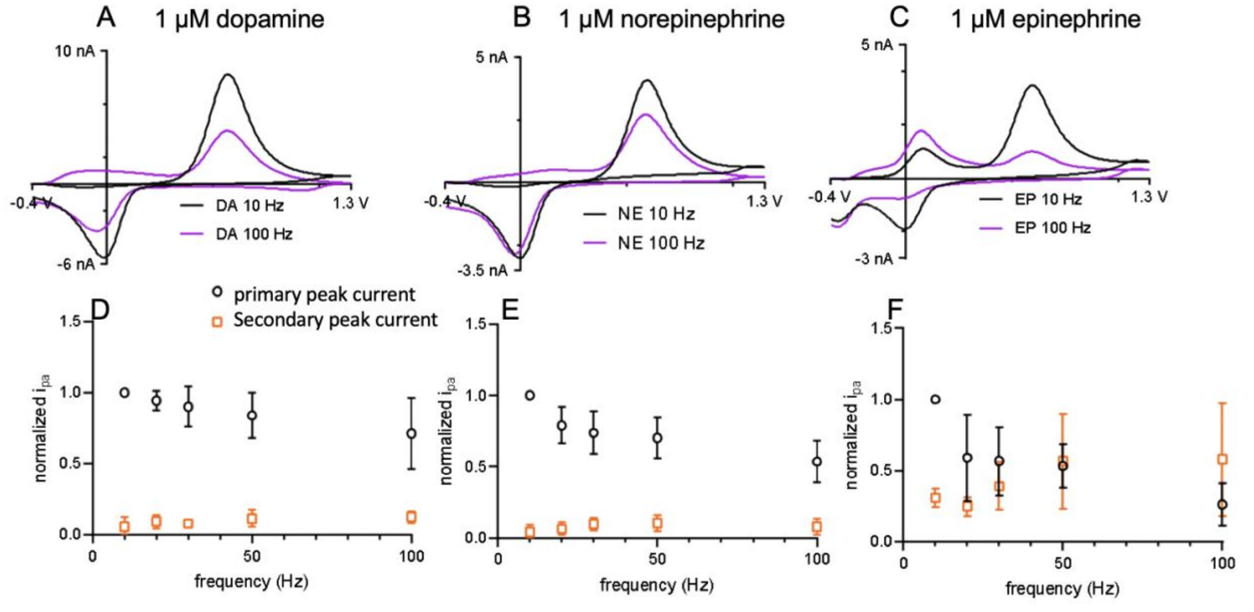

Figure 8. Cavity carbon nanopipette microelectrode detection of catecholamines at different FSCV frequencies. Cyclic voltammograms of 10 μM **(A)** dopamine, **(B)** norepinephrine, and **(C)** epinephrine at 10 Hz and 100 Hz. Normalized current vs frequency for CNPEs **(D)** dopamine, **(E)** norepinephrine, **(F)** epinephrine.

The CVs in Figure 8 indicate peak currents decrease slightly with increasing repetition frequency for dopamine and norepinephrine, but not as at CFMEs. Dopamine (Fig. 8A) and norepinephrine (Figure 8B) have smaller drops in current from 10 to 100 Hz, whereas epinephrine has the largest current drop, but also the largest secondary peaks. Interestingly, epinephrine has a well-defined secondary oxidation couple, but the peak at 1.3 V is not as large as for CNTYMEs. This indicates that the 1.3 V peak is likely enhanced at CNTYMEs due to electrocatalytic effects and not trapping effects. The trends for dopamine (Fig. 8D) and norepinephrine (Fig.8E) primary and secondary currents at CNPEs are similar to CNTYMEs. The primary currents do not decay as much as CFMEs with increasing frequency and the secondary peak increases with increasing frequency. However, the primary current of epinephrine (Fig. 8F) decays a lot as the secondary anodic peak increases. The secondary oxidation peak current dominates the primary one at 100 Hz. With increasing frequencies, more epinephrine-o-quinone is made and more irreversibly cyclizes to leucoepinephrine, which is detected in future scans. Overall, the catecholamine neurotransmitter electrochemistry is similar at both CNTYMEs and cavity CNPEs. They both have thin layer cell behavior and trapping effects that lead to frequency independent current response and enhanced secondary oxidation peaks.

2.4 Discussion

Electrochemical performance for catecholamines is different at CNTYMEs than for CFMEs. The CVs at CNTYMEs have a smaller peak-to-peak difference, more reversible CV shapes, and more frequency independent peak current responses. Secondary oxidation peaks are more readily apparent at CNTYMEs, especially at higher repetition frequencies, a result that is similar to catecholamine oxidation at cavity CNPEs. These results lead to the hypothesis that CNTYMEs act as a thin-layer electrode and that secondary peaks are enhanced by trapping effects.

Thin layer cell electrodes were first developed in the 1960s and have two flat working electrodes separated by a thin electrolyte space, where the gap is smaller than the diffusion layer thickness.[33,39] Mass transfer can be neglected in a thin-layer cell, and the analyte concentration on the surface is maintained due to lack of depletion. Cyclic voltammograms in a thin-layer cell have different properties: the peak current is proportional to scan rate (rather than the square root of scan rate with diffusion control) and the voltammogram is perfectly symmetrical and has a ΔE_p of 0 for a reversible redox couple.[33]

CNTYMEs consist of vertically aligned CNTs, which can be treated as separate working electrodes, with cavities in between them that act as the narrow gaps in a thin-layer cell. If the depth of the cavity is larger than the diffusion layer, molecules will be trapped in the cavity and will remain close to the CNT for the timescale of the experiment. For one dimensional diffusion, the diffusion layer thickness is calculated by

$$\delta = (2Dt)^{1/2}$$

The calculated diffusion length is 0.9 μm, based on a diffusion coefficient of 2×10^{-6} cm^2 s^{-1} [40] and time for DOQ to exist of 4.25 ms with 400 V/s scan rate (the time is based on when oxidation of DA occurs but DOQ is not yet reduced back to DA). Thus, the diffusion layer thickness is approximately the same as the surface roughness of CNTYMEs, which was measured to be

0.95 µm by laser scanning confocal microscopy. Note however, the trapping effect will be larger in two or three dimensions, because the cavities are deep and narrow, and catecholamine will hit “walls” as it diffuses. Thus, the CNTYME has a structure that makes it equivalent to thousands of small thin layer cells. Consistent with this theory, the CVs obtained from CNTYMEs exhibit a smaller ΔE_p and a larger cathodic current compared with CFMEs. The same result is observed at cavity CNPEs, which also have a thin-layer like structure. Unlike CNTYMEs, CNPEs have one, submicron-sized cavity, instead of surface roughness, but molecules are still trapped inside, increasing the local concentration of the analytes.

The thin layer structure leads to the frequency independent current response of catecholamines at CNTYMEs. The kinetics of dopamine are adsorption controlled at carbon fibers,[8] but the theory and behavior for adsorption control is derived from thin-layer electrochemistry because it assumes there is no diffusion.[33] At carbon electrodes, if dopamine remained adsorbed to the electrode while it was oxidized to DOQ and the reduced back to dopamine, the current response would be frequency independent. However, the rate for DOQ desorption is 10-fold higher than for dopamine at CFMEs, and much of the DOQ falls off and diffuses away from the electrode surface before it is reduced back to dopamine.[41] Time at the holding potential is necessary to re-adsorb dopamine, and that time is controlled by the repetition frequency.[8,42] At CNTYMEs or cavity CNPEs, molecules that enter the cavities can’t diffuse out on the FSCV time scale. Thus, even if DOQ desorbs from the electrode, it would still be trapped near the surface and be able to undergo redox reaction back to dopamine. If no side reactions occur, the reaction would be perfectly reversible and repetition frequency independent at CNTYMEs. The response of norepinephrine is the most ideal, because it had the lowest rate of side reaction.

The thin layer structure of CNTYMEs also contributes to detecting more secondary oxidation peaks. For a CFME, if DOQ desorbed and cyclized, it might diffuse away from the surface and the cyclization product would not be detected; indeed, leucodopamine is typically only observed with high concentrations, in the mM range.[40] Here, cyclization products were observed at low concentrations more frequently for all the catecholamines at CNTYMEs and CNPEs because leucocatecholamines are restricted near the surface. However, the downside to observing cyclization peaks is that the primary oxidation peak decreases with repetition frequency, because some of the original catecholamine is not recycled in the redox reaction, but is “consumed” in the side chemical reaction. Therefore, for molecules that undergo extensive cyclization, the primary current decays with frequency at CNTYMEs, but for a different reason than the decay observed at CFMEs. Still, CNTYMEs maintained higher currents for high frequencies than CFMEs. The upside to observing more cyclization products is that it could be a method to distinguish different molecules. Norepinephrine and epinephrine are more easily discriminated at CNTYMEs, especially at 10 Hz FSCV frequency, because side peaks are amplified for epinephrine. Differentiating dopamine and norepinephrine is still challenging, but using more advanced data analysis techniques, such as machine learning or principal components analysis,[43,44] it may be possible to discriminate the shapes because there are differences in the secondary peaks in the CVs.

Our work also shows cyclization peak currents are larger with increasing frequencies for all three catecholamines. When applying the dopamine waveform at 10 Hz, the voltage ramp where redox reactions occur is only 8.5% of the time, but at 100 Hz, the voltage ramp takes 85% of the time. With ten times number of reactions happening in a given time at 100 Hz, the product concentrations also increase. Leucocatecholamines are further oxidized to aminochromes and this reaction is reversible, so the same product can be detected again on future scans. Higher cyclization peak currents are observed at both CFMEs and CNTYMEs at high frequencies. Moreover, with the thin-layer structure on CNTYMEs, the accumulated leucocatecholamines are trapped in the restricted area near the electrode where they are detected. Thus, CNTYMEs have enhanced secondary peaks due to both trapping effect and frequency effects.

2.5 Conclusions

CNTYMEs are a good alternative to CFMEs in detection of neurotransmitters due to the fast electron transfer kinetics, good electrochemical properties, and high temporal resolution. Both CNTYMEs and cavity CNPEs have trapping effects caused by thin-layer structure: CNTYMEs have micron-sized surface roughness, whereas cavity-CNPEs have nano-cavities on the tip. Overall, this paper shows that CNTYMEs and cavity CNPEs have surface structures that give rise to thin layer cell electrochemistry on the time scale of FSCV. The trapping effects cause the primary current to be largely independent of FSCV frequency, because any o-quinone that desorbs is trapped near the electrode surface and can be detected again. However, catecholamines can also cyclize and detection of these products is amplified by trapping effects at CNTYMEs and cavity CNPEs, especially at higher frequencies. Epinephrine has the highest rate of cyclization and thus detection of secondary peaks is more evident at CNTYMEs and at high repetition frequencies. Thus, this study shows that thin layer cell electrodes are useful in fundamental understanding of ECE reactions and may be useful for discriminating different compounds with similar structure based on secondary products.

Acknowledgement

This study is supported by National Institution of Health (NIH) grant R01 EB026497 and NSF grant CHE-1763337 (M.V.M.). A portion of this research was conducted at Nanoscale Material Characterization Facility, University of Virginia (NMCF, UVA) and Center for Nanophase Materials Science, Oak Ridge National Laboratory (CNMS, ORNL), which is a DOE Office of Science User Facility under user agreement CNMS 2019-034.

The authors declare no conflicts of interest.

2.6 References

(1) Jaquins-Gerstl, A.; Michael, A. C. A Review of the Effects of FSCV and Microdialysis Measurements on Dopamine Release in the Surrounding Tissue. *Analyst* **2015**, *140* (11), 3696–3708. https://doi.org/10.1039/c4an02065k.

(2) Roberts, J. G.; Sombers, L. A. Fast-Scan Cyclic Voltammetry: Chemical Sensing in the Brain and Beyond. *Anal. Chem.* **2018**, *90* (1), 490–504. https://doi.org/10.1021/acs.analchem.7b04732.

(3) Nguyen, M. D.; Venton, B. J. Fast-Scan Cyclic Voltammetry for the Characterization of Rapid Adenosine Release. *Comput. Struct. Biotechnol. J.* **2015**, *13*, 47–54. https://doi.org/10.1016/j.csbj.2014.12.006.

(4) Ganesana, M.; Lee, S. T.; Wang, Y.; Venton, B. J. Analytical Techniques in Neuroscience: Recent Advances in Imaging, Separation, and Electrochemical Methods. *Anal. Chem.* **2017**, *89* (1), 314–341. https://doi.org/10.1021/acs.analchem.6b04278.

(5) Huffman, M. L.; Venton, B. J. Carbon-Fiber Microelectrodes for in Vivo Applications. *The Analyst* **2009**, *134* (1), 18–24. https://doi.org/10.1039/b807563h.

(6) Yang, C.; Denno, M. E.; Pyakurel, P.; Venton, B. J. Recent Trends in Carbon Nanomaterial-Based Electrochemical Sensors for Biomolecules: A Review. *Anal. Chim. Acta* **2015**, *887*, 17–37. https://doi.org/10.1016/j.aca.2015.05.049.

(7) McCreery, R. L. Advanced Carbon Electrode Materials for Molecular Electrochemistry. *Chemical Reviews*. July 2008, pp 2646–2687. https://doi.org/10.1021/cr068076m.

(8) Bath, B. D.; Michael, D. J.; Trafton, B. J.; Joseph, J. D.; Runnels, P. L.; Wightman, R. M. Subsecond Adsorption and Desorption of Dopamine at Carbon-Fiber Microelectrodes. *Anal. Chem.* **2000**, *72* (24), 5994–6002. https://doi.org/10.1021/ac000849y.

(9) Yang, C.; Trikantzopoulos, E.; Jacobs, C. B.; Venton, B. J. Evaluation of Carbon Nanotube Fiber Microelectrodes for Neurotransmitter Detection: Correlation of Electrochemical Performance and Surface Properties. *Anal. Chim. Acta* **2017**, *965*, 1–8.

(10) Cao, Q.; Hensley, D. K.; Lavrik, N. V; Venton, B. J. Carbon Nanospikes Have Better Electrochemical Properties than Carbon Nanotubes Due to Greater Surface Roughness and Defect Sites. *Carbon* **2019**, *155*, 250–257. https://doi.org/10.1016/j.carbon.2019.08.064.

(11) Li, W.; Jayasinghe, C.; Shanov, V.; Schulz, M. Spinning Carbon Nanotube Nanothread under a Scanning Electron Microscope. *Materials* **2011**, *4* (9), 1519–1527. https://doi.org/10.3390/ma4091519.

(12) Jayasinghe, C.; Chakrabarti, S.; Schulz, M. J.; Shanov, V. Spinning Yarn from Long Carbon Nanotube Arrays. *J. Mater. Res.* **2011**, *26* (5), 645–651. https://doi.org/10.1557/jmr.2010.91.

(13) Schmidt, A. C.; Wang, X.; Zhu, Y.; Sombers, L. A. Carbon Nanotube Yarn Electrodes for Enhanced Detection of Neurotransmitter Dynamics in Live Brain Tissue. *ACS Nano* **2013**, *7* (9), 7864–7873. https://doi.org/10.1021/nn402857u.

(14) Jacobs, C. B.; Ivanov, I. N.; Nguyen, M. D.; Zestos, A. G.; Venton, B. J. High Temporal Resolution Measurements of Dopamine with Carbon Nanotube Yarn Microelectrodes. *Anal. Chem.* **2014**, *86* (12), 5721–5727. https://doi.org/10.1021/ac404050t.

(15) Yang, C.; Venton, B. J. High Performance, Low Cost Carbon Nanotube Yarn Based 3D Printed Electrodes Compatible with a Conventional Screen Printed Electrode System. *2017 IEEE Int. Symp. Med. Meas. Appl. MeMeA* **2017**, 100–105. https://doi.org/10.1109/MeMeA.2017.7985857.

(16) Akinoglu, E. M.; Kätelhön, E.; Pampel, J.; Ban, Z.; Antonietti, M.; Compton, R. G.; Giersig, M. Nanoscopic Carbon Electrodes: Structure, Electrical Properties and Application for Electrochemistry. *Carbon.* **2018**, *130*, 768–774. https://doi.org/10.1016/j.carbon.2018.01.064.

(17) Cao, Q.; Puthongkham, P.; Venton, B. J. Review: New Insights into Optimizing Chemical and 3D Surface Structures of Carbon Electrodes for Neurotransmitter Detection. *Anal. Methods* **2019**, *11* (3), 247–261. https://doi.org/10.1039/c8ay02472c.

(18) Zestos, A. G.; Venton, B. J. Communication—Carbon Nanotube Fiber Microelectrodes for High Temporal Measurements of Dopamine. *J. Electrochem. Soc.* **2018**, *165* (12), G3071–G3073. https://doi.org/10.1149/2.0111812jes.

(19) Yang, C.; Trikantzopoulos, E.; Nguyen, M. D.; Jacobs, C. B.; Wang, Y.; Mahjouri-Samani, M.; Ivanov, I. N.; Venton, B. J. Laser Treated Carbon Nanotube Yarn Microelectrodes for Rapid and Sensitive Detection of Dopamine in Vivo. *ACS Sens.* **2016**, *1* (5), 508–515. https://doi.org/10.1021/acssensors.6b00021.

(20) Yang, C.; Wang, Y.; Jacobs, C. B.; Ivanov, I. N.; Venton, B. J. O2 Plasma Etching and Antistatic Gun Surface Modifications for CNT Yarn Microelectrode Improve Sensitivity and Antifouling Properties. *Anal. Chem.* **2017**, *89* (10), 5605–5611. https://doi.org/10.1021/acs.analchem.7b00785.

(21) Yang, C.; Hu, K.; Wang, D.; Zubi, Y.; Lee, S. T.; Puthongkham, P.; Mirkin, M. V.; Venton, B. J. Cavity Carbon-Nanopipette Electrodes for Dopamine Detection. *Anal. Chem.* **2019**, *91* (7), 4618–4624. https://doi.org/10.1021/acs.analchem.8b05885.

(22) Ciolkowski, E. L.; Cooper, B. R.; Jankowski, J. A.; Jorgenson, J. W.; Wightman, R. M. Direct Observation of Epinephrine and Norepinephrine Cosecretion from Individual Adrenal Medullary Chromaffin Cells. *J. Am. Chem. Soc.* **1992**, *114* (8), 2815–2821. https://doi.org/10.1021/ja00034a009.

(23) Venton, B. J.; Wightman, R. M. Psychoanalytical Electrochemistry: Dopamine and Behavior. *Anal. Chem.* **2003**, *75* (19), 414 A-421 A.

(24) Meredith, M. E.; May, J. M. Regulation of Embryonic Neurotransmitter and Tyrosine Hydroxylase Protein Levels by Ascorbic Acid. *Brain Res.* **2013**, *1539*, 7–14. https://doi.org/10.1016/j.brainres.2013.09.040.

(25) Wong, D. L. Epinephrine Biosynthesis: Hormonal and Neural Control during Stress. *Cell. Mol. Neurobiol.* **2006**, *26* (4–6), 891–900. https://doi.org/10.1007/s10571-006-9056-6.

(26) Adams, R. N. Anodic Oxidation Pathways of Aromatic Hydrocarbons and Amines. *Acc. Chem. Res.* **1969**, *2* (6), 175–180. https://doi.org/10.1021/ar50018a003.

(27) Baur, J. E.; Kristensen, E. W.; May, L. J.; Wiedemann, D. J.; Wightman, R. M. Fast-Scan Voltammetry of Biogenic Amines. *Anal. Chem.* **1988**, *60* (13), 1268–1272.

(28) Pihel, Karin.; Schroeder, T. J.; Wightman, R. Mark. Rapid and Selective Cyclic Voltammetric Measurements of Epinephrine and Norepinephrine as a Method to Measure Secretion from Single Bovine Adrenal Medullary Cells. *Anal. Chem.* **1994**, *66* (24), 4532–4537. https://doi.org/10.1021/ac00096a021.

(29) Hawley, M. D.; Tatawawadi, S. V.; Piekarski, S.; Adams, R. N. Electrochemical Studies of the Oxidation Pathways of Catecholamines. *J. Am. Chem. Soc.* **1967**, *89* (2), 447–450. https://doi.org/10.1021/ja00978a051.

(30) Xiang, L.; Lin, Y.; Yu, P.; Su, L.; Mao, L. Laccase-Catalyzed Oxidation and Intramolecular Cyclization of Dopamine: A New Method for Selective Determination of Dopamine with Laccase/Carbon Nanotube-Based Electrochemical Biosensors. *Electrochimica Acta* **2007**, *52* (12), 4144–4152. https://doi.org/10.1016/j.electacta.2006.11.040.

(31) Strand, A. M.; Venton, B. J. Flame Etching Enhances the Sensitivity of Carbon-Fiber Microelectrodes. *Anal. Chem.* **2008**, *80* (10), 3708–3715. https://doi.org/10.1021/ac8001275.

(32) Venton, B. J.; Cao, Q. Fundamentals of Fast-Scan Cyclic Voltammetry for Dopamine Detection. *Analyst* **2020**, *145*, 1158–1168. https://doi.org/10.1039/C9AN01586H.

(33) Bard, A. J.; Faulkner, L. R. *Electrochemical Methods: Fundamentals and Applications*, 2nd ed.; John Wiley and Sons: New York, 2001.

(34) Borovansky, J.; Edge, R.; Land, E. J.; Navaratnam, S.; Pavel, S.; Ramsden, C. A.; Riley, P. A.; Smit, N. P. M. Mechanistic Studies of Melanogenesis: The Influence of N-Substitution on Dopamine Quinone Cyclization. *Pigment Cell Res.* **2006**, *19* (2), 170–178. https://doi.org/10.1111/j.1600-0749.2006.00295.x.

(35) Keithley, R. B.; Takmakov, P.; Bucher, E. S.; Belle, A. M.; Owesson-White, C. A.; Park, J.; Wightman, R. M. Higher Sensitivity Dopamine Measurements with Faster-Scan Cyclic Voltammetry. *Anal. Chem.* **2011**, *83* (9), 3563–3571. https://doi.org/10.1021/ac200143v.

(36) Hu, K.; Wang, D.; Zhou, M.; Bae, J. H.; Yu, Y.; Xin, H.; Mirkin, M. V. Ultrasensitive Detection of Dopamine with Carbon Nanopipets. *Anal. Chem.* **2019**, *91* (20), 12935–12941. https://doi.org/10.1021/acs.analchem.9b02994.

(37) Wang, Y.; Wang, D.; Mirkin, M. V. Resistive-Pulse and Rectification Sensing with Glass and Carbon Nanopipettes. *Proc. R. Soc. Math. Phys. Eng. Sci.* **2017**, *473*, 20160931. https://doi.org/10.1098/rspa.2016.0931.

(38) Hu, K.; Wang, Y.; Cai, H.; Mirkin, M. V; Gao, Y.; Friedman, G.; Gogotsi, Y. Open Carbon Nanopipettes as Resistive-Pulse Sensors, Rectification Sensors, and Electrochemical Nanoprobes. *Anal. Chem.* **2014**, *86* (18), 8897–8901. https://doi.org/10.1021/ac5022908.

(39) Davis, J. M.; Fan, F. R. F.; Bard, A. J. Currents in Thin Layer Electrochemical Cells with Spherical and Conical Electrodes. *J. Electroanal. Chem.* **1987**, *238* (1–2), 9–31. https://doi.org/10.1016/0022-0728(87)85163-X.

(40) Trouillon, R.; Lin, Y.; Mellander, L. J.; Keighron, J. D.; Ewing, A. G. Evaluating the Diffusion Coefficient of Dopamine at the Cell Surface during Amperometric Detection: Disk vs Ring Microelectrodes. *Anal. Chem.* **2013**, *85* (13), 6421–6428. https://doi.org/10.1021/ac400965d.

(41) Fowler, J. C. Changes in Extracellular Adenosine Levels and Population Spike Amplitude during Graded Hypoxia in the Rat Hippocampal Slice. *Naunyn. Schmiedebergs Arch. Pharmacol.* **1993**, *347* (1), 73–78.

(42) Kawagoe, K. T.; Zimmerman, J. B.; Wightman, R. M. Principles of Voltammetry and Microelectrode Surface States. *Journal of Neuroscience Methods*. 1993, pp 225–240. https://doi.org/10.1016/0165-0270(93)90094-8.

(43) Puthongkham, P.; Venton, B. J. Recent Advances in Fast-Scan Cyclic Voltammetry. *Analyst* **2020**, *145*, 1087–1102. https://doi.org/10.1039/C9AN01925A.

(44) Johnson, J. A.; Rodeberg, N. T.; Wightman, R. M. Failure of Standard Training Sets in the Analysis of Fast-Scan Cyclic Voltammetry Data. *ACS Chem. Neurosci.* **2016**, *7* (3), 349–359. https://doi.org/10.1021/acschemneuro.5b00302.

Chapter 3

Different electrochemical behavior of cationic dopamine from anionic ascorbic acid and DOPAC at CNT yarn microelectrodes

Chapter 3 was reprinted from *Journal of The Electrochemical Society* 169.2 (**2022**): 026506.

Abstract

Carbon nanotube yarn microelectrodes (CNTYMEs) have micron-scale surface crevices that momentarily trap molecules. CNTYMEs improve selectivity among cationic catecholamines because secondary reactions are enhanced, but no anions have been studied. Here, we compared fast-scan cyclic voltammetry (FSCV) of dopamine and anionic interferents 3,4 dihydroxyphenylacetic acid (DOPAC) and L-ascorbic acid (AA) at CNTYMEs and carbon fiber microelectrodes (CFMEs). At CFMEs, dopamine current decreases with increasing FSCV repetition frequency at pH 7.4, whereas DOPAC and AA have increasing currents with increasing frequency, because of less repulsion at the negative holding potential. Both DOPAC and AA have side reactions after being oxidized, which are enhanced by trapping. At pH 4, the current increases for DOPAC and AA because they are not repelled. In addition, AA has a different oxidation pathway at pH 4, and an extra peak in the CV is enhanced by trapping effects at CNTYMEs. At pH 8.5, co-detection of dopamine in the presence of DOPAC and AA is enhanced at 100 Hz frequency because of differences in secondary peaks. Thus, the trapping effects at CNTYMEs affects anions differently than cations and secondary peaks can be used to identify dopamine in mixture of AA and DOPAC with FSCV.

3.1 Introduction

Initial experiments to probe dopamine in the brain encountered ascorbic acid and 3,4-dihydroxyphenylacetic acid (DOPAC) as interferents, and thus discrimination of dopamine, ascorbic acid, and DOPAC is an old question in electrochemistry.[1,2] Dopamine (DA) is associated with the reward system in the brain and the decreased level of dopamine results in motor symptoms resembling Parkinson's disease.[3–5] Ascorbic acid is an antioxidant that combats oxidative stress, is present in high concentrations in the brain (over 200 μM), and has a similar oxidation potential to dopamine.[6,7] DOPAC is a major metabolite of dopamine that has a similar structure to dopamine, and therefore similar electrochemistry, and can build up to higher concentrations in the extracellular space.[1] Substantial efforts have been devoted to discriminate dopamine in the presence of AA and DOPAC using differential pulse voltammetry (DPV) by showing slight potential shifts in the voltammograms with different electrode materials.[8,9] However, the measurements with DPV take several minutes, which is not suitable for tracking rapid neurotransmitter release. Fast-scan cyclic voltammetry (FSCV) is used for rapid neurotransmitter measurements with subsecond temporal resolution,[10] and it is often paired with Nafion-coated carbon-fiber microelectrodes (CFMEs) to repel the anions DOPAC and ascorbic acid from the electrode surface.[11–13] Recently, Mao's group developed laccase/multi-walled carbon nanotube-based biosensors for selective determination of dopamine in the presence of ascorbic acid and DOPAC.[14] However, coatings slow the time response, and new approaches to manipulate selectivity without coatings would be welcome.

Carbon nanotube-yarn microelectrodes (CNTYMEs) are a potential alternative to conventional carbon fiber microelectrodes with unique electrochemical properties due to the micron-sized surface roughness, which leads to thin layer electrochemistry with FSCV.[15] They have improved sensitivity and electron transfer kinetics for neurotransmitter detection.[16–20] Our previous study demonstrated that CNTYMEs trap compounds in the crevices of CNT forests, leading to thin layer cell-like electrochemical behavior.[15,16,21] Unlike CFMEs, which experience a dramatic signal loss at high repetition frequencies in FSCV, the trapping effect of CNTYMEs result in high signals for catecholamine neurotransmitters at high repetition frequencies. Thus, the temporal resolution is higher than CFMEs.[18,21,22] In addition, the secondary oxidation peak, due to cyclization of the reduced species, is enhanced at CNTYMEs.[21] These peaks are not typically observed at CFMEs, because they would diffuse away from the surface, but in a structure that promotes trapping, they are easily detected. Epinephrine is the easiest compound to be cyclized among three catecholamines and has a much larger secondary peak current at CNTYMEs, which increases in intensity with increasing FSCV repetition frequency. The different CV shapes enable the selective determination of catecholamines. The trapping effect of CNTYMEs are improved when the surface is treated with an anti-static gun or laser to increase the surface roughness.[17,23] Thus, CNTYMEs have trapping effects that lead to unique electrochemistry, improving sensitivity and selectivity, but the trapping effect has only been studied for cationic catecholamines.

The goal of this study was to understand how trapping effects at CNTYMEs influence the electrochemistry of anions and the extent to which secondary peaks could be exploited to improve selectivity. With a FSCV waveform that holds at a negative voltage, the adsorption of cationic dopamine is favored at low frequencies but with the trapping effect at CNTYMEs, the current decays less for dopamine with increasing frequencies. The effects are opposite for anions, where the signal increases with frequency at CFMEs because of repulsion during the holding potential. Current decreases with frequency for AA at CNTYMEs due to the continuous consumption of trapped products in the irreversible electrochemistry. CV shapes change with pH, which facilitates dopamine determination in the presence of DOPAC or ascorbic acid with FSCV. These experiments show that trapping effects, as well as electrostatic effects, play a large role in the detection of anions and facilitate designing conditions for identifying dopamine with interference of other neurochemicals.

3.2 Experimental

3.2.1 Electrode fabrication.

CFMEs were fabricated by inserting a single T650 carbon fiber into a glass capillary (0.68 mm ID × 1.2 mm OD), and were then pulled to form a sharp tip with fiber exposed. The exposed fiber was then cut to be 100 μm, and sealed with Epoxy Resin 828 (Miller-Stephenson, Danbury, CT). The insulated electrodes were left overnight, and then were placed in 100 °C oven for 2 hours and then 150 °C for 12 hours to cure.

CNTYMEs are disk electrodes made with commercial carbon nanotube yarns with diameter of 50 μm (Nanoworld Lab, Department of Chemical and Environmental Engineering, University of Cincinnati). A glass capillary was pulled by a glass puller (model PE-21, Narishige, Tokyo, Japan) to form a cylinder tip, which was then cut to form an open-tip with diameter of approximately 70 μm. A piece of yarn with 2 cm length was soaked in isopropanol, and inserted into the glass capillary from the open tip carefully during soaking. With the assistance of surface tension, the CNT yarn was placed at the glass tip without structure deformation. After insulation with Epon epoxy Resin 828, the electrode was then polished to a 45° angle with a fine diamond abrasive plate (Sutter Instruments model BV-10, Novato, CA). The polishing process for an electrode was control to be less than 3 min and the electrode was then soaked in isopropanol to remove surface impurities. The whole structure of the disk electrode is shown in Fig. S1.

3.2.2 Electrochemical methods.

Dopamine hydrochloride, L-ascorbic acid and 3,4-Dihydroxyphenylacetic acid (DOPAC) were purchased from Sigma-Aldrich (St. Louis, MO). Compounds were dissolved in 0.1 M $HClO_4$ to make 10 mM stock solution, and were diluted with PBS buffer (131.25 mM NaCl, 3.00 mM KCl, 10 mM NaH_2PO_4, 1.2 mM $MgCl_2$, 2.0 mM Na_2SO_4, and 1.2 mM $CaCl_2$) to corresponding concentration (dopamine 1 μM, DOPAC 20 μM and L-ascorbic acid 20 μM). Solutions were further adjusted to different pH (pH 4, pH 7.4 and pH 8.5) for FSCV detection.

Fast-scan cyclic voltammetry was performed in a flow cell with dual syringe pump pumping buffer and dopamine into a cell with a six-port switching valve (Valco Instruments Co. Inc. Houston, TX). The potentiostat was a Dagan with a 10 MΩ headstage (Dagan, Minnesota). Electrodes were filled with KCl solution to be connected to Ag/AgCl reference electrode, and dopamine waveform (-0.4 V to 1.3 V at a scan rate of 400 V/s from frequencies from 10 Hz to 100 Hz) was applied. The data was analyzed with HDCV software developed at University of North Carolina, Chapel Hill.

3.2.3 Surface characterization.

SEM images (spot size 2, accelerating voltage 2 kV) of CFMEs and CNTYMEs was performed on ZEISS Merlin High- Resolution Scanning electron microscope (Oberkochen, Germany), provided by Center for Nanophase Materials Science (CNMS), Oak Ridge National Laboratory.

3.2.4 Simulation of electrostatic effect.

The simulations of electrostatic effects with analytes with different charges were performed in COMSOL Multiphysics (Burlington, MA). The 2D model of CFMEs was simplified as a line segment, since CFMEs are cylinder electrodes with little surface structure. The model of CNTYMEs was composed of dense CNT arrays standing vertically to show surface roughness of a disk electrode. Simulation of electric field was achieved with COMSOL Multiphysics 5.5. “Transport of Diluted Species” module and “Electrostatics” module was coupled to model the concentration profiles of analytes in the electrochemical system. The structure of carbon electrode and electrochemical cell were modeled (Figure 1) with several boundary conditions. The 2D model of carbon electrode was simplified as a rectangle (50 μm long and 6 μm width). On the electrode surface, the electric potential was set to be the -0.4 V, which is the holding potential of the dopamine waveform. The bulk solution, in contrast, has the electric potential at 0 V, but with initial analyte concentration of 1 μM. Analytes with positive (+1), neutral (0) and negative (-1) charges were investigated, and concentration gradient was generated by mass transport and migration in the electric field, which were described by Nernst-Planck equation and Poisson equation:

$$J_i = -D_i \nabla c_i - \frac{z_i F}{RT} D_i \nabla c_i \nabla \varphi$$

$$\nabla^2 (\varepsilon_o \varepsilon_r \phi) = -F \sum_i z_i c_i$$

Where J_i is flux, D_i is diffusion coefficient, c_i is concentration, z_i is charge of species i, F and R are Faraday and gas constant, φ is potential and ε is the dielectric constant, respectively. "Electrostatics" and "Transport of Diluted Species" modules were coupled to simulate mass transport and analyte migration in an electric field.

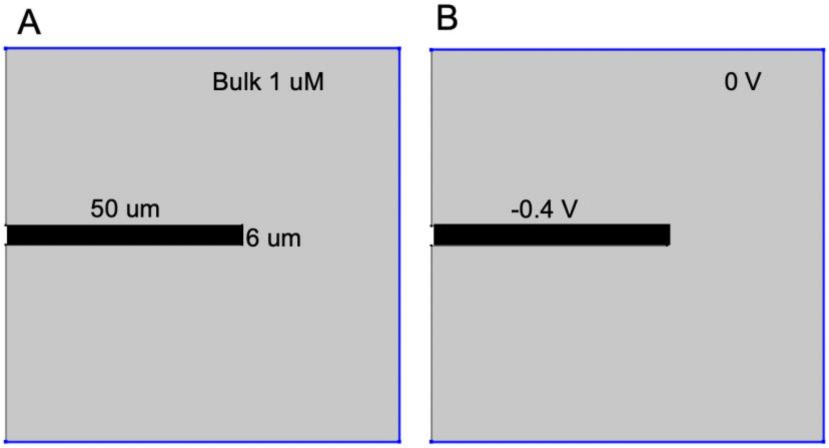

Figure 1. Electrochemical cell model. A) The 2D carbon electrode is 50 um long and 6 μm wide placed in the middle of the electrochemical cell. Blue line represents the bulk solution, where the concentration of the analyte is 1 μM. B) The potential at the electrode surface is -0.4 V, and 0 V in the bulk.

3.3 Results and Discussion

3.3.1 Surface characterization

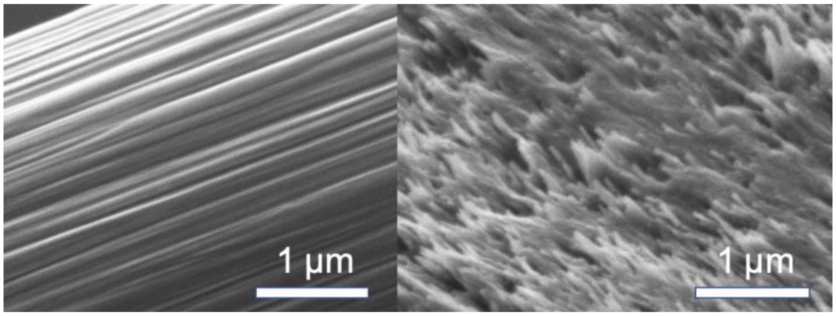

Figure 2. SEM image of A) CFME and B) CNTYME.

Fig. 2 shows SEM images of the electrodes used in this study: a cylindrical CFME (Fig. 2A) with a diameter of 7 μm and a disk CNTYME (Fig. 2B) using a 50 μm diameter CNT yarn., which was made by twisting long CNT arrays into bundles.[19,24] The CFME has smooth striations on the surface, whereas the CNTYME has micron-depth surface roughness with twisted CNT bundles.[19,24] After polishing, a CNT forest is formed of vertically aligned CNT arrays, and crevices are observed between the CNT bundles.

3.3.2 Dopamine, Ascorbic acid, and DOPAC CVs obtained at CFMEs and CNTYMEs.

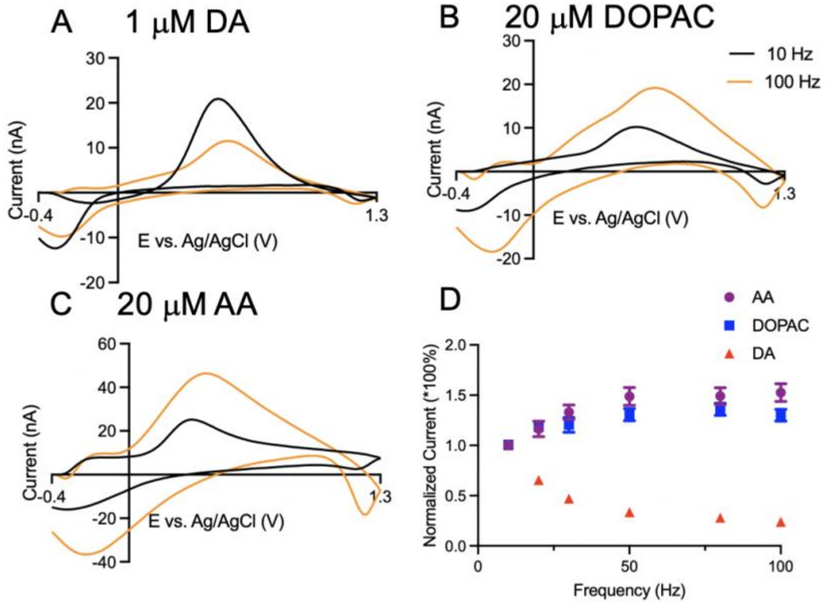

Figure 3. Cyclic voltammograms at CFMEs of A) 1 μM dopamine, B) 20 μM DOPAC and C) 20 μM ascorbic acid at 10 Hz and 100 Hz. D) Normalized current trends of three analytes with FSCV repetition frequencies from 10 Hz to 100 Hz. n = 5 electrodes, error bars SEM.

First, we studied CFMEs by comparing dopamine, DOPAC, and ascorbic acid at different FSCV repetition frequencies. For FSCV flow cell experiments, we run buffer past the electrode for 5 s, then analyte for 5 s, and finally switch back to buffer for 5 s. The CVs shown are collected at the end of the analyte injection, approximately the 50th CV at 10 Hz, and the 500th CV at 100 Hz. Figure 3A shows the CVs of dopamine at 10 Hz and 100 Hz. Dopamine is reversibly oxidized to dopamine-o-quinone (DOQ) via two-electron transfer (Scheme 1A), and the oxidation peak occurs at 0.6 V and reduction at -0.2 V at the back scan. The peak-to-peak separation is larger than the conventional cyclic voltammetry because of the fast scan rate (400 V/s), so that the voltage ramp is faster than electron transfer. The reduction peak current is smaller than the primary oxidation one is due to the desorption of DOQ molecules.[10] The primary peak current at 100 Hz (11 ± 3 nA) is much smaller than that at 10 Hz (26 ± 2 nA) because there is less time at the holding potential for dopamine to be adsorbed on the electrode.[25] In Fig. 3B, 20 μM DOPAC has a similar CV shape as dopamine at 10 Hz, with similar oxidation peak potentials. In Fig. 23, ascorbic acid has a wider oxidation peak at around 0.5 V and a reduction peak at -0.2 V in the back scan. At CFMEs, both DOPAC and ascorbic acid have broadened CV peaks at 100 Hz, which makes selective detection more challenging because the peaks may overlap. Figure 3D plots the primary current vs frequency and shows that the current for dopamine dramatically decays with increasing FSCV repetition frequency. In contrast, DOPAC and ascorbic acid have increasing peak currents at high frequencies, which is explained by electrostatic effects. The anions will be repelled during the holding time at a negative voltage. At higher FSCV repetition frequencies, there are secondary oxidation peaks at a lower potential (approximately 0.15 to 0.2 V) for dopamine and DOPAC due to cyclization reactions[26].

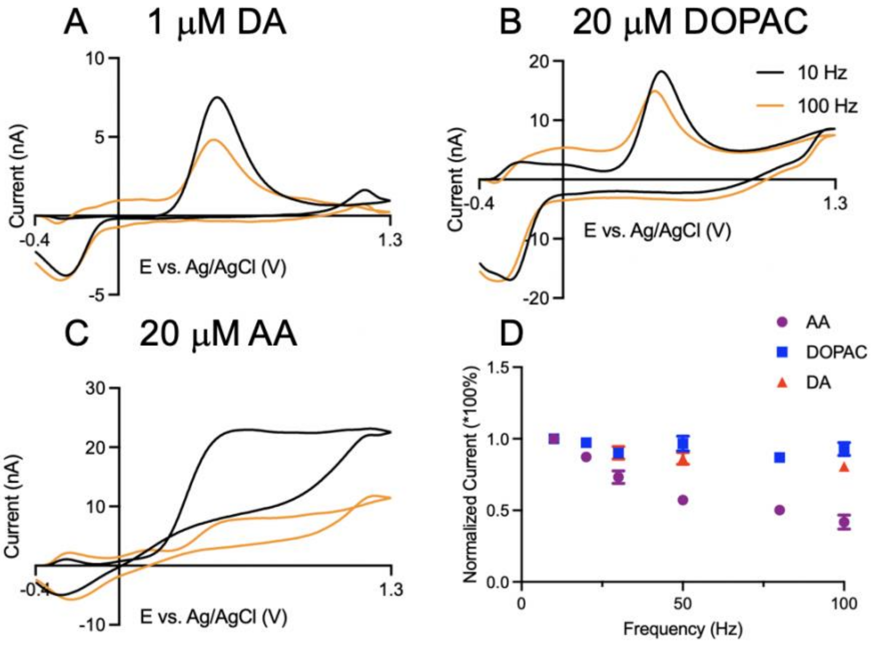

Figure 4. Cyclic voltammograms at CNTYMEs of A) dopamine, B) DOPAC and C) ascorbic acid at 10 Hz and 100 Hz. D) Normalized primary peak current trends of three analytes with frequencies ranging from 10 Hz to 100 Hz. n = 5 electrodes, error bars SEM.

Next, the repetition frequency experiment was performed at CNTYMEs. The primary oxidation current for dopamine (Fig. 4A) at 0.6 V is only slightly smaller at 100 Hz than 10 Hz, and the secondary peak current increases with frequency. DOPAC (Fig. 4B) has a similar CV shape to dopamine, and similar trends, with a small drop in primary peak current (at 0.6 V) and an increase in secondary peak current (at around 0 V) at 100 Hz. Ascorbic acid (Fig. 4C) has an oxidation peak at approximately 0.5 V, and the signal drops dramatically for the 100 Hz repetition frequency. Both DOPAC and ascorbic acid have a peak current at the switching potential 1.3 V, which may be due to changes in the background current after increased adsorption of compounds with more oxide groups.[27] Secondary oxidation peaks of dopamine and DOPAC that appear at a lower potential are enhanced at CNTYMEs and are easier to distinguish at 100 Hz than at CFMEs.

Figure 4D shows that ascorbic acid has a large decrease in primary oxidation current with frequency at CNTYMEs but that the current declines only slightly for DOPAC and dopamine. This pattern is a contrast to CFMEs, where dopamine decreased with FSCV repetition frequency but AA and DOPAC did not. Given the possibility of ascorbic acid fouling, the response at different frequencies was tested for AA, then the electrode was exposed to AA for 25 cycles, and the current responses at different frequencies tested again. Figure 5 shows the currents did not drop after 25 cycles, which indicates that no fouling happens during AA redox cycling at CNTYMEs. The decreasing currents for AA at the CNTYME at high repetition frequencies may be due to restricted diffusion, as the solution may not easily reach into the crevices with rapid repetition frequencies. In contrast, DOPAC redox is adsorption controlled so it has a less current drop and may be less susceptible to effects of restricted diffusion. AA is a diffusion-controlled process and the oxidation is irreversible and products are consumed in the following hydration reaction, whereas DOPAC with a quasi-reversible redox mechanism that partially recycles the primary product back to DA. Thus, restricted diffusion and irreversibility may cause the larger current drop for AA than for DOPAC.

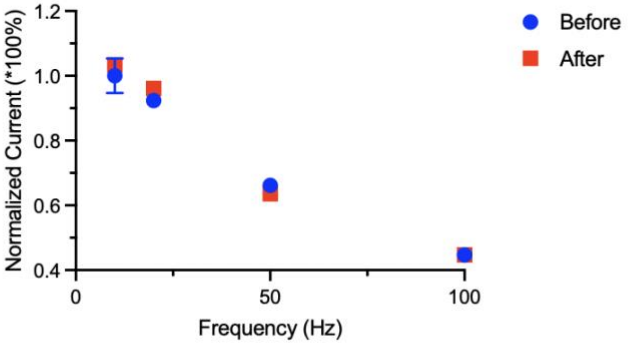

Figure 5. The primary current trend of AA oxidation with frequencies at CNTYMEs. The blue trend represents the signal obtained originally; The red trend represents the repeated test after 25-minute exposure to the AA solution. The currents of AA oxidation are similar for both tests, which indicates fouling is not occurring and the signal is similar after long exposure to AA.

3.3.3 Electrostatic and trapping effects lead to different current responses

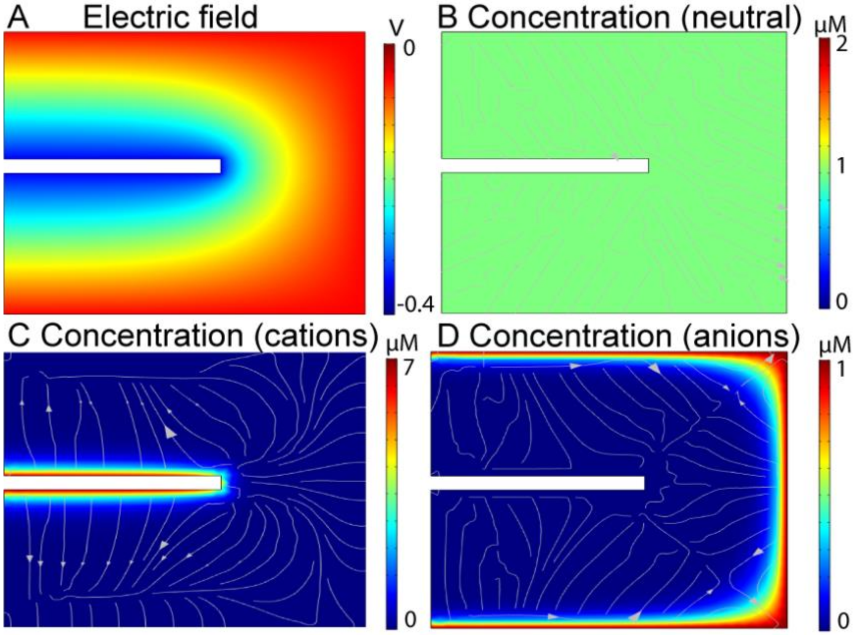

Figure 6. A) Simulated electric field with CNTYMEs in an electrochemical system at a holding potential of -0.4 V. The concentration profiles of B) neutral molecules, C) cations and D) anions. Red is a high concentration (bulk concentration was 1 μM) and blue is a low concentration. Analyte movements was driven by diffusion and migration in the electric field. The half 2D model

of electrode was 50 μm* 6 μm, so the black electrode in the figure is 25 μm long. D = 10^{-9} m^2/s, C_{bulk} = 1 μM, charge of species z_c = +1, z_a = -1.

To understand the electrostatic effects for different charged molecules, a model of the electric field was built with COMSOL Multiphysics; details can be found in the supporting information. In Figure 6, an electrode (white rectangle representing half CFME) was placed in an electrochemical cell with zero potential. When applying a potential of -0.4 V to the electrode, an electric field was generated around the microelectrode, as shown in Figure 6A. Then electroactive species were introduced to the system from the bulk solution on the right side. To simply show the effect of migration in the analyte movements, convection was not considered in the model.[28] The concentration is 1 μM everywhere in the electrochemical cell when there is no migration (arrows represent the solution flux in the electrochemical system). Figure 6C shows the concentration profile of a cationic species, which not only diffuses but also migrates to the electrode. The positively charged molecule is attracted by the negative holding potential applied at the electrode by electrostatic forces; thus, concentrations of cations are enriched near the electrode surface. Figure 6D is the concentration of an anionic species, and the concentration near the electrode is smaller because anions are repelled by the negative potential applied to the electrode. With an opposite direction of migration due to repulsion, fewer molecules approach to the electrode surface so the amount that undergo redox reactions is less. In the real experiment, a flow injection system will introduce convection with molecules continuously flowing to the electrode.

The concentration of anions was 20 μM instead of 1 μM, so the real concentration near the electrode is larger than the results in the model. In this study, dopamine (pKa = 9.27) is cationic, whereas DOPAC (pKa = 4.25) and ascorbic acid (pKa = 4.2) are anionic at physiological pH 7.4.[27,28] Thus, dopamine is present at a higher concentration on the surface (such as Fig. 46), while DOPAC and ascorbic acid are at lower concentrations at the electrode surface (such as Fig. 46). The electrostatic effect explains the different current trends of dopamine, DOPAC, and ascorbic acid with increasing frequencies. At 10 Hz, the holding time at -0.4 V between each cycle is 91.5 ms, and the time dramatically decreases when repetition frequency increases. With less time at negative potential, there is less attraction of dopamine to the electrode, so the current goes down as the result at CFMEs shows (Figure 3A). But for DOPAC and ascorbic acid that are repelled by the electrode at holding potential, the shorter time is less time for repulsion, so the current trends higher (Figure 3C, 3D).

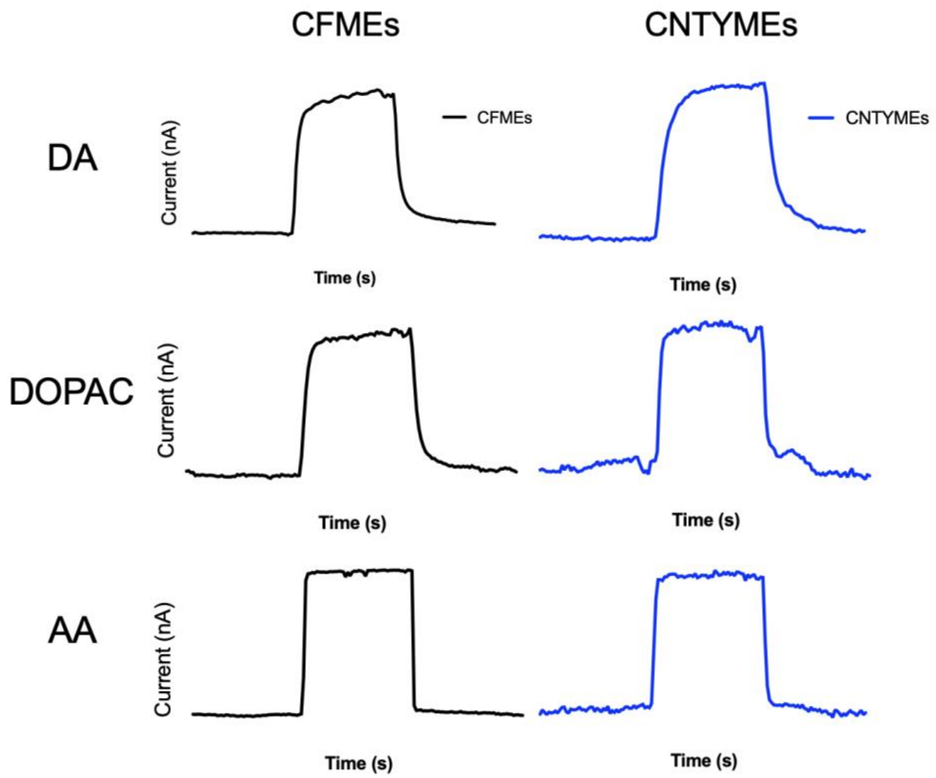

Figure 7. Current vs. time plots dopamine, DOPAC, and AA at CFMEs and CNTYMEs. Both electrodes show fast time response during 5s injection in the flow cell.

The electrostatic effect is the same at both CFMEs and CNTYMEs, and both electrodes show fast time responses of three compounds based on the current vs. time plots (Fig. 7), however, the frequency effects are different at CNTYMEs (Figure 4D). Dopamine has less primary current decay at CNTYMEs (Figure 4D) than at CFMEs (Figure 3D) and DOPAC has a slight decrease at CNTYMEs. AA decreases with frequency at CNTYMEs in contrast to its increasing trend at CFMEs. The reason for the different current response at CNTYMEs is due to the trapping effect introduced by the creviced surface structure as shown in SEM image (Figure 2B). At CNTYMEs, the crevices on the surface with micron depth act as many thin layer cells that trap molecules in the CNT forests, limiting diffusion on the FSCV time scale.[21,32] Thus, cations such as dopamine are trapped near the surface and can be readily detected after redox cycling at high repetition frequencies. Anions will be repelled by electrostatic forces, but those that are at the surface will also be trapped in the crevices and consumed in the redox reactions. The current for ascorbic acid decreases with frequency at CNTYMEs because it is an irreversible redox reaction (Scheme 1C) and AA is consumed more quickly with high repetition frequency in the thin layer cell. Dopamine and DOPAC have less current decay than AA, because they undergo quasi-reversible redox reactions (Scheme 1A, 1B), and side products are recycled in the thin layer cell. As a result, current trends at CNTYMEs with high surface roughness are different from CFMEs with smooth surface.

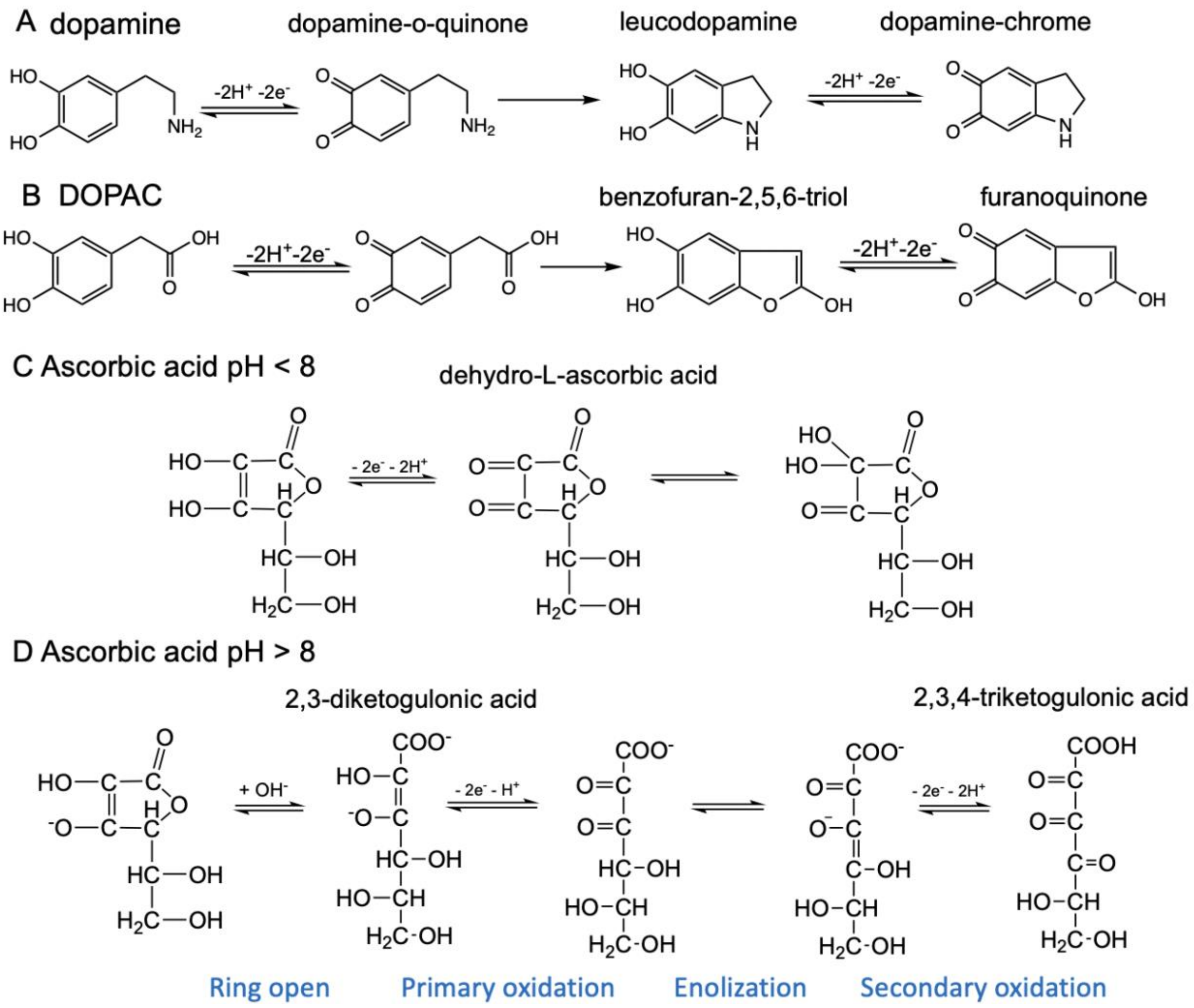

Scheme 1. Redox pathways of A) dopamine, B) DOPAC and C) ascorbic acid at physiological condition at pH 7.4, and D) ascorbic acid at pH 8.5.

At CFMEs only one oxidation peak is typically present for FSCV detection at 10 Hz, but additional peaks can be detected at CNTYMEs, especially at high repetition frequencies (Fig. 3 and 4). For DA and DOPAC, these extra peaks are attributed to the cyclization reactions following an ECE (electron transfer-chemical-electron transfer) mechanism as shown in Scheme 1. Dopamine (Scheme 1A) is oxidized to dopamine-o-quinone (DOQ) via two-electron transfer, the primary oxidation reaction, and the peak appears at 0.6 V in FSCV. After forming DOQ, it can either be reduced back to dopamine or undergo a cyclization reaction by intramolecular Michael addition to generate leucodopamine. Leucodopamine is then electrochemically oxidized to dopamine-chrome, which causes a secondary oxidation current that appears at 0.15 V.[26,33] DOPAC, a major metabolite of dopamine, has same catechol structure and undergoes a similar redox pathway, with an initial oxidation reaction that is then cyclized to benzofuran-2,5,6-triol, which can be oxidized to furanoquinone.[14,34] The redox pathway of L-ascorbic acid (Scheme 1C) is irreversible because the hydration reaction after oxidation largely consumes the oxidant dehydro-L-ascorbic acid to generate a more stable product.[35,36] However, side reactions have been reported, such as ring cleavage.[6]

At CNTYMEs, secondary oxidation peaks are enhanced (Figure 4), because the cyclization products that are made in the crevices are trapped in the crevices on the FSCV time scale and therefore are detected electrochemically.[21] At 100 Hz, there is even less time for molecules to escape (1.5 ms between scans), leading to further enhancement. In addition, there is an increasing number of reactions in a unit time at high frequencies, and more primary products are consumed since the cyclization reaction is irreversible. With 10 times more reactions at 100 Hz, there are more secondary products accumulated in the crevices, thus the secondary peak currents are higher. The different CV responses of CFMEs and CNTYMEs caused by the different surface structure facilitates the discrimination of analytes by different secondary peaks, but it is not enough to provide selectivity among three analytes with FSCV.

3.3.4 pH changes reaction mechanisms and cyclic voltammogram shapes

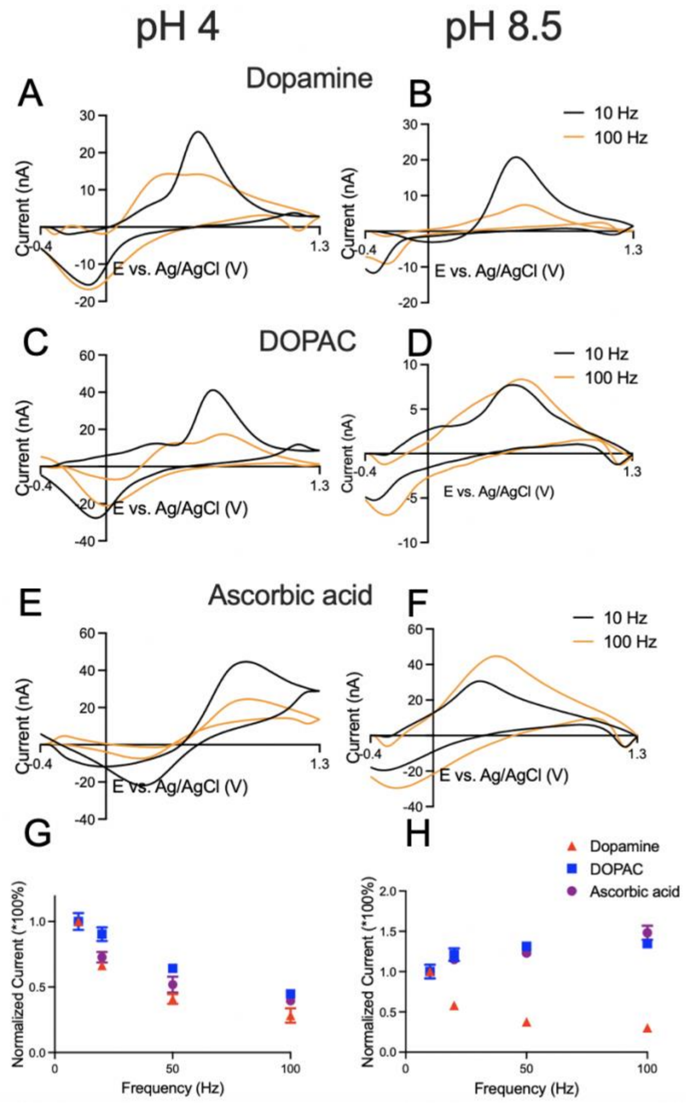

Figure 8. CFMEs at different pH. Left column is CVs at pH 4, and right column is at pH 8.5.Cyclic voltammogram comparisons of A & B) 1 μM dopamine, C & D) 20 μM DOPAC and E & F) 20 μM ascorbic acid at 10 Hz and 100 Hz. G, H) Normalized trends of primary peak currents with frequency.

For *in vivo* studies, detection of neurochemicals is performed at physiological pH (7.4), but the redox mechanisms are pH dependent and worth understanding for detection *ex vivo*. Figure 8 shows dopamine, DOPAC, and AA detection at CFMEs at pH 4 and 8.5. For all three molecules, reduction peaks are right shifted in acid and left shifted in base, because the reactions are pH dependent, and more protons in solution favors reduction, while fewer protons favors oxidation.[2,28,37] Dopamine (pKa = 9.27) is a cation at both pH 4 and 8.5 and is attracted by the electrode at a negative holding potential, so the current is frequency dependent. DOPAC (pKa = 4.25) is cationic at pH 4, so it has a larger current due to migration to the surface, but the current decays at 100 Hz. However, at pH 8.5 DOPAC is an anion that is normally repelled by the electrode at the holding potential, so the overall current is much smaller (due to differences in migration) but the current increases with repetition frequency as there is less time at negative potentials. Ascorbic acid has a pKa of 4.2, and it is positively charged at pH 4, so it has a larger current due to migration and a signal that decays with repetition frequency. Dopamine and DOPAC have enhanced secondary peaks at acidic pH, that become more apparent at 100 Hz. The normalized trends in Figure 8G, 8H show different electrostatic effect of three analytes at acidic or basic conditions. Cationic dopamine has decreasing currents at both pH values, whereas the currents for DOPAC and AA decrease with frequency at pH 4 but increase at pH 8.5.

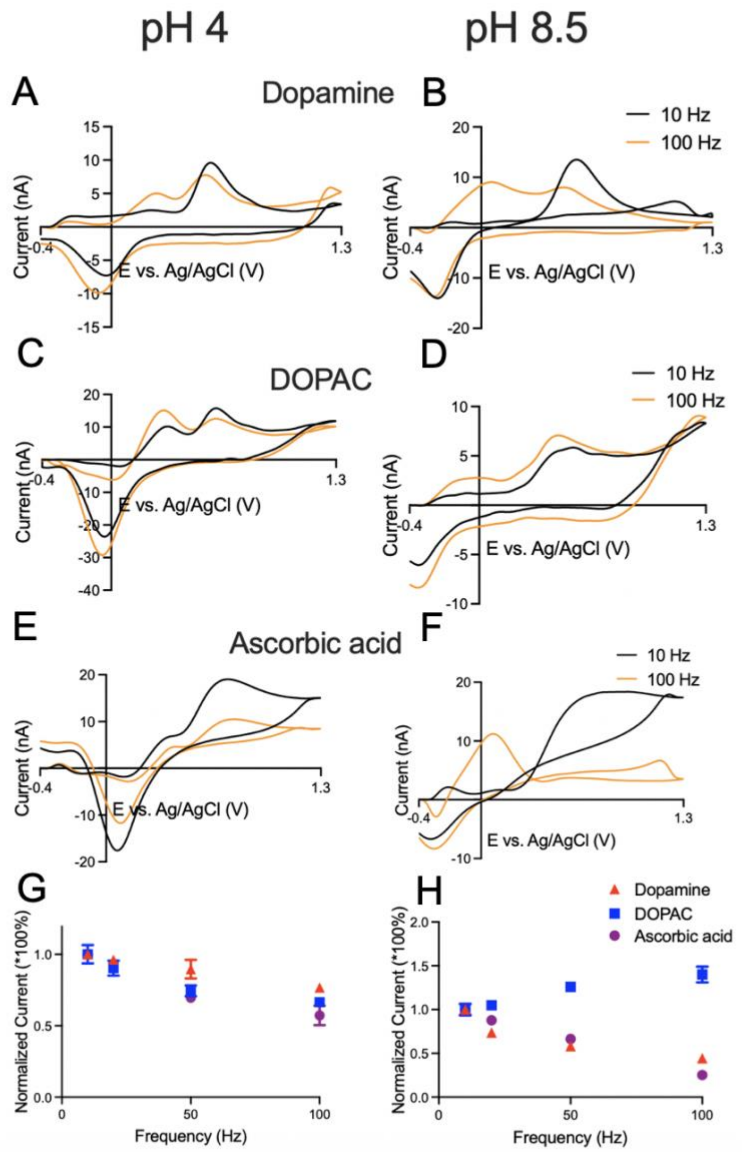

Figure 9. Cyclic voltammograms of at CNTYMEs. Left column is CVs at pH 4, and right column is at pH 8.5. A & B) 1 μM dopamine, C & D) 20 μM DOPAC and E & F) 20 μM ascorbic acid at 10 Hz (black line) and 100 Hz (orange line). G, H) Normalized trends of primary peak currents with frequency.

Figure 9 shows CVs from CNTYMEs for dopamine, DOPAC, and AA at acidic and basic pH. Similar to CFMEs, even in CNTYMEs, the peaks shift due to the pH dependence of the reactions, as the reduction peaks are right shifted in acid and left shifted in base. For dopamine (Fig. 9A-B), the primary peak currents at CNTYMEs are smaller at 100 Hz, and secondary peaks are enhanced at both pH values. DOPAC has the same peak positions as dopamine, but a high current at 1.3 V at CNTYMEs because of the background current change introduced by the adsorption of molecules. Secondary peak currents for DOPAC are enhanced at both pH values, especially at pH 4, where the secondary peak dominates at 100 Hz. Secondary peak currents for both dopamine and DOPAC are larger at pH 8.5 than at pH 7.4, because nitrogen and oxygen in the chains become more nucleophilic and cyclization reactions are more facile [38,39]. At pH 4, AA has primary current decreasing at 100 Hz, and secondary peaks are seen in the cyclic voltammogram. At pH 8.5, the primary peak has nearly disappeared at 100 Hz, and only a secondary reaction is observed. The normalized trends of three analytes at CNTYMEs (Figure 9G, 9H) are mostly the same as those at CFMEs (Figure 8G, 8H), but the decreasing trends are flatter. However, AA has dramatically decreasing currents at pH 8.5 which is opposite that at CFMEs.

Ascorbic acid is interesting because it has a different redox mechanism at different pH values (Scheme 1D).[2,35,40] As Scheme 1C shows, in acid or neutral solution, ascorbic acid is oxidized to dehydroascorbic acid via two-electron transfer. The redox reaction is followed by a hydration reaction to form a stable product, which causes it to be an irreversible process. In Figure 9E, the CV shape at pH 4 (10 Hz) is more reversible at CNTYMEs because dehydroascorbic acid that does not undergo hydration is trapped and can be cycled back to AA. The additional wave at the lower potential in the cyclic voltammogram of ascorbic acid is attributed to the background change since trapped molecules are easily adsorbed on the CNTYMEs. When pH is above 8 (Scheme 1D), ascorbic acid opens its lactone ring and is oxidized to 2,3-diketogulonic acid, the primary reaction. However, in basic solutions, 2,3-diketogulonic acid dissociates and is enolized[2,36]. Two-electron oxidation of the enolate generates 2,3,4-triketogulonic acid, which causes a secondary oxidation peak at a lower potential[36]. As an unstable compound acid with four adjoining carbonyl groups, 2,3,4-triketogulonic acid degenerates quickly. The CVs obtained at CNTYMEs in Figure 6F show a large difference between 10 Hz and 100 Hz at pH 8.5. At 10 Hz, the primary oxidation appears at around 0.6 V and secondary peak is not easily observed but at 100 Hz, the largest peak in the CV is due to a secondary reaction and the primary peak is small. Note that CV shapes vary in time with FSCV and these CVs were taken at the end of a 5 s flow injection. Figure 10 plots CVs of the three compounds at 100Hz, pH 8.5 at different time during a 5 s flow cell injection. The results show that the secondary peaks are not observed at the beginning of the injection, but grow in with time, while primary peak currents decrease over time as the primary products are consumed.

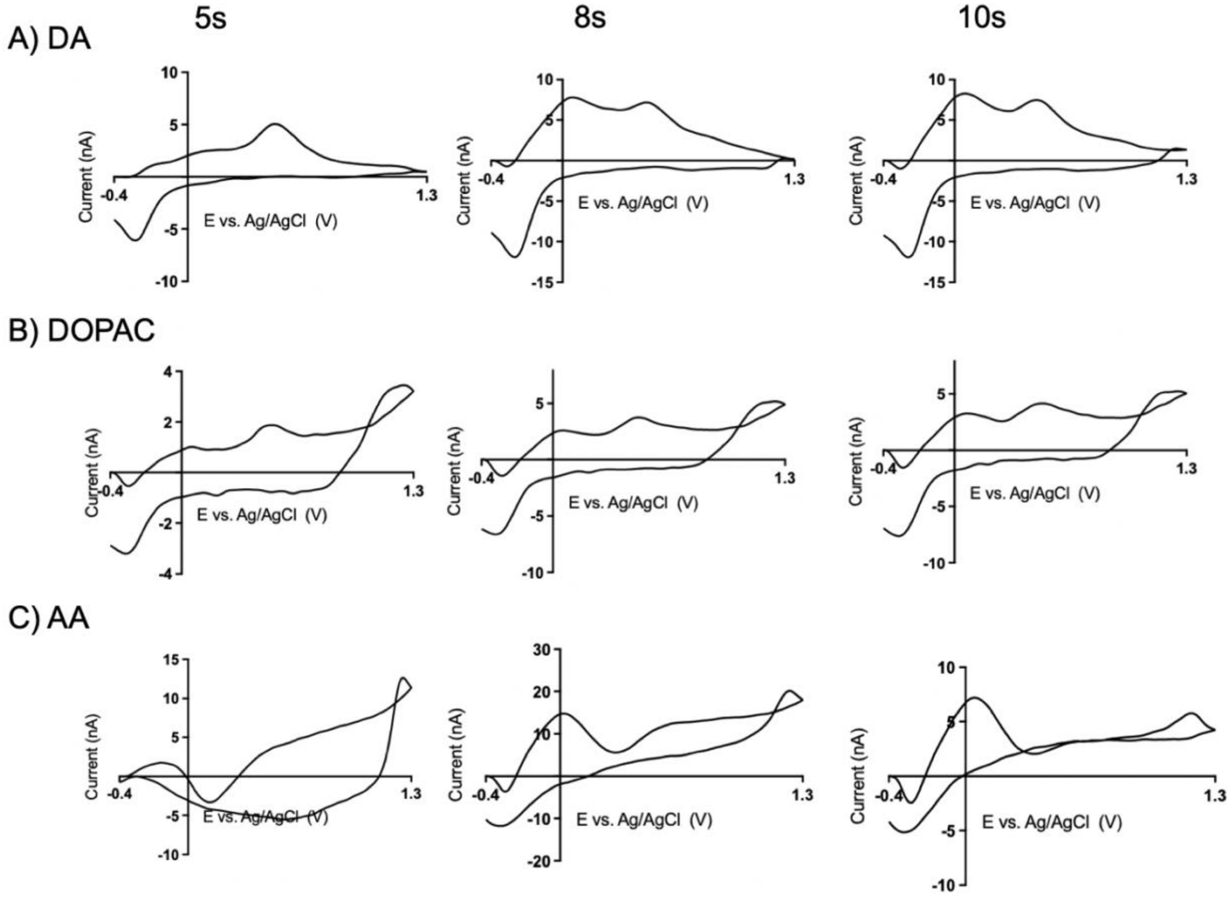

Figure 10. At pH 8.5, CVs of A) DA, B) DOPAC, and C) AA that obtained at 100Hz with different time. Left column are CVs obtained at 5s, at the beginning of the injection; The middle ones are obtained at 8s, in the middle of the injection; And the right ones are at 10s, in the end of the injection.

3.3.4 Selective dopamine detection with interference of DOPAC and L-ascorbic acid at CNTYMEs

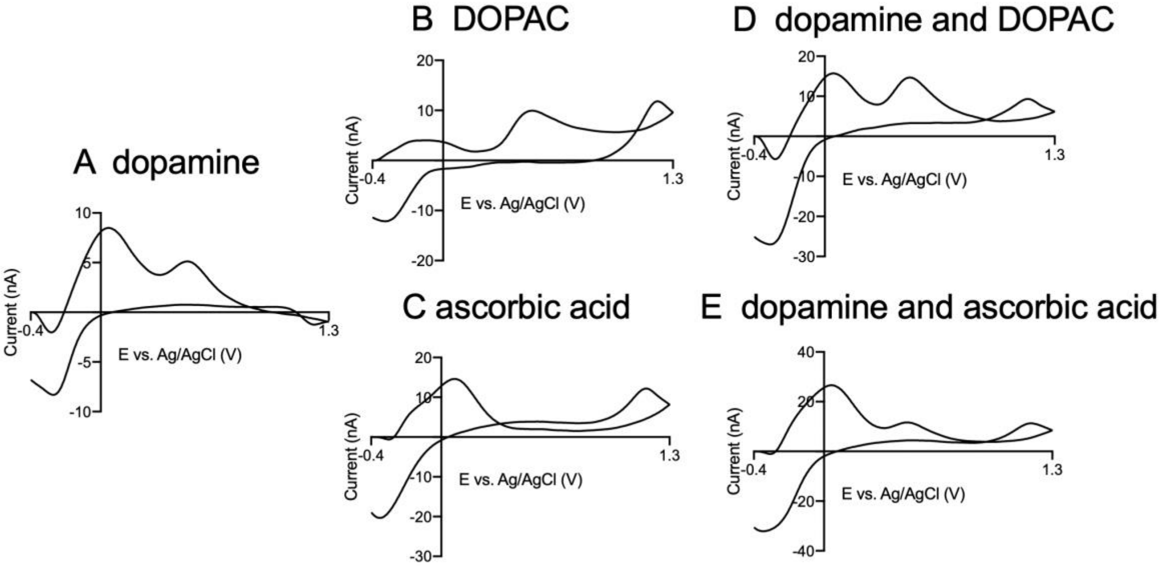

Figure 11. Codetection of dopamine, DOPAC, and ascorbic acid at CNTYMEs at pH 8.5. A.) CVs of pristine 1 μM dopamine, B) CV of 20 μM DOPAC, and C.) CV of 20 μM ascorbic acid. D) Mixture of 1 μM dopamine and 20 μM DOPAC. E.) Mixture of 1 μM dopamine and 20 μM AA All the cyclic voltammograms were obtained at 100 Hz, pH 8.5.

Multiple analyte detection is difficult in FSCV due to the extremely fast voltage ramp that leads to peak broadening or overlapping when analytes have similar formal potentials. Codetection experiments are most often performed with conventional cyclic voltammetry or differential pulse voltammetry, because peak separation is easier at slower scan or step rates.[8,41] Here, our strategy is to use secondary peaks at different pH values to identify dopamine in the mixture solutions. Figure 11 plots CVs of three analytes at CNTYMEs and mixtures solutions at pH 8.5, 100 Hz. In this condition, dopamine (Figure 11A) has a favored cyclization reaction while DOPAC (Figure 11B) has similar peak potentials, but a much smaller secondary peak, as well as an extra wave at the switching potential. At pH 8.5, ascorbic acid (Figure 11C) has a very large secondary peak at 0.1 V as well as a peak at the switching potential, but little primary peak because the product is used up. Figure 11D is a CV obtained in solutions of 1 μM dopamine with 20 μM DOPAC and the while the primary peak is a combination of dopamine and DOPAC, the large secondary peak is attributed to dopamine. The additional peak at switching potential also indicates the existence of DOPAC in the mixture solution. Figure 11E is a CV of 1 μM dopamine with 20 μM ascorbic acid and the primary peak at 0.6 V is evidence of dopamine, while ascorbic acid is identified by the peak at 1.3 V. Thus, at CNYMEs, we can identify the components of the mixture solution, although quantitation might be difficult. To achieve that goal, we would need machine learning[42] or principle component analysis[43] for accurate quantification.

The codetection of dopamine with DOPAC and ascorbic acid at pH 8.5 indicates the good selectivity of CNTYMEs by showing distinctive CV shapes without losing sensitivity. While animal and brain slice experiments are conducted at physiological pH 7.4, [44,45] *ex vivo* studies, such as electrochemical detection of neurotransmitters after HPLC separation are not limited to physiological pH.[9] This study shows that manipulating the pH can amplify secondary peaks that are trapped by CNTYMEs, which could be an important tool for tuning selectivity when primary peaks overlap. Thus, the trapping nature of the surface structure at CNTYMEs allows redox reactions to be observed that are not typically detected and these insights are useful for assay development in FSCV.

3.4 Conclusions

CNTYMEs are a good alternative to CFMEs, exhibiting a high sensitivity and temporal resolution. With the trapping effect introduced by the thin layer structures on the surface of CNTYMEs, neurotransmitters can be determined by the different CV shapes of dopamine, DOPAC, and ascorbic acid, which provides a better selectivity than CFMEs. Trapping effect at CNTYMEs also allows the detection of secondary oxidation products that would usually diffuse away from the surface. Secondary peak currents are also enhanced at higher repetition frequencies when more reactions occur. Ascorbic acid has pH dependent redox mechanisms, and side reactions are observed clearly with trapping effect amplifying secondary peak currents. At a more basic pH of 8.5, dopamine, DOPAC and ascorbic acid have unique CV shapes at 100 Hz, which enables the determination of dopamine with co-existence of interferences at CNTYMEs. Trapping in the thin layer cell enables the dopamine determination with the presence of DOPAC and AA. Any one of the neurochemicals can be discriminated with the presence of other interference if the proper condition was applied to CNTYMEs.

Acknowledgments

This work was funded by NIH R01EB026497 and NIH R01MH085159. The SEM images of carbon electrodes were conducted at the Center for Nanophase Materials Sciences, which is a DOE Office of Science User Facility. The authors declare no competing financial interest.

3.5 References

(1) Basse-Tomusk, A.; Rebec, G. V. Regional Distribution of Ascorbate and 3,4-Dihydroxyphenylacetic Acid (DOPAC) in Rat Striatum. *Brain Res.* **1991**, *538* (1), 29–35. https://doi.org/10.1016/0006-8993(91)90372-3.

(2) Deakin, M. R.; Kovach, P. M.; Stutts, K. J.; Wightman, R. M. Heterogeneous Mechanisms of the Oxidation of Catechols and Ascorbic Acid at Carbon Electrodes. *Anal. Chem.* **1986**, *58* (7), 1474–1480. https://doi.org/10.1021/ac00298a046.

(3) Huffman, M. L.; Venton, B. J. Carbon-Fiber Microelectrodes for in Vivo Applications. *Analyst* **2009**, *134* (1), 18–24. https://doi.org/10.1039/b807563h.

(4) Ribeiro, J. A.; Fernandes, P. M. V.; Pereira, C. M.; Silva, F. Electrochemical Sensors and Biosensors for Determination of Catecholamine Neurotransmitters: A Review. *Talanta* **2016**, *160*, 653–679. https://doi.org/10.1016/j.talanta.2016.06.066.

(5) Baur, J. E.; Kristensen, E. W.; May, L. J.; Wiedemann, D. J.; Wightman, R. M. Fast-Scan Voltammetry of Biogenic Amines. *Anal. Chem.* **1988**, *60* (13), 1268–1272.

(6) Pisoschi, A. M.; Pop, A.; Serban, A. I.; Fafaneata, C. Electrochemical Methods for Ascorbic Acid Determination. *Electrochim. Acta* **2014**, *121*, 443–460. https://doi.org/10.1016/j.electacta.2013.12.127.

(7) Meredith, M. E.; May, J. M. Regulation of Embryonic Neurotransmitter and Tyrosine Hydroxylase Protein Levels by Ascorbic Acid. *Brain Res.* **2013**, *1539*, 7–14. https://doi.org/10.1016/j.brainres.2013.09.040.

(8) Safavi, A.; Maleki, N.; Moradlou, O.; Tajabadi, F. Simultaneous Determination of Dopamine, Ascorbic Acid, and Uric Acid Using Carbon Ionic Liquid Electrode. *Anal. Biochem.* **2006**, *359* (2), 224–229. https://doi.org/10.1016/j.ab.2006.09.008.

(9) Downard, A. J.; Roddick, A. D.; Bond, A. M. Covalent Modification of Carbon Electrodes for Voltammetric Differentiation of Dopamine and Ascorbic Acid. *Anal. Chim. Acta* **1995**, *317* (1–3), 303–310. https://doi.org/10.1016/0003-2670(95)00397-5.

(10) Bath, B. D.; Michael, D. J.; Trafton, B. J.; Joseph, J. D.; Runnels, P. L.; Wightman, R. M. Subsecond Adsorption and Desorption of Dopamine at Carbon-Fiber Microelectrodes. *Anal. Chem.* **2000**, *72* (24), 5994–6002. https://doi.org/10.1021/ac000849y.

(11) Vreeland, R. F.; Atcherley, C. W.; Russell, W. S.; Xie, J. Y.; Lu, D.; Laude, N. D.; Porreca, F.; Heien, M. L. Biocompatible PEDOT:Nafion Composite Electrode Coatings for Selective Detection of Neurotransmitters in Vivo. *Anal. Chem.* **2015**, *87* (5), 2600–2607. https://doi.org/10.1021/ac502165f.

(12) Gerhardt, G. A.; Oke, A. F.; Nagy, G.; Moghaddam, B.; Adams, R. N. Nafion-Coated Electrodes with High Selectivity for CNS Electrochemistry. *Brain Res.* **1984**, *290* (2), 390–395. https://doi.org/10.1016/0006-8993(84)90963-6.

(13) Durairaj, V.; Wester, N.; Etula, J.; Laurila, T.; Lehtonen, J.; Rojas, O. J.; Pahimanolis, N.; Koskinen, J. Multiwalled Carbon Nanotubes/Nanofibrillar Cellulose/Nafion Composite-Modified Tetrahedral Amorphous Carbon Electrodes for Selective Dopamine Detection. *J. Phys. Chem. C* **2019**, *123* (40), 24826–24836. https://doi.org/10.1021/acs.jpcc.9b05537.

(14) Xiang, L.; Lin, Y.; Yu, P.; Su, L.; Mao, L. Laccase-Catalyzed Oxidation and Intramolecular Cyclization of Dopamine: A New Method for Selective Determination of Dopamine with Laccase/Carbon Nanotube-Based Electrochemical Biosensors. *Electrochim. Acta* **2007**, *52* (12), 4144–4152. https://doi.org/10.1016/j.electacta.2006.11.040.

(15) Cao, Q.; Shao, Z.; Hensley, D. K.; Lavrik, N. V; Venton, B. J. Influence of Geometry on Thin Layer and Diffusion Processes at Carbon Electrodes. *Langmuir* **2021**, *37*, 2667–2676. https://doi.org/10.1021/acs.langmuir.0c03315.

(16) Yang, C.; Trikantzopoulos, E.; Jacobs, C. B.; Venton, B. J. Evaluation of Carbon Nanotube Fiber Microelectrodes for Neurotransmitter Detection: Correlation of Electrochemical Performance and Surface Properties. *Anal. Chim. Acta* **2017**, *965*, 1–8.

(17) Yang, C.; Wang, Y.; Jacobs, C. B.; Ivanov, I. N.; Venton, B. J. O2 Plasma Etching and Antistatic Gun Surface Modifications for CNT Yarn Microelectrode Improve Sensitivity and Antifouling Properties. *Anal. Chem.* **2017**, *89* (10), 5605–5611. https://doi.org/10.1021/acs.analchem.7b00785.

(18) Yang, C.; Venton, B. J. High Performance, Low Cost Carbon Nanotube Yarn Based 3D Printed Electrodes Compatible with a Conventional Screen Printed Electrode System. *2017 IEEE Int. Symp. Med. Meas. Appl.* **2017**, 100–105. https://doi.org/10.1109/MeMeA.2017.7985857.

(19) Li, W.; Jayasinghe, C.; Shanov, V.; Schulz, M. Spinning Carbon Nanotube Nanothread under a Scanning Electron Microscope. *Materials (Basel).* **2011**, *4* (9), 1519–1527. https://doi.org/10.3390/ma4091519.

(20) Mccreery, R. L.; Mccreery, R. L. Advanced Carbon Electrode Materials for Molecular Electrochemistry Advanced Carbon Electrode Materials for Molecular Electrochemistry. *2646 Chem. Rev.* **2008**, *108* (June), 2646–2687. https://doi.org/10.1021/cr068076m.

(21) Shao, Z.; Puthongkham, P.; Hu, K. K.; Jia, R.; Mirkin, M. V.; Venton, B. J. Thin Layer Cell Behavior of CNT Yarn and Cavity Carbon Nanopipette Electrodes: Effect on Catecholamine Detection. *Electrochim. Acta* **2020**, *361*, 137032. https://doi.org/10.1016/j.electacta.2020.137032.

(22) Schmidt, A. C.; Wang, X.; Zhu, Y.; Sombers, L. A. Carbon Nanotube Yarn Electrodes for Enhanced Detection of Neurotransmitter Dynamics in Live Brain Tissue. *ACS Nano* **2013**, *7* (9), 7864–7873. https://doi.org/10.1021/nn402857u.

(23) Yang, C.; Trikantzopoulos, E.; Nguyen, M. D.; Jacobs, C. B.; Wang, Y.; Mahjouri-Samani, M.; Ivanov, I. N.; Venton, B. J. Laser Treated Carbon Nanotube Yarn Microelectrodes for Rapid and Sensitive Detection of Dopamine in Vivo. *ACS Sensors* **2016**, *1* (5), 508–515. https://doi.org/10.1021/acssensors.6b00021.

(24) Jayasinghe, C.; Chakrabarti, S.; Schulz, M. J.; Shanov, V. Spinning Yarn from Long Carbon Nanotube Arrays. *J. Mater. Res.* **2011**, *26* (5), 645–651. https://doi.org/10.1557/jmr.2010.91.

(25) Venton, B. J.; Cao, Q. Fundamentals of Fast-Scan Cyclic Voltammetry for Dopamine Detection. *Analyst* **2020**, *145*, 1158–1168. https://doi.org/10.1039/C9AN01586H.

(26) Adams, R. N. Anodic Oxidation Pathways of Aromatic Hydrocarbons and Amines. *Acc. Chem. Res.* **1969**, *2* (6), 175–180. https://doi.org/10.1021/ar50018a003.

(27) Puthongkham, P.; Lee, S. T.; Jill Venton, B. Mechanism of Histamine Oxidation and Electropolymerization at Carbon Electrodes. *Anal. Chem.* **2019**, *91* (13), 8366–8373. https://doi.org/10.1021/acs.analchem.9b01178.

(28) Bard, A. J.; Faulkner, L. R. *Fundamentals and Fundamentals and Applications*; 2015; Vol. 8. https://doi.org/10.1016/B978-0-08-098353-0.00003-8.

(29) Zachek, M. K.; Hermans, A.; Wightman, R. M.; McCarty, G. S. Electrochemical Dopamine Detection: Comparing Gold and Carbon Fiber Microelectrodes Using Background Subtracted Fast Scan Cyclic Voltammetry. *J. Electroanal. Chem.* **2008**, *614* (1–2), 113–120. https://doi.org/10.1016/j.jelechem.2007.11.007.

(30) Allred, C. D.; McCreery, R. L. Adsorption of Catechols on Fractured Glassy Carbon Electrode Surfaces. *Anal. Chem.* **1992**, *64* (4), 444–448. https://doi.org/10.1021/ac00028a020.

(31) Yang, C.; Denno, M. E.; Pyakurel, P.; Venton, B. J. Recent Trends in Carbon Nanomaterial-Based Electrochemical Sensors for Biomolecules: A Review. *Anal. Chim. Acta* **2015**, *887*, 17–37. https://doi.org/10.1016/j.aca.2015.05.049.

(32) Davis, J. M.; Fan, F. R. F.; Bard, A. J. Currents in Thin Layer Electrochemical Cells with Spherical and Conical Electrodes. *J. Electroanal. Chem.* **1987**, *238* (1–2), 9–31. https://doi.org/10.1016/0022-0728(87)85163-X.

(33) Yang, C.; Hu, K.; Wang, D.; Zubi, Y.; Lee, S. T.; Puthongkham, P.; Mirkin, M. V.; Venton,

B. J. Cavity Carbon-Nanopipette Electrodes for Dopamine Detection. *Anal. Chem.* **2019**, *91* (7), 4618–4625. https://doi.org/10.1021/acs.analchem.8b05885.

(34) Huffman, M. L.; Venton, B. J. Electrochemical Properties of Different Carbon-Fiber Microelectrodes Using Fast-Scan Cyclic Voltammetry. *Electroanalysis* **2008**, *20* (22), 2422–2428. https://doi.org/10.1002/elan.200804343.

(35) Rueda, M.; Aldaz, A.; Sanchez-Burgos, F. Oxidation of L-Ascorbic Acid on a Gold Electrode. *Electrochim. Acta* **1978**, *23* (5), 419–424. https://doi.org/10.1016/0013-4686(78)87040-6.

(36) Ruiz, J. J.; Aldaz, A.; Dominguez, M. Mechanism of L -Ascorbic Acid Oxidation on a Mercury Electrode. II. Basic Medium . *Can. J. Chem.* **1978**, *56* (11), 1533–1537. https://doi.org/10.1139/v78-248.

(37) Venton, B.J. Troyer, K. P.; Wightman, R. M. Response Times of Carbon Fiber Microelectrodes to Dynamic Changes in Catecholamine Concentration. *Anal. Chem.* **2002**, *74* (3), 539–546. https://doi.org/10.1021/ac010819a.

(38) Bacil, R. P.; Chen, L.; Serrano, S. H. P.; Compton, R. G. Dopamine Oxidation at Gold Electrodes: Mechanism and Kinetics near Neutral PH. *Phys. Chem. Chem. Phys.* **2020**, *22* (2), 607–614. https://doi.org/10.1039/c9cp05527d.

(39) Schindler, S.; Bechtold, T. Mechanistic Insights into the Electrochemical Oxidation of Dopamine by Cyclic Voltammetry. *J. Electroanal. Chem.* **2019**, *836* (January), 94–101. https://doi.org/10.1016/j.jelechem.2019.01.069.

(40) Ruiz, J. J.; Aldaz, A.; Dominguez, M. Mechanism of L Ascorbic Acid Oxidation and Dehydro L Ascorbic Acid Reduction on a Mercury Electrode. I. Acid Medium. *Can. J. Chem.* **1977**, *55* (15), 2799–2806. https://doi.org/10.1139/v77-389.

(41) Oh, Y.; Heien, M. L.; Park, C.; Kang, Y. M.; Kim, J.; Boschen, S. L.; Shin, H.; Cho, H. U.; Blaha, C. D.; Bennet, K. E.; Lee, H. K.; Jung, S. J.; Kim, I. Y.; Lee, K. H.; Jang, D. P. Tracking Tonic Dopamine Levels in Vivo Using Multiple Cyclic Square Wave Voltammetry. *Biosens. Bioelectron.* **2018**, *121*, 174–182. https://doi.org/https://doi.org/10.1016/j.bios.2018.08.034.

(42) Kishida, K. T.; Saez, I.; Lohrenz, T.; Witcher, M. R.; Laxton, A. W.; Tatter, S. B.; White, J. P.; Ellis, T. L.; Phillips, P. E. M.; Montague, P. R. Subsecond Dopamine Fluctuations in Human Striatum Encode Superposed Error Signals about Actual and Counterfactual Reward. *Proc. Natl. Acad. Sci.* **2016**, *113* (1), 200–205. https://doi.org/10.1073/pnas.1513619112.

(43) Heien, M. L. A. V; Johnson, M. A.; Wightman, R. M. Resolving Neurotransmitters Detected by Fast-Scan Cyclic Voltammetry. *Anal. Chem.* **2004**, *76* (19), 5697–5704. https://doi.org/10.1021/ac0491509.

(44) Jeon, J.; Hwang, I.; Chung, T. D. Electrochemical Detection of Neurotransmitters: Toward Synapse-Based Neural Interfaces. *Biomedical Engineering Letters*. 2016, pp 123–133. https://doi.org/10.1007/s13534-016-0230-6.

(45) Venton, B. J.; Wightman, R. M. Psychoanalytical Electrochemistry: Dopamine and Behavior. *Anal. Chem.* **2003**, *75* (19), 414 A-421 A.

Chapter 4

Carbon nanospike coated nanoelectrodes for measurements of neurotransmitters

Chapter 4 was reprinted from *Faraday Discussions* 233 (**2022**): 303-314.

Abstract

Carbon nanoelectrodes enable the detection of neurotransmitters at the level of single cells, vesicles, synapses, and small brain structures. Previously, etching of carbon fibers and 3D printing based on direct laser writing were used to fabricate carbon nanoelectrodes, but these methods lack the ability for mass manufacturing. In this paper, we mass fabricate carbon nanoelectrodes by growing carbon nanospikes (CNSs) on metal wires. CNSs have a short, dense, and defect-rich surface that produces remarkable electrochemical properties, and they can be mass fabricated on almost any substrate without using catalysts. Tungsten wires and niobium wires were electrochemically etched in batch to form sub micrometer sized tips, and a layer of CNSs were grown on the metal wires using plasma-enhanced chemical vapor deposition (PE-CVD). The thickness of the CNS layer was controlled by deposition time, and a thin layer of CNSs can effectively cover the entire metal surface while maintaining the tip size within sub micrometer scale. Etched tungsten wires produced tapered conical nanotips, while etched niobium wires were long and thin. Both showed excellent sensitivity for detection of outer sphere ruthenium hexamine and inner sphere test compound ferricyanide. CNS nanosensors were used for measurements of dopamine, serotonin, ascorbic acid and DOPAC with fast-scan cyclic voltammetry. The CNS nanoelectrodes had a large surface area and numerous defect sites, which improves sensitivity, electron transfer kinetics and adsorption. Finally, the CNS nanoelectrodes are compared other nanoelectrode fabrication methods, including flame etching, 3D printing, and nanopipettes, which are slower to make and more difficult for mass fabrication. Thus, CNS nanoelectrodes are a promising strategy for mass-fabrication of nanoelectrode sensors for neurotransmitters.

4.1 Introduction

Carbon-based electrodes are standard electrochemical sensors for neurotransmitter detection due to their conductivity, biocompatibility, and small size.[1,2] Nanoelectrodes are required to approach the site of neurotransmitter release in tiny spaces, such as single synapses, or in small brain structures, such as those in *Drosophila* or zebrafish which have micrometer-scale brain structures,.[3–5] In recent studies, several methods have been developed to fabricate carbon nanoelectrode sensors for neurotransmitter detection.[6–8] Carbon fibers are the standard electrode material for neurotransmitter detection,[9] and they can be flame etched or electrochemically etched to sub micrometer scale.[10–16] For example, the Ewing group used flame etched carbon-fiber nanotip electrodes to study catecholamine released by single cells.[14,17,18] However, the manual etching of a carbon fiber lacks precise control in electrode size and geometry, and the method is not suitable for batch manufacturing. Our group developed 3D printed carbon nanoelectrodes based on direct laser writing,[8,19] allowing customizable electrode size and geometry with perfect reproducibility. 3D printing requires a specialized printer and is not extremely rapid. Another approach is to make nanopipettes, where quartz capillaries are pulled to create a nanoscale orifice, and carbon can be selectively deposited onto the inner wall of quartz capillary templates.[20–23] The opening of the carbon nanopipette can be correlated with vesicle size.[24] The Shen group developed nanopipette electrodes without carbon deposition, which facilitates the detection of non-redox-active neurotransmitters such as acetylcholine.[25–27] The active surface areas of carbon nanopipette electrodes are located inside the capillary, so their surface area is smaller and the analyte must diffuse into the nanopipette. Overall, there are still limited methods to fabricate carbon nanoelectrodes for neurotransmitter detection, and better approaches are needed to mass produce nanoelectrode sensors with high sensitivity.

Carbon nanospikes (CNSs) are a new electrode material, used for electrochemical energy and neurotransmitter applications.[28,29] They exhibit curled, spike-like structures approximately 50 nm in length, which densely overlap to increase the electrode surface area.

CNSs are rich in edge-plane carbon sites, improving electron transfer and adsorption kinetics.[28,30–32] With larger surface area and more defect carbon sites, CNSs outperform carbon nanotubes and carbon fibers as neurochemical sensors.[33] CNSs are produced by plasma-enhanced chemical vapor deposition (PE-CVD) without any catalyst; thus, they can be uniformly grown onto almost any substrate.[34] The deposition time controls the layer thickness, and a thin layer of CNSs effectively covers the entire substrate surface. The fabrication of CNSs is simple and suitable for mass fabrication, and their electrochemical properties for neurotransmitter detection outperform carbon nanotubes and carbon fibers.[32] Although CNS electrodes have been grown on various substrate for neurotransmitter detection, they have not been grown on nanometer scale substrates to form carbon nanoelectrodes.

In this work, we demonstrated the growth of CNSs on metal wires with nanotips to fabricate CNS nanoelectrodes. Tungsten and niobium wires were electrochemically etched to the nanoscale, and a thin layer of CNSs was grown onto the tungsten and niobium surface to form W/CNS and Nb/CNS nanoelectrodes. The CNS layers completely cover the metal wires while the electrode tip is still on the nanometer scale. The CNSs have a larger surface area to improve sensitivity, and numerous defect sites improve electron transfer and adsorption kinetics. Cyclic voltammetry (CV) and electrochemical impedance spectroscopy (EIS) were used to characterize the CNS nanoelectrodes. The Nb/CNS nanoelectrodes have good sensitivity for dopamine and other neurochemical detection using fast-scan cyclic voltammetry (FSCV) detection. The growth of CNSs on nanoscale substrate was compared with other carbon nanoelectrode fabrication methods, including flame etching of carbon fibers, nano 3D printing, and nanopipettes. The entire fabrication process of CNS nanoelectrodes can be done in batches; we fabricated 30 nanosensors on a 2.5 cm long substrate, but even more could be mounted on a larger conductive substrate. Therefore, the method has promising potential to for the mass fabrication of carbon nanoelectrode sensors.

4.2Methods

4.2.1 Etching of metal wires

Tungsten wires and niobium wires (50 µm diameter) were purchased from Advent Research Materials, Ltd (Oxford, England). The metal wires were cut to approximately 2 cm in length, and parallelly immobilized at the edge of a niobium foil. The extended length of the metal was about 1 cm, and metal wires were vertically inserted into the etching solution at about 0.5 cm depth. About thirty 50 µm diameter metals wires can be mounted onto a 2.5 cm × 2.5 cm niobium foil. An AC current supplier (Interworld Highway LLC, Long Branch, NJ) was used to etch the metal wires to sub-micrometer diameter at the tip. One clamp of the AC supplier was connected to the niobium foil, and another was connected to a graphite electrode. The tungsten wires were etched at 2 V and 60 Hz in 2 M NaOH for about 5 min, and the niobium wires were etched at 2 V and 60 Hz in concentrated HCl for about 20 min.

4.2.2 Growth of CNSs

Metal wires were immobilized to a stainless-steel stage and placed into a custom-built DC plasma-enhanced chemical vapor deposition (PE-CVD) chamber. The metal wires served as the cathode for the DC plasma. The pressure of the chamber was 6 Torr, and the wires were exposed to 100 sccm ammonia and 80 sccm acetylene for 6 min. The DC plasma discharge was operated at 250 mA and 480 - 550 V at 650 °C.

4.2.3 Surface and electrochemical characterizations

Scanning electron microscope (SEM) images were taken on Merlin field emission SEM (Zeiss, Thornwood, NY) and FEI Quanta 650 SEM (Thermo Fisher Scientific, Waltham, MA). Secondary electron detector was used at an accelerating voltage of 1.0 - 3.0 kV.

Cyclic voltammetry and electrochemical impedance spectroscopy experiments were performed with Reference 600 potentiostat (Gamry Instruments, Warminster, PA). Prior to the measurements, the CNS coated wires were inserted into a pulled glass capillary and sealed with 5-min epoxy (J- B weld, Sulphur Springs, TX). A three electrodes system was used. The working electrode was a CNS electrode, the reference electrode was a standard Ag/AgCl electrode, and the counter electrode was a Pt wire. EIS measurements were performed with frequency range 100 kHz to 0.1 Hz, and the amplitude of the AC voltage was 10 mV with a DC biased potential of 0.2 V.

FSCV experiments were performed with a ChemClamp potentiostat and head-stage (Dagan, Minneapolis, MN). The CNS coated wires were inserted into a pulled glass capillary and sealed with 5-min epoxy, and 1 M KCl solution was filled into the glass capillary to make an electrical connection. A two-electrode system was used. The working electrode was the CNS nanoelectrode and the reference electrode was Ag/AgCl. The PBS buffer (131.5 mM NaCl, 3.25 mM KCl, 1.2 mM $CaCl_2$, 1.25 mM NaH_2PO_4, 1.2 mM $MgCl_2$, and 2.0 mM Na_2SO_4, and the pH was adjusted to 7.4 by concentrated NaOH) and neurochemical solutions were injected through a flow cell at 2 mL/min by a syringe pump (Harvard Apparatus, Holliston, MA) and modulated by a six-port loop injector with an air actuator (VIVI Valco Instruments, Houston, TX). The data were analyzed with HDCV Analysis software (Department of Chemistry, University of North Carolina at Chapel Hill).

4.3 Results and Discussion

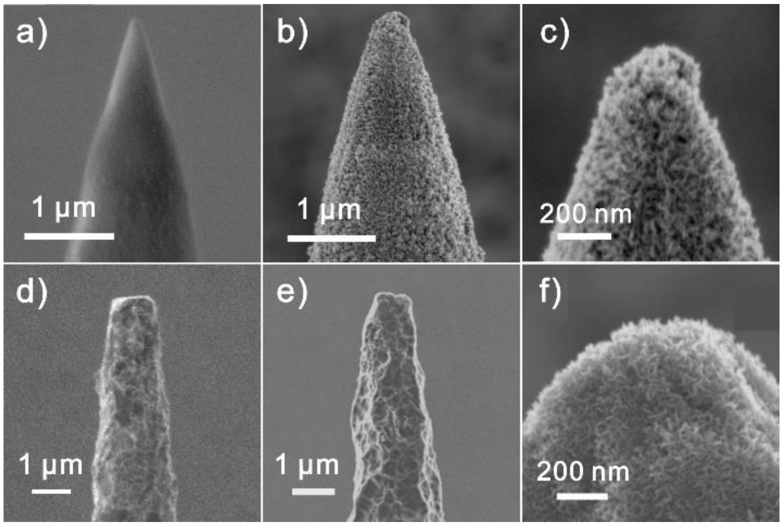

Figure 1. SEM images of (a) etched tungsten wire, (b) CNSs grown on tungsten wire, (c) more enlarged images of CNSs on tungsten wire, (d) etched niobium wire, (e) CNSs grown on etched niobium wire, and (f) more enlarged images of CNSs on niobium wire.

We used electrochemically etched tungsten wires and niobium wires for the growth of CNSs. Figure 1a shows the etched tungsten wire has a conical geometry with sharp nanotips measured to be 286 ± 92 nm (n = 10, s.d), and the surface is smooth, which is beneficial for the growth of CNSs. Tungsten wires are advantageous because they can be easily etched to sharp nanotips,[35] but they are not electrochemically inert at the potential of 1.3 V, which is the switching potential of the typical FSCV waveform for dopamine detection.[30] Therefore, the CNSs must cover the entire tungsten wire so that the electroactive surface is only carbon. Figure 1b shows the SEM image of CNSs grown on etched tungsten wires, and the CNSs are uniformly grown. The nanotip size of W/CNS electrodes were measured to be 448 ± 90 nm (n = 10, s.d). Therefore, the thickness of the CNS layer is approximately 80 nm, which slightly blunts the nanotip, but the tip size is still at nanoscale (Figure 1c). Figure 1d shows the etched niobium wires are not as sharp and smooth as tungsten wires, because niobium is relatively inert and difficult to etch.[36] But the apex angle of the Nb/CNS electrode is smaller, yielding a long and thin tip. The nanotip size of etched Nb wires are 908 ± 242 nm (n = 6, s.d). In Figure 1e, the growth of CNSs on niobium wire slightly adds the tip size to 1015 ± 133 nm (n = 6, s.d). The adding of nanotip size is about 50 nm because etched Nb wires have rough surface. More enlarged SEM images of CNSs are shown in Figure 1c and 1f, which exhibit the dense spike-like features of the CNSs grown on tungsten and niobium substrates. We calculated the roughness of CNS nanoelectrodes by measuring the background double layer charging current.[33] We fabricated two batches of Nb/CNS nanoelectrodes, the first batch has a roughness of 4.9 ± 0.5, and the second batch has a roughness of 5.1 ± 0.8, indicating the roughness of the electrode surface are nearly identical among batches.

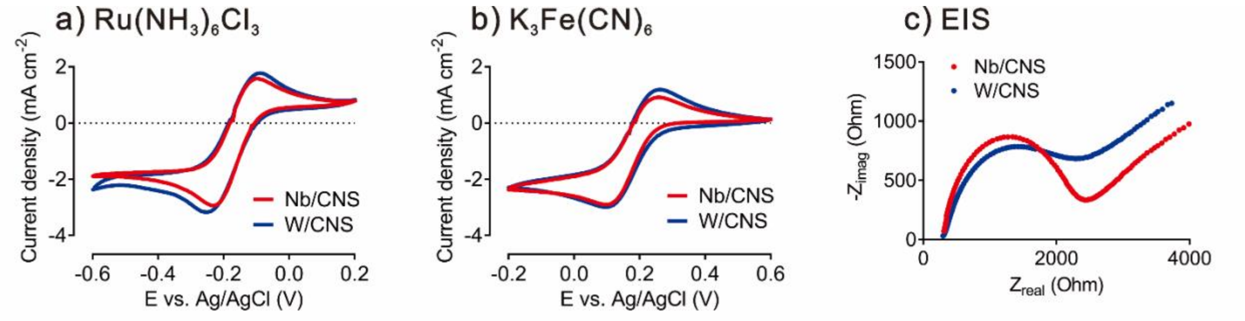

Figure 2. Cyclic voltammogram and electrochemical impedance measurements at W/CNS and Nb/CNS electrodes. (a) Cyclic voltammogram in 10 mM $Ru(NH_3)_6Cl_3$ and (b) Cyclic voltammogram in 10 mM $K_3Fe(CN)_6$ (Scan rate = 100 mV s^{-1}). (c) Nyquist plot of Nb/CNS and W/CNS electrodes.

In Figure 2, the W/CNS nanoelectrodes and Nb/CNS nanoelectrodes were characterized by cyclic voltammetry (CV) and electrochemical impedance spectroscopy (EIS). CV was performed with a surface insensitive redox system $Ru(NH_3)_6^{3+/2+}$ (Figure 2a) and a surface sensitive redox system $Fe(CN)_6^{3-/4-}$ (Figure 2b).[37] For both redox complex, Nb/CNS and W/CNS electrodes exhibit similar shapes and current densities, indicating the CNSs on the two types of wires exhibit similar electrochemical behavior. Figure 2c shows the Nyquist plot from EIS obtained in $K_3Fe(CN)_6$ solution. The Nb/CNS and W/CNS electrodes have similar semicircles in size, demonstrating the CNSs grown on them have similar electron transfer kinetics. The Nyquist plot shows only one semicircle for both W/CNS and Nb/CNS nanoelectrodes, indicating no other capacitance exists other than the double layer capacitance. These results further demonstrate the CNSs effectively cover the metal wires, and the electrochemical responses only come from the CNSs but not the metal wires.

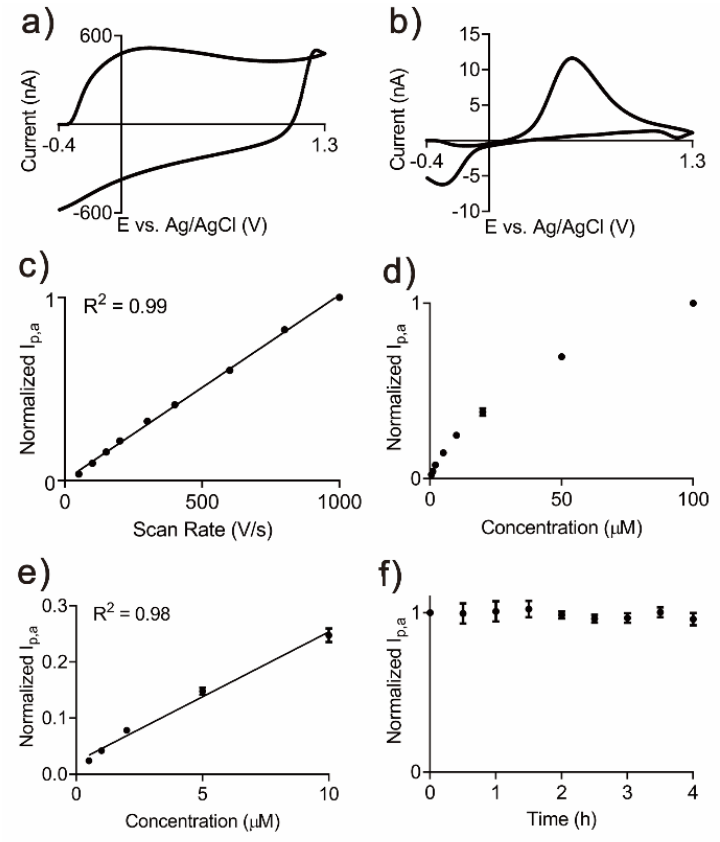

Figure 3. FSCV study of Nb/CNS nanoelectrodes. (a) Background current. (b) Background-subtracted current of 1 μM dopamine. (c) Dopamine current is linear with scan rate (R^2 = 0.99, n = 3). (d) Dopamine response at concentration 1 μM to 100 μM (n = 3). (e) Dopamine current is linear with a concentration up to 10 μM (R^2 = 0.98). (f) Stability test. 1 μM dopamine was measured every 0.5 h for 4 h.

Fast-scan cyclic voltammetry (FSCV) is the standard technique for real-time measurement of neurotransmitters, and we used FSCV to characterize the detection of dopamine of Nb/CNS nanoelectrodes.[38] Figure 3a-b show the background current and the background-subtracted dopamine response of Nb/CNS nanoelectrodes, which have characteristic shapes similar to cyclic voltammograms at carbon-fiber electrodes. Dopamine is oxidized to dopamine-o-quinone around 0.6 V and the reduction happens at −0.2 V. The oxidation peak is larger than reduction peak because dopamine has tighter adsorption than dopamine-o-quinone.[39] Figure S1 shows the background signal and the detection of dopamine at W/CNS nanoelectrodes, which has similar behavior as Nb/CNS electrodes. Figure 3c shows the anodic peak current has a linear relationship with scan rate, indicating the detection of dopamine is an adsorption-controlled process.[39] Figure 3d-e show the current is linear with concentration up to 10 µM. If the concentration of dopamine is higher than 10 µM, the electrode surface will be saturated with adsorbed dopamine and diffusion will contribute to the current. To test the stability of the CNS nanoelectrodes, we continuously applied the FSCV waveform for 4 h and measured the dopamine response every 0.5 h. The peak current did not drop significantly during the time, so the electrodes are stable during the period of a typical biological experiment.

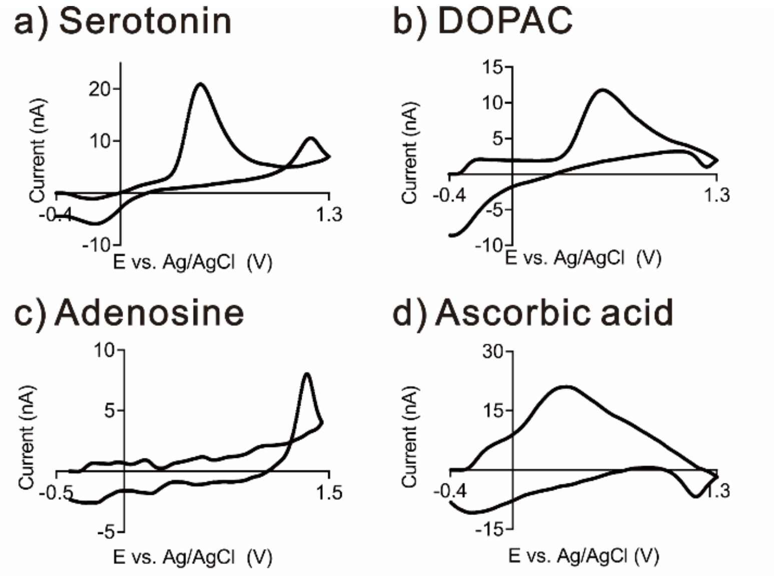

Figure 4. Detection of other neurochemicals using CNS nanoelectrodes. (a) 1 µM serotonin, (b) 20 µM DOPAC, (c) 1 µM adenosine, and (d) 200 µM ascorbic acid.

FSCV detection was tested for other neurochemicals, including serotonin, DOPAC, adenosine and ascorbic acid using the Nb/CNS nanoelectrodes. Serotonin is a monoamine neurotransmitter,[40] and its reduction peak is more positive than for dopamine (Figure 4a). Here, using the dopamine waveform for detection, the peaks for serotonin are very characteristic, including a peak at the switching potential.[40] Compared with carbon fiber and carbon nanotube electrodes, CNS electrodes are less sensitive to serotonin, probably due to serotonin fouling which blocks more active sites for CNS electrodes.[33] DOPAC is a catechol that is present in the brain in higher concentration, and is a major metabolite of the neurotransmitter dopamine.[41] At physiological pH DOPAC is an anion, and the molecules are electrostatically repelled from adsorption, so its CV reduction peak is more negative than dopamine (Figure 4b).[42] Adenosine has a higher oxidation potential, and the oxidation peak of adenosine shows up on the reverse scan with a 1.45 V switching potential (Figure 4c).[43] Interestingly, a secondary peak is observed for adenosine on carbon-fibers, but is less evident at CNS electrodes.[44] A broad peak is observed for ascorbic acid, which is a common interferent in the brain at concentrations 100 to 1000-fold higher than dopamine (Figure 4d).[45] One major advantage of CNSs nanoelectrodes is they exhibit a very high surface to volume ratio. Compared with smooth carbon fiber electrodes, the surface area of CNS electrodes is 5-fold larger given the same geometric area. Therefore, the background signal and the current responses are larger at CNS nanoelectrodes, and they exhibit to enhanced sensitivity for neurotransmitter sensing.[32,46] Also, CNS electrodes have greater selectivity for cationic neurochemicals over anionic neurochemicals than other carbon materials,[32] which may be explored in future works.

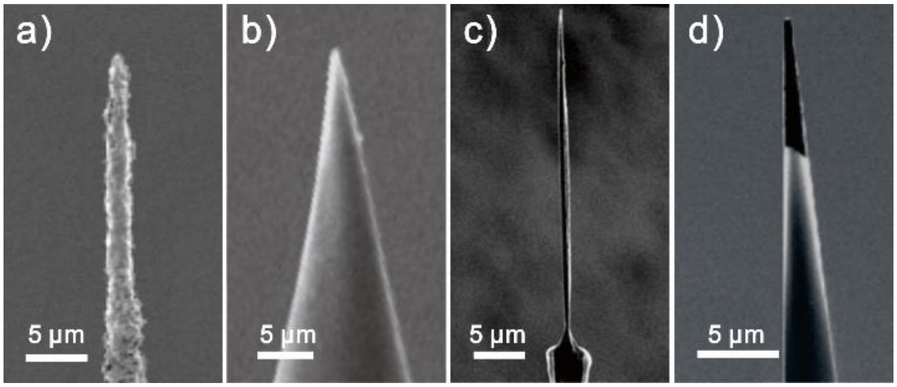

Figure 5. SEM images comparing different carbon nanoelectrodes. (a) Nb/CNS nanoelectrode, (b) 3D printed nanoelectrode, (c) flame etched carbon fiber nanoelectrode. Adapted with permission from ref. [14], copyright (2015) Wiley-VCH, and (d) carbon nanopipette. Reprinted with permission from ref. [22]. Copyright (2015) American Chemical Society.

Compared with other carbon nanoelectrode fabrication methods, growing CNSs grown on etched metal wires is promising for mass fabrication. Figure 5 and Table 1 compare the advantages and disadvantages of different fabrication techniques, including CNS nanoelectrodes, flame etched carbon fiber nanoelectrodes, 3D printing nanoelectrodes, and carbon nanopipettes. Flame etching of carbon fiber is simple and it is easy to obtain small nanotips, so it is the most used method for carbon nanoelectrode fabrication.[7,47] Both CNS nanoelectrodes and carbon-fiber nanoelectrodes have conical nanotips, which is the most common morphology yielded in an etching process. Flame etching is easier than growing CNSs, but it is a hand fabrication process and not amenable for batch fabrication. Nano 3D printing enables fully customized electrode geometry and surface structures, but the method is not very fast and it requires specialized equipment.[8,19] Therefore, nano 3D printing is most useful for fabrication of rationally designed carbon nanoelectrode sensors with high reproducibility. Carbon nanopipettes are fabricated by chemical vapor deposition, similar to CNS electrodes, but for carbon nanopipettes, carbon is selectively deposited on the inner surface of the quartz capillary. Both methods are suitable for batch manufacturing. Carbon nanopipettes have the cavity structure which confines the analytes, so thin layer electrochemistry is the the main electrochemical process when using FSCV[46,48] Also, the nanoscale cavity of carbon nanopipettes can be used for unique applications such as resistive-pulse sensors and rectification sensors.[21,24,49] Thus, there are different applications for different types of carbon nanoelectrodes, but CNS electrodes would be suitable for direct implantation into small organisms or near synapses.

CNS nanoelectrodes require the deposition of a thin layer of CNSs, so the nanotip areas are larger than other types of nanoelectrodes, even though the geometric areas may be similar. CNSs are short and dense, so they increase the electroactive surface to volume ratio to improve the sensitivity. Thus, currents measured here are larger than those for other nanoelectrodes of similar size, because CNS electrodes have rough surfaces with greater surface area. CNSs are also rich in edge-plane carbon sites, which enhances the detection of neurotransmitters by improving adsorption. One issue with carbon nanoelectrodes is that currents are small, and these CNS electrodes overcome that challenge. The CNS electrodes also show more resistance to anion neurochemicals, such as ascorbic acid; and they are less sensitive to neurotransmitters which can induce fouling, such as serotonin. The benefits of CNS electrodes in selectivity should be emphasized in future studies. Overall, CNSs have large surface areas and enhanced electrochemical performance. We fabricated thirty nanoelectrode sensors on a 2.5 cm wide substrate for etching in one batch, and then put all the wires into the PECVD simultaneously. Therefore, the fabrication of CNS nanoelectrodes is a promising strategy for mass manufacturing of carbon nanoelectrode sensors.

Table 1. Comparisons of CNS nanoelectrodes, carbon fiber nanoelectrodes, 3D printed nanoelectrodes and carbon nanopipettes.

Nano-electrode	Tip size	Electrode geometry	Surface morphology	Fabrication method	Features	Limitations	Ref.
CNS	300 nm – 1 µm	Conical	Rough	PE-CVD	Suitable for mass fabrication	Relatively large nanotip	30,32,34
Carbon fiber	50 – 300 nm	Conical	Smooth	Flame etching	Simple and small size	Manual fabrication	10–14,17,18,50–52
3D printing	100 - 600 nm	Custom	Custom	Direct laser writing	Customized geometry	Require specific equipment	8,19,53–58
Carbon nano-pipettes	20 – 600 nm	Conical	Cavity	CVD	Cavity structure	Small surface area	22–24,48,59–61

In summary, we have developed a new carbon nanoelectrode batch fabrication method by growing CNSs onto etched metal wires. In one batch, we mounted approximately 30 tungsten or niobium wires on a 2.5 cm wide substrate and electrochemically etched them to form nanotips. For mass manufacturing, more than one hundred metal wires may be mounted on a larger conductive substrate. A thin layer of CNSs was uniformly grown on the metal surface using PE-CVD, which is also a mass fabrication process. The CNS nanoelectrodes exhibit large surface to volume ratio and good electrochemical properties. The CNS nanoelectrodes were characterized by FSCV detection for dopamine, and they are useful to detect a variety of neurochemicals. Compared with other fabrication methods of carbon nanoelectrodes, CNS nanoelectrodes have a larger surface to volume area, and thus larger currents. All the fabrication processes of CNS nanoelectrodes are operated in batch, therefore, the development of CNS nanoelectrodes exhibit promising potential to mass fabricate carbon nanoelectrode sensors.

Acknowledgments

This work was funded by NIH R01EB026497 and NIH R01MH085159. Growth and SEM imaging of carbon nanospikes were conducted at the Center for Nanophase Materials Sciences, Oak Ridge National Laboratory, which is a DOE Office of Science User Facility.

4.4 References

1 Q. Cao, P. Puthongkham and B. J. Venton, *Anal. Methods*, , DOI:10.1039/c8ay02472c.
2 C. Yang, M. E. Denno, P. Pyakurel and B. J. Venton, *Anal. Chim. Acta*, 2015, **887**, 17–37.
3 X. Zhang, A. Hatamie and A. G. Ewing, *Curr. Opin. Electrochem.*, 2020, **22**, 94–101.
4 M. Shin, Y. Wang, J. R. Borgus and B. J. Venton, *Annu. Rev. Anal. Chem.*, 2019, **12**, 297–321.
5 M. Shin, J. M. Copeland and B. J. Venton, *ACS Chem. Neurosci.*, 2018, **9**, 1872–1883.
6 R. Chen, K. Alanis, T. M. Welle and M. Shen, *Anal. Bioanal. Chem.*, 2020, 6121–6132.
7 M. Shen and M. L. Colombo, *Anal. Methods*, 2015, **7**, 7095–7105.
8 Q. Cao, M. Shin, N. V. Lavrik and B. J. Venton, *Nano Lett.*, 2020, **20**, 6831–6836.
9 M. L. Huffman and B. J. Venton, *Analyst*, 2009, **134**, 18–24.
10 W. Z. Wu, W. H. Huang, W. Wang, Z. L. Wang, J. K. Cheng, T. Xu, R. Y. Zhang, Y. Chen and J. Liu, *J. Am. Chem. Soc.*, 2005, **127**, 8914–8915.
11 T. G. Strein and A. G. Ewing, *Anal. Chem.*, 1992, **64**, 1368–1373.
12 X. Zhang, W. Zhang, X. Zhou and B. Ogorevc, *Anal. Chem.*, 1996, **68**, 3338–3343.
13 Y.-T. Li, S.-H. Zhang, L. Wang, R.-R. Xiao, W. Liu, X.-W. Zhang, Z. Zhou, C. Amatore and W.-H. Huang, *Angew. Chemie - Int. Ed.*, 2014, **53**, 12456–12460.
14 X. Li, S. Majdi, J. Dunevall, H. Fathali and A. G. Ewing, *Angew. Chemie - Int. Ed.*, 2015, **54**, 11978–11982.
15 A. M. Strand and B. J. Venton, *Anal. Chem.*, 2008, **80**, 3708–3715.
16 Q. Cao, J. Lucktong, Z. Shao, Y. Chang and B. J. Venton, *Anal. Bioanal. Chem.*, , DOI:10.1007/s00216-021-03539-6.
17 C. Gu, X. Zhang and A. G. Ewing, *Anal. Chem.*, 2020, **92**, 10268–10273.
18 Y. Wang and A. Ewing, *ChemBioChem*, 2021, 22, 807–813.
19 C. Yang, Q. Cao, P. Puthongkham, S. T. Lee, M. Ganesana, N. V. Lavrik and B. J. Venton, *Angew. Chemie - Int. Ed.*, 2018, **57**, 14255–14259.
20 B. M. Kim, T. Murray and H. H. Bau, *Nanotechnology*, 2005, **16**, 1317–1320.
21 K. Hu, Y. Wang, H. Cai, M. V Mirkin, Y. Gao, G. Friedman and Y. Gogotsi, *Anal. Chem.*, 2014, **86**, 8897–8901.
22 H. R. Rees, S. E. Anderson, E. Privman, H. H. Bau and B. J. Venton, *Anal. Chem.*, 2015, **87**, 3849–3855.
23 C. Yang, K. Hu, D. Wang, Y. Zubi, S. T. Lee, P. Puthongkham, M. V. Mirkin and B. J. Venton, *Anal. Chem.*, , DOI:10.1021/acs.analchem.8b05885.
24 A. G. Ewing, K. Hu, R. Jia, A. Hatamie, K. L. Le Vo and M. V. Mirkin, *J. Am. Chem. Soc.*, 2020, **142**, 16910–16914.
25 M. L. Colombo, J. V. Sweedler and M. Shen, *Anal. Chem.*, 2015, **87**, 5095–5100.
26 N. T. Iwai, M. Kramaric, D. Crabbe, Y. Wei, R. Chen and M. Shen, *Anal. Chem.*, 2018, **90**, 3067–3072.
27 M. L. Colombo, S. McNeil, N. Iwai, A. Chang and M. Shen, *J. Electrochem. Soc.*, 2016, **163**, H3072–H3076.
28 L. B. Sheridan, D. K. Hensley, N. V. Lavrik, S. C. Smith, V. Schwartz, C. Liang, Z. Wu, H. M. Meyer and A. J. Rondinone, *J. Electrochem. Soc.*, 2014, **161**, H558–H563.
29 Y. Song, R. Peng, D. K. Hensley, P. V. Bonnesen, L. Liang, Z. Wu, H. M. Meyer, M. Chi, C. Ma, B. G. Sumpter and A. J. Rondinone, *ChemistrySelect*, 2016, **1**, 1–8.
30 A. G. Zestos, C. Yang, C. B. Jacobs, D. Hensley and B. J. Venton, *Analyst*, 2015, **140**, 7283–7292.
31 A. S. Shanta, S. Shamsir, Y. Song, D. K. Hensley, A. J. Rondinone, S. K. Islam and N. McFarlane, *2018 40th Annu. Int. Conf. IEEE Eng. Med. Biol. Soc.*, 2018, 4281–4284.
32 Q. Cao, D. K. Hensley, N. V. Lavrik and B. J. Venton, *Carbon N. Y.*, 2019, **155**, 250–257.

33 Q. Cao, D. K. Hensley, N. V Lavrik and B. J. Venton, *Carbon N. Y.*, 2019, **155**, 250–257.

34 A. S. Shanta, K. A. Al Mamun, S. K. Islam, N. McFarlane and D. K. Hensley, *Int. J. High Speed Electron. Syst.*, 2017, **26**, 1740008.

35 S. Kerfriden, A. H. Nahlé, S. A. Campbell, F. C. Walsh and J. R. Smith, *Electrochim. Acta*, 1998, **43**, 1939–1944.

36 Y. Uehara, T. Fujita, M. Iwami and S. Ushioda, *Rev. Sci. Instrum.*, 2001, **72**, 2097–2099.

37 R. L. McCreery, *Chem. Rev.*, 2008, **108**, 2646–2687.

38 B. J. Venton and Q. Cao, *Analyst*, 2020, 145, 1158–1168.

39 B. D. Bath, D. J. Michael, B. J. Trafton, J. D. Joseph, P. L. Runnels and R. M. Wightman, *Anal. Chem.*, 2000, **72**, 5994–6002.

40 K. E. Dunham and B. J. Venton, *Analyst*, 2020, **145**, 7437–7446.

41 P. Takmakov, M. K. Zachek, R. B. Keithley, E. S. Bucher, G. S. McCarty and R. M. Wightman, *Anal. Chem.*, 2010, **82**, 9892–9900.

42 M. L. Huffman and B. J. Venton, *Electroanalysis*, 2008, **20**, 2422–2428.

43 M. D. Nguyen and B. J. Venton, *Comput. Struct. Biotechnol. J.*, 2015, 13, 47–54.

44 B. E. K. Swamy and B. J. Venton, *Anal. Chem.*, 2007, **79**, 744–750.

45 H. Cheng, L. Li, M. Zhang, Y. Jiang, P. Yu, F. Ma and L. Mao, *TrAC - Trends Anal. Chem.*, 2018, **109**, 247–259.

46 Q. Cao, Z. Shao, D. K. Hensley, N. V. Lavrik and B. J. Venton, *Langmuir*, 2021, **37**, 2667–2676.

47 J. Clausmeyer and W. Schuhmann, *TrAC - Trends Anal. Chem.*, 2016, 79, 46–59.

48 Z. Shao, P. Puthongkham, K. K. Hu, R. Jia, M. V. Mirkin and B. J. Venton, *Electrochim. Acta*, 2020, **361**, 137032.

49 Y. Yu, J.-M. Noël, M. V Mirkin, Y. Gao, O. Mashtalir, G. Friedman and Y. Gogotsi, *Anal. Chem.*, 2014, **86**, 3365–3372.

50 Y.-T. Li, S.-H. Zhang, X.-Y. Wang, X.-W. Zhang, A. I. Oleinick, I. Svir, C. Amatore and W.-H. Huang, *Angew. Chemie - Int. Ed.*, 2015, **54**, 9313–9318.

51 X. Li, J. Dunevall and A. G. Ewing, *Acc. Chem. Res.*, 2016, **49**, 2347–2354.

52 J. G. Roberts, E. C. Mitchell, L. E. Dunaway, G. S. McCarty and L. A. Sombers, *ACS Nano*, 2020, **14**, 2917–2926.

53 A. Abdalla and B. A. Patel, *Curr. Opin. Electrochem.*, 2020, **20**, 78–81.

54 X. Zhang, A. Vyatskikh, H. Gao, J. R. Greer and X. Li, *Proc. Natl. Acad. Sci. U. S. A.*, 2019, **116**, 6665–6672.

55 C. M. Portela, B. W. Edwards, D. Veysset, Y. Sun, K. A. Nelson, D. M. Kochmann and J. R. Greer, *Nat. Mater.*, , DOI:10.1038/s41563-021-01033-z.

56 G. Seniutinas, A. Weber, C. Padeste, I. Sakellari, M. Farsari and C. David, *Microelectron. Eng.*, 2018, **191**, 25–31.

57 J. Bauer, A. Schroer, R. Schwaiger and O. Kraft, *Nat. Mater.*, 2016, **15**, 438–443.

58 B. Cardenas-Benitez, C. Eschenbaum, D. Mager, J. G. Korvink, M. J. Madou, U. Lemmer, I. De Leon and S. O. Martinez-Chapa, *Microsystems Nanoeng.*, 2019, **5**, 1–13.

59 Y. Yu, Y. Gao, K. Hu, P. Y. Blanchard, J. M. Noël, T. Nareshkumar, K. L. Phani, G. Friedman, Y. Gogotsi and M. V. Mirkin, *ChemElectroChem*, 2015, **2**, 58–63.

60 S. E. Anderson and H. H. Bau, *Nanotechnology*, 2014, **25**, 245102.

61 K. Hu, D. Wang, M. Zhou, J. H. Bae, Y. Yu, H. Xin and M. V. Mirkin, *Anal. Chem.*, 2019, **91**, 12935–12941.

Chapter 5

MPCVD-grown nanodiamond microelectrodes with oxygen plasma activation for neurochemical applications

Chapter 5 was reprinted from *ACS sensors* 7.10 (**2022**): 3192-3200. Copyright 2022 American Chemical Society.

Abstract

Nanodiamonds (NDs) are a carbon nanomaterial that have a diamond core with heteroatoms and defects at the surface. The large surface area, defect sites, and functional groups on NDs make them a promising material for electrochemical sensing. Previously, we dip coated ND onto carbon-fiber electrodes and found increases in sensitivity, but the coating was sparse. Here, we directly grew thin films of ND on Niobium wires using microwave plasma chemical vapor deposition (MP-CVD) to provide full surface coverage. ND microelectrodes show a reliable performance in neurotransmitter detection with good anti-fouling properties. To improve sensitivity, we oxygen plasma etched ND films to activate the surface and intentionally add defects and oxygen surface functional groups. For fast-scan cyclic voltammetry detection of dopamine, oxygen plasma-etching increases the sensitivity from 21 nA/μM to 90 nA/μM after treatment. Fouling was tested by repeated injections of serotonin or tyramine and both ND and NDO microelectrodes maintain their currents better compared to CFMEs and therefore are more antifouling. A biofouling test in brain slices shows that ND microelectrodes barely have any current drop, while the more hydrophilic NDO microelectrodes decrease more, but still not as much as CFMEs. Overall, grown ND microelectrodes are promising in neurotransmitter detection with excellent fouling resistance, whereas oxygen plasma etching slightly lowers the fouling resistance, but dramatically increases sensitivity.

Keywords: Nanodiamond, FSCV, carbon nanomaterials, neurotransmitter detection, electrochemistry.

5.1 Introduction

Diamond is normally an electrical insulator due to its complete sp3 hybridization and tetrahedral carbon bonding; thus, impurities or dopants are introduced intentionally to increase the conductivity.[1,2] Nanodiamond, or nanocrystalline diamond, however, has a diamond core surrounded by other forms of carbon, such as amorphous carbon and graphite at the surface. NDs are usually more structurally imperfect than bulk sp3 diamonds because they have more defects and surface functional groups, such as phenols, carboxylic groups, and hydroxyl groups.[3–8] The original ND particles were synthesized from detonation of an oxygen-deficient explosive mixture.[9,10] Now, NDs are synthesized by microwave plasma chemical vapor deposition (MPCVD), electrochemical synthesis, or hydrothermal synthesis and these methods can be customized with ND grain sizes ranging from micro- to nano-scale.[11,12] With MPCVD, randomly oriented ND particles are synthesized from a CH_4/Ar plasma with a rapid nucleation reaction and uniformly coated on the substrate.[3,11,13] Thus, there are new ways to coat NDs that could be useful in fields such as electrochemistry.

Carbon-fiber microelectrodes (CFMEs) are the most widely-used neurotransmitter sensor due to their excellent electrochemical performance and good biocompatibility.[14,15] However, CFMEs experience electrochemical fouling, due to electroactive products that polymerize on the surface, and biofouling, due to protein sticking to the electrode.[16,17] Fouling decreases electrode performance by reducing electroactive sites, sensitivity, and electron transfer kinetics.[18–21] As a result, many treatments and electrode materials have been studied to reduce fouling. Boron-doped diamond electrodes, with low surface polar functional groups, have good antifouling properties to aromatic compounds and saturate compounds.[22–25] Swain group systematically studied the grain features of BDD thin films and the material exhibits a wide potential window, abundant density of electronic states and a rapid electron transfer.[26,27] Nanodiamonds (NDs) have drawn attention in electrochemistry because ND electrodes provide fouling resistance, have a high surface area, and high thermal conductivity.[3,11,28–30] NDs also have extensive applications in biomedical imaging, drug delivery, and tissue engineering due to good biocompatibility and rich surface chemistry.[3,4,31] Previously, our group reported ND-coated CFMEs possess good fouling resistance for serotonin detection.[32] However, the CFMEs were not fully covered with NDs CFMEs. Thus, NDs could be grown for full coverage on an electrode to improve electrochemical performance.

Oxygen functional groups on carbon electrodes, including carbonyls, phenolic OH, and carboxylate groups, serve an important role in electrochemical sensing, because they have significant electrochemical effects on adsorption and electron transfer rates.[20,33–35] The anionic oxide groups lead to a negative electrostatic charge on the electrode surface and attract cationic neurotransmitter molecules at physiological pH, and electrocatalytic effect occurs when oxide groups interact with biological redox agents.[33,34] Oxygen plasma etching is a low-cost and simple technique to functionalize carbon electrodes by adding oxide groups.[36,37] Previous studies indicated that oxygen plasma etching breaks carbon bonds and introduces more defects on graphene sheets or graphite.[38–40] Due to the depletion of the plasma strength, the etching process affects primarily on the surface; thus, the bulk structure of carbon materials is not changed.[37,38] Oxygen plasma etching has been applied to carbon nanotube-based electrodes to improve the sensitivity in dopamine measurement; however, it has not been investigated on nanodiamond films.[41,42]

In this study, we developed ND microelectrodes by directly growing a thin film of ND on a piece of Nb wire to fabricate cylinder microelectrodes.[43] The ND is uniformly coated on the metal and the electrodes are sensitive to dopamine with fast-scan cyclic voltammetry (FSCV) detection. To add surface oxygen groups, the ND film was treated with oxygen plasma to favor dopamine adsorption and the resultant electrodes (called NDO) have a 4-fold increase in sensitivity compared to ND electrodes. Characterization of ND microelectrodes shows excellent electrochemical fouling resistance and biofouling resistance in brain tissue, whereas NDO microelectrodes have slightly less anti-fouling response, but are better than CFMEs. Overall, ND microelectrodes have good sensitivity and fouling resistance, and oxygen plasma etching treatment enhances the sensitivity, which makes grown ND and NDO electrodes useful as in vivo neurotransmitter sensors.

5.2 Experimental

5.2.1 Nanodiamond electrode fabrication

A piece of Nb wire (25 um diameter) was soaked in the 5 nm diamond nanoparticle/methanol suspension and sonicated for 3 min to seed. After seeding, nanocrystalline diamond films were grown on the Nb wires with DiamoTek 700-6 Microwave Plasma CVD system (Microwave Enterprises, Morrisville, NC). A mixture of methane, hydrogen, and argon gas was added to the chamber in the proportion of 2.45%, 7.55%, and 90% at a pressure in the range of 40 to 105 Torr. The growth of ND films was ignited in the microwave plasma (6 kW, 2.45 GHz) and the temperature was ramped up to approximately 800 °C under 105 Torr for 5 min. To make microelectrodes, the ND-coated wires are inserted in a glass capillary and sealed well with Epon Resin 828 (Danbury, CT) with only the tip exposed. The length of the exposed tip is approximately 40 μm, and the overall surface area of the electrodes is approximately $0.36*10^4$ μm^2.

5.2.2 Oxygen plasma treatment

The ND-coated Nb wires were etched by oxygen using PVA-TePla Microwave Plasma System 400 H2 (PVA TEPLA, Corona, CA). Wires were placed on a silicon wafer in the plasma generator and etched for 1 min with a 250 sccm oxygen flow rate in room temperature.

5.2.3 Electrochemical methods

Dopamine, serotonin and tyramine were purchased from Sigma-Aldrich (St. Louis, MO). Compounds were dissolved in 0.1 M $HClO_4$ to make 10 mM stock solution, and were diluted with PBS buffer (131.25 mM NaCl, 3.00 mM KCl, 10 mM NaH_2PO_4, 1.2 mM $MgCl_2$, 2.0 mM Na_2SO_4, and 1.2 mM $CaCl_2$) to 1 μM.

The analytes and buffer were injected through a six-port switching valve (Valco Instruments Co. Inc. Houston, TX). The electrodes that were filled with 1 M KCl were inserted into an electrode holder and connected to the headstage (Dagan, Minnesota). Ag/AgCl electrode was used as the reference electrode. Fast-scan cyclic voltammetry data was obtained with HDCV software (University of North Carolina, Chapel Hill). A triangular dopamine waveform was applied (-0.4 V to 1.3 V, 400 V/s scan rate, 10 Hz repetition frequency) to the microelectrode to measure the electrochemical signals of neurotransmitters.

5.2.4 Brain slice experiments

The animal experiments were approved by the Animal Care and Use Committee at the University of Virginia. Male C57BL/6J mice from Jackson Labs (6–8 weeks old) were anesthetized with isoflurane and decapitated immediately. The mouse brain was quickly removed and transferred to an artificial cerebral spinal fluid (aCSF) buffer (0–5 °C) and recovered for 2 minutes. Coronal slices (400-μm thickness) of caudate-putamen region were collected by using a vibratome (LeicaVT1000S, Bannockburn, IL, USA). Slices were transferred into an oxygenated aCSF buffer (95% oxygen, 5% CO_2) and recovered for 30 min at 35 °C in the water bath. Oxygenated aCSF (maintained at 35–37 °C) flowed over the brain slices using a perfusion pump (Watson-Marlow 205U, Wilmington, MA, USA) at a rate of 2 mL/min for the experiments. The electrode was inserted around 75 μm deep in the brain tissue, and a glass capillary contained with dopamine solution was implanted into the tissue close to the working electrode. Five pmol dopamine was applied into the tissue via picospritzer (Picospritzer III-Intracellular microinjection dispense systems, Hollis, NH, USA) every 10 minutes for the exogenous dopamine measurement in the brain. Electrically-stimulated dopamine release was evoked by biphasic stimulation pulses (300 μA, 20 pulses at 60 Hz).[10,44,45] The distance between the electrode and the stimulated electrode was 50–100 μm.

5.2.5 Surface characterization

Scanning electron microscopy (SEM) was performed on a ZEISS Merlin High-Resolution SEM (Oberkochen, Germany) with accelerating voltage of 2 kV. Raman spectroscopy was performed on a Reinshaw InVia Confocal Raman microscope (Renishaw, Hoffman Estates, IL). A 514 nm laser with 50% intensity was used to scan from 100 to 3200 cm^{-1}. The diffraction grating was 1800 lines/mm. X-ray photoelectron spectrometer (Physical Electronics, Chanhassen, MN) was used to characterize elemental composition and bonding information. The pass energy for elemental composition was 224 eV, and 55 eV for electronic state information.

5.3 Results and discussion

5.3.1 Surface characterization

Nanodiamonds were synthesized on 25 μm diameter Nb wires. First, Nb wires were soaked in a 5 nm diamond nanoparticle/methanol suspension for 3 min to seed the wire. Figure 1A shows the Nb wire has a clean and uneven surface, and Figure 1B shows the seeded nanodiamond particles are hardly seen on the metal wire after pretreatment. ND coatings were then grown using MP-CVD and nanocrystalline diamonds agglomerated on the wire to make a uniform, thin coating (Fig. 1C).[3,46] Fig. 1D shows the diameter of the particles is approximately 50 nm. To modify the surface of the ND film, oxygen plasma etching was performed with a 250 sccm oxygen flow for 1 min. The etching protocol is based on our previous study etching CNT yarn microelectrodes, which indicated this etching process gave better electrochemical performance without any morphology change on the carbon surface.[47] Figure 1E and 1F show the morphology of oxygen plasma-etched ND (NDO) is the same as the pristine ND.

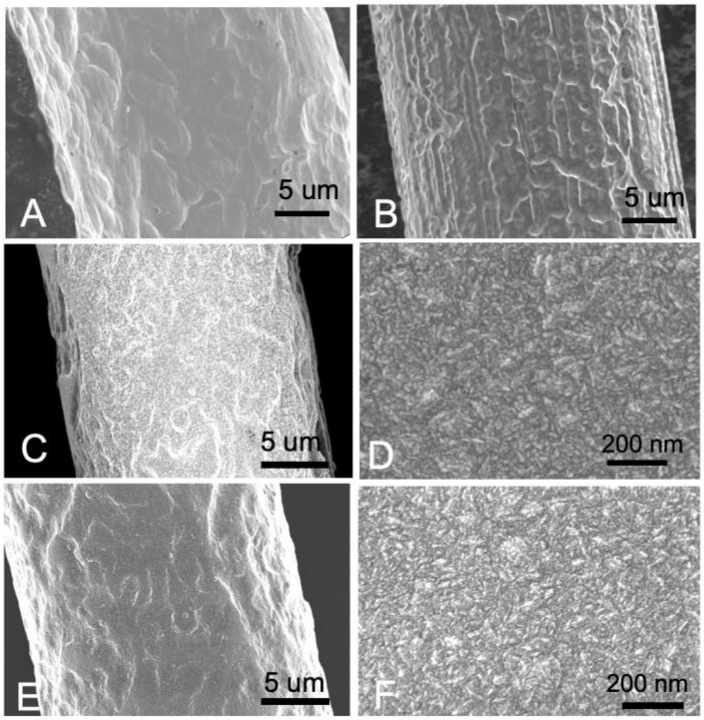

Figure 1. SEM images of (**A**) 25 μm Nb bare wire, (**B**) Nb wire after seeding for 3 min, (**C**) Nanodiamond (ND) film on the Nb wire, (**D**) Zoomed in ND, **(E)** Oxygen plasma etched ND film (NDO), **(F)** Zoomed in NDO.

To better characterize the surface chemistry, a thin film of ND and NDO was uniformly deposited on a silicon wafer with a flat surface. XPS and Raman spectra were collected to study the elemental and bonding information. Figure 2A and 2B shows the full XPS spectrum and specific C1s peak of ND and NDO. C1s peaks were further deconvoluted into sp3 C (284.3 eV), sp2 C (282.9 eV), and C-O (285.8 eV) bonds. Pristine ND film has an abundant amount of C (approximately 86%), the majority of which is sp3 C due to its diamond structure. ND has defects on the surface so a small amount of sp2 C and C-O bond is present in the deconvoluted C 1s peak.[37,46] Pristine ND has a low oxygen content (approximately 7.9%) and a negligible amount of nitrogen (< 1%). The small peaks at around 100 eV and 150 eV belong to Si 2s and Si 2p, which come from the silicon wafer because the ND coverage on a substrate is approximately 90%, which is shown in the previous work.[48] After oxygen plasma etching treatment, the content of oxygen increases to 17.9% and the overall C/O ratio decreases from approximately 12.1 to 4.4. The content of C-O bond increases in the C 1s spectra and the amount of sp2 C also increases, because of the presence of argon in the plasma during etching.[3,11,49] Table 1 gives the detailed elemental percentages.

Raman spectra of ND and NDO were collected to study the defects on the surface (Figure 2B). Both ND and NDO show a distinct disordered graphite band (~1360 cm^{-1}) and a graphite band (~ 1580 cm^{-1}) on the spectrum, and both peaks are enlarged by the 633 nm laser and hide the diamond peak (~ 1330 cm^{-1}).[1,49] The shoulders at the lower Raman shift represent the disordered sp3 C because of the distorted lattice of nanocrystalline diamonds.[50] The spectra of ND and NDO are highly similar, indicating that oxygen plasma etching does not cause major surface structural change, but a slightly increased amount of defect sites. As Table 1 lists, the D/G ratio of nanodiamond film increases from 1.07 to 1.15 after the treatment.

To test the hydrophobicity of ND and NDO, contact angle measurements were performed on a flat ND or NDO-coated Si wafer by dropping a water droplet on the substrate (Figure 2C). The pristine ND film has a contact angle of 114.5°, which indicates that ND has a hydrophobic surface due to the diamond structure.[51,52] The contact angle decreases to 86.5° after the oxygen plasma treatment, indicating a slightly hydrophilic surface. The hydrophobicity change is due to the increasing amount of sp2 C and oxygen that makes the surface more wettable.[37,41,53] Although the surface treatment makes NDO become hydrophilic, it is still more hydrophobic than normal graphitic carbon. In Figure 3, the contact angle of the droplet on a commercially-available screen-printed electrode is 78.2°.[32] Overall, oxygen plasma treatment turns nanocrystalline diamond films into hydrophilic surface, but it is not as wettable as graphitic carbon.

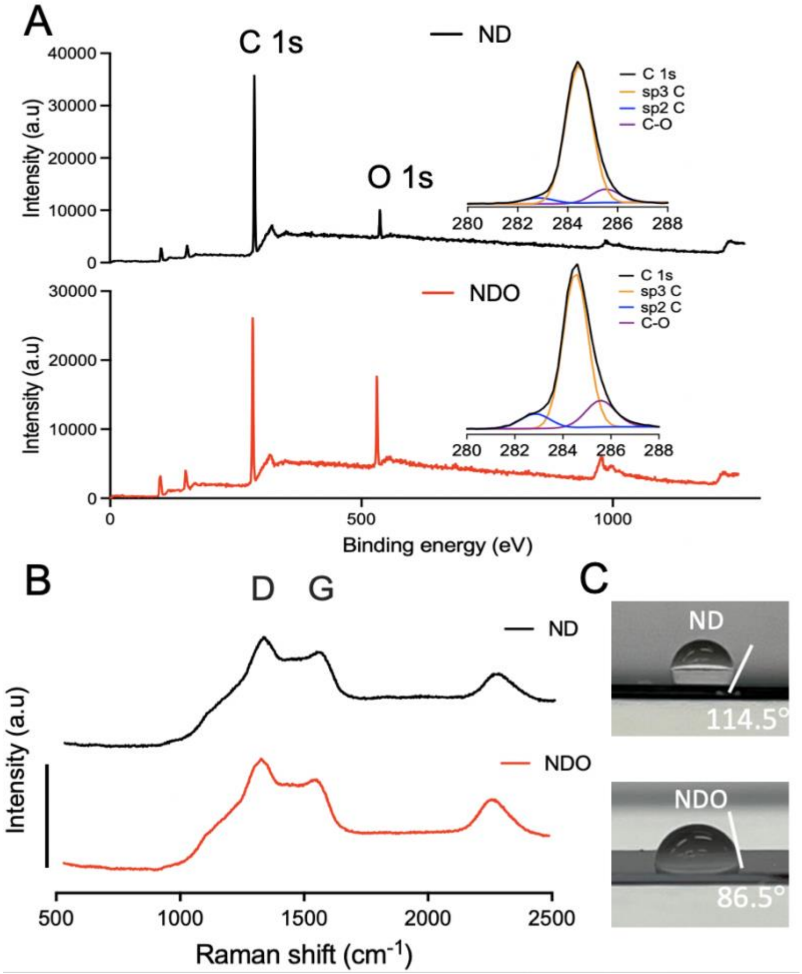

Figure 2. Surface characterization. (**A**) X-ray photoelectron spectra of ND (black) and NDO (red). The elemental composition information was obtained with the binding energy range from 0 to 1300 eV. C1s peaks were deconvoluted into sp3 C (284.3 eV), sp2 C (282.9 eV), and C-O (285.8 eV) bonds. (**B**) Raman spectra of ND (black) and NDO (red). (**C**) Hydrophobicity test of ND (top) and NDO (bottom).

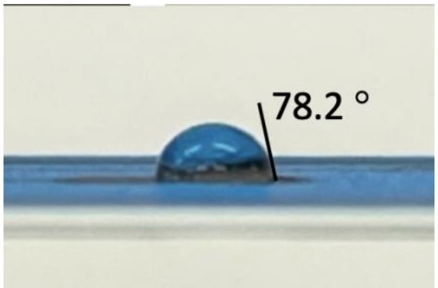

Figure 3. The contact angle of a water droplet on a screen-printed carbon electrode.

Table 1. Surface characterization of ND and NDO, including XPS, Raman and contact angle measurement.

	C%	O%	C/O	Sp3 C%	Sp2 C%	C-O%	D/G	Contact angle (°)
ND	86 ± 35	7.9 ± 0.3	12.1 ± 0.6	83.9	11.2	4.9	1.07	114.5
NDO	75 ± 1	17.9 ± 0.9	4.4 ± 0.2	74.8	16.9	9.1	1.15	86.5

5.3.2 Oxygen plasma etching enhances sensitivity of dopamine detection

ND and NDO-coated niobium wires were fabricated into electrodes with similar surface areas to compare the electrochemical performance. Cyclic voltammetry and electrochemical impedance spectroscopy were performed in 10 mM $K_3Fe(CN)_6$ as shown in Figure 4. The cyclic voltammograms of $Fe(CN)_6^{3-/4-}$ redox couple have similar shapes for both ND and NDO (Figure S3A). The S-shaped voltammograms are typically evidence for microelectrodes where steady-state component dominates Faradaic current.[33,54] However, the CV of NDO shows a higher current due to a higher content of oxygen on the surface; thus, there are more interactions with the inner-sphere redox couple $Fe(CN)_6$.$^{3-/4-}$ Compared with ND, oxygen plasma treatment also slightly decreases ΔE_p indicating a faster electron transfer rate due to the increasing amount of sp2 C on the surface.[1,55,56] The EIS tests were performed using the equivalent circuit as shown in Figure 4B to fit the impedance plots of ND and NDO electrodes (Table 2). The x-axis is manually shifted to compensate the solution resistance. NDO has a slightly smaller charge transfer resistance than ND, and it also has a smaller semicircle in the EIS Nyquist plot that demonstrating a slightly reduced impedance after treatment (Figure 4B).[30,57,58] The Nyquist plots of both electrodes have only one semicircle and fit a Randles Cell model with semi-infinite diffusion, where solution resistance is the only other cell impedance.[59] The spectra indicate a dense and uniform coating of both ND and NDO, and the electric double-layer capacitance is coming from the ND film only without any metal exposed.[58,60] The capacitance of NDO is slightly smaller than ND, which could be attributed to the etching process slightly smoothing and cleaning the surface.

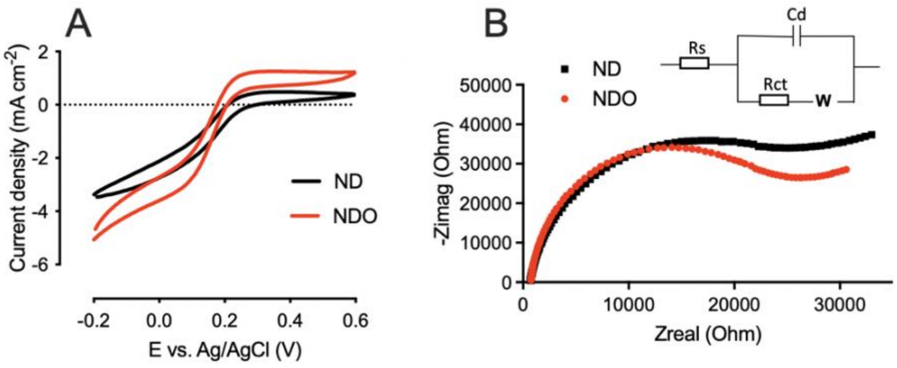

Figure 4. Electrochemical characterization of ND (black) and NDO (red). (**A**) CV of 10 mM $K_3Fe(CN)_6$ with scan rate of 100 mV/s. (**B**) EIS Nyquist plot with equivalent circuit, where R_s is the solution resistance, R_{ct} is the charge transfer resistance, W is the Warburg impedance, and C_d is the double layer capacitance

Table 2. the EIS fitting results of ND and NDO electrodes (with approximately 2 cm exposed).

	Rct (kΩ)	Rs (kΩ)	Cd (pF)	W (Ω*s$^{-0.5}$)
ND	40.5	3.4	310.6	238.8
NDO	38.7	2.9	247.6	261.9

R_s is the solution resistance, R_{ct} is the charge transfer resistance, W is the Warburg impedance, and C_d is the double layer capacitance

Then ND and NDO-coated wires were fabricated into microelectrodes and the responses of 1 μM dopamine was characterized using FSCV because it is the standard technique to detect neurotransmitters in real-time. Since the surface area of microelectrodes are slightly different, two electrodes with similar background currents were intentionally chosen. Figure 5A shows the electrochemical signal comparison at ND and NDO microelectrodes with background currents of approximately 5000 nA. However, the shape of the backgrounds is different, as NDO microelectrodes have an additional wave at around 0 V due to the electroactive phenolic groups on the surface.[61] Figure 5B shows the background-subtracted oxidation current versus time plot during 15 s flow cell injection, where dopamine was injected at 5 s and then PBS buffer at 10 s. Both electrodes show a similar dynamic response with a slightly slow temporal response due to adsorption.[14] However, the NDO microelectrode has about a 4-fold increase in Faradaic current compared to the pristine ND microelectrode. The rise time of 1 μM dopamine at ND and NDO microelectrodes were calculated by determining the time difference from 10% to 90% of the maximum current. The rise time is 1.2 s for ND and 1.4 s for NDO microelectrodes, which indicates that the more adsorption introduced by oxide groups affects the time response very little. Figure 5C compares the background-subtracted CVs of 1 μM dopamine. Both electrodes show typical CV shapes of dopamine with the oxidation peak around 0.6 V and reduction at -0.2 V.[62] The ND microelectrode has an oxidation peak current of about 41 nA, whereas NDO has about 151 nA. Since they have approximately the same electrode surface area (Figure 5A), the dramatic oxidation current increase is due to the surface chemistry of the NDO microelectrode, as increasing the number of anionic oxide groups attracts more cationic dopamine molecules by electrostatic interactions. The ΔE_p of NDO (0.83 V) is also slightly smaller than ND (0.86V) indicating a slightly faster electron transfer rate on NDO because the NDO has a small increase in of sp2 C content.

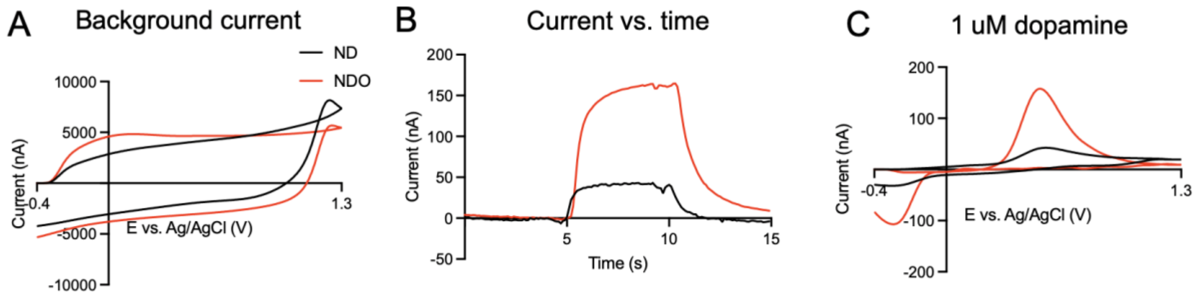

Figure 5. Comparison of the FSCV response to 1 μM dopamine at ND (black) and NDO (red). (**A**) background charging current in PBS buffer. (**B**) Oxidation current vs time traces during a 15 s flow cell injection (dopamine was injected at 5 s and rinsed by PBS at 10 s). (**C**) background subtracted CVs of 1 μM dopamine at ND and NDO using dopamine waveform (-0.4 V to 1.3 V, scan rate 400 V/s, 10 Hz).

To characterize the analytical performance of ND and NDO, we tested the effects of varying FSCV scan rate from 50 V/s to 1000 V/s. Both ND and NDO microelectrodes show a linear relationship with scan rate (R^2 = 0.99 for both), indicating an adsorption-controlled process at the electrode surface for dopamine detection (Figure 6A). Figure 6B plots the oxidation peak currents with increasing dopamine concentration up to 100 μM. Both electrodes have a linear response of oxidation peak current with concentration in the range of 0.1 μM to 10 μM (Figure 6C), and currents increase less at higher concentrations due to the saturation of the carbon electrode surface. The slope for NDO in the linear range (slope = 90) is about 4-fold larger than ND (slope = 21), indicating NDO has a much higher sensitivity to dopamine because of the increasing number of oxide groups that provide more sites for dopamine adsorption. To test the stability of ND and NDO coating, the FSCV waveform was applied to the electrodes continuously in the flow cell and dopamine response measured every 30 min up to 4 hours. Figure 6D shows that both ND and NDO have stable signals for hours without significant current drop, indicating a reliable performance.

ND and NDO microelectrodes are also capable of measuring other neurochemicals, including serotonin, norepinephrine, DOPAC, and ascorbic acid (Figure 7). Both electrodes have typical CV responses for detecting these compounds with good sensitivity and selectivity.

Similar to dopamine, NDO microelectrodes have approximately 3- to 4-fold current increase for other neurochemicals compared with ND microelectrodes. The oxidation peaks for ascorbic acid is at a lower potential for ascorbic acid at ND or NDO electrodes and thus dopamine is easily distinguished from ascorbic acid. In addition, the oxidation peaks of NDO microelectrodes occur at a lower potential, indicating faster electron transfer kinetics due to the treatment.

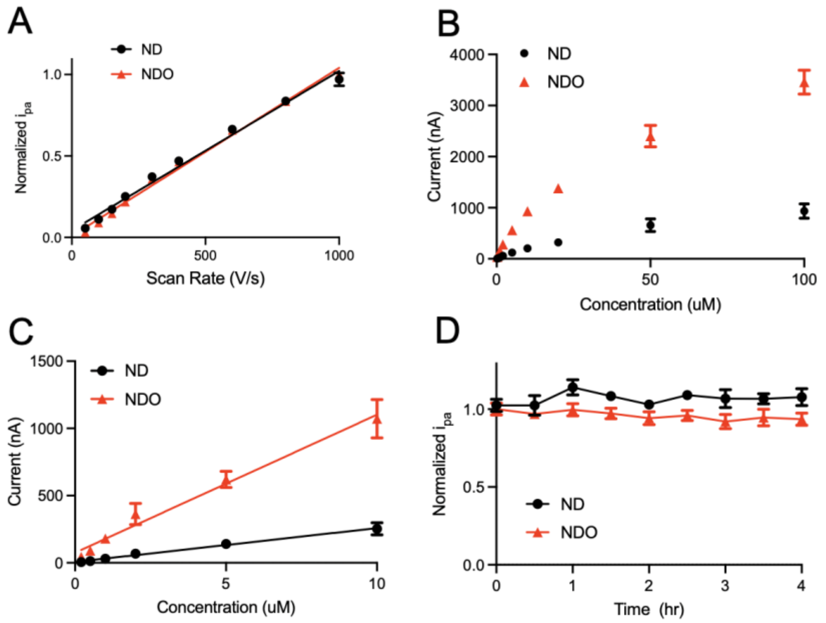

Figure 6. FSCV study of ND (black) and NDO (red) in dopamine solution. (**A**) Current of 1 μM dopamine is linear with scan rate ranging from 50 V/s to 1000 V/s for both ND and NDO. R^2 = 0.99 for both ND and NDO. (**B**) The trends of dopamine signals with dopamine solution ranging from 1 to 100 μM. (**C**) The linear range of dopamine signal with concentration is up to 10 μM. R^2 = 0.88 for ND and R^2 = 0.90 for NDO. (**D**) Stability test. Dopamine signals were collected every 30 min for up to 4 hours. (Error bars are SEM with n = 4)

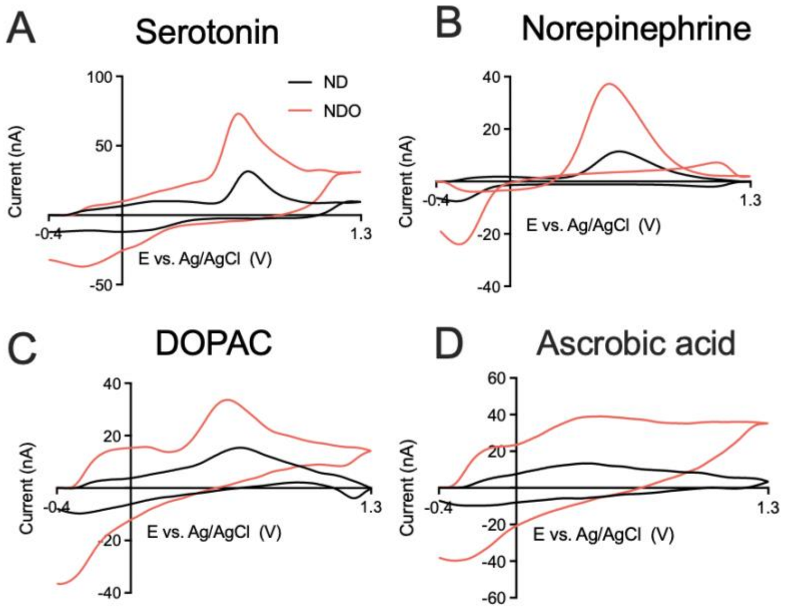

Figure 7. CV comparison of ND and NDO in (A) 1 μM serotonin, (B) 1 μM norepinephrine, (C) 20 μM DOPAC, and (D) 20 μM ascorbic acid.

5.3.3 Electrochemical fouling test

Electrode fouling is a severe problem that affects electrode performance in a negative way, reducing the electroactive area and decreasing the electron transfer kinetics by blocking the surface. Here, we studied two types of electrode fouling during neurotransmitter detection: chemical fouling caused by neurotransmitter polymerization, and biofouling caused by biological macromolecules. Results are compared to carbon-fiber microelectrodes, the most widely-used neurotransmitter electrode.

To study the electrochemical fouling, 25 cycles of injections were repeated, with a 5 s injection every 30 s. First, we studied serotonin, a major biogenic amine neurotransmitter known to foul electrodes,[32,63] by repeatedly measuring injections of 1 μM serotonin in a flow injection analysis system. FSCV was performed with Jackson waveform (1000 V/s scan rate, 0.2 V holding potential ramped up to 1.0 V, then back to -0.1 V, and finally 0.2 V) to provide a good selectivity for serotonin detection.[16,64] Because the surface area of electrodes are different, all CVs are normalized to first injection, to clearly show the current changes during electrode fouling. Figures 8A-C show CVs of 1 μM serotonin from the 1st and 25th cycle at different electrodes with the Jackson waveform. All three electrodes have oxidation peaks of serotonin appearing at 0.8 V and a reduction peak at 0 V. The oxidation peak slightly shifted to the right at the 25th cycle indicating a slower electron transfer result from the polymerized serotonin blocking the surface. Figure 8D shows normalized serotonin oxidation peak currents obtained from CF, ND, and NDO microelectrodes after 25 injections. At CFMEs, the oxidation peak decreased to half (54%) because the polymerized serotonin partially blocked the electrode surface by forming an impermeable layer.[65] ND and NDO microelectrodes show significantly less current drop than CFMEs; the current is approximately 90% of the initial current for ND microelectrodes and 85% for NDO microelectrodes (One-way ANOVA with Tukey's multiple comparison test, $p < 0.01$ for ND, $p < 0.05$ for NDO, $n = 4$ electrodes). Considering serotonin fouls more at a higher concentration, 10 μM serotonin was also used to study the electrode fouling (Figure S6). There is more current decrease at all three microelectrodes but the results are similar in that ND microelectrodes have the least fouling, whereas CFMEs have the most. Decreased serotonin fouling at ND microelectrodes is similar to studies on boron-doped diamond (BDD) that have good fouling resistance due to the fewer adsorption sites for surface-active molecules.[66,67] ND microelectrodes have fewer adsorption sites for the fouling agent on the surface; as a result, the polymer layer attaches less to the electrode.[68] With oxygen plasma etching, more oxide groups were added to the surface that improve the adsorption of surface-active species; thus, the Faradaic current increases but the surface is slightly more susceptible to fouling. However, the reduction in fouling resistance is negligible, only 5% more than ND, and the currents are still high after fouling.

Next, we studied fouling in 1 μM tyramine solution, which is an insect phenolamine neurotransmitters that also fouls the electrode by polymerization.[69] With the dopamine waveform, tyramine has a primary oxidation peak at 0.85 V, a secondary peak at 0.5 V on the forward scan, and a reduction peak at -0.2 V on the reverse scan. The secondary peak is actually easier to observe in the CVs at ND and NDO electrodes, which aids in analyte identification. The secondary peak appears slightly later in time than the primary peak and grows with time;[70] the CV signals shown in Figure 8E-G were obtained at around 6s, when the secondary peaks is just beginning to appear. Similar to the result for serotonin, ND and NDO microelectrodes display high anti-fouling properties and the primary currents decrease much less for ND microelectrodes than for CFMEs in Figure 8H. After 25 injections of tyramine, there is 65% of the primary current remaining for CFs, 92% for ND, and 91% for NDO.

Overall, the electrochemical fouling test illustrates that ND and NDO microelectrodes have much higher fouling resistance than CFMEs due to the diamond structure of the nanomaterial. Oxygen plasma etching slightly decreases the anti-fouling performance, but it is negligible compared with the large signal increase introduced by the oxide groups. NDO microelectrodes also have slightly better resistance to tyramine fouling compared with serotonin.

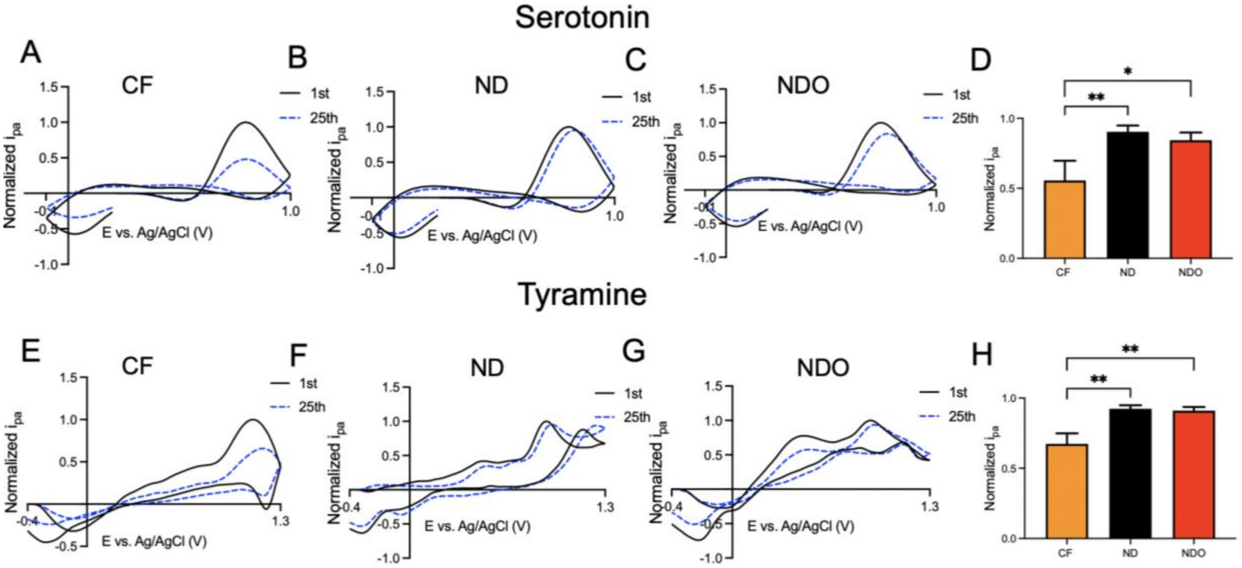

Figure 8. Fouling study of CF, ND and NDO in 1 μM serotonin and 1 μM tyramine with FSCV. Jackson waveform (1000 V/s scan rate, 0.2 V holding potential ramped up to 1.0 V, then back to -0.1 V, and finally 0.2 V) was used for serotonin and dopamine waveform (-0.4 V to 1.3 V, 400 V/s scan rate, 10 Hz repetition frequency) was used for tyramine. CVs of 1st and 25th injection are compared. **(A)** serotonin at CFMEs, **(B)** serotonin at ND microelectrodes, **(C)** serotonin at NDO microelectrodes, **(D)** Normalized current comparison of serotonin after 25 injections (n=5). **(E)** tyramine at CFMEs, **(F)** tyramine at ND microelectrodes, **(G)** tyramine at NDO microelectrodes, **(H)** Normalized current comparison of tyramine after 25 continuous injections. $^*p < 0.05$, $^{**}p < 0.01$. Error bars are SEM with n = 5.

5.3.4 ND and NDO microelectrodes are more biofouling-resisted than CF

Next, we performed a biofouling test by inserting the electrodes in a mouse brain slice and continuously applying the FSCV waveform for 1 hour because the biofouling on CFMEs is similar to 2 h implantation in the brain.[19,45,71–73] The CV signals obtained in the flow cell were compared before and after the insertion to assess the anti-fouling properties of CF, ND, and NDO microelectrodes in Figure 9. The result shows that CFMEs have a dramatic current decrease after the 1 hour in tissue because protein macromolecules adhere to the carbon surface. Figures 9A, B, and C show CV comparison before and after insertion into the tissue. Fouling varied with the type of electrode (One-way ANOVA with Tukey's multiple comparison test, $p < 0.05$, n = 4 electrodes). CFMEs have the most current decrease (approximately 71%

current drop), and ND microelectrodes have the least (27% current drop), indicating a similar result as mentioned in the electrochemical fouling test. There is no significant difference between NDO and CFMEs (One-way ANOVA with Tukey's multiple comparisons test, $p > 0.05$, $n = 4$ electrodes), but the current drops less at NDO microelectrodes (56% drop).

ND with a hydrophobic surface has better biofouling resistance, and there is a significant difference from CFMEs (Figure 6D). Often proteins stick to carbon surfaces due to hydrophobic effects but here the more hydrophilic surfaces have more fouling, indicating charged or polar amino acids may cause more fouling to those surfaces. ND microelectrodes also have less adsorption sites for macromolecules to bind. NDO microelectrodes with more oxide groups have less bio-fouling resistance than ND because of the more hydrophilic nature of the surface. Thus, ND microelectrodes have the best fouling resistance among three types of electrodes.[68,72] Although there is no significant difference in anti-fouling properties between CF and NDO microelectrodes, the current obtained from NDO decreased to half, whereas CFMEs decreased more and have about 30% current remaining after the brain slice insertion. In addition, considering the dramatic current increase (3- to 4-fold) after the surface treatment, NDO microelectrodes still maintain a higher sensitivity after exposure to tissue. As a result, ND microelectrodes display excellent anti-biofouling response, and NDO microelectrodes have a reliable performance even with the negative influence of biofouling. Considering the dramatic sensitivity increase introduced by oxygen plasma etching, the electrode fouling on NDO microelectrodes is minimal.

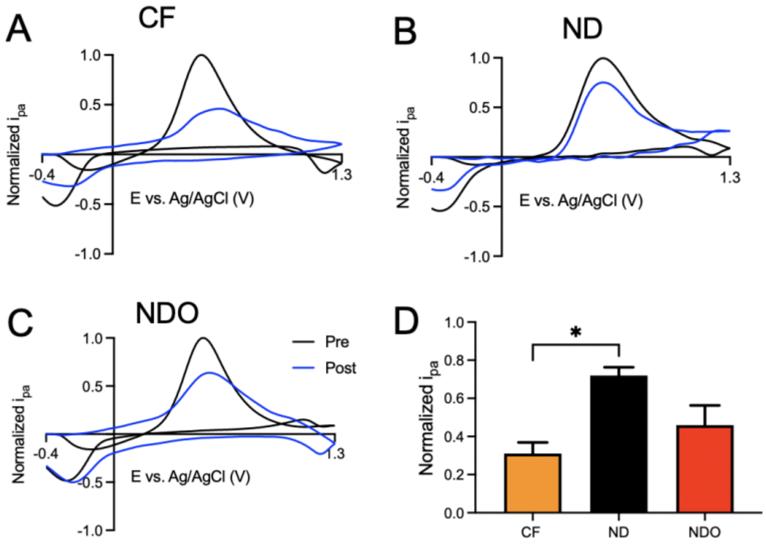

Figure 9. Biofouling study of CF, ND and NDO. The electrodes were inserted in mice brain slices applying voltage waveform for 1 hour. The normalized CVs of 1 μM dopamine were collected before and after the insertion. (**A, B, C**) Dopamine CV comparisons of (**A**) CF, (**B**) ND, and (**C**) NDO before and after insertion. **(D**) Normalized peak current ratio (after tissue/before tissue implantation). *$p < 0.05$. Error bars are SEM with n = 5.

5.3.5 Dopamine detection in mouse brain slices

The ND microelectrodes and NDO microelectrodes were both tested in mouse brain slices to monitor dopamine. The electrode was implanted in the caudate-putamen region and 5 pmol dopamine was applied into the brain tissue nearby the working electrode via a picospritzer. Figure 10A and 11 show the example color plot of NDO and ND microelectrode detection of dopamine detection. The characteristic CV shapes above the color plots indicating dopamine is detected. Both ND and NDO microelectrodes showed good responses on exogenous dopamine proving the ND-coated microelectrode is compatible for dopamine detection in the brain tissue. Figure 10B displays electrically-stimulated dopamine release in a brain slice using NDO microelectrode. The CV on the top shows the CV of dopamine and the i-t curve shows that the transient DA only lasts few seconds. The wider oxidation peak is due to the ionic changes after the stimulation, and the CV shape is similar to others for dopamine detection in brain slices.[74–76] There is no evidence of ascorbic acid detection. In addition, the amplitude of the stimulated dopamine signal on NDO microelectrodes (around 15 nA) is much higher than previous carbon-fiber microelectrodes and 3D-printed microelectrodes.[45,77] Thus, the grown NDO microelectrode is suitable for dopamine detection in brain slices with higher sensitivity and will be useful for biological detection.

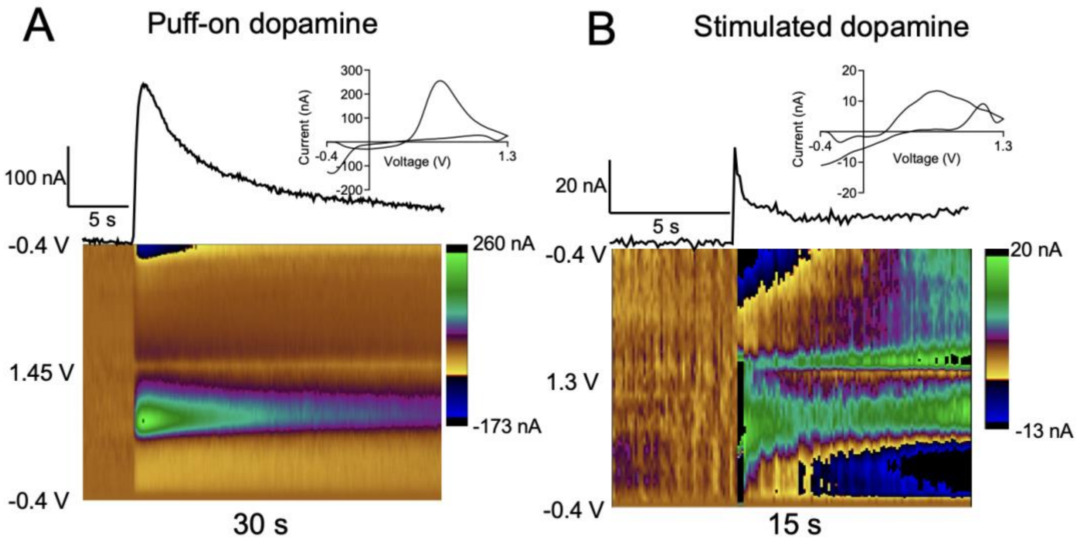

Figure 10. Detection of dopamine in brain slices using NDO microelectrode. (**A**) Example color plot of dopamine detection, 5 pmol DA was applied in the caudate-putamen region. The i-t curve and cyclic voltammogram of puff-on DA are listed above the color plot. **(B)** Electrically-stimulated dopamine release (biphasic, 300 μA, 20 pulses at 60 Hz) in the caudate-putamen region. Top: i-t curve and cyclic voltammogram of DA. Bottom: color plot.

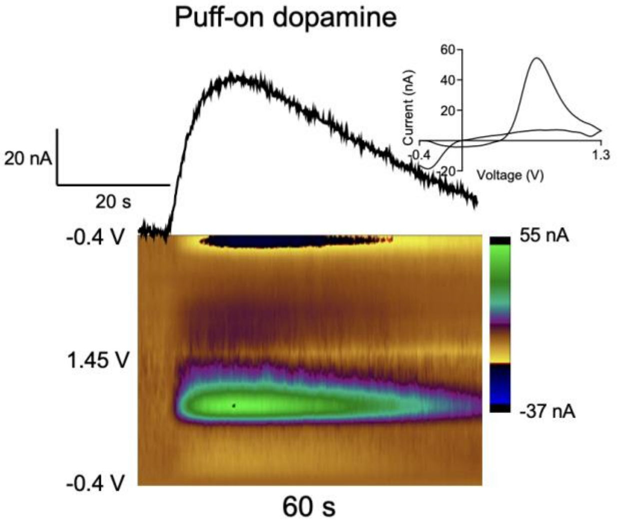

Figure 11, Detection of dopamine in brain slices using ND microelectrode detection. Five pmol dopamine was injected into the brain slice via picospritzer. Top: i-t curve and cyclic voltammogram of dopamine. Bottom: Color plot.

5.4 Conclusions

In summary, we developed a new electrochemical sensor by coating a thin and uniform ND film on Nb metal wires with MPCVD. In this work, ND microelectrodes show a reliable performance for neurotransmitter detection with good fouling resistance, which will enable long-term measurements without much current drop. Then, the electrochemical performance of ND microelectrodes was improved by oxygen plasma etching that adds oxygen functional groups and defects to the surface. NDO microelectrodes have faster electron transfer and the about 4-fold current increase in dopamine. ND and NDO electrodes have less fouling for serotonin and tyramine detection. NDO electrodes were used to detect dopamine in mice brain slices. Overall, ND microelectrodes are promising and reliable electrochemical sensors in neurotransmitter detection with excellent antifouling properties, whereas NDO microelectrodes have greater prospects in bioanalytical sensing due to the largely enhanced sensitivity and neglectable reduced fouling resistance.

Acknowledgements

The authors declare no financial conflicts. This study is supported by NIH R01EB026497 and R01NS125663. Nanodiamond film growth, oxygen plasma etching, SEM, and Raman spectroscopy were conducted at Nanophase Materials Science, Oak Ridge National Laboratory (CNMS, ORNL) under user agreement CNMS-2022-A-01117. XPS spectroscopy was conducted at Nanoscale Material Characterization Facility, University of Virginia (NMCF, UVA).

5.5 References

(1) McCreery, R. L. Advanced Carbon Electrode Materials for Molecular Electrochemistry. *Chem. Rev.* **2008**, *108* (7), 2646–2687. https://doi.org/10.1021/cr068076m.

(2) Bauer, J.; Schroer, A.; Schwaiger, R.; Kraft, O. Approaching Theoretical Strength in Glassy Carbon Nanolattices. *Nat. Mater.* **2016**, *15* (4), 438–443. https://doi.org/10.1038/nmat4561.

(3) Schrand, A. M.; Hens, S. A. C.; Shenderova, O. A. Nanodiamond Particles: Properties and Perspectives for Bioapplications. *Crit. Rev. Solid State Mater. Sci.* **2009**, *34* (1–2), 18–74. https://doi.org/10.1080/10408430902831987.

(4) Neugart, F.; Zappe, A.; Jelezko, F.; Tietz, C.; Boudou, J. P.; Krueger, A.; Wrachtrup, J. Dynamics of Diamond Nanoparticles in Solution and Cells. *Nano Lett.* **2007**, *7* (12), 3588–3591. https://doi.org/10.1021/nl0716303.

(5) Nunn, N.; Torelli, M.; McGuire, G.; Shenderova, O. Nanodiamond: A High Impact Nanomaterial. *Curr. Opin. Solid State Mater. Sci.* **2017**, *21* (1), 1–9. https://doi.org/10.1016/j.cossms.2016.06.008.

(6) Zhang, Y.; Rhee, K. Y.; Hui, D.; Park, S. J. A Critical Review of Nanodiamond Based Nanocomposites: Synthesis, Properties and Applications. *Compos. Part B Eng.* **2018**, *143* (January), 19–27. https://doi.org/10.1016/j.compositesb.2018.01.028.

(7) Enoki, T.; Takai, K.; Osipov, V.; Baidakova, M.; Vul, A. Nanographene and Nanodiamond; New Members in the Nanocarbon Family. *Chem. - An Asian J.* **2009**, *4* (6), 796–804. https://doi.org/10.1002/asia.200800485.

(8) Mochalin, V.; Osswald, S.; Gogotsi, Y. Contribution of Functional Groups to the Raman Spectrum of Nanodiamond Powders. *Chem. Mater.* **2009**, *128*, 273–279. https://doi.org/10.1021/cm802057q.

(9) Danilenko, V. V. On the History of the Discovery of Nanodiamond Synthesis. *Phys. Solid State* **2004**, *46* (4), 595–599. https://doi.org/10.1134/1.1711431.

(10) Cao, Q.; Puthongkham, P.; Venton, B. J. Review: New Insights into Optimizing Chemical and 3D Surface Structures of Carbon Electrodes for Neurotransmitter Detection. *Anal. Methods* **2019**, *11* (3), 247–261. https://doi.org/10.1039/c8ay02472c.

(11) Butler, J. E.; Sumant, A. V. The CVD of Nanodiamond Materials. *Chem. Vap. Depos.* **2008**, *14* (7-8 SPEC. ISS.), 145–160. https://doi.org/10.1002/cvde.200700037.

(12) Baidakova, M.; Vul', A. New Prospects and Frontiers of Nanodiamond Clusters. *J. Phys. D. Appl. Phys.* **2007**, *40* (20), 6300–6311. https://doi.org/10.1088/0022-3727/40/20/S14.

(13) Manawi, Y. M.; Ihsanullah; Samara, A.; Al-Ansari, T.; Atieh, M. A. A Review of Carbon Nanomaterials' Synthesis via the Chemical Vapor Deposition (CVD) Method. *Materials (Basel).* **2018**, *11* (5). https://doi.org/10.3390/ma11050822.

(14) Bath, B. D.; Michael, D. J.; Trafton, B. J.; Joseph, J. D.; Runnels, P. L.; Wightman, R. M. Subsecond Adsorption and Desorption of Dopamine at Carbon-Fiber Microelectrodes. *Anal. Chem.* **2000**, *72* (24), 5994–6002. https://doi.org/10.1021/ac000849y.

(15) Huffman, M. L.; Venton, B. J. Carbon-Fiber Microelectrodes for in Vivo Applications. *Analyst* **2009**, *134* (1), 18–24. https://doi.org/10.1039/b807563h.

(16) Dunham, K. E.; Venton, B. J. Improving Serotonin Fast-Scan Cyclic Voltammetry Detection: New Waveforms to Reduce Electrode Fouling. *Analyst* **2020**, *145* (22), 7437–7446. https://doi.org/10.1039/d0an01406k.

(17) Takmakov, P.; Zachek, M. K.; Keithley, R. B.; Walsh, P. L.; Donley, C.; McCarty, G. S.; Wightman, R. M. Carbon Microelectrodes with a Renewable Surface. *Anal. Chem.* **2010**, *82* (5), 2020–2028. https://doi.org/10.1021/ac902753x.

(18) Geise, R. J.; Adams, J. M.; Barone, N. J.; Yacynych, A. M. Electropolymerized Films to Prevent Interferences and Electrode Fouling in Biosensors. *Biosens. Bioelectron.* **1991**, *6* (2), 151–160. https://doi.org/10.1016/0956-5663(91)87039-E.

(19) Weese, M. E.; Krevh, R. A.; Li, Y.; Alvarez, N. T.; Ross, A. E. Defect Sites Modulate Fouling Resistance on Carbon-Nanotube Fiber Electrodes. *ACS Sensors* **2019**, *4* (4). https://doi.org/10.1021/acssensors.9b00161.

(20) Kawde, A. N.; Morsy, M. A.; Odewunmi, N.; Mahfouz, W. From Electrode Surface Fouling to Sensitive Electroanalytical Determination of Phenols. *Electroanalysis* **2013**, *25* (6), 1547–1555. https://doi.org/10.1002/elan.201300101.

(21) Manica, D. P.; Mitsumori, Y.; Ewing, A. G. Characterization of Electrode Fouling and Surface Regeneration for a Platinum Electrode on an Electrophoresis Microchip. *Anal. Chem.* **2003**, *75* (17), 4572–4577. https://doi.org/10.1021/ac034235f.

(22) Rusinek, C. A.; Guo, Y.; Rechenberg, R.; Becker, M. F.; Purcell, E.; Verber, M.; McKinney, C.; Li, W. All-Diamond Microfiber Electrodes for Neurochemical Analysis. *J. Electrochem. Soc.* **2018**, *165* (12). https://doi.org/10.1149/2.0141812jes.

(23) Bennet, K. E.; Tomshine, J. R.; Min, H. K.; Manciu, F. S.; Marsh, M. P.; Paek, S. B.; Settell, M. L.; Nicolai, E. N.; Blaha, C. D.; Kouzani, A. Z.; et al. A Diamond-Based Electrode for Detection of Neurochemicals in the Human Brain. *Front. Hum. Neurosci.* **2016**, *10* (MAR2016). https://doi.org/10.3389/fnhum.2016.00102.

(24) Fan, B.; Rusinek, C. A.; Thompson, C. H.; Setien, M.; Guo, Y.; Rechenberg, R.; Gong, Y.; Weber, A. J.; Becker, M. F.; Purcell, E.; et al. Flexible, Diamond-Based Microelectrodes Fabricated Using the Diamond Growth Side for Neural Sensing. *Microsystems Nanoeng.* **2020**, *6* (1), 1–12. https://doi.org/10.1038/s41378-020-0155-1.

(25) Zeng, H.; Konicek, A. R.; Moldovan, N.; Mangolini, F.; Jacobs, T.; Wylie, I.; Arumugam, P. U.; Siddiqui, S.; Carpick, R. W.; Carlisle, J. A. Boron-Doped Ultrananocrystalline Diamond Synthesized with an H-Rich/Ar-Lean Gas System. *Carbon N. Y.* **2015**, *84* (1), 103–117. https://doi.org/10.1016/j.carbon.2014.11.057.

(26) Show, Y.; Witek, M. A.; Sonthalia, P.; Swain, G. M. Characterization and Electrochemical Responsiveness of Boron-Doped Nanocrystalline Diamond Thin-Film Electrodes. *Chem. Mater.* **2003**, *15* (4), 879–888. https://doi.org/10.1021/cm020927t.

(27) Wang, S.; Swope, V. M.; Butler, J. E.; Feygelson, T.; Swain, G. M. The Structural and Electrochemical Properties of Boron-Doped Nanocrystalline Diamond Thin-Film Electrodes Grown from Ar-Rich and H2-Rich Source Gases. *Diam. Relat. Mater.* **2009**, *18* (4), 669–677. https://doi.org/https://doi.org/10.1016/j.diamond.2008.11.033.

(28) Li, H. Improvement of Voltammetric Detection of Sulfanilamide with a Nanodiamond−Modified Glassy Carbon Electrode. *Int. J. Electrochem. Sci.* **2019**, *14*, 7858–7870. https://doi.org/10.20964/2019.08.47.

(29) Dutta, G.; Tan, C.; Siddiqui, S.; Arumugam, P. U. Enabling Long Term Monitoring of Dopamine Using Dimensionally Stable Ultrananocrystalline Diamond Microelectrodes. *Mater. Res. Express* **2016**, *3* (9). https://doi.org/10.1088/2053-1591/3/9/094001.

(30) Siddiqui, S.; Dutta, G.; Tan, C.; Arumugam, P. U. Nanocrystalline Diamond Electrodes: Enabling Electrochemical Microsensing Applications with High Reliability and Stability. *IEEE Nanotechnol. Mag.* **2016**, *10* (3), 12–20. https://doi.org/10.1109/MNANO.2016.2572243.

(31) Mochalin, V. N.; Pentecost, A.; Li, X. M.; Neitzel, I.; Nelson, M.; Wei, C.; He, T.; Guo, F.; Gogotsi, Y. Adsorption of Drugs on Nanodiamond: Toward Development of a Drug Delivery Platform. *Mol. Pharm.* **2013**, *10* (10), 3728–3735. https://doi.org/10.1021/mp400213z.

(32) Puthongkham, P.; Venton, B. J. Nanodiamond Coating Improves the Sensitivity and Antifouling Properties of Carbon Fiber Microelectrodes. *ACS Sensors* **2019**, *4* (9), 2403–2411. https://doi.org/10.1021/acssensors.9b00994.

(33) Mccreery, R. L.; Mccreery, R. L. Advanced Carbon Electrode Materials for Molecular Electrochemistry Advanced Carbon Electrode Materials for Molecular Electrochemistry. *2646 Chem. Rev.* **2008**, *108* (June), 2646–2687. https://doi.org/10.1021/cr068076m.

(34) Roberts, J. G.; Moody, B. P.; McCarty, G. S.; Sombers, L. A. Specific Oxygen-Containing Functional Groups on the Carbon Surface Underlie an Enhanced Sensitivity to Dopamine at Electrochemically Pretreated Carbon Fiber Microelectrodes. *Langmuir* **2010**, *26* (11), 9116–9122. https://doi.org/10.1021/la9048924.

(35) Runnels, P. L.; Joseph, J. D.; Logman, M. J.; Wightman, R. M. Effect of PH and Surface Functionalities on the Cyclic Voltammetric Responses of Carbon-Fiber Microelectrodes. *Anal. Chem.* **1999**, *71* (14), 2782–2789. https://doi.org/10.1021/ac981279t.

(36) Hartney, M. A. Mechanistic Studies of Oxygen Plasma Etching. *J. Vac. Sci. Technol. B Microelectron. Nanom. Struct.* **1988**, *6* (6), 1892. https://doi.org/10.1116/1.584196.

(37) Vivensang, C.; Turban, G.; Anger, E.; Gicquel, A. Reactive Ion Etching of Diamond and Diamond-like Carbon Films. *Diam. Relat. Mater.* **1994**, *3* (4–6), 645–649. https://doi.org/10.1016/0925-9635(94)90241-0.

(38) Childres, I.; Jauregui, L. A.; Tian, J.; Chen, Y. P. Effect of Oxygen Plasma Etching on Graphene Studied Using Raman Spectroscopy and Electronic Transport Measurements. *New J. Phys.* **2011**, *13*. https://doi.org/10.1088/1367-2630/13/2/025008.

(39) Al-Mumen, H.; Rao, F.; Li, W.; Dong, L. Singular Sheet Etching of Graphene with Oxygen Plasma. *Nano-Micro Lett.* **2014**, *6* (2), 116–124. https://doi.org/10.1007/BF03353775.

(40) Cvelbar, U.; Pejovnik, S.; Mozetiè, M.; Zalar, A. Increased Surface Roughness by Oxygen Plasma Treatment of Graphite/Polymer Composite. *Appl. Surf. Sci.* **2003**, *210* (3–4), 255–261. https://doi.org/10.1016/S0169-4332(02)01286-2.

(41) Yang, C.; Wang, Y.; Jacobs, C. B.; Ivanov, I. N.; Venton, B. J. O2 Plasma Etching and Antistatic Gun Surface Modifications for CNT Yarn Microelectrode Improve Sensitivity and Antifouling Properties. *Anal. Chem.* **2017**, *89* (10), 5605–5611. https://doi.org/10.1021/acs.analchem.7b00785.

(42) Valentini, F.; Romanazzo, D.; Carbone, M.; Palleschi, G. Modified Screen-Printed Electrodes Based on Oxidized Graphene Nanoribbons for the Selective Electrochemical Detection of Several Molecules. *Electroanalysis* **2012**, *24* (4), 872–881. https://doi.org/10.1002/elan.201100415.

(43) Purcell, E. K.; Becker, M. F.; Guo, Y.; Hara, S. A.; Ludwig, K. A.; McKinney, C. J.; Monroe, E. M.; Rechenberg, R.; Rusinek, C. A.; Saxena, A.; et al. Next-Generation Diamond Electrodes for Neurochemical Sensing: Challenges and Opportunities. *Micromachines* **2021**, *12* (2), 1–29. https://doi.org/10.3390/mi12020128.

(44) Robinson, D. L.; Venton, B. J.; Heien, M. L. A. V; Wightman, R. M. Detecting Subsecond Dopamine Release with Fast-Scan Cyclic Voltammetry in Vivo. *Clin. Chem.* **2003**, *1773*, 1763–1773.

(45) Cao, Q.; Lucktong, J.; Shao, Z.; Chang, Y.; Venton, B. J. Electrochemical Treatment in KOH Renews and Activates Carbon Fiber Microelectrode Surfaces. *Anal. Bioanal. Chem.* **2021**. https://doi.org/10.1007/s00216-021-03539-6.

(46) Arnault, J. C. X-Ray Photoemission Spectroscopy Applied to Nanodiamonds: From Surface Chemistry to in Situ Reactivity. *Diam. Relat. Mater.* **2018**, *84* (November 2017), 157–168. https://doi.org/10.1016/j.diamond.2018.03.015.

(47) Yang, C.; Wang, Y.; Jacobs, C. B.; Ivanov, I. N.; Venton, B. J. O2 Plasma Etching and Antistatic Gun Surface Modifications for CNT Yarn Microelectrode Improve Sensitivity and Antifouling Properties. *Anal. Chem.* **2017**, *89* (10), 5605–5611. https://doi.org/10.1021/acs.analchem.7b00785.

(48) Shaw, R. W.; Plum, M. A.; Wilson, L. L.; Luck, C. F.; McDermott, A. G.; Chen, Y. J.; Coleman, R. L.; Gardner, D. M.; Feigerle, C. S.; Spickermann, T.; et al. Diamond Stripper Foil Experience at SNS and PSR. *EPAC 2008 - Contrib. to Proc.* **2008**, 3563–3565.

(49) Osswald, S.; Yushin, G.; Mochalin, V.; Kucheyev, S. O.; Gogotsi, Y. Control of Sp2/Sp3 Carbon Ratio and Surface Chemistry of Nanodiamond Powders by Selective Oxidation in Air. *J. Am. Chem. Soc.* **2006**, *128* (35), 11635–11642. https://doi.org/10.1021/ja063303n.

(50) Ferrari, A. C.; Robertson, J. Raman Spectroscopy of Amorphous, Nanostructured, Diamond-like Carbon, and Nanodiamond. *Philos. Trans. R. Soc. A Math. Phys. Eng. Sci.* **2004**, *362* (1824), 2477–2512. https://doi.org/10.1098/rsta.2004.1452.

(51) Hummer, G.; Garde, S.; García, A. E.; Pohorille, A.; Pratt, L. R. An Information Theory Model of Hydrophobic Interactions. *Proc. Natl. Acad. Sci. U. S. A.* **1996**, *93* (17), 8951–8955. https://doi.org/10.1073/pnas.93.17.8951.

(52) Aljumaily, M. M.; Alsaadi, M. A.; Das, R.; Abd Hamid, S. B.; Hashim, N. A.; AlOmar, M. K.; Alayan, H. M.; Novikov, M.; Alsalhy, Q. F.; Hashim, M. A. Optimization of the Synthesis of Superhydrophobic Carbon Nanomaterials by Chemical Vapor Deposition. *Sci. Rep.* **2018**, *8* (1), 1–12. https://doi.org/10.1038/s41598-018-21051-3.

(53) Welle, E. J.; Patel, P. R.; Woods, J. E.; Petrossians, A.; Della Valle, E.; Vega-Medina, A.; Richie, J. M.; Cai, D.; Weiland, J. D.; Chestek, C. A. Ultra-Small Carbon Fiber Electrode Recording Site Optimization and Improved in Vivo Chronic Recording Yield. *J. Neural Eng.* **2020**, *17* (2). https://doi.org/10.1088/1741-2552/ab8343.

(54) Bard, A. J.; Faulkner, L. R. *Electrochemical Methods: Fundamentals and Applications*, 2nd ed.; John Wiley and Sons: New York, 2001.

(55) Unwin, P. R.; Güell, A. G.; Zhang, G. Nanoscale Electrochemistry of Sp 2 Carbon Materials: From Graphite and Graphene to Carbon Nanotubes. *Acc. Chem. Res.* **2016**, *49*, 2041–2048. https://doi.org/10.1021/acs.accounts.6b00301.

(56) Shao, Z.; Puthongkham, P.; Hu, K. K.; Jia, R.; Mirkin, M. V.; Venton, B. J. Thin Layer Cell Behavior of CNT Yarn and Cavity Carbon Nanopipette Electrodes: Effect on Catecholamine Detection. *Electrochim. Acta* **2020**, *361*, 137032. https://doi.org/10.1016/j.electacta.2020.137032.

(57) Mishra, G. K.; Kant, R. Modular Theory for DC-Biased Electrochemical Impedance Response of Supercapacitor. *J. Power Sources* **2020**, *473* (May), 228467. https://doi.org/10.1016/j.jpowsour.2020.228467.

(58) Lasia, A. *Electrochemical Impedance Spectroscopy and Its Applications*; 2014; Vol. 9781461489. https://doi.org/10.1007/978-1-4614-8933-7.

(59) Dutta, G.; Siddiqui, S.; Zeng, H.; Carlisle, J. A.; Arumugam, P. U. The Effect of Electrode Size and Surface Heterogeneity on Electrochemical Properties of Ultrananocrystalline Diamond Microelectrode. *J. Electroanal. Chem.* **2015**, *756*, 61–68. https://doi.org/10.1016/j.jelechem.2015.08.016.

(60) Arumugam, P. U.; Zeng, H.; Siddiqui, S.; Covey, D. P.; Carlisle, J. A.; Garris, P. A. Characterization of Ultrananocrystalline Diamond Microsensors for in Vivo Dopamine Detection. *Appl. Phys. Lett.* **2013**, *102* (25). https://doi.org/10.1063/1.4811785.

(61) Kawagoe, K.; Zimmerman, J.; Wightman, R. M. Principles of Voltammetry and Microelectrode Surface States. J. Neuroscl. Meth. 48,225-240. *J. Neurosci. Methods* **1993**, *48*, 225–240.

(62) Venton, B. J.; Cao, Q. Fundamentals of Fast-Scan Cyclic Voltammetry for Dopamine Detection. *Analyst* **2020**. https://doi.org/10.1039/C9AN01586H.

(63) Vreeland, R. F.; Atcherley, C. W.; Russell, W. S.; Xie, J. Y.; Lu, D.; Laude, N. D.; Porreca, F.; Heien, M. L. Biocompatible PEDOT:Nafion Composite Electrode Coatings for Selective Detection of Neurotransmitters in Vivo. *Anal. Chem.* **2015**, *87* (5). https://doi.org/10.1021/ac502165f.

(64) Abdalla, A.; Atcherley, C. W.; Pathirathna, P.; Samaranayake, S.; Qiang, B.; Peña, E.; Morgan, S. L.; Heien, M. L.; Hashemi, P. In Vivo Ambient Serotonin Measurements at Carbon-Fiber Microelectrodes. *Anal. Chem.* **2017**, *89* (18). https://doi.org/10.1021/acs.analchem.7b01257.

(65) Trouillon, R.; Gijs, M. A. M. Paper-Based Polymer Electrodes for Bioanalysis and Electrochemistry of Neurotransmitters. *ChemPhysChem* **2018**, *19* (10), 1164–1172. https://doi.org/10.1002/cphc.201701124.

(66) Wood, G. F.; Zvoriste-Walters, C. E.; Munday, M. G.; Newton, M. E.; Shkirskiy, V.; Unwin, P. R.; Macpherson, J. V. High Pressure High Temperature Synthesis of Highly Boron Doped Diamond Microparticles and Porous Electrodes for Electrochemical Applications. *Carbon N. Y.* **2020**, *171*, 845–856. https://doi.org/10.1016/j.carbon.2020.09.038.
(67) Shin, D.; Tryk, D. A.; Fujishima, A.; Merkoçi, A.; Wang, J. Resistance to Surfactant and Protein Fouling Effects at Conducting Diamond Electrodes. *Electroanalysis* **2005**, *17* (4), 305–311. https://doi.org/10.1002/elan.200403104.
(68) Hanssen, B. L.; Siraj, S.; Wong, D. K. Y. Recent Strategies to Minimise Fouling in Electrochemical Detection Systems. *Reviews in Analytical Chemistry*. 2016. https://doi.org/10.1515/revac-2015-0008.
(69) Pyakurel, P.; Privman Champaloux, E.; Venton, B. J. Fast-Scan Cyclic Voltammetry (FSCV) Detection of Endogenous Octopamine in Drosophila Melanogaster Ventral Nerve Cord. *ACS Chem. Neurosci.* **2016**, *7* (8). https://doi.org/10.1021/acschemneuro.6b00070.
(70) Shao, Z.; Venton, B. J. Different Electrochemical Behavior of Cationic Dopamine from Anionic Ascorbic Acid and DOPAC at CNT Yarn Microelectrodes. *J. Electrochem. Soc.* **2022**. https://doi.org/10.1149/1945-7111/ac4d67.
(71) Puthongkham, P.; Venton, B. J. Nanodiamond Coating Improves the Sensitivity and Antifouling Properties of Carbon Fiber Microelectrodes. *ACS Sensors* **2019**, *4* (9). https://doi.org/10.1021/acssensors.9b00994.
(72) Feng, T.; Ji, W.; Tang, Q.; Wei, H.; Zhang, S.; Mao, J.; Zhang, Y.; Mao, L.; Zhang, M. Low-Fouling Nanoporous Conductive Polymer-Coated Microelectrode for in Vivo Monitoring of Dopamine in the Rat Brain. *Anal. Chem.* **2019**, *91* (16), 10786–10791. https://doi.org/10.1021/acs.analchem.9b02386.
(73) Zhou, L.; Hou, H.; Wei, H.; Yao, L.; Sun, L.; Yu, P.; Su, B.; Mao, L. In Vivo Monitoring of Oxygen in Rat Brain by Carbon Fiber Microelectrode Modified with Antifouling Nanoporous Membrane. *Anal. Chem.* **2019**, *91* (5), 3645–3651. https://doi.org/10.1021/acs.analchem.8b05658.
(74) Takmakov, P.; Zachek, M. K.; Keithley, R. B.; Bucher, E. S.; McCarty, G. S.; Wightman, R. M. Characterization of Local PH Changes in Brain Using Fast-Scan Cyclic Voltammetry with Carbon Microelectrodes. *Anal. Chem.* **2010**, *82* (23), 9892–9900. https://doi.org/10.1021/ac102399n.
(75) Cryan, M. T.; Li, Y.; Ross, A. E. Sustained Delivery of Focal Ischemia Coupled to Real-Time Neurochemical Sensing in Brain Slices. *Lab Chip* **2022**, *22* (11), 2173–2184. https://doi.org/10.1039/d1lc00908g.
(76) Li, Y.; Jarosova, R.; Weese-Myers, M. E.; Ross, A. E. Graphene-Fiber Microelectrodes for Ultrasensitive Neurochemical Detection. *Anal. Chem.* **2022**, *94* (11), 4803–4812. https://doi.org/10.1021/acs.analchem.1c05637.
(77) Cao, Q.; Shin, M.; Lavrik, N. V.; Venton, B. J. 3D-Printed Carbon Nanoelectrodes for In Vivo Neurotransmitter Sensing. *Nano Lett.* **2020**, *20* (9), 6831–6836. https://doi.org/10.1021/acs.nanolett.0c02844.

Chapter 6

Pulling-induced 3D-printing produces long, straight carbon nanoneedle electrodes for neurotransmitter detection

Abstract

Carbon-fiber microelectrodes, with a 7 um-diameter, have been widely used for neurotransmitter detection; however, the size limits the applications of electrochemical sensing at vesicles or in synapses on a submicron scale. Previously, we reported a novel 3D printing technique using a Nanoscribe two-photon printer to fabricate tunable carbon electrodes, but tips can curl when annealed if the tip is long and thin. Here, we propose a new 3D printing strategy that uses a pulling force to fabricate a carbon electrode with a straight nanoneedle structure. A thin bridge with micron width is printed between the electrode tip and a 3D printed box. When the whole structure is annealed and heated, the box creates a pulling force to form a long, thin, and straight structure. With focused ion beam, the bridge was cut at the desired position to remove the box, resulting in a clean edge nanoneedle, which is still straight after cutting. The size of the needle is customizable and we constructed widths varying from 400 nm to 2 μm and lengths varying from 75 μm to 150 μm. Printing parameters such as hashing and slicing were optimized for different size nanoneedles. For electrode fabrication, the nanoneedle was insulated with aluminum oxide and the electrochemical properties are similar to that of glassy carbon that has a good performance in dopamine detection with fast-scan cyclic voltammetry. The new design of the nanoelectrode is capable of biological applications requiring nanoelectrodes, such as neurotransmitter detection in a *Drosophila* neuromuscular junction.

6.1 Introduction

For decades, the development of implantable microelectrodes has significantly benefited neuroscience. The detection of neurotransmitters in the brain using microsensors have been extensively studied, most of which used carbon fibers with a diameter of 6 to 7 μm.[1–3] However, new designs of electrodes are needed for detection in small brain regions and synapses that meet rigid requirements. First, the size of the electrode should be in sub-micron scale for sensing at single vesicle or small brain regions, such as Drosophila, which has brain size in micrometer scale.[2,4–6] Second, the electrode needs to have a long, thin tip for easy implantation with little damage. Third, the electrode material needs to have good electrochemical performance to ensure rapid sensing. Carbon is the traditional material for neurotransmitter sensing because carbon has good biocompatibility, excellent electrochemical performance and a wide potential window.[7–9] However, new methods are needed to reproducibly fabricate an implantable probe with a sub-micron size.

Recently, many groups have developed different approaches for making carbon nanoelectrodes for neurotransmitter detection. The Huang group and the Sombers group successfully etched carbon fiber into nanoelectrodes and applied them for neurotransmitter detection in synapses and single cells.[10,11] Nanopipettes with a nano-size cavity have been used in many studies, such as electrochemical sensing, imaging, and cell counting.[12–15] Our group fabricated carbon nanospike-coated nanoelectrodes by depositing carbon nanomaterials on metal wires with a nanotip.[16] Recently, we developed 3D-printed carbon electrodes with photolithography by polymerizing and carbonizing the photoresist.[17] The printed carbon structure has a nanotip, which is then polished by a focused ion beam to form a disk. Although these electrodes are nano-sized, they are too blunt for implantation in small brain regions. A long and thin needle-shaped probe is needed to reduce the tissue damage.[18–20] For example, Hegarty, et al. designed carbon loaded microneedles for pH measurements with reduced damage during insertion.[21,22]

3D-printing with laser lithography enables fabrication of customized carbon micro- and nanoelectrodes with a higher reproducibility. The designed structure is printed in a thin layer of photoresist by a focused laser using two-photon adsorption and the photoresist is then pyrolyzed to carbon with a glassy-carbon-like surface.[18,23] A shrinkage was observed after pyrolysis because the decomposition of the polymer generates byproducts, including H_2O, CO, CH_2O, and CO_2;[24,25] While the shape of the final structure is well retained.[24,26] To build a needle shape, we printed a cylinder with a submicron diameter on the cone. However, curling of the ultra-small tip occurred due to the asymmetric force in the needle structure during annealing, which only happens when the printed structure is nano-sized with a high aspect ratio. Similarly, del Campo and Greiner observed a curling of the printed cylinder structure when they are fabricating a microcylinder array using SU-8 photoresist.[27] Thus, additional conditions need to be considered to fabricate nanostructures with shapes retaining straight.

Here, we designed a novel pulling method to generate a carbon-based nano-sized needle structure without any curling. The 3D nano-printing technique enables the printing of a nanoneedle bridge between two bulk structures. With the connection between two bridgeheads, a pulling force is generated along the bridge by shrinking during pyrolysis, and the bridge is finally stretched to a long, thin, and straight nanoneedle structure. One of the bridgeheads becomes the base of the nanoneedle, the other is then cut off by a focused ion beam to leave cabon exposed. The carbon-based nanoneedle is then fabricated into nanoelectrodes for dopamine detection with fast-scan cyclic voltammetry (FSCV) and show a reliable performance. With the high aspect ratio, the carbon nanoneedle will be capable for electrochemical sensing in synapses or small organisms.

6.2 Methods

6.2.1 Chemicals and Materials

Dopamine hydrochloride was purchased from Sigma-Aldrich (St. Louis, MO). Analytes were dissolved in 0.1 M $HClO_4$ to make 10 mM stock solutions and were diluted daily to 1 µM in PBS pH 7.4 buffer (131.25 mM NaCl, 3.00 mM KCl, 10 mM NaH_2PO_4, 1.2 mM $MgCl_2$, 2.0 mM Na_2SO_4, and 1.2 mM $CaCl_2$). IP-DIP and IP-S photoresist were purchased from Nanoscribe (Nanoscribe GmbH, Karlsruhe, Germany).

6.2.2 3D structure designs

3D structures were designed and drawn in COMSOL Multiphysics and imported to the Nanoscribe Pro GT laser lithography system. The CAD model of the printed structures is shown in the supplemental file. The tip-etched niobium wires (50 mm diameter) served as metal substrates and were placed horizontally on a silicon chip. A drop of the negative-tone photoresist, IP-DIP (Nanoscribe GmbH, Karlsruhe, Germany), was added to the silicon chip to fully cover the tips of the wires. The Nanoscribe instrument is equipped with a pulsed femtosecond fiber laser source at a center wavelength of 780 nm. With the two-photon adsorption, the laser-focused on the interior spot of the IP-DIP photoresist based on the design, which then got polymerized by chemical crosslinking. A bridge was built between two block structures (200 * 200 * 200 μm), one of which was printed against a wall, and the other was printed on the tip of the etched niobium wire. The length of the bridge varies from 100 μm to 200 μm, and the width varies from 2 μm to 16 μm. Additional blocks (400 * 400 * 800) that serve as anchors were built on the silicon stage to help mount and immobilize the wires.

After printing the 3D structures, they are transferred to the photoresist developer for 15 min. Then UV flood exposure was conducted with a constant dose of 500 mJ/cm^2 to help solidify the photoresist.

6.2.3 Annealing

Annealing was performed by First Nano Rapid Thermal Processor (RTP) (Firstnano CVD Equipment Corporation, NY). The pyrolysis of IP-DIP photoresist follows a three-step procedure: 1) 400 °C in oxygen for 15 min. 2) 600 °C in argon atmosphere at 9 Torr for 10 min. 3) 950 °C in argon at 1 Torr for 10 min.

6.2.4 Surface characterization

Scanning electron microscope images were taken by ZEISS Merlin High Resolution Scanning electron microscope (Oberkochen, Germany) with an accelerating voltage of 2 KV. Raman spectroscopy measurements were performed with a Renishaw 100 confocal micro Raman system (Renishaw, Hoffman Estates, IL) with 1800 lines/mm diffraction grating and 632 nm He-Ne laser. Laser intensity was 50% and scan range was 100 cm^{-1} to 3200 cm^{-1}.

6.2.5 Atomic layer deposition

To insulate the electrode tip, Atomic Layer Deposition (ALD) was performed on FlexAl Atomic Layer Deposition (Oxford Instruments, Concord, MA). A layer of aluminum oxide with 100 nm thickness was deposited using the trimethylaluminium (TMA) precursor for an hour at a temperature of 150 °C. The aluminum oxide was then removed by NaOH solution to expose the electrode tip.

6.3 Results and Discussion

Previously, we successfully designed a carbon nanoelectrode constructed from photoresist IP-S via 3D nano-printing, or direct laser writing technique (Fig. 1). With 3D printing, a customized structure is printed in the photoresist by using the laser to trigger a chemical cross-linking of the photoresist polymer. The printed structure is then developed in the SU-8 developer solution, which also rinses away the rest of the non-cross-linked photoresist. After pyrolysis at a higher temperature, the printed structure becomes glassy carbon. In our previous design, a cone shape structure was printed and annealed on an etched Nb wire and the surface was insulated by a thin layer of aluminum oxide coating. By cutting the tip of the cone using focused ion beam, a nano-sized carbon disk was exposed. However, the limitations of this method cannot be ignored: First, although the disk at the tip is nano-sized, the bottom of the cone has a diameter of 50 μm, which is relatively large for implantation in small organisms. Second, the tips are blunt and short. As Figure 1D shows, when the tip was printed long and thin, the tip curled due to gravity and asymmetric strength during pyrolysis. Curled tips cannot be implanted into tissue. Thus, a new 3D structure was designed to keep the tip straight during annealing using a pulling force between two blocks, as illustrated in Figure 1E. The bridge is printed between the metal tip and a block, and it shrinks to a nano-sized width during annealing; meanwhile, the bridge retains straight due to the pulling force of the block. This design solves the curling problem and enables the construction of a long and thin tip.

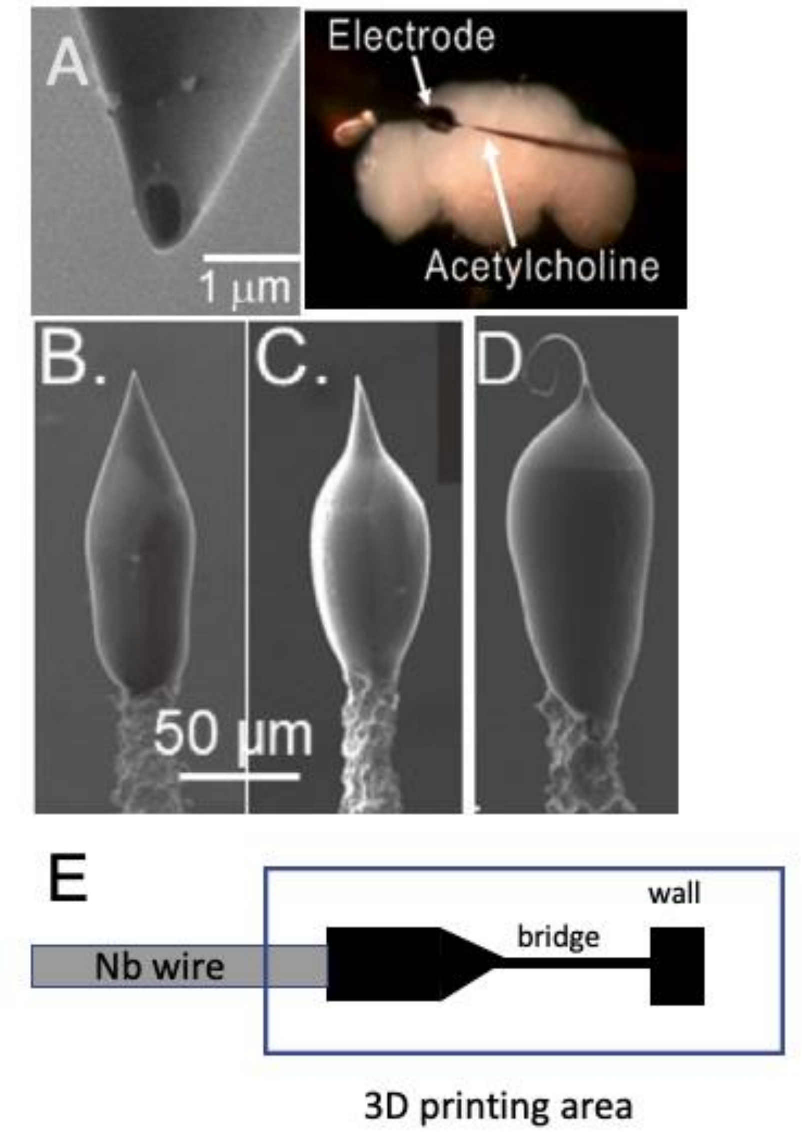

Figure 1. 3D-printed carbon electrodes with photoresist IP-S. A) A disk-shape 3D-printed carbon nanoelectrode that is reported before. The electrode was inserted into an adult fruit fly brain for endogenous dopamine detection. (Reprinted from American Chemical Society and ScienceDirect) B, C, D) Different designs of the cone structure with different aspect ratios. After thermal annealing, the tip curls when it was printed thin and long. E) New design of a nanoelectrode. A complex structure is printed, including two bulk structures and a bridge in between.

6.3.1 Printing parameters optimization

The Nanoscribe 3D printer with two-photon adsorption has a sub-micron resolution, which determines the size of the final printed structure. Fortunately, shrinkage occurs during the carbonization process, which reduces the size of the structure to 30% to 50%.[24,25] One can take advantage of the shrinkage to build a structure smaller than the printer resolution. However, the construction of ultra-small structures is challenging, because the printed polymer needs to be dense enough to avoid distortion and deformation of the final structure. The printing quality is controlled by several factors, such as the printing process and laser properties. When importing a STL model in the software, the bulk structure is divided into layers by slicing, which are then subdivided to a set of trajectories by hatching. Slicing distance controls the distance between the layers and hatching distance defines the lateral distance of two adjacent lines within a layer (Figure 2). Slicing and hatching distances determine the density of the printed structure. The degree of photoresist crosslinking is also correlated with the laser intensity or energy deposited within the voxel, which are determined by the laser power and scan speed parameters. The denser the structure, the more chemical crosslinking during polymerization, but the longer time for printing. Table 1 lists parameters that were varied for the bridges. Since the photoresist resin is viscous, the polymer structure will flow in the resin and deform if there is not enough chemical cross-linking. As a result, for the smallest structure, with a 1 μm-wide bridge, we observed bridges slightly curl during printing with larger hatching and slicing distances, which causes the deformation of the bridges in the slow flowing photoresist. Those thin bridges often break during annealing. Thus, for 1 μm bridges, the optimal slicing and hatching distance was 0.1 nm, which is the minimum value available in the Nanoscribe instrument. For larger structures, the density can be decreased to shorten the printing time; for example, slicing and hatching distance of 0.5 nm are sufficient for bridges wider than 4 μm.

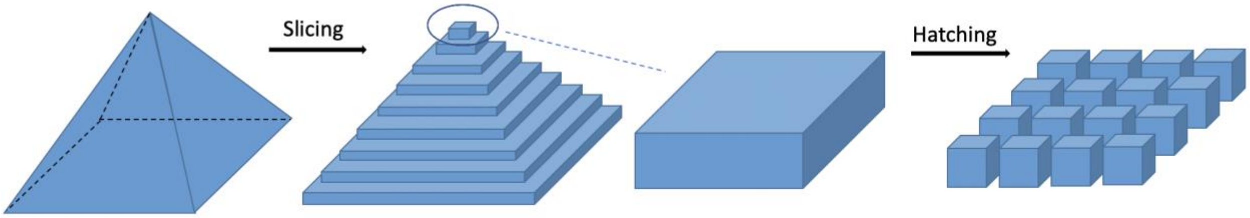

Figure 2. Illustration of defining a printing process. The example pyramid structure is sliced into multiple layers and then subdivided by hatching into a set of trajectories.

Table 1. The optimized printing parameters of different structures.

Block size (μm)	**Bridge width (μm)**	**Slicing distance (nm)**	**Hatching distance (nm)**	**Printing time (min)**
100*200*200	1	0.1	0.1	~30 min
100*200*200	2	0.2	0.2	~12 min
100*200*200	> 4	0.5	0.5	~6 min

6.3.2 Nanoneedles with different bridge lengths and widths

To understand 3D printing of the structures, several nanoneedle designs were batch printed on a silicon chip and annealed (Figure 3). Figure 3 shows the images from an optical profilometer before and after the first annealing step, which enables the real-time observation of shrinking on a hot plate. The bridges between blocks in Figure 3A and 3B have lengths ranging from 50 μm to 200 μm (5 μm width), and Figure 3C and 3D have different thicknesses of 3, 5, 7, and 10 μm (200 μm length). The left column is the printed structure after soaking in the SU-8 developer solution and UV flood exposure, and the right column is after annealing at 340 °C for 10 min on a hot plate. Under the microscope, the polymerized photoresist is a grey color (Figure

3A, 3C), which indicates that the material has good transparency. It becomes darker and less transparent after annealing (Figure 3B, 3D) because the photoresist hardened and partially carbonized at 340 °C. The structures slightly shrink, but the shape is well retained. Since the shrinkage is uniform over all the structure, the area of adhesion area between the blocks and silicon wafer is also slightly decreased. In Figure 3D, the right block slightly moved and deformed, which might be due to the strength of the thickest bridge with 10 μm width, whereas the other blocks are stabile at the same position.

Then the sample was annealed at 600 °C for 15 min and 950 °C for 10 min at 1 Torr pressure for full carbonization. More shrinkage occurs after complete pyrolysis conducted at 950 °C, which generates a glassy carbon structure with no transparency. The SEM image of one example pyrolyzed structure in Figure 3E indicates that two printed carbon blocks are still adhered on the silicon substrate and have obvious shrinkage compared with the square shadow around the structure, which is the initial printing trace on the substrate (marked in red in panel E). The needle-like bridge between the two blocks is stretched and pulled long and straight due to mechanical stress during pyrolysis. The size of the bridge is approximately 80 μm long and 1 μm wide. Figure 3F shows the smooth transition at the junction that produces a robust and firm connection.

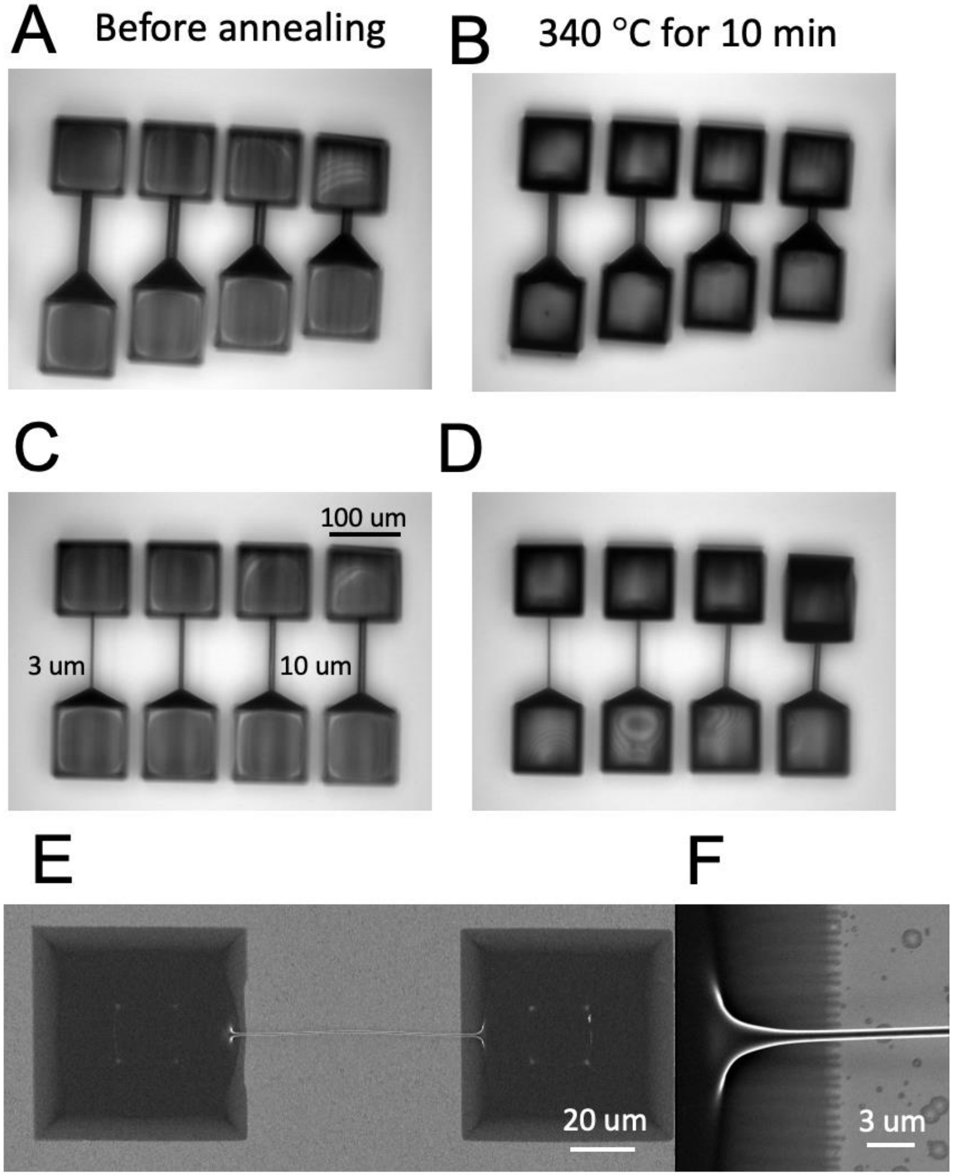

Figure 3. The blocks and bridge complex structure printed on a silicon wafer with varying length and width. A to D were obtained from an optical profilometer before and after partial carbonization in the condition of 340 °C for 10 min. A) The bridges with length of 50, 100, 150, and 200 μm. B) The bridges in Panel A after annealing at 340 °C for 10 min. C) The bridges with width of 3, 5, 7 and 10 μm and D) The bridges in Panel C after annealing. E) The SEM image of the final pyrolyzed structure. The bridge was pulled to a long and thin needle structure

(approximately 80 μm long and 1 μm wide). F) The smooth transition between the block and the bridge.

6.3.3 Focused ion beam cutting

After pyrolysis, the bridge is cut by a focused ion beam (FIB) to generate a long nanoneedle tip. Figure 4 shows a series of pyrolyzed structures with bridges designed in different lengths and widths. Figure 4A has the thinnest and longest bridge, which is approximately 330 nm in width and 150 μm in length. Both bridges in Figure 4B and 4C are about 75 μm long, but the bridge in Figure 4B has a width of 1.5 μm, wheras the bridge in Figure 4C is 2.2 μm. The structures are well retained after complete anneal and carbonization and have a smooth surface. The center position of the bridges was exposed to a beam of Ga ion at an accelerating voltage of 30 kV. As shown in the middle and right columns, the bridges are still straight after they were cut in half, with smooth edges. The results indicate that FIB cutting is neat and precisely controlled. With the combination of 3D printing and FIB technique, the shapes of the bridges are totally customizable.

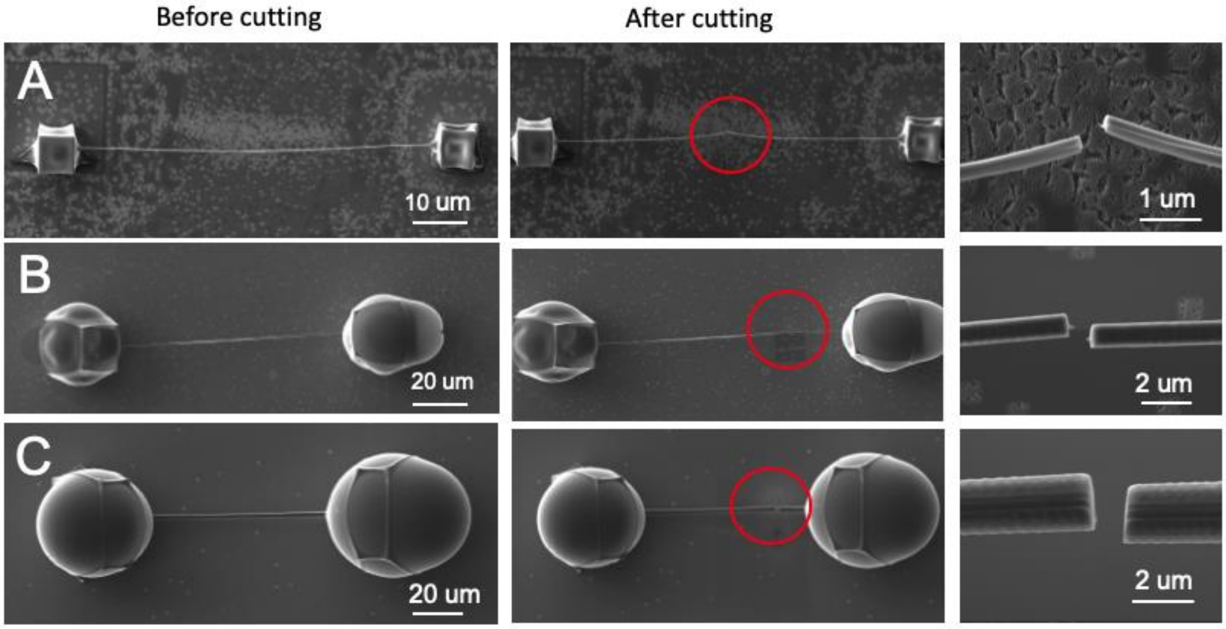

Figure 4. The pyrolyzed carbon structure of the bridges with different lengths and widths before and after FIB cutting: A) 150 μm * 330 nm, B) 75 μm * 1.5 μm, C)75 μm * 2.2 μm. The accelerating voltage of FIB was 30 kV.

6.3.4 Construction of nanoneedles on metal wires

For electrode fabrication, the structure must be printed on a wire that can be inserted into a glass capillary. Nb wires (with a diameter of 50 μm) were wet-etched in 4 M NaOH with 2 V applied to reduce their tips to a sharp tip to 1 μm size. The design on the metal wire must meet several requirements: First, the two ends of the complex structure must be mounted tightly to the Si substrate to generate a pulling force, and the anchors must survive the high temperature. Thus, the traditional method to anchor the wires using tape is not effective, because the gel on the tape dissolves in the organic solvent and the tape burns during annealing. Second, base of the needle must not contact the Si wafer to allow for pulling to happen. Third, the adhesion between the printed structure and the metal wire must be strong.

The wire assembly and fabrication process are illustrated in Figure 5A. The metal wire was placed on the Si wafer and several blocks were printed as anchors to mount and stabilize the wire. The complex structure was printed in a bottom-up direction from the Si wafer, where the left part covers the metal tip and the right block adheres on the wafer tightly. The left part serves as a base of the nanoneedle on the metal wire and the right part will be removed to expose the needle tip after pyrolysis. Figure 5B and 5C show the final structure with a glassy-carbon-like surface after pyrolysis. Compared with the original cubic design, the pyrolyzed bulk structure has a curved surface due to the surface tension during shrinkage. The bridge was pulled long and straight with a diameter of approximately 400 nm and a length of 100 μm. After pyrolysis, the sample was deposited with a thin film of Al_2O_3 (100 nm thickness) with atomic layer deposition to insulate the surface. Figure 5D shows the bridge was cut by FIB at a desired position to fabricate the nanoneedle with a straight and long shape. With the surface insulated, the cross section cut by FIB has carbon exposed to generate a nano-size sensing area.

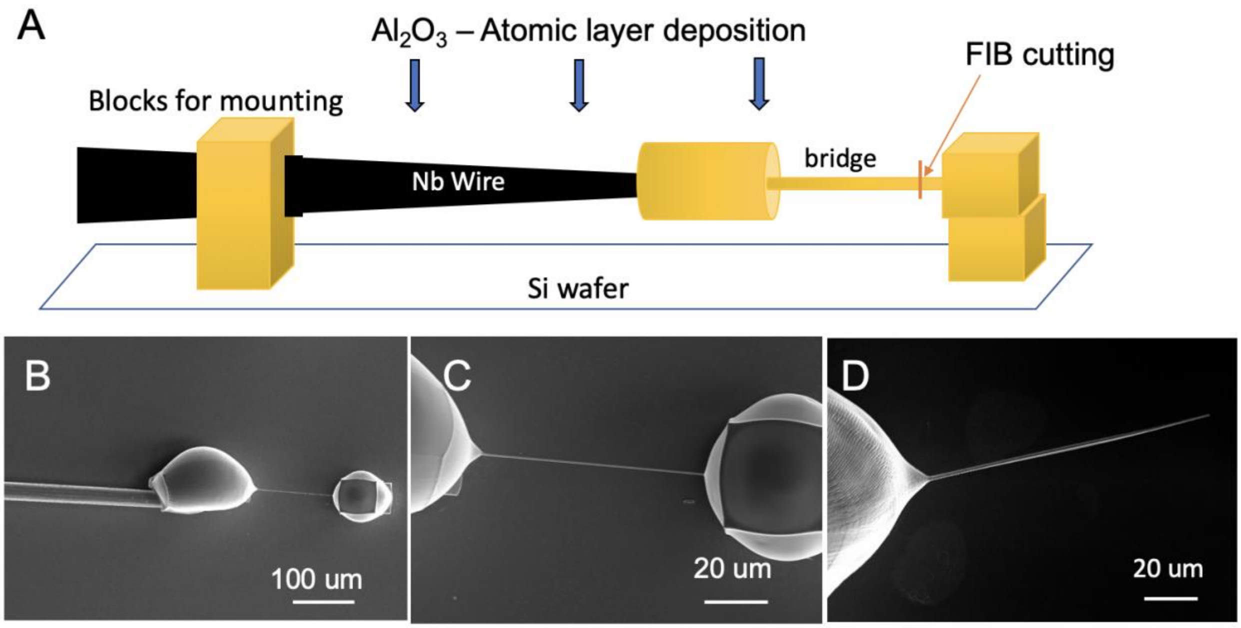

Figure 5. The printing procedure of the nanoneedle on a Nb wire. A) The illustration of the design. The whole structure was printed separately, including a base block printed on a silicon

substrate and a complex structure printed on the Nb wire. B, C) The printed complex structure was pyrolyzed to carbon. Two bulk structures were connected by a thin and straight bridge in between. D) After depositing with Al_2O_3, the bridge was cut to a needle by FIB with 30 kV accelerating voltage. The needle has a diameter around 400 nm with a straight shape.

6.3.5 Electrochemistry of carbon nanoneedle electrodes

The Nb wire with a carbon nanoneedle structure on the tip was then fabricated into a nanoelectrode for dopamine detection with fast-scan cyclic voltammetry. Figure 6A shows a small background current (approximately 20 nA) due to the ultra-small sensing area. The nanoneedle electrode shows a typical dopamine CV shape (Figure 6B) with oxidation peak occurs as around 0.5 V and a reduction peak at -0.3 V. The current of 10 μM dopamine was 0.45 nA. To investigate the adsorption of dopamine on the electrode surface, we varied the scan rate and plotted the log peak current (i) vs. log scan rate (v) curve of the electrodes. In Figure 6C and 6D, the fitted line shows a linear correlation between the scan rate and the current and the slop of the log-log plot is close to 1. They both indicate an adsorption-controlled process on the nanoneedle electrode, because the current is proportional to the scan rate when the electrochemistry is governed by adsorption. The results show that the 3D printed nanoneedle electrodes have a good electrochemical performance in dopamine detection.

With this novel fabrication method of the carbon nanoneedles, we produce disk electrodes by exposing the carbon at the cross section with an ultra-small sensing area. In the future, we could also dip the tip of the electrode into the sodium hydroxide solution to dissolve the aluminum oxide layer to fabricate a cylinder electrode, which gives a larger surface area for sensing.

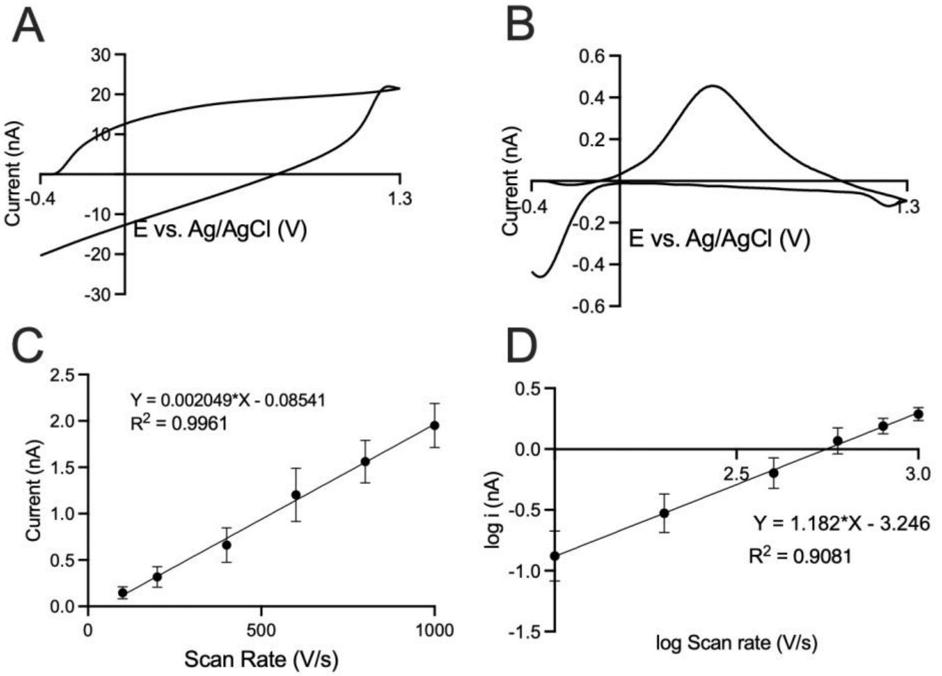

Figure 6. The electrochemical performance of the carbon nanoneedle electrode in dopamine detection with fast-scan cyclic voltammetry. A dopamine waveform was used to obtain the signal (scan rate of 400 V/s, sweep from -0.4 V to 1.3 V at 10 Hz). A) Background current of the nanoelectrode. B) The CV response of 10 μM dopamine. C) Current response with scan rate ranging from 100 V/s to 1000 V/s. D) log-log plot of scan rate test result. Error bar = SEM, n=2.

6.4 Conclusions

In this chapter, we improved the fabrication of carbon nanoelectrodes and demonstrate a novel method to print a needle-shape nanoelectrode with 3D nano-printing. By printing a bridge structure between two blocks, a long, thin, and straight carbon structure was generated by pulling force during pyrolysis. After cutting with FIB, a straight, nano-sized needle was fabricated with designed width and length. The produce an electrode, the structure printed on metal wires was insulated with a thin film of Al_2O_3 and carbon exposed at the cutting position. The carbon nanoneedle electrodes show a reliable electrochemical performance for dopamine detection.

Considering the ultra-small and sharp tip of the needle, the nanoelectrode can be easily implanted in small organisms in future studies, including fruit fly brains and synapse between neurons.

6.5 Reference

(1) Liu, T. C.; Chuang, M. C.; Chu, C. Y.; Huang, W. C.; Lai, H. Y.; Wang, C. T.; Chu, W. L.; Chen, S. Y.; Chen, Y. Y. Implantable Graphene-Based Neural Electrode Interfaces for Electrophysiology and Neurochemistry in In Vivo Hyperacute Stroke Model. *ACS Appl. Mater. Interfaces* **2016**, *8* (1), 187–196. https://doi.org/10.1021/acsami.5b08327.

(2) Yoon, E.; Koo, B.; Wong, J.; Elyahoodayan, S.; Weiland, J. D.; Lee, C. D.; Petrossians, A.; Meng, E. An Implantable Microelectrode Array for Chronic in Vivo Epiretinal Stimulation of the Rat Retina. *J. Micromechanics Microengineering* **2020**, *30* (12). https://doi.org/10.1088/1361-6439/abbb7d.

(3) Hascup, E. R.; af Bjerkén, S.; Hascup, K. N.; Pomerleau, F.; Huettl, P.; Strömberg, I.; Gerhardt, G. A. Histological Studies of the Effects of Chronic Implantation of Ceramic-Based Microelectrode Arrays and Microdialysis Probes in Rat Prefrontal Cortex. *Brain Res.* **2009**, *1291*, 12–20. https://doi.org/10.1016/j.brainres.2009.06.084.

(4) Sung, C.; Jeon, W.; Nam, K. S.; Kim, Y.; Butt, H.; Park, S. Multimaterial and Multifunctional Neural Interfaces: From Surface-Type and Implantable Electrodes to Fiber-Based Devices. *J. Mater. Chem. B* **2020**, *8* (31), 6624–6666. https://doi.org/10.1039/d0tb00872a.

(5) Bath, B. D.; Michael, D. J.; Trafton, B. J.; Joseph, J. D.; Runnels, P. L.; Wightman, R. M. Subsecond Adsorption and Desorption of Dopamine at Carbon-Fiber Microelectrodes. *Anal. Chem.* **2000**, *72* (24), 5994–6002. https://doi.org/10.1021/ac000849y.

(6) Cao, Q.; Lucktong, J.; Shao, Z.; Chang, Y.; Venton, B. J. Electrochemical Treatment in KOH Renews and Activates Carbon Fiber Microelectrode Surfaces. *Anal. Bioanal. Chem.* **2021**. https://doi.org/10.1007/s00216-021-03539-6.

(7) Alvarez, N. T.; Buschbeck, E.; Miller, S.; Le, A. D.; Gupta, V. K.; Ruhunage, C.; Vilinsky, I.; Ma, Y. Carbon Nanotube Fibers for Neural Recording and Stimulation. *ACS Appl. Bio Mater.* **2020**, *3* (9), 6478–6487. https://doi.org/10.1021/acsabm.0c00861.

(8) McCreery, R. L. Advanced Carbon Electrode Materials for Molecular Electrochemistry. *Chem. Rev.* **2008**, *108* (7), 2646–2687. https://doi.org/10.1021/cr068076m.

(9) Andriianov, V. S.; Mironov, V. S.; Smikhovskaia, A. V.; Khairullina, E. M.; Tumkin, I. I. Laser-Induced Synthesis of Carbon-Based Electrode Materials for Non-Enzymatic Glucose Detection. *Opt. Quantum Electron.* **2020**, *52* (1), 1–8. https://doi.org/10.1007/s11082-019-2155-7.

(10) Li, Y. T.; Zhang, S. H.; Wang, L.; Xiao, R. R.; Liu, W.; Zhang, X. W.; Zhou, Z.; Amatore, C.; Huang, W. H. Nanoelectrode for Amperometric Monitoring of Individual Vesicular Exocytosis inside Single Synapses. *Angew. Chem. - Int. Ed.* **2014**, *53* (46), 12456–12460. https://doi.org/10.1002/anie.201404744.

(11) Roberts, J. G.; Mitchell, E. C.; Dunaway, L. E.; McCarty, G. S.; Sombers, L. A. Carbon-Fiber Nanoelectrodes for Real-Time Discrimination of Vesicle Cargo in the Native Cellular Environment. *ACS Nano* **2020**. https://doi.org/10.1021/acsnano.9b07318.

(12) Ruan, Y. F.; Wang, H. Y.; Shi, X. M.; Xu, Y. T.; Yu, X. D.; Zhao, W. W.; Chen, H. Y.; Xu, J. J. Target-Triggered Assembly in a Nanopipette for Electrochemical Single-Cell Analysis. *Anal. Chem.* **2021**, *93* (2), 1200–1208. https://doi.org/10.1021/acs.analchem.0c04628.

(13) Hao, R.; Zhang, B. Nanopipette-Based Electroplated Nanoelectrodes. *Anal. Chem.* **2016**, *88* (1), 614–620. https://doi.org/10.1021/acs.analchem.5b03548.

(14) Hu, K.; Wang, Y.; Cai, H.; Mirkin, M. V.; Gao, Y.; Friedman, G.; Gogotsi, Y. Open Carbon Nanopipettes as Resistive-Pulse Sensors, Rectification Sensors, and Electrochemical Nanoprobes. *Anal. Chem.* **2014**, *86* (18), 8897–8901. https://doi.org/10.1021/ac5022908.

(15) Rees, H. R.; Anderson, S. E.; Privman, E.; Bau, H. H.; Venton, B. J. Carbon Nanopipette Electrodes for Dopamine Detection in Drosophila. *Anal. Chem.* **2015**, *87* (7), 3849–3855. https://doi.org/10.1021/ac504596y.

(16) Cao, Q.; Shao, Z.; Hensley, D.; Venton, B. J. Carbon Nanospike Coated Nanoelectrodes for Measurements of Neurotransmitters. *Faraday Discuss.* **2021**. https://doi.org/10.1039/d1fd00053e.

(17) Cao, Q.; Shin, M.; Lavrik, N. V.; Venton, B. J. 3D-Printed Carbon Nanoelectrodes for In Vivo Neurotransmitter Sensing. *Nano Lett.* **2020**, *20* (9), 6831–6836. https://doi.org/10.1021/acs.nanolett.0c02844.

(18) Abaddi, M. A.; Sasso, L.; Dimaki, M.; Svendsen, W. E. Fabrication of 3D Nano/Microelectrodes via Two-Photon-Polymerization. *Microelectron. Eng.* **2012**, *98*, 378–381. https://doi.org/10.1016/j.mee.2012.07.015.

(19) Abdalla, A.; Patel, B. A. 3D-Printed Electrochemical Sensors: A New Horizon for Measurement of Biomolecules. *Curr. Opin. Electrochem.* **2020**, *20*, 78–81. https://doi.org/10.1016/j.coelec.2020.04.009.

(20) Adelowo, E.; Baboukani, A. R.; Okpowe, O.; Khakpour, I.; Safa, M.; Chen, C.; Wang, C. A High-Energy Aqueous on-Chip Lithium-Ion Capacitor Based on Interdigital 3D Carbon Microelectrode Arrays. *J. Power Sources* **2020**, *455*, 227987. https://doi.org/10.1016/j.jpowsour.2020.227987.

(21) Hegarty, C.; Mckillop, S.; Dooher, T.; Dixon, D.; Davis, J. Composite Microneedle Arrays Modified with Palladium Nanoclusters for Electrocatalytic Detection of Peroxide. *IEEE Sens. Lett.* **2019**, *3* (9), 9–12. https://doi.org/10.1109/LSENS.2019.2935831.

(22) Hegarty, C.; McKillop, S.; McGlynn, R. J.; Smith, R. B.; Mathur, A.; Davis, J. Microneedle Array Sensors Based on Carbon Nanoparticle Composites: Interfacial Chemistry and Electroanalytical Properties. *J. Mater. Sci.* **2019**, *54* (15), 10705–10714. https://doi.org/10.1007/s10853-019-03642-1.

(23) Yang, C.; Cao, Q.; Puthongkham, P.; Lee, S. T.; Ganesana, M.; Lavrik, N. V.; Venton, B. J. 3D-Printed Carbon Electrodes for Neurotransmitter Detection. *Angew. Chem. - Int. Ed.* **2018**, *57* (43), 14255–14259. https://doi.org/10.1002/anie.201809992.

(24) Cardenas-Benitez, B.; Eschenbaum, C.; Mager, D.; Korvink, J. G.; Madou, M. J.; Lemmer, U.; Leon, I. D.; Martinez-Chapa, S. O. Pyrolysis-Induced Shrinking of Three-Dimensional Structures Fabricated by Two-Photon Polymerization: Experiment and Theoretical Model. *Microsyst. Nanoeng.* **2019**, *5* (1), 38. https://doi.org/10.1038/s41378-019-0079-9.

(25) Sharipova, M. I.; Baluyan, T. G.; Abrashitova, K. A.; Kulagin, G. E.; Petrov, A. K.; Chizhov, A. S.; Shatalova, T. B.; Chubich, D.; Kolymagin, D. A.; Vitukhnovsky, A. G.; Bessonov, V. O.; Fedyanin, A. A. Effect of Pyrolysis on Microstructures Made of Various Photoresists by Two-Photon Polymerization: Comparative Study. *Opt. Mater. Express* **2021**, *11* (2), 371. https://doi.org/10.1364/ome.416457.

(26) Yi, W.; Yang, Y.; Hashemi, P.; Cheng, M. M.-C. 3D Carbon Nanofiber Microelectrode Arrays Fabricated by Plasma-Assisted Pyrolysis to Enhance Sensitivity and Stability of Real-Time Dopamine Detection. *Biomed. Microdevices* **2016**, *18* (6), 112. https://doi.org/10.1007/s10544-016-0136-1.

(27) Del Campo, A.; Greiner, C. SU-8: A Photoresist for High-Aspect-Ratio and 3D Submicron Lithography. *J Micromech Microeng* **2007**, *17* (17), 81–95. https://doi.org/10.1088/0960-1317/17/6/R01.

(28) Yang, C.; Cao, Q.; Puthongkham, P.; Lee, S. T.; Ganesana, M.; Lavrik, N. V.; Venton, B. J. 3D-Printed Carbon Electrodes for Neurotransmitter Detection. *Angew. Chem. - Int. Ed.* **2018**, *57* (43). https://doi.org/10.1002/anie.201809992.

Chapter 7

Conclusions and Future Directions

7.1 Contribution of the Dissertation to the Field

7.1.1 Understanding thin-layer electrochemistry in neurotransmitter detection

In conventional cyclic voltammetry, thin-layer electrochemistry, with negligible mass transfer near the electrode surface, leads to a unique property on the voltammograms: a symmetrical CV shape. However, the effect of thin-layer electrochemistry had not been explored with fast-scan cyclic voltammetry, and may show different behavior than conventional CV. Chapters 2 and 3 systematically studied the role of trapping effects caused by thin-layer electrochemistry in selective detection of neurotransmitters with FSCV, including catecholamines and anionic neurochemicals. The results show that thin-layer electrochemistry within the crevices of CNT yarn microelectrodes leads to a higher temporal resolution because the current is independent of repetition frequencies of FSCV. The side reactions are favored during trapping and the detection of their products are amplified within the thin-layer cells. For example, catecholamines, including dopamine, norepinephrine and epinephrine, undergo cyclization reactions that are amplified by trapping and show an enhanced secondary oxidation peak on the CV. The trapping effect also helps the discrimination of dopamine from interferents of ascorbic acid and DOPAC by different CV shapes.

The selective detection of neurotransmitters is a highly studied topic in the analytical chemistry field. Chromatography and principal component analysis have been applied to separate and distinguish compound mixtures, but they are usually expensive and time consuming.[1,2] With these techniques, we get no information about redox cycling and mechanisms of electroactive species.[3–5] In the electrochemistry field, differential pulse voltammetry (DPV) is usually used for multiple electroactive compound detection; however, it may take a half hour to obtain the result.[6,7] FSCV measures neurotransmitters rapidly and provides unique fingerprints for different compounds, but it is hard to differentiate compounds with similar oxidative potentials.[6,8,9] With the thin-layer electrochemistry on the CNT yarn microelectrodes, the signals from side reactions are amplified by the continuous redox cycling and accumulation, which are often unique for a compound but are usually hidden behind the primary reaction. Combining thin-layer electrochemistry with FSCV, the detection of neurotransmitters is fast, cheap, and highly-selective. The amplified side reactions enable more fundamental electrochemistry studies, for example, a deep understanding of redox mechanisms or the study about the kinetics of a series of reactions.

7.1.2 Improved electrochemical sensing with various carbon surface structures

CFMEs have been the gold standard electrode for neurotransmitter detection for decades; however, limitations of CFMEs cannot be ignored, such as the electrode fouling and low selectivity. Various carbon nanomaterials have been used as electrode materials for electrochemical sensing with improved performance. Chapter 2 and 3 showed CNT yarn microelectrodes with trapping effect are capable of highly selective detection of multiple neurotransmitters based on the CV shapes. Chapter 4 explored the electrochemical performance of carbon nanospike (CNS) nanoelectrodes, which are fabricated by depositing CNSs on an etched metal wire. The nano-sized tip enables detection in small organisms with less damage. Chapter 5 developed a new nanodiamond microelectrode by uniformly coating a thin nanocrystalline diamond film on a piece of metal wires. The defect sites and oxide groups lead to a good performance after plasma treatment on the diamond surface for neurotransmitter measurement. In addition, the electrodes have an excellent electrode fouling resistance and biofouling resistance due to their hydrophobicity, which overcomes the limitation of CFMEs. Chapter 6 introduced a novel carbon-based nanoelectrode fabrication method with 3D nano-printing technique, which transfer the carbon-containing photoresist into polymer with customizable shapes with submicron resolution. In this study, a micron-scale needle was printed on the metal wire and it became a long, thin, and straight needle with nano-size width after pyrolysis. In the future, the small and long structure will be fabricated into nanoelectrodes for implantation in small organisms, such as fruit fly brains.

These works advance the field by studying the fundamental electrochemistry with various carbon electrode designs and answering why carbon nanomaterials are suitable for electrochemical sensing of neurotransmitters.

For decades, there have been numerous carbon-based microelectrode designs emerging for neurotransmitter detection and they show good electrochemical performance in an electrochemical cell or a flow cell. However, the number of designs that can be applied in biological studies is very limited, because the different sensing conditions between *in vitro* and *in vivo*. The detection in biological environment faces a series of challenges: First, the size of the electrode needs to be ultra-small to avoid tissue damage.[10–12] Second, the electrodes suffer severe biofouling and electrode fouling during a long-time measurement.[13–16] Third, the electrode must be sensitive and stable enough to be implanted in biological systems. Recently, carbon nanomaterial electrode studies are mainly focused on increasing the sensitivity and selectivity of the electrodes,[17–20] but it is also vital to design new probes with a smaller size, a stable surface, or a good fouling resistance. In this thesis, I explored the possibility to reduce size, coat nanomaterials uniformly, and improve the fouling resistance in electrode designs with novel techniques and show that our electrodes are capable of neurotransmitter detection both *in vitro* and *in vivo*. With a sensitive, robust, and reliable electrochemical sensing probe, the field will benefit both with more fundamental studies and more studies addressing neuroscience questions.

7.2 Challenges and Future Directions

7.2.1 Fundamental studies of trapping effect in neurotransmitter detection

Surface roughness and surface geometry on electrode surface strongly affect the mass transport near the sensing surface: When the diffusion thickness is comparable with surface roughness, thin-layer electrochemistry becomes the dominant mass transport near the electrode.[21,22] In conventional cyclic voltammetry, the CV shapes are symmetrical instead of typical duck shapes; in FSCV, the secondary oxidation peaks are enhanced when side products are trapped in the thin-layer cell.[23,24] We demonstrated that the trapping effect have brought new ideas about selective neurotransmitter detection, including differentiating catecholamines and dopamine from interference of ascorbic acid and DOPAC.[23,25] Future studies can be expanded to the fundamental studies about neurochemicals with a higher oxidative potential or neuropeptides, which also serve important roles in the nervous system.

In FSCV studies, the classic dopamine waveform uses the switching potential of 1.3 V to activate the carbon fiber surface by breaking the carbon bonds and adding more edge plane sites. However, some neurochemicals, including adenosine, hydrogen peroxide, and histamine, have oxidative potentials higher than 1.3 V; thus, 1.45 V needs to be used during measurement.[26–28] The differentiation of these compounds with high oxidative potentials is difficult because their CV shapes are similar and the primary oxidation peaks occur around the switching potential. Considering adenosine, H_2O_2, and histamine all have side products, most of which are also electroactive, CNT yarns may be beneficial to differentiate them by amplifying the side reactions.

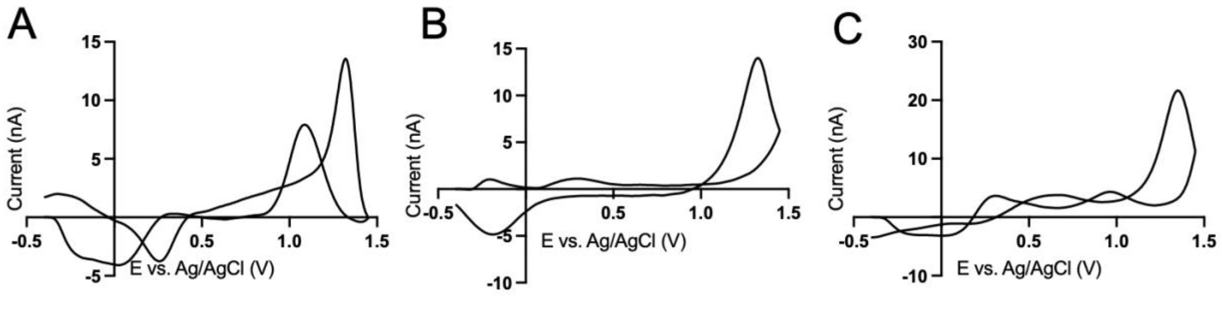

Figure 7.1. CVs obtained from CNT yarn microelectrodes at 10 Hz. A) 1 μm adenosine, B) 10 mM H_2O_2, C) 1 μm histamine.

Preliminary data in Figure 7.1 shows some example CVs obtained from CNT yarn microelectrodes. First, the secondary peak of adenosine is largely enhanced due to the trapping effect and an extinct reduction peak occurs at 0.3 V, which is not usually seen on CFMEs. Interestingly, the amplification of the secondary peak and the tertiary peak are not the same. Thus, future studies can explore the kinetics of the two side reactions of adenosine with thin-layer electrochemistry. Second, the CV shape of hydrogen peroxide obtained from CNT yarn is also different from CFMEs with small peaks at lower potentials. One hypothesis is that the ionic interactions between the oxygen radicals and carbon surfaces are amplified by the trapping effect. Another hypothesis is H_2O_2 undergoes various side reactions because, as an oxygen reactive species, H_2O_2 can form free radicals during electrochemical oxidation.[29–31] Third, the CV of histamine at CNT yarn microelectrodes has multiple peaks, which may be caused by various Faradaic or non-Faradaic processes.[28,32] The oxidation mechanism of histamine, as well as other mechanisms for adenosine and H_2O_2, are not fully investigated in a thin-layer cell; thus, future studies using trapping electrodes can explore fundamental reaction mechanisms and the thin-layer behavior of these neurochemicals. In addition, more fundamental studies can be achieved with the thin-layer electrochemistry on CNT yarn microelectrodes; for example, one could study the downstream redox pathways or the side reactions that are usually hidden behind the primary oxidation reaction. With the continuous redox cycling and product accumulation, the short-lived intermediates may also be amplified and detected.

7.2.2 Biological applications of thin-layer electrochemistry in neurotransmitter detection

Currently, thin-layer electrochemistry or trapping effects have only been studied in vitro, for example, in flow cells or a classic electrochemical cell, and the performance of a trapping electrode in a biological environment has not been explored. In theory, with continuous redox cycling in the thin-layer cell, the detection sensitivity in vivo should be enhanced by amplifying the sensing current. However, the in vivo experiment is difficult due to challenges of the size and the shape of the CNT yarn microelectrodes. The diameter of the CNT yarn that I used in this thesis is 50 μm, which is oversized for biological experiments. In addition, the disk shape limits the surface area because the sidewalls of the yarn are hidden. In future studies, new designs and smaller electrodes need to be developed to overcome the limitation of current trapping electrodes.

In addition to neurotransmitters, neuropeptides synthesized and released by neurons also play important roles in modulating neural activities. They are chemical massagers made of small chains of amino acids and they are often co-released with other neuropeptides and neurotransmitters in a neuron.[33–35] The electrochemical detection of neuropeptides is challenging because the steric effect prevents the chain from adsorbing to the electrode surface and the majority of the chain is not electroactive. However, it is possible to detect the short neuropeptide chains with electroactive amino acid residues. For example, enkephalin is a pentapeptide containing an oxidizable tyrosine.[36,37] Future studies can focus on using CNT yarn microelectrode to trap the enkephalin molecules and amplify the signal by continuous cycling in the thin-layer cell. In addition, the side reactions of tyrosine residue may provide clues for the selective detection of enkephalin. In future tissue experiments, the trapping effect may help discriminate multiple neuropeptides.

7.2.3 Nanoelectrodes for synapse or single vesicle measurement

Chapter 6 demonstrates a novel method to fabricate a nano-sized carbon needle using the 3D printing technique; however, the electrochemical sensing performance of the pyrolyzed carbon was not systematically studied. In addition, the electrochemical properties of 3D-printed nano-needle electrodes in the biological environment need to be explored and the nano-size enables measurement in small organisms. A previous study showed that the disk-shaped nanoelectrodes have successfully detected stimulated dopamine in the mushroom body of fruit flies (with brain structures of 10 mm wide), but the bulk structure on the bottom limits the applications in synapses (submicron size).[38] With the new long, thin, and straight structure of the electrode, it is possible to measure neurotransmitters in the synapse or a single vesicle with much less damage.

7.2.4 Advanced nanofabrication techniques

A reduction of electrode size is vital for neural studies because an ultra-small scale minimizes tissue damage and can probe a local cellular environment. I pioneered 3D printing with nanolithography in designing customizable micro- and nanoelectrodes with submicron resolution. It has the potential to revolutionize the development of ultra-small carbon electrodes combined with other novel techniques, such as focused ion beam (FIB). FIB can be used to decompose the carbon surface by a continuous electron beam exposure.[38] The currency and the pattern of the beam are precisely controlled. In Chapter 6, we demonstrate that FIB is capable of cutting the carbon needle at a desired position, which also inspired a new idea about constructing ultra-small carbon structures. When FIB is cutting the carbon wire (Figure 7.2), the material surface is gradually decomposed from top-down and two separate sections are generated at the end. Interestingly, an ultra-small carbon wire (with a diameter of 50 to 100 nm) can be constructed before the bulk structure is fully cut into halves. In future studies, it is possible to design a new carbon nanoelectrode by precisely removing the surface of the carbonized structures with FIB.

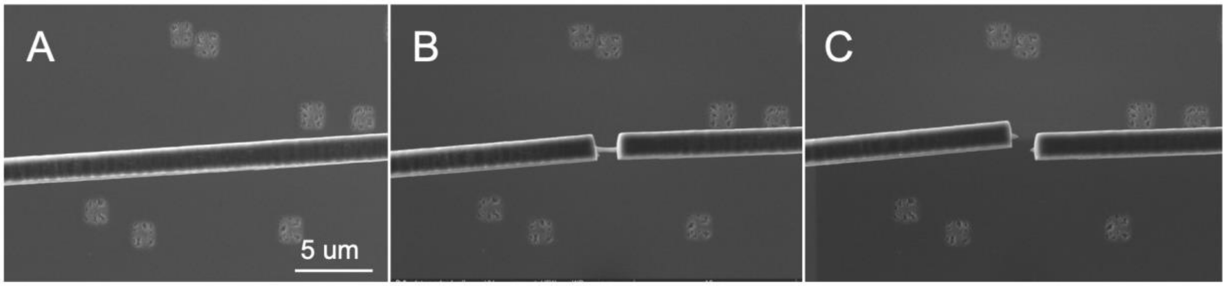

Figure 7.2. The 3D-printed carbon wire being cut by FIB. A) Before cutting. B) In the middle of the cutting. The focusing position has a gradual reduce in size. C) Finally, the wire was cut in half.

7.3 Final Remarks

Overall, this dissertation investigated the thin-layer electrochemistry in neurotransmitter detection, explored the surface chemistry of various carbon nanomaterials, and developed new carbon-based microelectrodes to overcome the limitations of CFMEs. For decades, the differentiation of catecholamines and discrimination of dopamine from interference using electrochemistry has been a challenge due to the highly similar CV shapes. In this thesis, Chapters 2 and 3 answer how thin-layer electrochemistry helps the selective detection of neurotransmitters based on different CV shapes. Chapters 4 and 5 explored the electrochemical properties of CNS and nanodiamonds in neurotransmitter measurement and how they overcome the limitation of CFMEs by reducing the electrode size and increasing the fouling resistance. Chapter 6 demonstrates a novel nanoelectrode fabrication method using pulling force during the 3D nano-printing technique. The glassy carbon structure pyrolyzed from photoresist has a customizable shape. The long, thin, and straight carbon nanoneedle is capable of future electrochemical sensing. Therefore, these fundamental electrochemistry works can potentially give rise to new insights into neuroscience studies and lead the carbon-based electrode development in a rational manner.

7.4 References

(1) Berglund, E. C.; Kuklinski, N. J.; Karagunduz, E.; Ucar, K.; Hanrieder, J.; Ewing, A. G. Freeze-Drying as Sample Preparation for Micellar Electrokinetic Capillary Chromatography-Electrochemical Separations of Neurochemicals in Drosophila Brains. *Anal. Chem.* **2013**, *85* (5), 2841–2846. https://doi.org/10.1021/ac303377x.

(2) Kuklinski, N. J.; Berglund, E. C.; Engelbrektsson, J.; Ewing, A. G. Biogenic Amines in Microdissected Brain Regions of Drosophila Melanogaster Measured with Micellar Electrokinetic Capillary Chromatography-Electrochemical Detection. *Anal. Chem.* **2010**, *82* (18), 7729–7735. https://doi.org/10.1021/ac101603d.

(3) Lima, D. R. S.; Cossenza, M.; Garcia, C. G.; Portugal, C. C.; Marques, F. F. D. C.; Paes-De-Carvalho, R.; Pereira Netto, A. D. Determination of Ascorbic Acid in the Retina during Chicken Embryo Development Using High Performance Liquid Chromatography and UV Detection. *Anal. Methods* **2016**, *8* (27), 5441–5447. https://doi.org/10.1039/c6ay01249c.

(4) Ream, P. J.; Suljak, S. W.; Ewing, A. G.; Han, K.-A. Micellar Electrokinetic Capillary Chromatography- Electrochemical Detection for Analysis of Biogenic Amines in *Drosophila m Elanogaster*. *Anal. Chem.* **2003**, *75* (16), 3972–3978. https://doi.org/10.1021/ac034219i.

(5) Sandron, S.; Heery, B.; Gupta, V.; Collins, D. a; Nesterenko, E. P.; Nesterenko, P. N.; Talebi, M.; Beirne, S.; Thompson, F.; Wallace, G. G.; Brabazon, D.; Regan, F.; Paull, B. 3D Printed Metal Columns for Capillary Liquid Chromatography. *The Analyst* **2014**, *139* (24), 6343–6347. https://doi.org/10.1039/C4AN01476F.

(6) Lane, R. F.; Hubbard, A. T. Differential Double Pulse Voltammetry at Chemically Modified Platinum Electrodes for in Vivo Determination of Catecholamines. *Anal. Chem.* **1976**, *48* (9), 1287–1292. https://doi.org/10.1021/ac50003a009.

(7) Lane, R. F.; Hubbard, A. T.; Fukunaga, K.; Blanchard, R. J. Brain Catecholamines: Detection in Vivo by Means of Differential Pulse Voltammetry at Surface-Modified Platinum Electrodes. *Brain Res.* **1976**, *114* (2), 346–352. https://doi.org/10.1016/0006-8993(76)90678-8.

(8) Dunevall, J.; Fathali, H.; Najafinobar, N.; Lovric, J.; Wigstrom, J.; Cans, A.-S.; Ewing, A. G. Characterizing the Catecholamine Content of Single Mammalian Vesicles by Collision-Adsorption Events at an Electrode. *J. Am. Chem. Soc.* **2015**, *137* (13), 4344–4346. https://doi.org/10.1021/ja512972f.

(9) Hawley, M. D.; Tatawawadi, S. V.; Piekarski, S.; Adams, R. N. Electrochemical Studies of the Oxidation Pathways of Catecholamines. *J. Am. Chem. Soc.* **1967**, *89* (2), 447–450. https://doi.org/10.1021/ja00978a051.

(10) Arrigan, D. W. M. Nanoelectrodes, Nanoelectrode Arrays and Their Applications. *Analyst* **2004**, *129* (12), 1157–1165. https://doi.org/10.1039/b415395m.

(11) Cao, Q.; Shao, Z.; Hensley, D.; Venton, B. J. Carbon Nanospike Coated Nanoelectrodes for Measurements of Neurotransmitters. *Faraday Discuss.* **2021**, *233*, 303–314. https://doi.org/10.1039/d1fd00053e.

(12) Chen, R.; Hu, K.; Yu, Y.; Mirkin, M. V.; Amemiya, S. Focused-Ion-Beam-Milled Carbon Nanoelectrodes for Scanning Electrochemical Microscopy. *J. Electrochem. Soc.* **2016**, *163* (4), H3032–H3037. https://doi.org/10.1149/2.0071604jes.

(13) Banerjee, I.; Pangule, R. C.; Kane, R. S. Antifouling Coatings: Recent Developments in the Design of Surfaces That Prevent Fouling by Proteins, Bacteria, and Marine Organisms. *Adv. Mater.* **2011**, *23* (6), 690–718. https://doi.org/10.1002/adma.201001215.

(14) Seaton, B. T.; Hill, D. F.; Cowen, S. L.; Heien, M. L. Mitigating the Effects of Electrode Biofouling-Induced Impedance for Improved Long-Term Electrochemical Measurements in Vivo. *Anal. Chem.* **2020**, *92* (9), 6334–6340. https://doi.org/10.1021/acs.analchem.9b05194.

(15) Dunham, K. E.; Venton, B. J. Improving Serotonin Fast-Scan Cyclic Voltammetry Detection: New Waveforms to Reduce Electrode Fouling. *Analyst* **2020**, *145* (22), 7437–7446. https://doi.org/10.1039/d0an01406k.

(16) Feng, T.; Ji, W.; Tang, Q.; Wei, H.; Zhang, S.; Mao, J.; Zhang, Y.; Mao, L.; Zhang, M. Low-Fouling Nanoporous Conductive Polymer-Coated Microelectrode for in Vivo Monitoring of Dopamine in the Rat Brain. *Anal. Chem.* **2019**, *91* (16), 10786–10791. https://doi.org/10.1021/acs.analchem.9b02386.

(17) Heien, M. L. A. V.; Phillips, P. E. M.; Stuber, G. D.; Seipel, A. T.; Wightman, R. M. Overoxidation of Carbon-Fiber Microelectrodes Enhances Dopamine Adsorption and Increases Sensitivity. *Analyst* **2003**, *128* (12), 1413–1419. https://doi.org/10.1039/b307024g.

(18) Jacobs, C. B.; Vickrey, T. L.; Venton, B. J. Functional Groups Modulate the Sensitivity and Electron Transfer Kinetics of Neurochemicals at Carbon Nanotube Modified Microelectrodes. *The Analyst* **2011**, *136* (17), 3557–3565. https://doi.org/10.1039/c0an00854k.

(19) Nam, K. H.; Abdulhafez, M.; Castagnola, E.; Tomaraei, G. N.; Cui, X. T.; Bedewy, M. Laser Direct Write of Heteroatom-Doped Graphene on Molecularly Controlled Polyimides for Electrochemical Biosensors with Nanomolar Sensitivity. *Carbon* **2022**, *188*, 209–219. https://doi.org/10.1016/j.carbon.2021.10.010.

(20) Puthongkham, P.; Venton, B. J. Nanodiamond Coating Improves the Sensitivity and Antifouling Properties of Carbon Fiber Microelectrodes. *ACS Sens.* **2019**, *4* (9), 2403–2411. https://doi.org/10.1021/acssensors.9b00994.

(21) Cao, Q.; Shao, Z.; Hensley, D. K.; Lavrik, N. V.; Venton, B. J. Influence of Geometry on Thin Layer and Diffusion Processes at Carbon Electrodes. *Langmuir* **2021**, *0* (0), acs.langmuir.0c03315. https://doi.org/10.1021/acs.langmuir.0c03315.

(22) Akinoglu, E. M.; Kätelhön, E.; Pampel, J.; Ban, Z.; Antonietti, M.; Compton, R. G.; Giersig, M. Nanoscopic Carbon Electrodes: Structure, Electrical Properties and Application for Electrochemistry. *Carbon* **2018**, *130*, 768–774. https://doi.org/10.1016/j.carbon.2018.01.064.

(23) Shao, Z.; Puthongkham, P.; Hu, K. K.; Jia, R.; Mirkin, M. V.; Venton, B. J. Thin Layer Cell Behavior of CNT Yarn and Cavity Carbon Nanopipette Electrodes: Effect on Catecholamine Detection. *Electrochimica Acta* **2020**, *361*, 137032. https://doi.org/10.1016/j.electacta.2020.137032.

(24) Keeley, G. P.; Lyons, M. E. G. The Effects of Thin Layer Diffusion at Glassy Carbon Electrodes Modified with Porous Films of Single-Walled Carbon Nanotubes. *Int. J. Electrochem. Sci.* **2009**, *4*, 794–809.

(25) Shao, Z.; Venton, B. J. Different Electrochemical Behavior of Cationic Dopamine from Anionic Ascorbic Acid and DOPAC at CNT Yarn Microelectrodes. *J. Electrochem. Soc.* **2022**. https://doi.org/10.1149/1945-7111/ac4d67.

(26) Adamah-Biassi, E. B.; Almonte, A. G.; Blagovechtchenski, E.; Grinevich, V. P.; Weiner, J. L.; Bonin, K. D.; Budygin, E. A. Real Time Adenosine Fluctuations Detected with Fast-Scan Cyclic Voltammetry in the Rat Striatum and Motor Cortex. *J. Neurosci. Methods* **2015**, *256*, 56–62. https://doi.org/10.1016/j.jneumeth.2015.08.017.

(27) Chen, S.; Yuan, R.; Chai, Y.; Hu, F. Electrochemical Sensing of Hydrogen Peroxide Using Metal Nanoparticles: A Review. *Microchim. Acta* **2013**, *180* (1–2), 15–32. https://doi.org/10.1007/s00604-012-0904-4.

(28) Puthongkham, P.; Lee, S. T.; Jill Venton, B. Mechanism of Histamine Oxidation and Electropolymerization at Carbon Electrodes. In *Analytical Chemistry*; 2019; Vol. 91. https://doi.org/10.1021/acs.analchem.9b01178.

(29) Roberts, J. G.; Voinov, M. A.; Schmidt, A. C.; Smirnova, T. I.; Sombers, L. A. The Hydroxyl Radical Is a Critical Intermediate in the Voltammetric Detection of Hydrogen

Peroxide. *J. Am. Chem. Soc.* **2016**, *138* (8), 2516–2519. https://doi.org/10.1021/jacs.5b13376.

(30) Meunier, C. J.; Mitchell, E. C.; Roberts, J. G.; Toups, J. V.; McCarty, G. S.; Sombers, L. A. Electrochemical Selectivity Achieved Using a Double Voltammetric Waveform and Partial Least Squares Regression: Differentiating Endogenous Hydrogen Peroxide Fluctuations from Shifts in PH. *Anal. Chem.* **2018**, *90* (3). https://doi.org/10.1021/acs.analchem.7b03717.

(31) Sanford, A. L.; Morton, S. W.; Whitehouse, K. L.; Oara, H. M.; Lugo-Morales, L. Z.; Roberts, J. G.; Sombers, L. A. Voltammetric Detection of Hydrogen Peroxide at Carbon Fiber Microelectrodes. *Anal. Chem.* **2010**, *82* (12), 5205–5210. https://doi.org/10.1021/ac100536s.

(32) Samaranayake, S.; Abdalla, A.; Robke, R.; Nijhout, H. F.; Reed, M. C.; Best, J.; Hashemi, P. A Voltammetric and Mathematical Analysis of Histaminergic Modulation of Serotonin in the Mouse Hypothalamus. *J. Neurochem.* **2016**, *138* (3), 374–383. https://doi.org/10.1111/jnc.13659.

(33) Anderson, M. S.; Halpern, M. E.; Keshishian, H. Identification of the Neuropeptide Transmitter Proctolin in Drosophila Larvae: Characterization of Muscle Fiber-Specific Neuromuscular Endings. *J. Neurosci. Off. J. Soc. Neurosci.* **1988**, *8* (1), 242–255. https://doi.org/10.1523/JNEUROSCI.08-01-00242.1988.

(34) Chen, X.; Ganetzky, B. A Neuropeptide Signaling Pathway Regulates Synaptic Growth in Drosophila. *J. Cell Biol.* **2012**, *196* (4), 529–543. https://doi.org/10.1083/jcb.201109044.

(35) Huidobro-Toro, J. P.; Donoso, M. V. Sympathetic Co-Transmission: The Coordinated Action of ATP and Noradrenaline and Their Modulation by Neuropeptide Y in Human Vascular Neuroeffector Junctions. *Eur. J. Pharmacol.* **2004**, *500*, 27–35. https://doi.org/10.1016/j.ejphar.2004.07.008.

(36) Kahsai, L.; Martin, J.-R.; Winther, Å. M. E. Neuropeptides in the Drosophila Central Complex in Modulation of Locomotor Behavior. *J. Exp. Biol.* **2010**, *213* (13), 2256–2265. https://doi.org/10.1242/jeb.043190.

(37) Kahsai, L.; Winther, Å. M. E. Chemical Neuroanatomy of the Drosophila Central Complex: Distribution of Multiple Neuropeptides in Relation to Neurotransmitters. *J. Comp. Neurol.* **2011**, *519* (2), 290–315. https://doi.org/10.1002/cne.22520.

(38) Cao, Q.; Shin, M.; Lavrik, N. V.; Venton, B. J. 3D-Printed Carbon Nanoelectrodes for In Vivo Neurotransmitter Sensing. *Nano Lett.* **2020**, *20* (9), 6831–6836. https://doi.org/10.1021/acs.nanolett.0c02844.

Appendix

COMSOL simulation

In COMSOL Multiphysics, the “Electrochemistry” module enables the study of customized physics interfaces in electrochemical cells. The physics interfaces include descriptions of the electrochemical reactions and the transport properties that affect the behaviors in the electrochemical cell, including chemical species transport, charge balances, heat transfer, and fluid flow. The module also enables the modeling of electroanalytical procedures at different operating conditions, dimensions, and electrode and electrolyte materials. In this thesis, the “Electrochemistry” or “Electroanalysis” module is used to simulate cyclic voltammetry and electric field in a two-dimensional electrochemistry cell.

Electrochemistry simulation

1. Determine the components of the electrochemical cell

To simulate a reversible redox reaction in an electrochemical cell, we defined two species A and B as the oxidant and reductant with concentrations of cA and cB. In an irreversible or quasi-reversible reaction, more species need to be introduced to the system. In the Parameters node, the parameters, values, and units are defined for simulation, which is totally changeable based on specific experiments. A variable can also be expressed in the functional form instead of numbers. The defined values are listed below:

v	0.1	[V/s]	Scan rate
c_bulk	1	[mmol/L]	Reactant bulk concentration
D	10^{-9}	[m^{-2}/s]	Diffusion coefficient
L	200	[μm]	Length of the electrochemical cell
le	30	[μm]	Length of the cylinder electrode

i0ref	$9.6485*10^{10}$	[A/m^2]	Reference exchange current density
Cdl	0.2	[F/m^2]	Double layer capacitance
E_vertex1	-0.4	[V]	Start potential
E_vertex2	0	[V]	Switching potential
c0	0	[mmol/L]	Initial product concentration at electrode

2. Create the geometry for modeling

Use the “Geometry” function to build an electrochemical cell. COMSOL allows multiple approaches to generate the geometry, by either drawing the geometry within the COMSOL software or importing an external file from a professional designing software. COMSOL allows sketching geometries and combining multiple structures in meaningful ways using geometry operations, such as Boolean, partition, move, copy, mirror, and array operations. COMSOL is only capable of generating simple structures, thus, one may need to draw complex 3D models with CAD or SOLIDWORKS.

3. Simplification when modeling electrochemical cells

In many cases, the simulation of electrochemical cells does not need to be completely thorough and detailed; instead, some insignificant factors are usually neglected to simplify the model. For example, cyclic voltammetry simulation usually neglects the charge transfer and potential gradients in electrodes, which indicates that the material is a good conductor with constant voltage and uniform current distribution over the electrode surface. The geometric structure of an electrode can be simplified as a cylinder or a plane if surface roughness is not important. The bulk boundary of an electrochemical cell in theory should be infinite far away from the electrode and a region with a fixed concentration is helpful to represent the bulk solution. If the electrolyte domain is a few orders of magnitude larger than the electrode, one could use the Infinite Elements function to project the simulation space to infinity.

In this thesis, the electrochemical cell is simplified to a square (200 μm * 200 μm) and the cylinder electrode is presented by a rectangle on the left (50 μm * 6 μm). Considering the goal of the study, the convection of the fluid flow, migration of charged ion, and thermal process are neglect in the simulation.

4. The electrochemistry behind the simulation

Cyclic voltammetry is a common electrochemical technique to study to the current against voltage as a function of time. In the simulation, a linear sweep potential is applied to the electrode from a potential E_vertex1 to a switching potential E_vertex2 and scan back to E_vertex1. The scan rate varies from 50 mV/s to 1 V/s. Electroactive species A and B are defined in the electrochemical system to represent the reducing agent and oxidant in the $Ru(NH_3)_6{}^{2+/3+}$ and undergoes a reversible redox reaction:

$$\mathrm{Ox} + e^- = \mathrm{Red}$$

The cylinder electrode is simplified to a rectangle with similar dimensions, which is assumed to have a uniform voltage and current distribution on the surface.

The "Electrolyte" node defines the mass transfer in the electrolyte. The mass transfer for reactant and product species is described by Fick's diffusion law:

$$J = -D\nabla\varphi$$

$$\frac{\partial\varphi}{\partial t} = \nabla \cdot (D\nabla\varphi)$$

Where J is the diffusion flux, D is the diffusion coefficient, ∇ is the Laplacian operator, φ is concentration, t is time.

The "No Flux" node is the default boundary condition on exterior boundaries, and "Insulation" node describes the boundaries that do not face a conductor. In the solid geometry model, there is no fluidic transmit through the electrodes and the edges of the bulk solution are well-insulated.

The "Electrode Surface" node is to model an electrochemical electrode-electrolyte interface between an electrolyte domain and an electrode boundary. The double layer current was not included in the simulation, so the current is only from the electrode reaction, following

$$\boldsymbol{n} \cdot \boldsymbol{i}_l = i_{total}$$

$$i_{total} = \sum_m i_{loc,m}$$

The "Electrode Reaction" sub-node defines the electrode kinetics for a charge transfer reaction that occurs on an electrolyte-electrode interface boundary. COMSOL defines **local current density**, $i_{loc,}$ (SI unit: A/m^2), to describe electrode kinetics at the interface between the electrolyte and the electrode. Butler-Volmer equation is

$$i_{loc} = i_0 \left[exp\left(\frac{\alpha_a F \eta}{RT}\right) - \ exp\left(-\frac{\alpha_c F \eta}{RT}\right) \right]$$

The exchange current density i_0 is defined as

$$i_0 = i_{0,0} c_R^{\alpha_c/n} c_O^{\alpha_a/n}$$

Where $i_{0,0}$ is the exchange current density at standard conditions.

The overpotential is defined as

$$\eta = E - E_{eq}$$

Where E_{eq} is the equilibrium potential is defined by the Nernst equation as

$$E_{eq} = E_{eq,0} - \frac{RT}{nF} ln \frac{c_R}{c_O}$$

For the model in this thesis, the right border of the electrochemical cell is defined as the bulk solution with a fix concentration of 1 mmol/L, and the reaction only occurs at the electrode surface, where the concentration is 0 initially. It is assumed that the solution has a uniform concentration equals to the bulk at the bulk boundary, and there is no product before the reaction occurs.

5. Set up a study and solve the problems

The “Study” node allows solving certain physics interfaces in a sequence in your model. A proper setting reduces computational time and improves convergence. “Stationary study” sub-node is capable when the initial values listed in the “Parameters node” are used in the study, or one may use the “Time-dependent study” to study sequences in a timely manner. For time-dependent studies, reducing the maximum step in the setting will smooth the CV curves and increase the accuracy. The “Parametric Sweep” sub-node allows a one-time study based on a variable with multiple values, which indicates the influence of a certain factor in the voltammograms.